HZDR-114

JOINT PROJECT: GEOCHEMICAL RETENTION OF RADIONUCLIDES ON CEMENT ALTERATION PHASES (GRAZ)

- SUBPROJECT B -

Katja Schmeide, Thimo Philipp, Jan-Martin Wolter,
Jérôme Kretzschmar, Paul Dullies, Holger Lippold,
Stefan Schymura, Thorsten Stumpf

Wissenschaftlich-Technische Berichte
HZDR-114 · 2021 · ISSN 2191-8708

WISSENSCHAFTLICH-
TECHNISCHE BERICHTE

HELMHOLTZ ZENTRUM
DRESDEN ROSSENDORF

Wissenschaftlich-Technische Berichte
HZDR-114

Katja Schmeide, Thimo Philipp, Jan-Martin Wolter,
Jérôme Kretzschmar, Paul Dullies,
Holger Lippold, Stefan Schymura, Thorsten Stumpf

JOINT PROJECT: GEOCHEMICAL RETENTION OF RADIONUCLIDES ON CEMENT ALTERATION PHASES (GRAZ)

- SUBPROJECT B -

HZDR
HELMHOLTZ ZENTRUM
DRESDEN ROSSENDORF

Druckausgabe: ISSN 2191-8708

Elektronische Ausgabe: ISSN 2191-8716

https://www.hzdr.de/publications/Publ-32735

https://nbn-resolving.org/urn:nbn:de:bsz:d120-qucosa2-751349

2021

Herausgegeben vom

Helmholtz-Zentrum Dresden - Rossendorf

Bautzner Landstraße 400

01328 Dresden

Germany

Final Report

BMWi Project No.: 02E11415B

Joint project:
Geochemical retention of radionuclides on cement alteration phases (GRaZ)

- Subproject B -

Katja Schmeide, Thimo Philipp, Jan-Martin Wolter, Jérôme Kretzschmar, Paul Dullies, Holger Lippold, Stefan Schymura, Thorsten Stumpf

Helmholtz-Zentrum Dresden-Rossendorf, Institute of Resource Ecology,
Bautzner Landstr. 400, 01328 Dresden, Germany

Gefördert durch:

Bundesministerium für Wirtschaft und Energie

aufgrund eines Beschlusses des Deutschen Bundestages

Das diesem Bericht zugrundeliegende Vorhaben wurde mit Mitteln des Bundesministeriums für Wirtschaft und Energie unter dem Förderkennzeichen 02E11415B gefördert. Die Verantwortung für den Inhalt dieser Veröffentlichung liegt bei den Autoren.

Vorhaben:

VERBUNDPROJEKT: Geochemische Radionuklidrückhaltung an Zementalterationsphasen (GRaZ), Teilprojekt B

Laufzeit des Vorhabens: 01.09.2015 bis 29.02.2020

Projektleiter: Dr. Katja Schmeide

Institut für Ressourcenökologie, Helmholtz-Zentrum Dresden-Rossendorf

Content

List of abbreviations and symbols

A/S	aluminum-to-silicon
a.u.	arbitrary units
ATR FT-IR	attenuated total reflectance Fourier transform infrared
BET	Brunauer Emmet Teller
C-S-H	calcium silicate hydrate
C-A-S-H	calcium aluminate silicate hydrate
CLQ	cross-linking quotients
Cm	curium
cryo	cryogenic (refers to low temperatures)
C/S	calcium-to-silicon
CT	charge transfer
CTR	crystal truncation rod
DIC	dissolved inorganic carbon
DSC	differential scanning calorimetry
E	resonant electronic transition line
EDX	energy dispersive X-ray spectroscopy
ESI-MS	electrospray ionization mass spectrometry
ESR	electron spin resonance
ESRF	European Synchrotron Radiation Facility
EXAFS	extended X-ray absorption fine structure
EXSY	exchange spectroscopy (NMR)
FEP	fluorinated ethylene propylene
GHS	Gipshut solution
Glenium	MasterGlenium 51®
HC	high carbonate concentration
HCP	hardened cement paste
HOMO	highest occupied molecular orbital
HT	hydrothermal
IC	internal conversion
ICP-MS	inductively coupled plasma mass spectrometry
IND	semi-empirical indicator function
ISA	isosaccharinic acid
ISC	inter system crossing
ITFA	iterative target transformation factor analysis
ITT	iterative target test
LC	low carbonate concentration
LSC	liquid scintillation counting
LUMO	lowest unoccupied molecular orbital
M	metal
MAS	magic angle spinning
MCL	mean chain length
M/L	metal-to-ligand
MS	multiple scattering
M-S-H	magnesium silicate hydrate
N_2	experiments in nitrogen atmosphere
NMR	nuclear magnetic resonance
PCE	polycarboxylate ether
PCS	photon correlation spectroscopy
PE	polyethylene
RAXR	resonant anomalous X-ray reflectivity

RN	radionuclide
RT	room temperature
S	a) surface, b) lines of vibronic progression in uranyl luminescence
S/L	solid to liquid ratio
SCM	surface complexation modelling
SEM	scanning electron microscopy
SIT	specific ion interaction
TGA	thermogravimetric analysis
TIC	total inorganic carbonate
TRLFS	time-resolved laser-induced luminescence spectroscopy
VR	vibrational relaxation
XANES	X-ray absorption near-edge structure
XAS	X-ray absorption spectroscopy
XRD	X-ray diffraction
U	uranium

A	pH correction parameter
a_{eq}	equilibrium amount of substance sorbed on a solid in mol/L
a_m	maximum amount of substance that can be sorbed on a solid
β	stability constant
b	Langmuir sorption coefficient
c_0	initial concentration in mol/L
c_{eq}	equilibrium concentration in mol/L
CN	coordination number
d	sample thickness
d_L	distance between crystallographic units
E_0	ionization energy in eV
E_h	redox potential
F	structure factor in X-ray reflectivity measurements
f	atomic scattering factor in X-ray reflectivity measurements
h	Planck's constant (6.626×10^{-34} J·s)
I	a) ionic strength in mol/L, b) intensity
k	wavenumber of photoelectron in $Å^{-1}$
K_d	distribution coefficient in L/kg
K_F	Freundlich coefficient in m^3/kg
λ	wavelength in nm
m	mass in kg
μ_E	absorption coefficient
n	number of components
n_F	Freundlich exponent
ν_s	total symmetric stretch vibration in cm^{-1}
q	momentum transfer in $Å^{-1}$
R	radial distance between atoms
σ^2	Debye-Waller factor
τ	luminescence lifetime in μs
t_i	delay time
V	volume in L
$\chi(E)$	EXAFS function
z	charge of an ion

Summary

The present report summarizes the results obtained by the Institute of Resource Ecology of the Helmholtz-Zentrum Dresden-Rossendorf within the BMWi-financed Joint Research Project "Geochemical retention of radionuclides on cement alteration phases (GRaZ)" (no. 02E11415B). The work presented here is a continuation of the studies performed in the previous BMWi project ("Retention of radionuclides relevant for final disposal in natural clay rock and saline systems", no. 02E10971), already focusing on increased ionic strengths (Schmeide et al., 2016). In the GRaZ project the focus was still on increased ionic strengths but extended to hyperalkaline conditions and moreover, beside clay materials (mainly Ca-bentonite as buffer material) also cementitious materials (calcium (aluminate) silicate hydrate (C-(A-)S-H) as main phases of hardened cement paste) were included in the radionuclide retention studies.

Thus, the objective of the GRaZ project was to study the influence of increased salinities and of hyperalkaline conditions on interaction processes in the system radionuclides – organics – clay/cementitious materials – aquifer. For this purpose, complexation, sorption and desorption studies were performed at alkaline to hyperalkaline pH conditions (pH 8-13) and under variation of the ionic strength (0.1 to 4 M) applying complex solution compositions.

Molecular structures of U(VI) citrate species dominating in the pH range 2-9 were studied by spectroscopic methods (^{1}H, ^{13}C, ^{17}O, ^{23}Na NMR, UV-Vis, FT-IR). As dominating species 2:2, 3:3, 3:2 and, above critical concentrations also 6:6 and 9:6 U(VI) citrate complexes were identified or confirmed by application of complementing methods and complex formation constants were determined.

U(VI) sorption on Ca-bentonite at (hyper)alkaline conditions in mixed electrolyte solutions (in 'diluted Gipshut solution', consisting of 2.5 M NaCl, 0.02 M $CaCl_2$, 0.02 M Na_2SO_4, and 0.0051 M KCl) was studied by means of batch sorption experiments as function of sorption time, S/L ratio, U(VI) concentration, pH value, and carbonate concentration. In addition, the influence of calcium on U(VI) and Np(VI) sorption on Ca-bentonite, Na-montmorillonite, synthetic kaolinite and/or muscovite was studied at (hyper)alkaline conditions. In further experiments, the effect of isosaccharinic acid and polycarboxylate ether on U(VI) and Eu(III) sorption, respectively, on Ca-bentonite was studied. Spectroscopic methods were applied to obtain information on aqueous speciation as well as on the underlying retention mechanisms and the local coordination environment of the retained actinide species.

The batch sorption experiments showed that U(VI) retention on Ca-bentonite can be very effective at pH>10, even in the presence of carbonate and despite the prevalence of anionic aqueous uranyl species. Above a certain pH, depending on the concentration of carbonate in solution, carbonate does not play a role in the aqueous U(VI) speciation anymore due to the predominance of hydrolysis. TRLFS measurements revealed a clear correlation between

sorption behavior and aqueous U(VI) speciation, showing that retention reaches a maximum at pH 10-12, where $UO_2(OH)_3^-$ is the predominant aqueous species. To decide whether the strong retention is caused by adsorption of anionic species to the negatively charged surface or rather by precipitation of uranates spectroscopic methods were applied. By *in situ* ATR FT-IR and CTR/RAXR experiments, which require high U(VI) concentrations (2×10^{-5} M and 5×10^{-5} M, respectively), the formation of U(VI) precipitates on the mineral surface was observed. However, solubility tests at sub-micromolar U(VI) concentrations, which were also applied for the batch sorption experiments, showed that the observed complete U(VI) removal at pH 10-12 cannot be attributed to precipitation of (earth) alkali-uranates from the solution. In order to unambiguously distinguish between surface precipitation and surface complexation, direct spectroscopic investigations of the U(VI) complexes on the Ca-bentonite surface were performed with site-selective TRLFS and EXAFS. The occurrence of luminescence line-narrowing and the frequency of the total symmetric stretch vibration obtained from the site-selective TRLFS emission spectra, indicate the presence of two U(VI) surface complexes. Also EXAFS spectroscopy confirmed the presence of two independent U(VI) sorption species on Ca-bentonite at pH 8-13. With increasing pH, the nature of the retained U(VI) complexes shifts from bidentate inner-sphere surface complexes with an overall equatorial coordination of five adsorbed on aluminol or silanol edge sites to surface complexes with a 4-fold equatorial coordination, resembling the aqueous species $UO_2(OH)_4^{2-}$. For the first time, a 4-fold coordination in the equatorial plane of U(VI) was univocally proven with the help of a multiple-scattering feature originating from the strong symmetry of the complexes, and without the need for error-prone shell fitting. The lack of scattering paths from the substrate and the comparatively high value for the total symmetric stretch vibration indicate that the high-pH-component is an outer-sphere complex.

In order to check, whether the sorption of anionic uranyl hydroxide complexes to the mineral surface is mediated by calcium cations, calcium sorption experiments and zeta potential measurements were performed. The results showed that calcium sorbs strongly on Ca-bentonite at pH 8-13 and simultaneously, the strongly negative surface charge of Ca-bentonite is partially compensated. The low U(VI) sorption on kaolinite and muscovite at pH>10 in absence of calcium is strongly increased between pH 10-12 in presence of calcium. Site-selective TRLFS confirmed the formation of calcium-induced outer-sphere U(VI) sorption complexes. An increase of sorption in presence of calcium was also observed for Np(VI) sorption on muscovite at pH 9-12.

The effect of isosaccharinic acid (ISA) on U(VI) sorption on Ca-bentonite was studied at different ISA concentrations (up to 50 mM ISA) at pH 8-13. Batch sorption experiments were complemented with TRLFS spectroscopic investigations on the aqueous U(VI) speciation in the presence of ISA. The results showed that a mobilization of U(VI) at (hyper)alkaline conditions due to formation of aqueous U(VI)-ISA complexes only occurs when ISA is

present in very high excess of U(VI) (e.g., U:ISA ratio of 1:100,000). Such high ISA concentrations are not likely to occur in deep geological repository environments.

Interaction of Eu(III) with a commercial cement superplasticizer of the polycarboxylate ether class was investigated by ultrafiltration using ^{152}Eu as a radiotracer. Based on the binding isotherm, complexation was parameterized according to the Charge Neutralization Model with respect to the content of carboxyl groups. At low ionic strength, interaction is comparable to humic substances. Potential mobilizing effects in case of release are, however, strongly counteracted by the high electrolyte contents typical of cement systems. The influence of the plasticizer on adsorption of Eu(III) onto Ca-bentonite was examined in the presence of NaCl and $CaCl_2$ (up to 4 M) at pH 9-13 under exclusion of CO_2. Already at moderate ionic strengths, the mobility of the metal is exclusively determined by the electrolyte effect, i.e., complexation is fully suppressed. Consequently, owing to the aqueous conditions in the vicinity of leached cement materials, carrier effects can be ruled out even if the polymers are set free in an intact state.

The stability of U(VI) and Cm(III) doped C-(A-)S-H phases at high ionic strengths conditions was studied applying 2.5 M NaCl, 2.5 M NaCl/0.02 M Na_2SO_4, 2.5 M NaCl/0.02 M $NaHCO_3$ or 0.02 M $NaHCO_3$ as leaching solutions which simulate the contact with North German claystone formation water. For this, actinide doped C-(A-)S-H phases were synthesized and characterized, and potential changes of actinide speciation as well as formation of secondary phases due to leaching effects were followed by spectroscopic methods.

TRLFS measurements of U(VI) doped C-S-H phases with various C/S ratios (0.6-2.0), representing different alteration stages of concrete, showed that U(VI) is mainly incorporated into the interlayer structure of C-S-H as well as sorbed on C-S-H surface. The leaching experiments showed that the composition of the leaching solution had a direct influence on the alteration of the C-S-H structure and U(VI) binding. 2.5 M NaCl led to an increased release of calcium from C-S-H gel, although the C-S-H structure remained intact. The U(VI) retention was largely unaffected due to formation of a uranophane-like phase detected by TRLFS. The additional presence of Na_2SO_4 did not show further effects on U(VI)/C-S-H stability. In the presence of carbonate (0.02 M), U(VI) retention was coupled to the alteration stage of the C-S-H structure as well as to pH evolution of leaching solution. In the case of C-S-H gel with a C/S ratio of 2, carbonate reacted preferentially with portlandite to form calcite and vaterite while the C-S-H structure and U(VI) binding remained largely unchanged. Only in the additional presence of 2.5 M NaCl, the U(VI) release was slightly increased due to an increased calcite solubility. In case of a C-S-H gel with lower C/S ratio, the polyhedral CaO plane of the C-S-H structure was increasingly destabilized due to a release of calcium into the carbonate-containing solution connected with an enhanced release of U(VI). Secondary $CaCO_3$ phases were formed, here mainly calcite and aragonite. The secondary $CaCO_3$ phases

contributed to a certain extent to U(VI) retention. At further increased carbonate concentrations (0.075 M), calcium uranyl tricarbonate was detected in solution by TRLFS.

Site-selective TRLFS measurements of Cm(III) doped C-S-H phases (C/S 1.0 and 2.0) identified at least two Cm(III) sorption sites: (i) Cm(III) with two to three water molecules in the first coordination sphere substituted against Ca^{2+} from the C-S-H interlayer and (ii) Cm(III) incorporated in the polyhedral CaO plane of the C-S-H structure with a total loss of the hydration sphere. The observed luminescence line-narrowing effect is an indication that beside the two main binding sites there are numerous, chemically similar binding sites for Cm(III) in the C-S-H phases which can be attributed to the amorphous to semi-crystalline structure of C-S-H gel. Furthermore, the C-S-H sample with a C/S ratio of 2.0 showed a co-incorporation of Cm(III) into portlandite. The Cm(III) mobilization due to leaching of the Cm(III) doped C-S-H gel in 0.02 M $NaHCO_3$ or 2.5 M NaCl/0.02 M $NaHCO_3$ was very low (0.1 to 0.7% after 60 d) regardless of C/S ratio, ionic strength, carbonate presence, or leaching time. Site-selective TRLFS investigations after leaching showed that Cm(III) was still incorporated in C-S-H gel and additionally either still partially incorporated in portlandite (at C/S 2.0) or partially incorporated into the secondary phase aragonite (at C/S 1.0). An incorporation of Cm(III) into calcite, which was clearly present in all samples as shown with XRD, was expected but could not be verified by TRLFS due to the overlap of the luminescence signals of Cm(III) incorporated in calcite with those of Cm(III) incorporated in C-S-H phases.

The C-A-S-H phases synthesized with different A/S ratios (0.06-0.18) and at different temperatures (RT and 200 °C) showed that high temperatures favor the formation of tobermorite over C-S-H whereby with increasing A/S ratio Al-tobermorite was increasingly formed. Al was identified to enter the bridging positions in the silica chain of C-S-H and tobermorite while a cross-linking between sheets was only observed at very high temperatures and A/S ratios. The U(VI) incorporation into tobermorite was decreased in comparison to C-S-H gel. Furthermore, TRLFS investigations of U(VI) doped Al-tobermorite suggest that at high A/S ratios U(VI) is sorbed on the Al-tobermorite surface and not in its interlayers. Under carbonate-containing leaching conditions Al-rich tobermorite possessed a lower retention capability for U(VI) probably due to interlayers cross-linked by Al which made the tobermorite interlayers inaccessible for U(VI). Instead the U(VI), sorbed on the tobermorite surface, was faster removed by carbonate compared to U(VI) that was bound in the tobermorite interlayer.

Zusammenfassung

Im vorliegenden Bericht sind die vom Institut für Ressourcenökologie des Helmholtz-Zentrum Dresden-Rossendorf innerhalb des BMWi-finanzierten Verbundprojektes "Geochemische Radionuklidrückhaltung an Zementalterationsphasen (GRaZ)" (Nr. 02E11415B) erzielten Ergebnisse zusammengefasst. Die hier präsentierten Studien stellen eine Weiterführung der im vorherigen BMWi-Projekt ("Rückhaltung endlagerrelevanter Radionuklide im natürlichen Tongestein und in salinaren Systemen", Nr. 02E10971) durchgeführten Untersuchungen dar, welche bereits auf erhöhte Ionenstärken fokussierten (Schmeide et al., 2016). Innerhalb des GRaZ-Projektes lag der Fokus weiterhin auf erhöhten Ionenstärken, wurde aber auf hyperalkaline Bedingungen erweitert und neben Ton (hauptsächlich Ca-Bentonit als Verfüllmaterial) wurden nun auch zementrelevante Materialien (Calcium (Aluminat) Silicat Hydrat (C-(A-)S-H) als Hauptphasen von Zementstein) in Radionuklid-Retentionsuntersuchen einbezogen.

Ziel des GRaZ-Projektes war es den Einfluss erhöhter Salinitäten und hyperalkaliner Bedingungen auf Wechselwirkungsprozesse im System Radionuklid – Organika – Ton/Zement – Aquifer zu untersuchen. Deshalb wurden Komplexierungs-, Sorptions- und Desorptionsstudien unter (hyper)alkalinen Bedingungen (pH 8-13) und bei variierenden Ionenstärken (0.1 bis 4 M) in komplex zusammengesetzten Lösungen durchgeführt.

Molekulare Strukturen von im pH-Bereich 2-9 dominierenden U(VI)-Citrat-Spezies wurden mittels spektroskopischer Methoden (^{1}H-, ^{13}C-, ^{17}O-, ^{23}Na-NMR, UV-Vis, FT-IR) untersucht. Als dominierende Spezies wurden mehrkernige U(VI)-Citrat 2:2-, 3:3- und 3:2-, oberhalb einer kritischen Konzentration auch 6:6- und 9:6-Komplexe identifiziert bzw. durch Anwendung komplementärer Methoden bestätigt und Komplexbildungskonstanten bestimmt.

Die U(VI)-Sorption an Ca-Bentonit wurde unter (hyper)alkalinen Bedingungen in komplexen Elektrolytlösungen (in 'verdünnter Gipshut-Lösung': 2.5 M NaCl, 0.02 M $CaCl_2$, 0.02 M Na_2SO_4, 0.0051 M KCl) mittels Batch-Sorptionsexperimenten als Funktion von Sorptionszeit, S/L-Verhältnis, U(VI)-Konzentration, pH-Wert und Carbonat-Konzentration untersucht. Zusätzlich wurde der Einfluss von Calcium auf die U(VI)- und Np(VI)-Sorption an Ca-Bentonit, Na-Montmorillonit, synthetischem Kaolinit bzw. Muskovit unter (hyper)alkalinen Bedingungen untersucht. In weiteren Experimenten wurde der Einfluss von Isosaccharinsäure und Polycarboxylatether auf die U(VI)- bzw. Eu(III)-Sorption an Ca-Bentonit untersucht. Spektroskopische Methoden wurden angewendet, um die aquatische Actinidenspeziation sowie zugrundeliegende Rückhaltemechanismen und lokale Koordinationsumgebungen der gebundenen Actinidenspezies zu ermitteln.

Die Sorptionsexperimente zeigten, dass die U(VI)-Rückhaltung an Ca-Bentonit bei pH>10 sehr effektiv sein kann, auch in Gegenwart von Carbonat und obwohl anionische Uranylspezies in Lösung vorliegen. Oberhalb eines bestimmten pH-Wertes, welcher von der

Carbonatkonzentration in Lösung bestimmt wird, bilden sich keine Carbonatspezies mehr sondern Hydrolysespezies. Es wurde eine starke Korrelation der U(VI)-Sorption mit der U(VI)-Speziation in Lösung gefunden. Das Sorptionsmaximum wird bei pH 10-12 beobachtet, wo $UO_2(OH)_3^-$ dominiert. Um zu entscheiden, ob die starke U(VI)-Rückhaltung auf die Sorption anionischer Spezies an die negativ geladene Mineraloberfläche oder auf das Ausfällen von Uranaten zurückzuführen ist, wurden spektroskopische Methoden angewendet. Mit den Methoden *in situ* ATR FT-IR und CTR/RAXR, welche hohe U(VI)-Konzentrationen (2×10^{-5} M bzw. 5×10^{-5} M) erfordern, wurde lediglich die Bildung von U(VI)-Ausfällungen auf der Mineraloberfläche beobachtet. Mittels site-selektiver TRLFS und EXAFS wurde hingegen die Bildung von zwei nicht-äquivalenten U(VI)-Oberflächenkomplexen bei pH 8-13 nachgewiesen und Oberflächenausfällung ausgeschlossen. Mit steigendem pH-Wert ändert sich die Struktur der sorbierten U(VI)-Komplexe von bidentaten inner-sphere Oberflächenkomplexen mit 5-facher äquatorialer Koordination zu outer-sphere Oberflächenkomplexen mit 4-facher äquatorialer Koordination, vergleichbar zu der aquatischen Spezies $UO_2(OH)_4^{2-}$.

Um zu überprüfen, ob die Sorption des anionischen Uranylhydroxid-Komplexes an die Mineraloberfläche über Calciumionen vermittelt wird, wurden Calcium-Sorptionsexperimente und Zetapotential-Messungen durchgeführt. Die Ergebnisse zeigten, dass das Calcium bei pH 8-13 stark an Ca-Bentonit sorbiert und gleichzeitig die stark negative Oberflächenladung von Ca-Bentonit teilweise kompensiert wird. Die in Abwesenheit von Calcium bei pH>10 geringe U(VI)-Sorption an Kaolinit und Muskovit wurde in Gegenwart von Calcium im pH-Bereich 10-12 stark erhöht. Site-selektive TRLFS bestätigte die Bildung von calcium-induzierten outer-sphere U(VI)-Sorptionskomplexen. Eine Erhöhung der Sorption in Anwesenheit von Calcium wurde auch für die Np(VI)-Sorption an Muskovit gezeigt.

Der Einfluss von Isosaccharinsäure (ISA) auf die U(VI)-Sorption an Ca-Bentonit wurde bei unterschiedlichen ISA-Konzentrationen (bis 50 mM ISA) im pH-Bereich 8-13 untersucht. Sorptionsexperimente wurden mit TRLFS-spektroskopischen Untersuchungen der aquatischen U(VI)-Speziation in Gegenwart von ISA ergänzt. Die Ergebnisse zeigten, dass eine U(VI)-Mobilisierung bei (hyper)alkalinen Bedingungen aufgrund der Bildung aquatischer U(VI)-ISA-Komplexe nur erfolgt, wenn ISA in sehr hohem Überschuss gegenüber U(VI) vorliegt (z.B. U:ISA = 1:100,000). Solche hohen ISA-Konzentrationen sind allerdings in tiefen geologischen Endlagern nicht zu erwarten.

Die Komplexbildung von Eu(III) mit einem kommerziellen Zement-Superplasticizer auf Polycarboxylatether-Basis wurde mittels Ultrafiltration und ^{152}Eu als Radiotracer konzentrationsabhängig vermessen und auf der Grundlage des Ladungsneutralisationsmodells mit Bezug auf den Carboxylgruppengehalt parametrisiert. Bei geringer Ionenstärke besteht demnach ein hohes Mobilisierungspotential im Freisetzungsfall, vergleichbar mit Huminstoffen. Die für Zementsysteme typischen hohen Elektrolytgehalte schränken den

Effekt allerdings stark ein. Die Auswirkung des Plasticizers auf das Adsorptionsverhalten von Eu(III) an Ca-Bentonit als Puffermaterial wurde in Gegenwart von NaCl und $CaCl_2$ (bis 4 M) unter CO_2-Ausschluss im pH-Bereich 9-13 untersucht. Die Mobilität des Metalls wird bereits bei moderaten Ionenstärken ausschließlich durch den Elektrolyteffekt bestimmt, eine Komplexbildung also vollständig unterbunden. Somit ist aufgrund des chemischen Milieus im Umfeld von gelaugten Zementmaterialien selbst im Falle einer Freisetzung der intakten Polymere nicht von Carrier-Effekten auszugehen.

Die Stabilität von U(VI)- und Cm(III)-dotierten C-(A-)S-H-Phasen bei erhöhten Ionenstärken wurde unter Anwendung verschiedener Laugungslösungen (2.5 M NaCl, 2.5 M NaCl/0.02 M Na_2SO_4, 2.5 M NaCl/0.02 M $NaHCO_3$ bzw. 0.02 M $NaHCO_3$) untersucht, welche den Kontakt mit norddeutschem Tonsteinformationswasser simulieren sollen. Actinid-dotierte C-(A-)S-H-Phasen wurden synthetisiert und charakterisiert, und potentielle Änderungen der Actinidenspeziation bzw. die Bildung von Sekundärphasen aufgrund von Laugungseffekten wurden mittels spektroskopischer Methoden nachgewiesen.

TRLFS-Messungen U(VI)-dotierter C-S-H-Phasen mit variierenden C/S-Verhältnissen (0.6-2.0, unterschiedliche Alterungsgrade von Beton darstellend) zeigten, dass das U(VI) hauptsächlich in die C-S-H-Zwischenschichten eingebaut ist und auch an die C-S-H-Oberfläche sorbiert. Laugungsexperimente zeigten, dass die Lösungszusammensetzung einen direkten Einfluss auf eine Änderung der C-S-H-Struktur und der U(VI)-Bindung hat. 2.5 M NaCl führte zu einer verstärkten Freisetzung von Calcium aus dem C-S-H-Gel, wobei die C-S-H-Struktur intakt blieb. Die U(VI)-Rückhaltung blieb weitestgehend unbeeinflusst, da sich eine Uranophan-artige Phase bildete. Die zusätzliche Anwesenheit von Na_2SO_4 zeigte keine weiteren Einflüsse auf die U(VI)/C-S-H-Stabilität. In Gegenwart von Carbonat (0.02 M) war die U(VI)-Rückhaltung mit dem Alterungsgrad der C-S-H-Struktur und mit dem pH-Wert in Lösung gekoppelt. Bei C-S-H mit einem C/S-Verhältnis von 2 reagierte das Carbonat bevorzugt mit Portlandit unter Bildung von Calcit und Vaterit, wobei die C-S-H-Struktur und die U(VI)-Bindung weitestgehend unverändert blieben. Nur bei zusätzlicher Anwesenheit von 2.5 M NaCl war die U(VI)-Freisetzung aufgrund einer erhöhten Calcit-Löslichkeit leicht erhöht. Bei C-S-H mit niedrigeren C/S-Verhältnissen wurde die oktaedrische CaO-Schicht der C-S-H-Struktur aufgrund der Freisetzung von Calcium in die carbonathaltige Lösung zunehmend destabilisiert, was zu einer erhöhten Freisetzung von U(VI) führte. $CaCO_3$-Sekundärphasen, hauptsächlich Calcit und Aragonit, wurden gebildet und trugen in gewissem Maße zur U(VI)-Rückhaltung bei. Bei weiterer Erhöhung der Carbonat-Konzentration (0.075 M) wurde Calciumuranyltricarbonat mittels TRLFS in Lösung nachgewiesen.

Mittels site-selektiver TRLFS wurden in Cm(III)-dotierten C-S-H-Phasen (C/S 1.0 und 2.0) mindestens zwei Cm(III)-Sorptionsstellen identifiziert: (i) Cm(III) mit 2-3 Wassermolekülen in der ersten Koordinationssphäre ausgetauscht gegen Ca^{2+} aus der C-S-H-Zwischenschicht und (ii) Cm(III) eingebaut in die oktaedrische CaO-Schicht der C-S-H-Struktur mit totalem

Verlust der Hydratationssphäre. Der beobachtete ‘luminescence line-narrowing’ Effekt ist ein Hinweis darauf, dass es neben den beiden Hauptbindungsstellen zahlreiche chemisch sehr ähnliche Bindungsstellen für Cm(III) in den C-S-H-Phasen gibt, was auf die amorphe bis halbkristalline Struktur von C-S-H zurückgeführt werden kann. Die C-S-H-Probe mit einem C/S-Verhältnis von 2.0 zeigte weiterhin einen Co-Einbau von Cm(III) in Portlandit. Die Cm(III)-Mobilisierung aufgrund einer Laugung der Cm(III)-dotierten C-S-H-Gele in 0.02 M $NaHCO_3$ oder 2.5 M NaCl/0.02 M $NaHCO_3$ war sehr gering (0.1 bis 0.7% nach 60 d) unabhängig vom C/S-Verhältnis, der Ionenstärke, Anwesenheit von Carbonat oder Laugungszeit. Site-selektive TRLFS-Messungen nach der Laugung zeigten, dass das Cm(III) immer noch im C-S-H-Gel und zusätzlich entweder teilweise im Portlandit eingebaut war (bei C/S 2.0) oder teilweise in der Sekundärphase Aragonit eingebaut war (bei C/S 1.0). Obwohl Calcit in allen C-S-H-Proben mittels XRD nachgewiesen wurde, konnte ein Cm(III)-Einbau in Calcit mittels TRLFS nicht bestätigt werden, da die Lumineszenzsignale für Cm(III)-Einbau in Calcit mit denen für Cm(III)-Einbau in C-S-H-Phasen überlagerten.

Die bei unterschiedlichen A/S-Verhältnissen (0.06-0.18) und unterschiedlichen Temperaturen (RT bzw. 200 °C) synthetisierten C-A-S-H-Phasen zeigten, dass hohe Temperaturen die Bildung von Tobermorit gegenüber der Bildung von C-S-H-Phasen begünstigen, wobei mit steigendem A/S-Verhältnis zunehmend Al-Tobermorit gebildet wird. Es konnte gezeigt werden, dass Aluminium verbrückende Positionen in den Silicatketten von C-S-H und Tobermorit einnimmt, wohingegen eine Vernetzung der Tobermorit-Zwischenschichten nur bei hohen Temperaturen und hohen A/S-Verhältnissen beobachtet wurde. Im Vergleich zu C-S-H-Gel wird in Tobermorit weniger U(VI) eingebaut. Zudem zeigten TRLFS-Untersuchungen von U(VI)-dotiertem Al-Tobermorit, dass bei hohen A/S-Verhältnissen das U(VI) an der Al-Tobermorit-Oberfläche sorbiert und nicht in die Zwischenschichten eingebaut wird. In carbonathaltigen Lösungen zeigte Al-reiches Tobermorit ein geringeres U(VI)-Retentionsvermögen, da die vernetzten Zwischenschichten nicht für U(VI) zugänglich waren. Das an der Tobermorit-Oberfläche sorbierte U(VI) wurde durch Carbonat leichter freigesetzt, als in den Tobermorit-Zwischenschichten eingebautes U(VI).

1. Introduction and objectives

The final disposal of high-level nuclear waste in deep geological formations behind multiple protective barriers is followed worldwide as preferred approach for the long-term management of such wastes. Objective is to ensure long-term confinement of the waste to protect people and environment. The multi-barrier system consists of three principal parts, an engineered barrier (steel or copper containers enclosing the nuclear waste), a geo-engineered barrier (low-permeability bentonite clay buffer surrounding the canisters as well as cementitious materials to ensure mechanical stability and sealing of disposal tunnels), and the geological barrier (argillaceous, crystalline or salt host rock).

Water ingress into the repository is regarded as a worst case scenario which could result in a mobilization of radionuclides. Thus, for a reliable long-term safety assessment of nuclear waste repositories the migration behavior of potentially released radionuclides in the near and far field environment has to be known. An important mechanism for retarding migration of radionuclides is the retention of radionuclides by the various components of the multi-barrier system by sorption and incorporation processes. Thus, parameters and processes that govern sorption and incorporation processes (e.g., pH value, ionic strength, initial radionuclide concentration, presence of inorganic or organic complexing ligands, colloid formation, redox conditions, kind and concentration of mineral surface sites) have to be studied.

The present project focuses on the retention behavior of Ca-bentonite and cementitious material, both constituents of the geo-engineered barrier, towards radionuclides. Due to large specific surface areas, high cation exchange capacities and availability of sorption sites these materials show high retention capacities towards radionuclides. So far, radionuclide retention was mainly studied under simplified laboratory conditions, such as pure minerals and electrolyte solutions, low ionic strengths and acidic to neutral pH conditions. There is still a lack of understanding with regard to radionuclide retention and migration at conditions prevailing in the near-field of a repository, where pore waters can be highly saline and alkaline and contain a number of different ions.

The current research aligns to conditions reported by the AnSichT project, which evaluated the feasibility of a repository in German clay formations (Jobmann et al., 2017). According to the developed site model ‘NORD’, Ca-bentonite will be used in the geo-engineered barrier as buffer material and borehole sealing. Concrete will be emplaced at different places within the repository for sealing and stabilization (Lommerzheim and Jobmann, 2014). Moreover, cementitious materials are commonly used for the solidification of low and intermediate level radioactive waste. A schematic sketch of a reposition borehole is depicted in Figure 1-1. Pore waters in cretaceous clay formations in the North German Basin at repository depth (~800 m) are characterized by high ionic strengths (Brewitz, 1982), with salinities of approx. 150 g/L (Jahn and Sönnke, 2013; Nowak and Maßmann, 2013; Wolfgramm et al., 2011)). These high

salinities can lead to an enhanced degradation of concrete upon water ingress and thus promote the formation of (hyper)alkaline cement pore waters (10 < pH < 13) (Berner, 1992). As a consequence, (hyper)alkaline conditions can prevail in deep geological repository environments for 105 years (Van Loon et al., 1997). In addition, the pore water chemistry is characterized by high complexity, whereby the various ions ubiquitous in geological environments can alter the retention potential of mineral surfaces towards radionuclides. Carbonate concentrations in the pore waters of North German clay formations are in the range of 1 mM – 0.1 M (Wolfgramm et al., 2011).

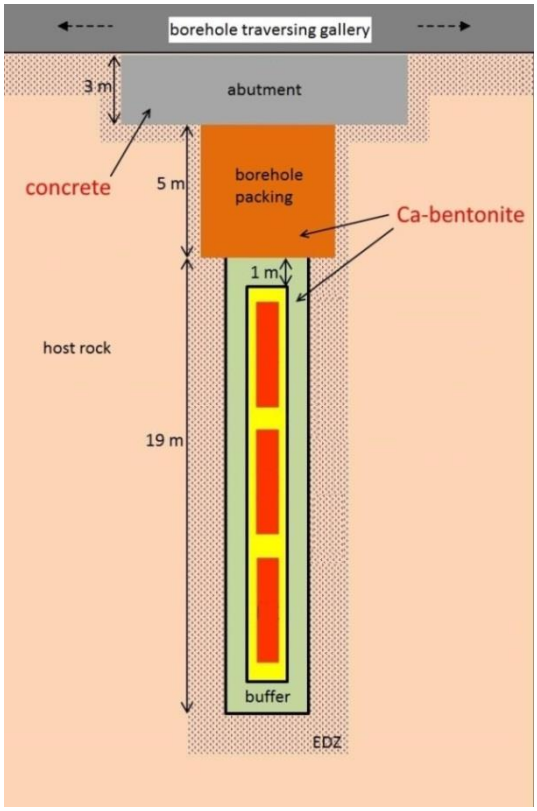

Figure 1-1: Schematic sketch of a repository borehole according to the AnSichT project (Lommerzheim and Jobmann, 2014).

In the near and far field of a deep geological repository several sources of organic material, potentially acting as mobilizing agents for radionuclides, have been identified. For instance, organic matter was detected in pore waters of Callovo-Oxfordian argillite (France) and Opalinus clay (Switzerland) formations, which represent potential host rocks for the disposal of radioactive waste (Courdouan et al., 2007a, b). Further organic material is often contained in the radioactive waste itself such as citrate and EDTA, used as decontaminants (Hummel, 2008; Suzuki et al., 2010), as well as resins, cellulose, halogenated/non-halogenated polymers (PVC, PE, PP). Moreover, cement contains polymeric additives (so-called superplasticizers) at amounts of ~ 1% to reduce the viscosity of the grout. The required percentage is higher in low-pH cement due to the content of SiO_2 nanoparticles. Nowadays, mostly polycarboxylate ethers are in use. In case of a release of these organic molecules or of their degradation

products they can act as ligands for radionuclides, leading to the formation of highly soluble and mobile radionuclide complexes.

Thus, for a realistic safety assessment of deep geological repositories, all these parameters and factors expected to influence radionuclide mobility in complex natural systems have to be considered in laboratory experiments and modelling.

Citric acid as a hydroxy-tricarboxylic acid ranks among the most prominent ubiquitous molecules in environmental processes and, eponymous for the citric acid cycle as the paramount metabolic pathway in aerobic organisms, it is also an essential and highly concentrated constituent *in vivo*. Based on its suitability for both multi-fashion and stable metal-ion complexation by its four functional groups, it is applied as a chelating and stabilizing agent or used as a model molecule for artificial substances or to mimic high molecular mass biomolecules such as humic acids or cell surfaces of microorganisms.

Accordingly, and against the background of uranium being the most relevant actinide for both its environmental abundance in general and its importance in industrial applications as raw material, such as (spent) nuclear fuel in particular, the uranium–citric acid system has been and is still employed for studying actinide interaction. For instance, the aqueous chemistry of the uranium–citric acid system has been investigated for about 70 years by potentiometry, diffraction and multi-spectroscopic methods (Allen et al., 1996; Basile et al., 2015; Berto et al., 2012; Feldman et al., 1954; Feldman and Neuman, 1951; Hummel et al., 2005; Kakihana et al., 1987; Nunes and Gil, 1987; Pasilis and Pemberton, 2003; Rajan and Martell, 1965; Vanura and Kuca, 1980). However, the aqueous chemistry of the uranium–citrate system is complex, as evidenced by both still controversial discussions on speciation, i.e. the complexes' stoichiometries and geometries, and the lack of robust thermodynamic constants.

The compilation of thermodynamic data represents a resume of 50 years of research in this area (Hummel et al., 2005). However, since this work discarded various publications for different reasons such as unspecified experimental parameters (temperature, concentrations, pH, ionic strength, etc.) or lacking structural evidence for species merely proposed – but in later publications verified – for some critical species log $\beta°$ values are poorly determined. So far, only the 1:1 and 2:2 species $[(UO_2)(Cit)]^-$ and $[(UO_2)_2(Cit)_2]^{2-}$, respectively, are well-established, with the latter known to exist in a large pH range (≈ 2–9). Furthermore, upon increasing pH values also ternary complex species $[(UO_2)_x(Cit)_y(OH)_z]$ form, but are poorly investigated.

The objective is, therefore, a rigorous structure determination of the U(VI)–citrate species over the entire pH range and, where possible, to provide critical thermodynamic constants for a better modelling of the migration behavior for adequate safety and risk assessment.

Bentonite is defined as rock that mainly consists of smectite (i.e. montmorillonite) (Hiltmann and Stribrny, 1998). Additionally it can contain variable amounts of illite, kaolinite, chlorite,

quartz, feldspars and carbonate minerals. It occurs naturally as in situ degradation product of volcanic ash (Jasmund and Lagaly, 1993) and can be subdivided into Na-bentonite and Ca-bentonite, depending on the montmorillonite interlayer cations. While the sorption behavior of U(VI) by bentonite and its main constituent montmorillonite has been extensively studied at up to weakly alkaline conditions (e.g. (Chisholm-Brause et al., 2004; Marques Fernandes et al., 2012; Tournassat et al., 2018)), its sorption affinity and the underlying mechanisms are largely unknown at hyperalkaline conditions. Moreover, no U(VI) sorption studies on clay minerals exist, which would additionally consider the effect of carbonate in the pH range 10-13.

Thus, the U(VI) sorption on Ca-bentonite at (hyper)alkaline conditions in mixed electrolyte solutions is studied by means of batch sorption experiments. Thereby, the effect of various experimental parameters (sorption time, S/L ratio, U(VI) concentration, pH value, carbonate concentration) on U(VI) sorption is assessed. Moreover, at (hyper)alkaline conditions the stability and surface charge of Ca-bentonite is studied and U(VI) solubility tests are performed. In addition, the influence of calcium on U(VI) and Np(VI) sorption on Ca-bentonite, Na-montmorillonite, synthetic kaolinite and/or muscovite is studied at (hyper)alkaline conditions. In further experiments, the effect of isosaccharinic acid, as a cellulose degradation product that might be released from radioactive waste, on U(VI) sorption on Ca-bentonite is studied. Polycarboxylate ether, a representative superplasticizer used as additive in cement production, was applied for Eu(III) complexation studies as well as to study its effect on Eu(III) sorption on Ca-bentonite. The aqueous actinide speciation is investigated with TRLFS, while the surface actinide speciation is studied applying ATR FT-IR, site-selective TRLFS, EXAFS and CTR/RAXR in order to clarify retention mechanisms on a molecular level.

Concrete is an artificial rock-like composite material that consists of hardened cement paste (HCP) and additives like sand, gravel or stones. Calcium silicate hydrate (C-S-H) is the main phase of HCP formed during hydration of cement. In modern concretes, calcium aluminate silicate hydrate (C-A-S-H) is formed since Al-containing compounds like fly ash or blast furnace slag are used to substitute sand to reduce resource consumption and the carbon dioxide footprint of the product. C-S-H is a sheet silicate consisting of polyhedral CaO planes, SiO tetrahedral chains or dimers, and interlayers filled with water or cations such as Na^+, K^+ or Ca^{2+}, similar to a defected 14 Å tobermorite-like structure. C-S-H properties are determined by the C/S ratio. In presence of Al-rich additives, Al tetrahedra can occupy bridging positions of the Si chain and cross-linking positions. C-S-H phases show a high immobilization potential for tri-, tetra- and hexavalent actinides such as Cm(III), Am(III), Np(IV), Pu(IV) and U(VI) potentially released from spent nuclear fuel (e.g. (Gaona et al., 2011; Pointeau et al., 2004; Stumpf et al., 2004)). The stability of C-(A-)S-H phases at high ionic strengths conditions, however, is hardly studied so far. High ionic strengths pore waters could modify dissolution/recrystallization processes of C-S-H gel leading to formation of

secondary phases, thus affecting the stability of C-(A-)S-H gel combined with a changed actinide retention behavior.

Thus, the influence of high ionic strength pore water on the C-(A-)S-H phase stability and their U(VI) and Cm(III) retention capability is systematically studied. For this, actinide doped C-(A-)S-H phases are synthesized applying various calcium-to-silicon (C/S 0.6-2.0) and aluminum-to-silicon (A/S 0-0.18) ratios and using different methods for actinide uptake (direct incorporation or sorption of actinides). The stability of the actinide doped C-(A-)S-H phases is studied by batch leaching experiments, where a potential release of actinides is followed over longer time spans. As leaching solutions 2.5 M NaCl, 2.5 M NaCl/0.02 M Na_2SO_4, 2.5 M NaCl/0.02 M $NaHCO_3$ or 0.02 M $NaHCO_3$, relevant to North German claystone formation water, are applied. Directly after synthesis as well as after leaching experiments, the actinide doped C-(A-)S-H phases are comprehensively characterized with TRLFS, Raman and IR spectroscopy, powder XRD, ^{27}Al and ^{29}Si MAS NMR spectroscopy, DSC, and TGA.

This research project (no. 02E11415B), funded by the German Federal Ministry for Economic Affairs and Energy (BMWi) within the framework of the Joint Research Project “Geochemical retention of radionuclides on cement alteration phases (GRaZ)”, was performed in collaboration with the R&D projects of the Johannes Gutenberg-Universität Mainz (Institut für Kernchemie), Karlsruher Institut für Technologie (Institut für Nukleare Entsorgung), Universität des Saarlandes (Anorganische Chemie), Technische Universität München (Fachgebiet Theoretische Chemie), Universität Potsdam (Institut für Chemie / Physikalische Chemie), Technische Universität Dresden (Sachgebiet Strahlenschutz) und Universität Heidelberg (Physikalisch-Chemisches Institut).

2. Complexation of U(VI) by citric acid

2.1. Experimental

2.1.1. Materials

Since the complexation concerns oxidized U(VI), samples were prepared under ambient conditions. In order to prevent light-induced degradation reactions, all samples were protected from light by aluminum foil covered vials. Appropriate aliquots of 0.5 M citric acid (ROTH, *p.a.*) and 0.5 M uranyl nitrate stock solutions in Milli-Q H_2O (18.2 MΩ cm^{-1}, Millipore) were mixed and diluted accordingly to yield the desired final concentrations, with pH adjusted by HCl and NaOH, respectively. Analogously, for NMR spectroscopy deuterated reagents, all by Deutero, were used: D_2O (99.98% D) as well as NaOD (40% in D_2O with 99% D) and DCl (37% in D_2O with 99% D) for pD adjustment according to pD = pH + 0.4 (Kresge, 1964). UV-Vis and FT-IR samples were prepared and measured under inert gas atmosphere.

2.1.2. Methods

2.1.2.1. NMR spectroscopy

Measurements were carried out at 25 °C on either a 9.4 T Varian Unity Inova 400 or a 14.1 T Agilent DD2-600 NMR system, corresponding to ^{1}H and ^{13}C resonance frequencies of 400.1 and 100.6 MHz and 599.8 and 150.8 MHz, respectively. Especially two-dimensional as well as ^{17}O (81.4 MHz) and ^{23}Na (158.6 MHz) NMR spectra were measured with the 14.1 T device. A 5 mm oneNMR™ probe together with quartz NMR tubes was used except for ^{17}O NMR, where a 10 mm low-gamma broadband direct detection probe together with 10 mm borosilicate glass NMR tubes was utilized. For all probed nuclei exact π/2 pulses were repeatedly verified; excitation was obtained by π/6 pulses, with the exception of the spin-5/2 and spin-3/2 nuclei ^{17}O and ^{23}Na, respectively, where π/2 pulses were applied. Since ^{17}O NMR signals cover a frequency range up to 100 kHz, sufficient excitation was assured by sweep-range partitioning. ^{1}H NMR spectra were acquired with solvent suppression by a pre-saturation sequence.

2.1.2.2. UV-Vis spectroscopy

By means of a continuous-flow set-up using a flow-through cuvette (d = 1 cm, quartz Suprasil®, Fisher Scientific) connected to a Varian Cary 5G spectrophotometer, UV-Vis spectra were acquired in the spectral range between 350 and 700 nm. A 100 mM $NaClO_4$ blank solution was used for baseline correction.

2.1.2.3. ATR FT-IR spectroscopy

ATR FT-IR difference spectra, averaged from 128 scans per sample, were measured in the 3900–400 cm^{-1} range on a Bruker Vertex 80/v spectrometer, utilizing a liquid-nitrogen cooled mercury cadmium telluride detector. A horizontal diamond crystal with 9 internal reflections was used as ATR accessory (DURA SamplIR II, Smiths Inc.).

2.1.2.4. Stability constant determination

UV-Vis and IR single-component spectra and stability constants together with their concentration distribution were calculated employing the multivariate factor analysis program SPECFIT/32 (Binstead et al., 2005; Gampp et al., 1985).

2.1.2.5. Quantum chemical calculation

Quantum chemical calculations were performed on DFT level (B3LYP (Becke, 1993; Lee et al., 1988)) in aqueous phase using Gaussian 09 (Frisch, 2009) utilizing the conductor-like polarizable continuum model (CPCM) (Barone and Cossi, 1998; Cossi et al., 2003). For uranium, the basis set suggested by Dolg et al. (Küchle et al., 1994) in combination with the energy-consistent small-core effective core potential (ECP) were used. As in previous studies, the most diffuse basis functions on uranium (with exponent 0.005) were omitted (Tsushima, 2011). Double-zeta plus polarization basis was used for H, C, and O valence (Krishnan et al., 1980). The Gibbs energy correction to the electronic energy was calculated at the same level from the vibrational energy levels in aqueous phase and the molecular partition functions. Obtained structures were checked to be energy minima upon justification of absence of imaginary vibrational frequencies. Basis set superposition error (BSSE) corrections and spin–orbit effect were neglected.

2.2. Results and discussion

2.2.1. Complex structures and dynamics

Remarkably, neither publication dealing with the U(VI)–citric acid system considers that, since citric acid itself is prochiral, upon complexation a chiral center in C_q is induced, with the resulting complexes possessing asymmetric carbons of different configuration and eventually forming spectroscopically distinct isomers. Moreover, although being aware of site exchange for the terminal carboxyl groups, changing configuration upon that process is not regarded.

As exemplarily depicted in Figure 2-1, the given initial orientation of the complex' two unbound $CH_2COO(H)$ is *anti*, *i.e.*, on opposite sides of the molecular plane, with the chiral centers of (*R*) and (*S*) configuration, respectively. Upon intramolecular site exchange between free (green) and U^{VI}-bound (black) terminal carboxyl, the configuration of one central carbon (C_q) changes. Finally, the $CH_2COO(H)$ are *syn*, *i.e.*, on the same side of the molecular plane,

with the molecule being of (*R*,*R*) configuration. The corresponding enantiomers, (*S*,*R*) and (*S*,*S*) respectively, are depicted below, resulting in two diastereomeric pairs of enantiomers.

Detailed ^{1}H and ^{13}C NMR spectroscopic investigations were conducted (Kretzschmar et al., 2021), however, did not allow for an unequivocal assignment of the two isomers to the respectively observed two sets of signals.

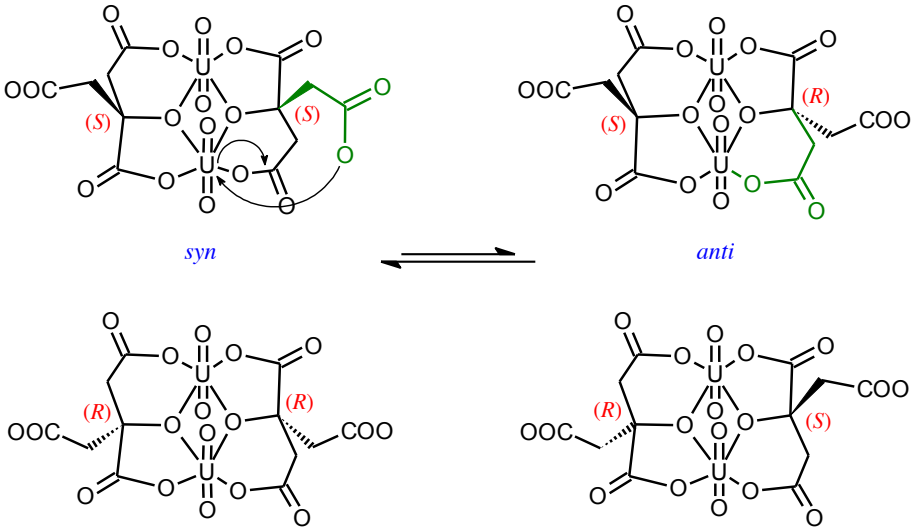

Figure 2-1: Generic structures of U(VI)–Cit 2:2 complexes, configurations of the chiral carbon atoms and an exemplary configuration change upon intramolecular site exchange (green carboxyl). Note that the resulting two diastereomeric pairs of enantiomers are denoted syn and anti, and that the water in uranyls' fifth coordination site is left out for clarity.

Finally, by means of the combination of ^{17}O NMR (note: at natural abundance) and DFT calculations an unambiguous decision on complex geometry and overall configurations was successful. It could be shown that the *syn* isomer is favored in aqueous solution in contrast to the preferably crystallizing *anti* isomer (Basile et al., 2015; Kretzschmar et al., 2021). Both isomers coexist and interconvert among one another, with exchange rates of ~30 s^{-1} at −6 °C and ~249 s^{-1} at 60 °C in acidic solution corresponding to an activation barrier of about 24 kJ mol^{-1}.

As evidenced by both UV-Vis (Figure 2-2) and ATR FT-IR spectroscopy, upon increasing pH, successive abstraction of a proton in either of the two uranium-bound water ligands yields ternary dinuclear U(VI)–citric acid mono- and bis-hydroxo (2:2:1 and 2:2:2 U(VI):Cit:OH) complexes (Berto et al., 2012; Kretzschmar et al., 2021), see Figure 2-3.

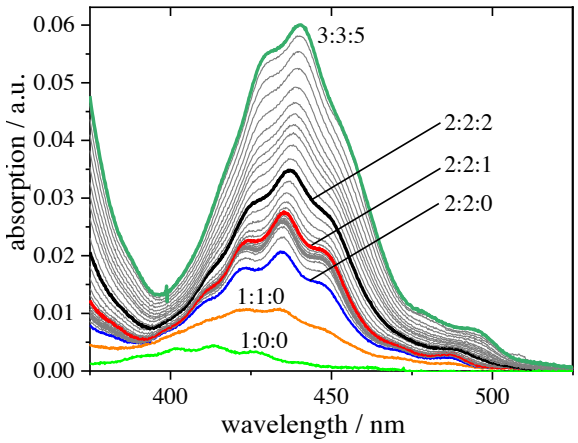

Figure 2-2: UV-Vis absorption spectra of $5 \cdot 10^{-4}$ M U(VI) solutions in presence of 0.01 M citric acid as a function of pH (I = 0.1 M, 25 °C), with the corresponding single-component spectra highlighted. Assignments denote complexes of composition U(VI):Cit:OH.

Another consequence of the increased pH value is an increasing intramolecular exchange of the CH_2COO moieties due to the reduced competition between U(VI) and H^+/D^+ for the carboxyl groups.

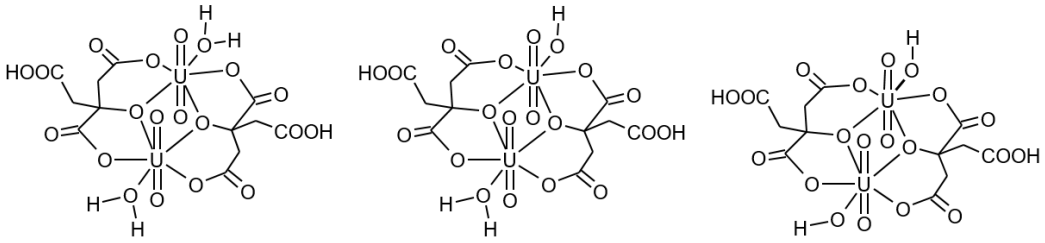

$(UO_2)_2(Cit)_2(H_2O)_2^{2-}$ 2:2:0 $(UO_2)_2(Cit)_2(H_2O)(OH)^{3-}$ 2:2:1 $(UO_2)_2(Cit)_2(OH)_2^{4-}$ 2:2:2

Figure 2-3: U(VI)–citrate–hydroxo 2:2:n ternary complexes formed upon hydrolysis of the U(VI)-coordinating water.

Depending on the sample composition, but in general above pH 5.5 also trinuclear U(VI)–citric acid complexes start to form (Figure 2-4) (Basile et al., 2015; Berto et al., 2012). Thereby, upon fine-tuning the sample conditions, especially for U:Cit ratios equal to or greater than unity, the 3:3 complex is favored. However, upon increasing pH, citric acid is displaced by hydroxo ligand, and the 3:2 complex predominates.

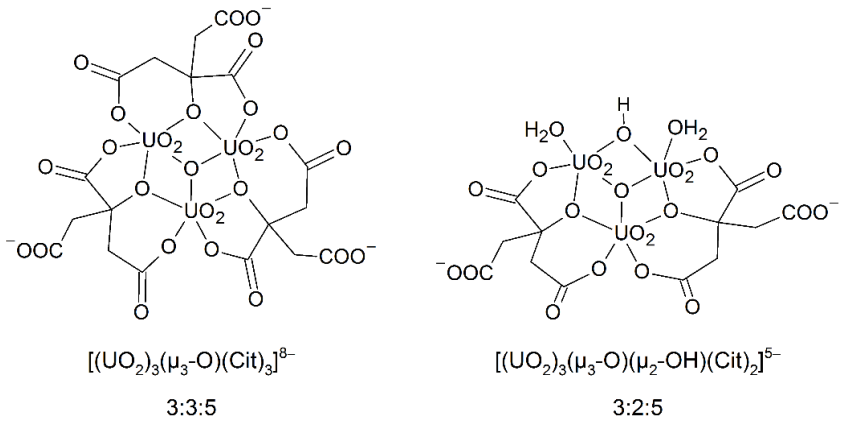

Figure 2-4: Generic structures of the trinuclear U(VI)–citrate complexes.

The molecular structures of the trinuclear complexes was evidenced in the single-crystal by Basile et al. (2015) who showed that these species can form superstructures, i.e., a 6:6 sandwich complex and a 9:6 macrocycle. In continuation of their work, focusing on aqueous solution, we found spectroscopic evidence for both the trinuclear complexes themselves and their corresponding superstructures. Particularly the formation and the solution structure of the 6:6 complex, formed by two 3:3 units sandwiching a Na^+ cation, were investigated in more detail (Kretzschmar et al., 2020).

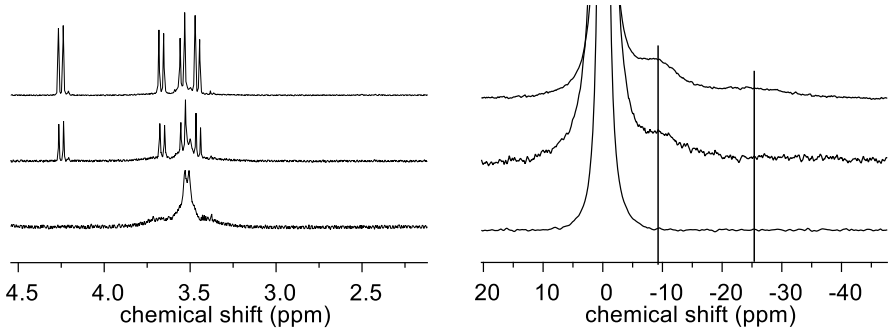

Figure 2-5: ^{1}H NMR (left) and ^{23}Na NMR (right) spectra of diluted pD 7 solutions of equimolar U(VI):Cit ratio; from top to bottom: 5, 4, and 2.5 mM, respectively. The lines indicate ^{23}Na NMR signals associated with the 6:6 sandwich complex.

Above a critical concentration determined as about 3 mM (at pD 7.0) the 6:6 U(VI)–citrate Na^+ sandwich persists in aqueous solution (Figure 2-5). This was proven both by ^{23}Na NMR spectroscopy being able to observe the sandwiched Na^+ (δ_{Na} −25 ppm) and the absence of any molecular dynamics implied by very sharp ^{1}H and ^{13}C NMR signals (Figure 2-6 A and B) in contrast to the very broad signals of the 3:2 complex (see arrows in Figure 2-6). The latter is subject to intramolecular site exchange between U(VI)-bound and free CH_2COO moieties, shows complete ligand exchange between U(VI)-bound and free citrate (EXSY, Figure 2-6 C), and likely features a dynamic equilibrium between 9:6 macrocycle formation from and disintegration into the 3:2 sub-units, with the former favored upon increasing [U(VI)].

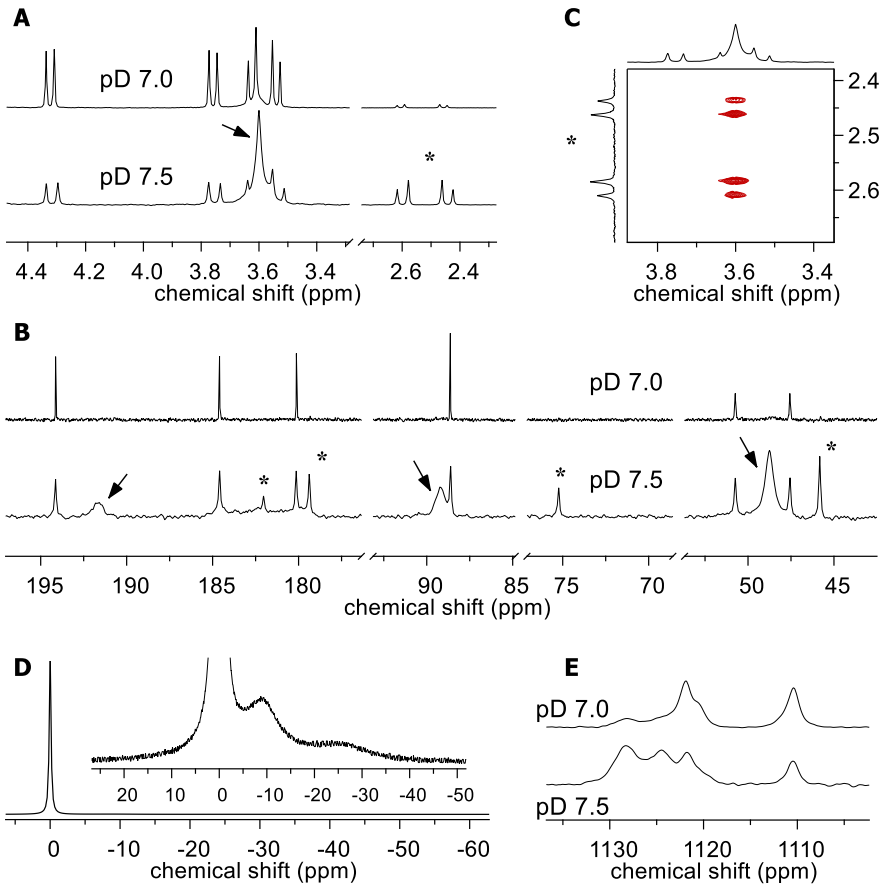

Figure 2-6: NMR spectra of solutions 250 mM each in U(VI) and citrate with pD values indicated. (A) ^{1}H, (B) ^{13}C, (C) EXSY, (D) ^{23}Na, and ^{17}O NMR. Free citrate is indicated by an asterisk. The inset in (D) is a magnified spectrum for better visualization of the broad signals.

The applied high sample concentrations allowed for acquisition of ^{17}O NMR signals (note: at natural ^{17}O abundance of 0.038%) for the uranyl-oxygen atoms. While the pD 7.0 sample contains almost exclusively the 6:6 sandwich complex, increasing pD yields species with 1.5:1 U(VI):Cit stoichiometry with concomitant liberation of citrate (NMR signals indicated by an asterisk), the latter of which being replaced by hydroxo as ligand.

Figure 2-7 (a) through (c) show NMR spectra of solutions with both increasing excess in citrate (1.67, 6.67, and 20, respectively) and increasing pD (7.5, 9.6, and 12.3, respectively). Firstly the 6:6 complex is displaced (sharp signals in (a)) so that in (b) only the 9:6 complex (dashed line) is present, existing up (strongly) alkaline media, where it is then displaced by a further complex (signal indicated by arrow, (c)).

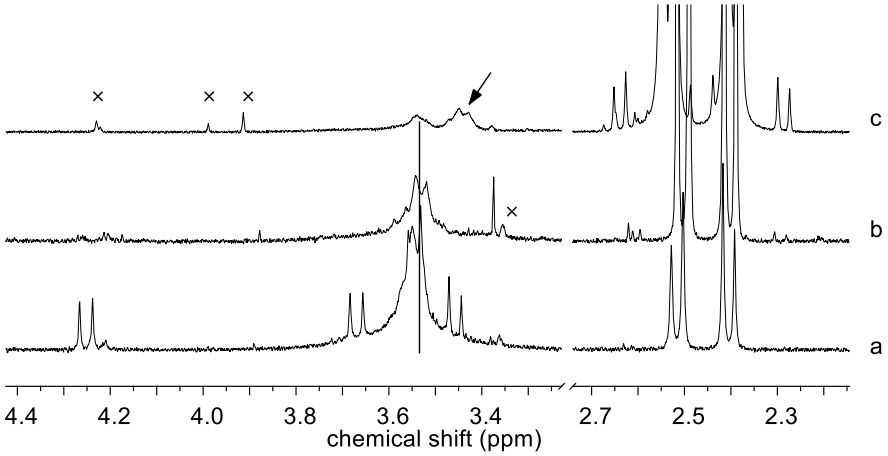

Figure 2-7: ^{1}H NMR spectra obtained from solutions of the following composition: (a) 3 mM U(VI), 5 mM Cit, pD 7.5; (b) 0.75 mM U(VI), 5 mM Cit, pD 9.6; (c) 3.75 mM U(VI), 75 mM Cit, pD 12.3. Note the signals associated with free citric acid between 2.2 and 2.7 ppm. Signals indicated by a cross are due to light-induced uranyl(VI)–citrate degradation products.

Taken together, (i) the continued red-shift of the uranyl(VI) antisymmetric stretching vibration observed in FT-IR spectroscopy, (ii) the hypsochromic shift and hypochromicity observed in UV-Vis spectra (data not shown), and (iii) the upfield-shift (increased ^{1}H shielding) indicate formation of mononuclear (ternary) uranyl(VI)–citrate–hydroxo complexes. Upon further increasing pD, even for excess citric acid, the complexes further hydrolyze as citrate cannot outcompete the hydoxo ligand.

For aqueous U(VI), at least for sub-millimolar concentrations and higher, in strongly acidic and alkaline media mononuclear hydrolytic species are found, in (slightly) acidic solution binuclear species form, and in (slightly acidic to) near-neutral up to slightly alkaline solution polynuclear species predominate. Interestingly, nuclearity and hydrolytic behavior is mirrored in the U(VI)–citric acid system (*isostructure principle*).

2.2.2. Stability constants

By means of UV-Vis absorption spectroscopy (cf. Figure 2-2) as well as ATR FT-IR absorption difference spectroscopy (not shown) the formation constants of the dinuclear and trinuclear species were determined. According to the concentrations applied, it can be assumed that the basic 3:3 and 3:2 trinuclear complexes form (instead of their superstructures). Table 2-1 summarizes the obtained constants according to

$$x\,UO_2^{2+} + y\,Cit^{3-} + z\,OH^- \rightleftharpoons (UO_2)_x(Cit)_y(OH)_z^{2x-3y-z} \qquad (2.1)$$

Table 2-1: Stability constants determined for aqueous species in the uranyl(VI) – citric acid system denoted U(VI):Cit:OH.

species		2:2:0	2:2:1	2:2:2	3:3:5	3:2:5
$\log \beta$	*a*	19.65 ± 0.04	13.79 ± 0.05	6.51 ± 0.09	–5.37 ± 0.16	—
	b	19.28 ± 0.21	14.22 ± 0.27		—	–1.03 ± 0.45

[a] UV-Vis, 0.1 M $NaClO_4$; [b] ATR FT-IR, 0.1 M NaCl

The stability constant for the 3:3:5 complex was so far not known to literature (Kretzschmar et al., 2021). Values of the other species are in good agreement with literature, only the stability constant for the 2:2:2 complex (0.1 M $NaClO_4$) is somewhat smaller compared to Berto et al. (2012): 8.22 ± 0.02 and 8.87 ± 0.01 for 0.1 M NaCl and 0.1 M KNO_3 solution, respectively. However, since these stability constants show significant dependence on the background electrolyte, particularly for highly charged species, the determined values can be considered reliable.

It can therefore concluded that citric acid / citrate forms water soluble complexes over the entire pH range. Already in strongly acid solution uranyl(VI) is chelated by multidentate coordination. The impact of citric acid on uranium(VI) mobility is remarkable up to alkaline solution owing to formation of highly negatively charged complexes. Only in strongly alkaline solution citrate's significance on U(VI) complexation and thus migration decreases.

3. U(VI) retention by Ca-bentonite at (hyper)alkaline conditions

3.1. Experimental (relates to chapters 3, 4 and 5)

In the following an overall view is given for all experimental conditions related to experiments studying (i) the U(VI) retention by Ca-bentonite at (hyper)alkaline conditions (chapter 3), (ii) the influence of Ca(II) on U(VI) and Np(VI) sorption on clay minerals at (hyper)alkaline conditions (chapter 4) and (iii) the influence of ISA on U(VI) sorption on Ca-bentonite at (hyper)alkaline conditions (chapter 5).

3.1.1. Materials

The Ca-bentonite was of the type *Calcigel*® (Clariant, Munich, Germany). This naturally occurring clay rock is mined in Bavaria (Germany) and was received as a powder with particle sizes between 0.5 and 150 μm, the dominant fraction (90%) of the particles being smaller than 90 μm (laser granulometer HELOS Series KF + Quixel (SYMPATEC, Clausthal-Zellerfeld, Germany), range "R3": 0.5-75 μm) (Figure 3-1). The mineral composition is given by the supplier according to Table 3-1, with montmorillonite being the major constituent (60-70%) and with a relatively large fraction of quartz (6-9%). The specific surface area of Ca-bentonite was determined to be 76.5 ± 0.3 m^2/g, applying the Brunauer-Emmet-Teller (BET) method, using a SA 3100 surface area analyzer (Beckman Coulter, Fullerton, USA). Before measurements, samples were degassed at the vacuum station of the instrument at 80 °C and at 100 °C for at least 8 h each. Nitrogen was used as adsorber gas.

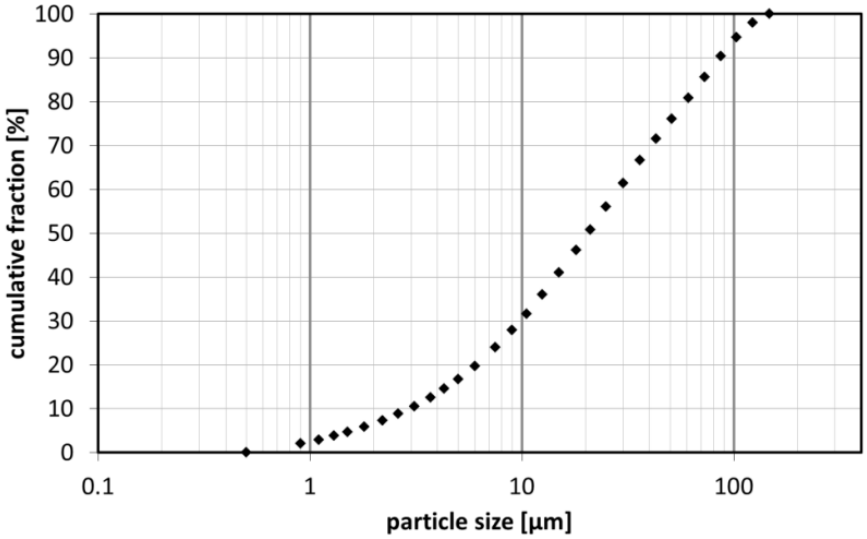

Figure 3-1: Particle size distribution of Ca-bentonite (Calcigel®) plotted as cumulative fraction against the grain size.

Table 3-1: Mineral composition of Ca-bentonite (Calcigel®) according to product information of Clariant (Munich, Germany).

Mineral phase	Fraction [%]
Montmorillonite	60 – 70
Quartz	6 – 9
Feldspar	1 – 4
Kaolinite	1 – 2
Mica	1 – 6
Others	5 – 10

Montmorillonite (SWy-2, Crook County, Wyoming, USA) was purified in the course of the PhD project of Katharina Fritsch (Fritsch, 2018) according to Bradbury and Baeyens (2009) to obtain the Na-form. A sieved fraction with particles < 63 μm and a BET surface area of 41.1 ± 0.8 m^2/g was used in the sorption experiments. Synthetic kaolinite was obtained by hydrothermal treatment of a aluminosilica gel at 220 °C by Huittinen et al. (2010) according to the procedure by Fialips et al. (2000). The BET surface area was determined to be 22.2 m^2/g. As observed by SEM, the size of the particles was < 1.1 μm and EDX mapping revealed that the synthetic kaolinite did not contain any impurities (only elements detected were O, Al and Si) (Huittinen et al., 2010). Muscovite was purchased in the form of single crystals (12.7 × 12.7 × 0.2 mm^3) from the Asheville-Schoonmaker Mica Company (USA). These single crystals were used for CTR/RAXR measurements. For the batch sorption experiments, the single crystals were milled with a ball mill, yielding a mineral powder, of which a < 63 μm grain size fraction was obtained by sieving. The BET surface area of the mineral fraction was determined to be 9.9 m^2/g (Hellebrandt, 2017). The elemental composition of muscovite and Ca-bentonite after digestion of the mineral and of kaolinite from SEM-EDX is shown in Table 3-2.

Table 3-2: Elemental composition of Ca-bentonite and muscovite from ICP-MS measurement after digestion and of synthetic kaolinite from SEM-EDX.

elemental composition [wt %]	Ca-bentonite	muscovite	kaolinite (syn.)*
Na	0.22	0.50	-
Mg	0.21	0.48	-
Al	1.87	16.35	15.81
Si	n.d.	18.28	15.98
K	0.40	8.05	-
Ca	0.60	0.04	-
Fe	3.89	1.65	-

n.d.= not determined, * Huittinen et al. (2010)

Background electrolytes in the sorption, solubility or leaching experiments were either pure NaCl (p.a., Carl Roth, Karlsruhe, Germany) solutions, mixed NaCl/$CaCl_2$ (puriss. AppliChem, Darmstadt, Germany) and NaCl/$SrCl_2$ (p.a., Merck, Darmstadt, Germany) solutions or a so called 'diluted Gipshut solution', consisting of 2.5 M NaCl, 0.02 M $CaCl_2$, 0.02 M Na_2SO_4 (p.a., Merck) and 0.0051 M KCl (p.a., Merck). Featuring a total ionic strength

of 2.63 M, it simulates in situ pore waters of North German clay and salt formations at hypothetical repository depth (Wolfgramm et al., 2011). Desorption experiments were also performed with 1 M HNO_3 (p.a., ISO, Carl Roth). Carbonate was introduced to the samples by adding aliquots of 1 M $NaHCO_3$ (p.a., Carl Roth) or 2 M Na_2CO_3 (p.a., Merck) stock solutions. The 0.636 M ISA stock solution was synthesized in a two-step procedure as described in detail in Brinkmann et al. (2019) and Dullies (2019). All solutions were prepared with deionized water (18 MΩ cm^{-1}; mod. Milli-RO/Milli-Q-System, Millipore, Schwalbach, Germany). For all experiments under N_2 atmosphere, water was additionally degassed prior to solution preparation.

$^{238}U(VI)$ addition was realized with a 1×10^{-3} M stock solution (U_{nat} in 0.005 M $HClO_4$). For the experiments applying ^{233}U, a 1.85×10^{-4} M UO_2Cl_2 stock solution was used. Np(VI) sorption experiments were performed with the highly active isotope ^{239}Np. The ^{239}Np stock solution was produced by irradiation of ^{238}U ($UO_2(NO_3)_2$ in Milli-Q water) at the TRIGA research reactor in Mainz. ^{239}Np was separated from its fission products by anion exchange chromatography with the resin Dowex AG 1-X8 (200–400 mesh, chloride form, Bio-Rad Laboratories GmbH, München, Germany) packed in a glass column. In a first step, the fission products were washed from the resin with 8 M HCl, while the neptunium remained adsorbed. Subsequently, ^{239}Np was eluted by washing with a mixture of 4 M HCl and 0.05 M HF. The obtained solution was fumed several times with 1 M $HClO_4$, to finally obtain a Np(VI) stock solution (Amayri et al., 2011). The concentration of the ^{239}Np stock solution was 1×10^{-11} M. The ^{45}Ca stock solution was purchased from PerkinElmer (Waltham, USA) as $^{45}CaCl_2$ in aqueous solution and had a concentration of 2×10^{-11} M.

3.1.2. Bentonite surface charge and stability at (hyper)alkaline conditions

3.1.2.1. Zeta potential

The surface charge of Ca-bentonite particles was determined by zeta potential measurements. Ca-bentonite suspensions (0.1 g/L) in the pH range 7-13 were prepared in 0.1 M NaCl, 0.1 M NaCl + 0.02 M $CaCl_2$ and 0.1 M NaCl + 0.02 M $SrCl_2$ in order to evaluate the effect of pH, calcium and strontium concentration. Samples were equilibrated with frequent pH adjustments until a constant pH was reached (after approx. 2 weeks). Measurements, based on laser Doppler velocimetry, were performed with a Zetasizer Nano ZS (Malvern Instruments, Malvern, United Kingdom). Potentials were averaged over ten measurements, each consisting of 10-50 scans.

3.1.2.2. Leaching at (hyper)alkaline conditions

Leaching experiments were performed as a function of pH and contact time in order to evaluate the stability of Ca-bentonite towards treatment with alkaline solutions. Duplicate samples of 10 g/L Ca-bentonite were contacted (a) with 0.1 M NaCl solution for three weeks

at pH 8-13 (increments of 0.5) and (b) with diluted Gipshut solution at pH 8 for different contact times (few seconds to three weeks). The suspensions were placed on an end-over-end shaker and frequent pH adjustments (every two or three days) were done with diluted NaOH or HCl solutions. After centrifugation (6800×*g*, 30 min) in an Avanti J-20 XP centrifuge (Beckman Coulter, Fullerton, USA), the supernatant was analyzed for Na, Mg, Al, Si, K and Ca with ICP-MS (NexION 350X, PerkinElmer, Waltham, USA), and for CO_3^{2-} with total inorganic carbon measurements (multiN/C 2100, Analytik Jena, Germany).

3.1.2.3. X-ray diffraction (XRD)

Powder XRD measurements were performed in order to evaluate the effect of saline and alkaline solutions on the stability of the main constituents of Ca-bentonite and to detect possible formation of secondary mineral phases. For that, the bentonite (10 g/L) was conditioned in the absence of CO_2 (N_2 glove box) with diluted Gipshut solution at pH 8-13 for 3 weeks with frequent pH adjustments in order to apply the same experimental conditions as in the sorption experiments. After centrifugation (6800×*g*, 30 min) the wet bentonite paste was loaded into an inert gas sample holder. The measurement was conducted with the powder X-ray diffractometer Rigaku MiniFlex 600 (Tokyo, Japan), using Cu Kα radiation and a Bragg-Brentano geometry (in θ-2θ geometry) with a step size of 0.02°2θ and a speed of 0.92 steps per second. For mineral phase identification, the ICDD PDF database was used.

3.1.3. Batch sorption experiments

In this section the general procedure of the batch sorption experiments is described. Details on radionuclide, carbonate, calcium and electrolyte concentrations, pH, S/L ratio and sorption time can be found in the sub-section to the respective type of experiment and in Table 3-3.

All sorption samples were prepared in duplicate. The mineral powder was weighed in 15 mL polypropylene centrifuge tubes (Greiner Bio-One, Frickenhausen, Germany), and was suspended with the respective background electrolyte. In the sorption experiments with ISA, calculated aliquots of the ISA stock solution were added. Experiments were carried out both at carbonate-free conditions (N_2 glove box) and in the presence of carbonate. Low dissolved carbonate (LC = 1 mM) and high dissolved carbonate (HC = 100 mM) concentrations were achieved by adding calculated amounts of $NaHCO_3$ or Na_2CO_3 to the solutions. These concentrations are representative of the lower and upper boundary of natural carbonate concentrations expected in pore waters in the North German Basin at repository depth (Wolfgramm et al., 2011). CO_2 from the ambient air did not lead to additional increase of carbonate concentration within the time frame of the experiments as analytical determination of the carbonate content confirmed stable concentrations of dissolved carbonate. Measured carbonate concentrations as a function of pH are shown exemplarily in Figure 3-2.

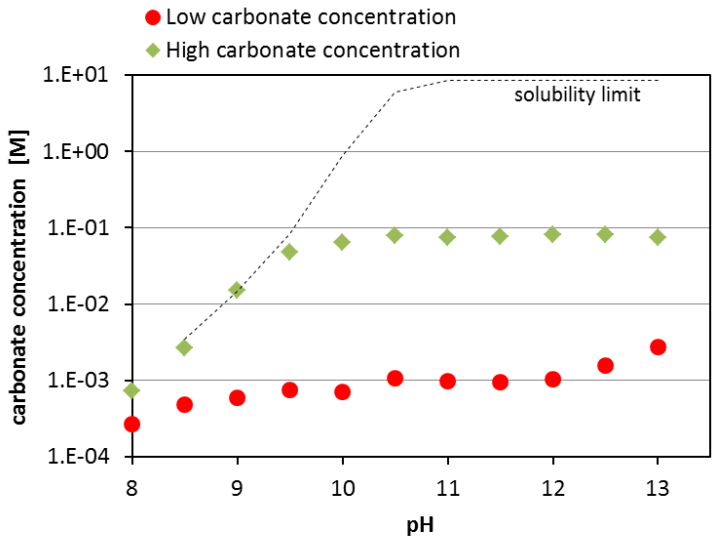

Figure 3-2: Measured carbonate concentrations in the supernatant of batch sorption samples after completion of the experiments with low (1 mM) and high (100 mM) amount of carbonate added (here exemplarily shown for U(VI) sorption on Na-montmorillonite).

Suspensions were pre-conditioned with pH-adjustments with diluted NaOH or HCl every other day until a constant pH value (±0.05) was reached (approx. two weeks). The pH was measured with an InoLab pH 7110 pH meter (WTW, Weilheim, Germany) and a SenTix MIC glass electrode (WTW). Three point calibration was executed with WTW buffer solutions (pH 6.865, 9.180 and 12.454). During this time, samples were placed in an end-over-end shaker.

In solutions with high ionic strengths, the measured potential at the pH electrode, and accordingly pH_{exp}, deviates from the true potential due to the great discrepancy between the activity coefficients of the sample and the electrolyte of the electrode (Altmaier et al., 2003). By introducing a correction parameter *A*, the true pH can be derived according to:

$$-\log[H^+] = pH_{exp} + A \quad (3.1)$$

At constant ionic strength, *A* is independent of pH. Empirical formulas exist to calculate *A* from given concentrations of pure electrolytes such as NaCl. Due to the complexity of the diluted Gipshut solution, the correction parameter *A* was determined for this system experimentally by measuring the pH of solutions with $I = 2.63$ M and known H^+ or OH^- concentrations. For several solutions with different pH, *A* was determined to be 0.4.

After pre-equilibration, U(VI), Np(VI) or Ca(II) were added to the suspensions by pipetting calculated volumes of the stock solutions. In the experiments with Np(VI), 0.01 M NaClO was added in order to stabilize the hexavalent oxidation state. The sorption time was always seven days for U(VI) based on kinetic sorption experiments (see chapter 3.2.2.1). For Np(VI), the sorption time was only three days due to the short half-life of ^{239}Np. Sorption time for Ca(II) was one day. During this time the samples were rotated in an end-over-end shaker.

For phase separation, U(VI) and Ca(II) samples were centrifuged for 30 min at 6800×*g* in an Avanti J-20 XP centrifuge (Beckman Coulter). Photon correlation spectroscopy (PCS) measurements (Zetasizer Nano ZS, Malvern Instruments) showed that this procedure led to a sufficient phase separation, leaving no measurable particle fraction in solution. Np(VI) samples were separated for 60 min at 3770×*g* in a SIGMA 3K30 centrifuge (Sigma Laborzentrifugen GmbH, Osterode, Germany).

U_{nat} concentrations in the supernatants were determined by ICP-MS (see above). ^{233}U concentrations applied for the sorption isotherms were derived from liquid scintillation counting (LSC) with a Hidex 300 SL instrument (Turku, Finland), using an Ultima Gold scintillation cocktail (PerkinElmer). Using the same scintillation cocktail, ^{45}Ca concentrations in the supernatant were measured with a Winspectral α/β, Wallac 1414 liquid scintillation counter (PerkinElmer). Equilibrium concentrations of ^{239}Np after sorption were determined with γ-ray spectroscopy, using a HPGe (GMX-13180-S, EG & G ORTEC) coaxial γ-ray detector, Canberra InSpector 2000 (model IN2K, Canberra Industries, Inc., USA). The counting time was adjusted for every measurement so that both peaks at the characteristic gamma lines at 103.4 and 106.1 keV featured at minimum 10,000 counts each.

From the radionuclide equilibrium concentration (c_{eq}) and the initial radionuclide concentration (c_0) [M] the percentage of radionuclide (RN) sorption is calculated according to equation (3.2).

$$RN\ sorbed\ [\%] = \frac{c_0 - c_{eq}}{c_0} \times 100\% \tag{3.2}$$

Furthermore, K_d values are determined using equation (3.3)

$$K_d = \frac{c_0 - c_{eq}}{c_{eq}} \times \frac{V}{m} \tag{3.3}$$

where V [L] is the volume of the solution and m [kg] the mass of the solid.

K_d values strongly depend on the experimental conditions (pH, ionic strength, metal concentration, temperature, present ligands, competing ions) and are therefore not applicable for extrapolation. The dependence of sorption on the metal concentration can be expressed with sorption isotherms. If the amount of substance sorbed on the solid in equilibrium a_{eq} is linearly dependent on the equilibrium concentration of substance in the solution c_{eq}, sorption can be described by the linear Henry isotherm (Henry, 1803) (equation (3.4)).

$$a_{eq} = K_d \times c_{eq} \tag{3.4}$$

In natural systems, however, sorption mechanisms are quite complex, which calls for more sophisticated sorption isotherms, considering more parameters. The most commonly used isotherms are the Freundlich and the Langmuir isotherm. The Freundlich isotherm (equation

(3.5)) considers interactions between the sorptive and ions that have already been adsorbed. The more ions/molecules are already adsorbed, the lower is the chance that additional sorption can take place.

$$a_{eq} = K_F \times c_{eq}^{n_F} \tag{3.5}$$

K_F is the Freundlich coefficient [m^3/kg] and n_F is the Freundlich exponent [-] with n < 1 (Stumm, 1992). The Langmuir isotherm (equation (3.6)) takes into account that there is saturation at the surface due to limited sorption sites by adding the parameter a_m, representing the maximum amount of substance that can be sorbed onto the solid. b is the Langmuir sorption coefficient (Langmuir, 1918).

$$a_{eq} = \frac{a_m \times b \times c_{eq}}{1 + b \times c_{eq}} \tag{3.6}$$

In order to evaluate the extent of U(VI) sorption onto the vial walls, samples without mineral phase (only background electrolyte and radionuclide) were prepared and treated equivalently to the sorption samples. In the absence of CO_2, the loss of U(VI) from the solution to the vial walls was significant. However, this effect only occurred when the mineral phase was absent. This was proven by treating the used and washed vials with 1 M HNO_3. While for the sample vials without mineral phase, the removed U(VI) could be fully retrieved, no U(VI) was detected after treating the sorption sample vials. Consequently, U(VI) sorption on the vial walls can be considered as insignificant as long as the sorbing mineral is present.

Table 3-3: Overview of all performed batch sorption experiments including experiments described in chapter 4 and chapter 5. 'N2' refers to experiments in the absence of CO_2 (minimal carbonate concentration from bentonite leaching), 'LC' to low carbonate concentration (1 mM) and 'HC' to high carbonate concentration (100 mM). 'Sorp.' = Sorptive, 'dil. GHS' = dil. Gipshut solution, 'ISA' = Isosaccharinic acid.

Sorptive	Experiment	Mineral	Electrolyte	S/L [g/L]	atm.	[Sorp.] [M]	pH
^{238}U(VI)	S/L ratio	Ca-bentonite	dil. GHS	0.1-20	N_2	5×10^{-7}	8, 10.5
					LC	1×10^{-6}	8
	Kinetics	Ca-bentonite	dil. GHS	10	N_2	5×10^{-7}	8, 10.5, 12.5
					LC	1×10^{-6}	8
					HC	1×10^{-6}	12.5
	pH-edge	Ca-bentonite	dil. GHS	10	N_2	5×10^{-7}	8-13
					LC	1×10^{-6}	8-13
					HC	1×10^{-6}	8-13
		Ca-bentonite	0.1 M NaCl + 5×10^{-4} M to 5×10^{-2} M ISA	10	N_2	5×10^{-7}	8-13
		Na-mont-morillonite	0.1 M NaCl	10	N_2	5×10^{-7}	8-13
					LC	1×10^{-6}	8-13
			2.6 M NaCl	10	N_2	5×10^{-7}	8-13
					LC	1×10^{-6}	8-13
		Kaolinite	0.1 M NaCl	0.5	N_2	5×10^{-7}	10-13
			0.1 M NaCl + 0.02 M $CaCl_2$	0.5	N_2	5×10^{-7}	10-13
		Muscovite	0.1 M NaCl	3	N_2	5×10^{-7}	8-13
			0.1 M NaCl + 0.02 M $CaCl_2$	3	N_2	5×10^{-7}	8-13
			0.1 M NaCl + 0.02 M $SrCl_2$	3	N_2	5×10^{-7}	10-13
	Desorption	Ca-bentonite	dil. GHS	10	N_2	5×10^{-7}	11, 13
			5 M NaCl	10	N_2	5×10^{-7}	11
			1 M HNO_3	10	N_2	5×10^{-7}	1
^{233}U(VI)	Isotherms	Ca-bentonite	dil. GHS	10	N_2	1×10^{-9} to 3.2×10^{-6}	8, 10.5, 12.5
					LC	1×10^{-9} to 3.2×10^{-4}	8
^{239}Np(VI)	pH-edge	Muscovite	0.1 M NaCl	3	Ar	1×10^{-11}	8-13
			0.1 M NaCl + 0.02 M $CaCl_2$	3	Ar	1×10^{-11}	8-13
[^{45}Ca]Ca(II)	S/L ratio	Ca-bentonite	-	0.2-20	N_2	2×10^{-4}	10
	pH-edge	Ca-bentonite	-	10	N_2	2×10^{-4}	8-13

3.1.3.1. S/L ratio dependence

In order to determine a reasonable solid to liquid ratio (S/L ratio) for all following experiments, the sorption of U(VI) by Ca-bentonite was tested with S/L ratios of 3, 5, 9, 13 and 20 g/L, both in the absence of CO_2 as well as at low carbonate concentration, at equilibrium pH of the Ca-bentonite in the diluted Gipshut solution (pH 8). Additional experiments were performed at pH 10.5 at S/L ratios of 0.1, 0.5, 1 and 5 g/L. The U(VI) concentration was 1×10^{-6} M in the presence and 5×10^{-7} M in the absence of CO_2.

The effect of the solid to liquid ratio on Ca(II) sorption on Ca-bentonite was investigated at pH 10 in a 2×10^{-4} M $CaCl_2$ solution with a spike of 1×10^{-12} M ^{45}Ca. S/L ratios of 0.2, 1, 2, 10 and 20 g/L were achieved by weighing in different amounts of Ca-bentonite powder.

3.1.3.2. Kinetic sorption experiments

The kinetics of the U(VI) sorption process on Ca-bentonite in the diluted Gipshut solution was studied by taking and analyzing aliquots from bentonite suspensions (10 g/L) at different times (1 h, 6 h, 1, 2, 3, 4, 7 days) after the addition of uranium. Such kinetic series were performed in the absence of CO_2 ([U] = 5×10^{-7} M) at pH 8, 10.5 and 12.5, at low carbonate concentration ([U] = 1×10^{-6} M) at pH 8 and at high carbonate concentration ([U] = 1×10^{-6} M) at pH 12.5.

3.1.3.3. Sorption isotherms

At the high ionic strength of the diluted Gipshut solution, ICP-MS is not suitable for determination of U(VI) concentrations < 1×10^{-7} M, since operation of the instrument in this case requires strong dilution. Therefore, ^{233}U was used as a tracer for U(VI) sorption isotherms and ^{233}U(VI) concentrations were determined with liquid scintillation counting. U(VI) sorption isotherms on Ca-bentonite were recorded at pH 8 both in the absence of CO_2 and at low carbonate concentration with [^{233}U]U(VI) concentrations of 1×10^{-9} M to 3.2×10^{-6} M and 1×10^{-9} M to 3.2×10^{-4} M, respectively. Additional sorption isotherms at pH 10.5 and 12.5 were recorded in the absence of CO_2.

3.1.3.4. pH dependency of sorption

U(VI) sorption on Ca-bentonite as a function of pH was investigated in diluted Gipshut solution and 0.1 M NaCl at a S/L ratio of 10 g/L in the absence of CO_2 ([U] = 5×10^{-7} M), at low carbonate concentration ([U] = 1×10^{-6} M) and at high carbonate concentration ([U] = 1×10^{-6} M), each in the pH range 8-13, with increments of 0.5.

The influence of isosaccharinic acid on U(VI) retention in this system was studied in three additional pH-edges with ISA concentrations of 5×10^{-4}, 5×10^{-3} and 5×10^{-2} M (corresponding to U:ISA ratios of 1:1,000, 1:10,000 and 1:100,000), achieved by addition of calculated

aliquots of the ISA stock solution after two weeks of pre-equilibration of Ca-bentonite suspensions. After another week of reaction time U(VI) was finally added to the suspensions.

The influence of calcium on U(VI) sorption was investigated in a number of pH-dependent sorption experiments with different minerals and different background electrolytes. These experiments include sorption on Ca-bentonite in 0.1 M NaCl (pH 8-13), on Na-montmorillonite in 0.1 and 2.6 M NaCl (pH 8-13), on kaolinite in 0.1 M NaCl and 0.1 M NaCl + 0.02 M $CaCl_2$ (pH 10-13) and on muscovite in 0.1 M NaCl, 0.1 M NaCl + 0.02 M $CaCl_2$ and 0.1 M NaCl + 0.02 M $SrCl_2$ (pH 8-13).

Np(VI) sorption on muscovite as a function of pH (pH 8-13, increments of 0.5) was investigated in 0.1 M NaCl and in 0.1 M NaCl + 0.02 M $CaCl_2$, both in the absence of CO_2 (Ar glove box) and at an initial Np(VI) concentration of 1×10^{-11} M.

Ca(II) sorption experiments on Ca-bentonite (10 g/L) as a function of pH (pH 8-13) were performed in the absence of CO_2 (N_2 glove box) in 2×10^{-4} M $CaCl_2$ spiked with 1×10^{-12} M ^{45}Ca.

3.1.3.5. Desorption

The stability and reversibility of U(VI) sorption on Ca-bentonite at pH 11 in the absence of CO_2 was tested in batch desorption experiments. After performing sorption experiments in diluted Gipshut solution (as described in chapter 3.1.3.4), the samples were centrifuged for 10 min at 3000×*g* (Avanti J-20 XP) and the supernatant was removed. After that, 10 mL of four different U(VI)-free solutions (dil. Gipshut solution at pH 11 and 13, 5 M NaCl and 1 M HNO_3) were added and the U-loaded Ca-bentonite was resuspended. After one week of reaction time the supernatant was analyzed for remobilized U(VI) with ICP-MS.

3.1.4. Solubility tests

Samples without mineral powder were prepared in order to investigate the solubility of U(VI) in the bentonite leachate under the given experimental conditions. As polypropylene centrifuge tubes showed significant uptake of U(VI) in the absence of the mineral, for these experiments fluorinated ethylene propylene (FEP) vials (Thermo Scientific Nalgene, Waltham, USA) were used, featuring an inert surface that minimizes uranium adsorption. Leachates of Ca-bentonite were produced at different pH values by contacting it with diluted Gipshut solution (10 g/L) for 2 weeks with continuous pH adjustments (pH 8 – 12.5, increments of 0.5). After phase separation, U(VI) was added to 10 mL of the leachate to reach a U(VI) concentration of 5×10^{-7} M. Seven days after U(VI) addition, the samples were ultracentrifuged (60 min, 187,000×*g*, Optima XL 100K, Beckman Coulter) and the supernatants were analyzed for uranium with ICP-MS. The solubility experiments were conducted in the absence of CO_2 (N_2 glove box).

3.1.5. TRLFS

The aqueous speciation of U(VI) in the diluted Gipshut solution was investigated with non-selective TRLFS at λ_{ex} = 266 nm. Measurements were performed in the absence of CO_2, at low and at high carbonate concentrations, equivalent to the pH-dependent sorption studies. Batch samples with uranium concentrations of 5×10^{-7} M in diluted Gipshut solution were prepared in FEP vials at pH 8-13. After 7 days, with frequent pH adjustments, 1 mL of each sample was filled in a polystyrene one time cuvette (Carl Roth, Karlsruhe, Germany) and quick-freezed with liquid nitrogen. TRLFS measurements were performed at 153 K by using a cryogenic cooling system. The laser system used was a Nd:YAG laser (Minilite high-energy solid-state laser; Continuum, San Jose, USA) as described in Steudtner et al. (2011) operating at an average pulsed energy of 0.3 mJ. The emission of the samples was recorded using an iHR550 spectrograph (HORIBA Jobin Yvon, Bensheim, Germany) and an ICCD camera (HORIBA Jobin Yvon). A gate width of 2000 μs and a slit width to the spectrograph of 2000 μm were chosen. Spectra were recorded at different delay times (t_i), defined by the equation $t_i = 0.1 + 0.005 \cdot x + i^{4/2000}$, with i being the step number. At each time step, 100 measurements were averaged. Peak positions were identified from second derivatives of FFT-filter smoothed spectra by determining their negative maxima. Luminescence lifetimes were obtained by plotting cumulative intensities at each time step against delay time. Data points were then fitted exponentially.

Site-selective TRLFS was applied to investigate the U(VI) species sorbed on the surface of Ca-bentonite, muscovite and kaolinite. Samples were prepared in the absence of CO_2 as described in chapter 3.1.3, but with lower S/L ratio (0.3 g/L) in order to increase the U(VI) surface coverage. Two samples were prepared with Ca-bentonite in diluted Gipshut solution at pH 11, where sorption is at maximum: One with the same U(VI) concentration as in the pH-dependent sorption experiments (5×10^{-7} M) and one with a U(VI) concentration two orders of magnitude higher than that (5×10^{-5} M) to provoke U(VI) precipitation for comparison. U(VI) sorption on muscovite was investigated in 0.1 M NaCl at pH 11 and in 0.1 M NaCl + 0.02 M $CaCl_2$ at pH 11 and 12. Kaolinite samples were prepared in 0.1 M NaCl at pH 10 and in 0.1 M NaCl + 0.02 M $CaCl_2$ at pH 12. After ultracentrifugation (187,000×g) each wet paste pellet was transferred into a copper sample holder with a sealable quartz glass lid. Measurements were performed with a pulsed Nd:YAG (Continuum Surelite II, San Jose, USA) pumped dye laser setup (Radiant Dyes Narrow Scan K, Wermelskirchen, Germany). The emitted luminescence light was directed into a spectrograph (Shamrock 303iAndor Oxford Instruments, Abingdon, United Kingdom) equipped with a polychromator with 300, 600, and 1200 lines/mm gratings, and the emission was monitored with an intensified CCD camera (Andor iStar, Oxford Instruments) 10 µs after the exciting laser pulse in a time window of 10 ms. The laser pulse energy and the exact excitation wavelength were monitored in every measurement with an optical power meter (Newport 1918-R, Irvine, USA) and a wavelength meter (High Finesse WS-5, Tübingen, Germany), respectively. Spectra were

recorded at excitation wavelengths between 460 and 520 nm with a step size of 0.2 nm. Additionally, time-resolved luminescence spectra were recorded at selected excitation wavelengths with a temporal step size of 10 μs. To achieve the desired spectral resolution the solid samples were cooled to ~10 K in a helium-refrigerated cryostat.

3.1.6. *In situ* ATR FT-IR spectroscopy

Infrared spectra were measured from 1800 to 800 cm^{-1} on a Bruker Vertex 80/v vacuum spectrometer equipped with a Mercury Cadmium Telluride (MCT) detector. A KRS-5 diamond crystal was used and 256 scans were averaged for each spectrum. 2.5 μL of a 2.5 g/L Ca-bentonite suspension in 0.1 M NaCl was evaporated to leave a mineral film on the surface of the ATR diamond crystal. First, the mineral film was conditioned by rinsing with the blank solution for 60 min at a flow rate of 100 µL/min. Thereafter, sorption was induced by rinsing the mineral film for 120 min with 0.1 M NaCl, containing 2×10^{-5} M U(VI). Finally, the mineral film was flushed again with 0.1 M NaCl for 60 min. Three samples at different pH (6.8, 8 and 10.5) were prepared in the absence of CO_2 in FEP vials (Thermo Scientific Nalgene) and the pH was adjusted several times until a constant value was obtained. The U(VI) containing solution was ultracentrifuged (60 min, 187,000×g, Optima XL 100K, Beckman Coulter) directly before the experiment in order to remove colloids from solution which might have been formed due to reduced U(VI) solubility at elevated pH.

3.1.7. EXAFS spectroscopy

Batch sorption samples (U(VI) on Ca-bentonite) for the EXAFS measurements were prepared as described in chapter 3.1.3. A total of 10 samples (Table 3-4) with variable pH and carbonate concentration was prepared with a S/L ratio of 0.3 g/L, leading to sufficiently high surface coverage, despite the low initial U(VI) concentrations. In order to achieve such a low S/L ratio with sufficient solid material (150 mg), the volume of suspensions was increased to 500 mL (polypropylene centrifuge tubes, Corning, Oneonta, USA). Phase separation was done with ultracentrifugation (see above), after which the Ca-bentonite wet paste was transferred into polyethylene (PE) sample holders. Samples were covered with capton tape, enclosed with a PE cap and finally sealed by soldering.

The U L_{III}-edge (17,166 eV) EXAFS spectra were recorded at the Rossendorf Beamline (ROBL, BM20) at the European Synchrotron Radiation Facility (ESRF) (Matz et al., 1999), operated at 6 GeV and an electron current of 200 mA. For rejection of higher harmonics two Rh-coated mirrors were used and the incident white X-rays were monochromatized with a liquid nitrogen cooled Si(111) double crystal monochromator. Samples were measured under cryogenic conditions (15 K) by using a closed cycle He-cryostat. In order to increase the signal-to-noise ratio for each sample, a maximum of 11 fluorescence spectra were recorded by counting the signal of the U $L\alpha_{1,2}$ fluorescence lines with a 13-element Ge-detector. For energy calibration the absorption of a Y metal foil at the K-edge (17,038 eV) was measured

simultaneously during each energy scan. The incident photon flux and the absorption were measured with gas filled ionization chambers. For the calculation of the photoelectron wave vector (k) the ionization potential (E_0) was set arbitrarily to $E_0 = 17{,}185$ eV.

EXAFSPAK (George and Pickering, 1995) and WinXAS (Ressler, 1998) were used for the data treatment which included a correction for the dead-time of the 13 fluorescence channels, energy calibration, averaging of the multiple sample scans, isolation of the EXAFS signal from the averaged data and shell fit. As a reference for the aqueous $UO_2(OH)_4^{2-}$ complex we used published data from Moll et al. (2014), where six absorption spectra were measured at room temperature. For the shell fit theoretical scattering phase and amplitude functions were calculated with the ab-initio scattering code FEFF 8.20 (Ankudinov et al., 1998) by using an arbitrary structural model of the sorption complex and of the aqueous $UO_2(OH)_4^{2-}$ complex.

Iterative target transformation factor analysis (ITFA) (Rossberg et al., 2003) was applied in order to quantify the structurally different sorption complexes and to isolate their spectra from the EXAFS spectral mixtures of the sorption samples. ITFA is a well-established tool for the decomposition of spectral mixtures into their spectral components and fractions. In the first step the spectral mixtures are decomposed into a set of eigenvectors and the semi-empirical indicator (*IND*) function (Malinowski, 2002) is applied in order to estimate the number of components (n), while *IND* reaches its lowest value at n. Once n is determined the linear combination of the n eigenvectors enables a reproduction of all spectral mixtures. The spectral components originate from the pure chemical species and/or backscattering signals stemming from atoms which change their fraction and/or coordination number (*CN*) as a function ($F(P)$) of a varied physicochemical parameter (P) like the pH, concentration, etc.. The distribution of the components as $F(P)$ is model independently estimated by an orthogonal rotation of the eigenvectors through the VARIMAX procedure (Kaiser, 1958). In the third step and in order to calculate the spectra of the components and their fractional contribution for each spectral mixture, n^2-n fractions of the components must be known and fixed during the iterative target test (ITT) (Brayden et al., 1988).

Table 3-4: EXAFS samples and their pH, carbonate concentration and U(VI) surface load.

Sample no.	Sample name	CO_3^{2-} conc. [M]	pH	U(VI) load [ppm]
1	U_Bent_N2_pH8	-	8.0	331.2
2	U_Bent_N2_pH9	-	9.0	327.6
3	U_Bent_N2_pH10.5	-	10.5	375.6
4	U_Bent_N2_pH11.5	-	11.5	259.0
5	U_Bent_LC_pH9	0.001	9.0	340.3
6	U_Bent_LC_pH10.5	0.001	10.5	1080.5
7	U_Bent_LC_pH11.5	0.001	11.5	1173.3
8	U_Bent_LC_pH12.5	0.001	12.5	1091.2
9	U_Bent_HC_pH12	0.1	12.0	591.4
10	U_Bent_HC_pH12.5	0.1	12.5	715.2

3.1.8. CTR/RAXR

X-ray reflectivity measurements were conducted at the GeoSoilEnviroCARS (GSECARS) beamline 13-ID-C at the Advanced Photon Source (APS, Lemont, USA). The used diffractometer was a Newport 6-circle kappa and the desired wavelength of the X-rays was controlled by a liquid nitrogen cooled Si (111) double crystal monochromator. The beam is collimated both vertically and horizontally using a pair of 1-m long Rh-coated silicon Kirkpatrick−Baez mirrors. To minimize beam damage the beam position on the sample was changed repeatedly. Sample stability during the experiments was monitored by multiple measurements of both CTR and RAXR data sets. The reflectivity data were collected with a Dectris PILATUS 100 K 2D pixel array detector. CTR scans were recorded by varying the momentum transfer between 0.09 and 5.48 $Å^{-1}$ at a fixed incident photon energy of 14 keV. RAXR spectra were measured by varying the incident X-ray energy around the L_{III} absorption edge of U(VI) (16.87 to 17.47 keV) at different fixed momentum transfer between 0.13 and 3.62 $Å^{-1}$.

U(VI) batch sorption samples on muscovite single crystals were prepared prior to the measurements. At first, two different electrolyte solutions, 0.1 M NaCl and 0.1 M NaCl + 0.02 M $CaCl_2$, were adjusted to pH 11. Then muscovite single crystals were freshly cleaved and immersed in the solutions. Finally, calculated amounts of a $UO_2(NO_3)_2$ stock solution were added in order to reach a U(VI) concentration of 5×10^{-5} M. One blank sample was prepared without addition of U(VI). Sorption time was 24 h, before the samples were transferred into a sample cell. After 20 μL of the reaction solution were pipetted on top of the sample, it was covered with a Kapton film and sealed with two additional Kapton domes (for details about the sample holder, the reader is referred to Schmidt et al. (2012)). The three samples which were prepared for measurement were (1) U(VI) sorption on muscovite at pH 11 in 0.1 M NaCl + 0.02 M $CaCl_2$, (2) U(VI) sorption on muscovite at pH 11 in 0.1 M NaCl, and (3) muscovite at pH 11 in 0.1 M NaCl + 0.02 M $CaCl_2$.

3.2. Results and discussion

3.2.1. Bentonite surface charge and stability at (hyper)alkaline conditions

3.2.1.1. Zeta potential

Zeta potential measurements of Ca-bentonite in 0.1 M NaCl show a negative surface charge over the entire pH range, as it can be expected from the permanent negative charge of 2:1 clay minerals due to isomorphous substitution of cations within the octahedral and tetrahedral layers (Figure 3-3). With increasing pH, surface charge becomes increasingly negative, reaching approximately -40 mV at pH ~12.5. A less negative surface charge was observed at pH ~13 due to extremely high ionic strength of the solution, caused by the addition of large amounts of NaOH. At high ionic strength the potential is generally dragged towards neutral charge due to the high density of cations close to the surface. The influence of the additional presence of bivalent cations (Ca^{2+} and Sr^{2+}) on the zeta potential is presented in chapter 4.2.1.

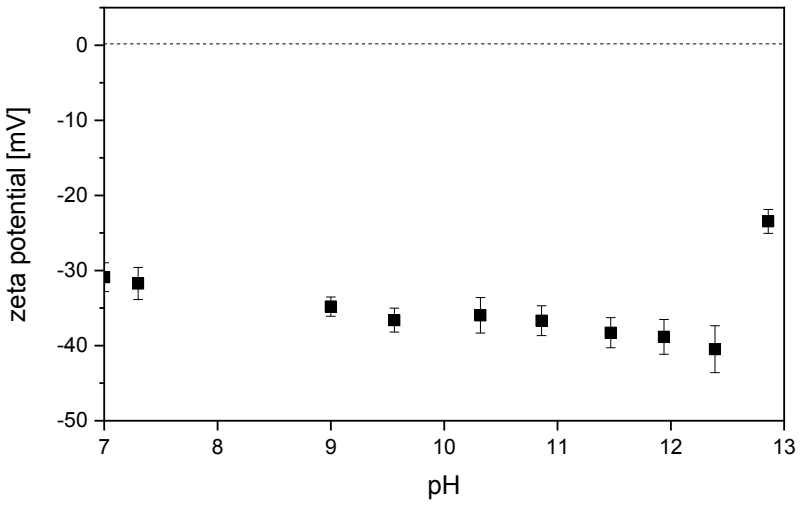

Figure 3-3: Surface potential of Ca-bentonite (0.1 g/L) as a function of pH in 0.1 M NaCl.

3.2.1.2. Powder X-ray diffraction (PXRD)

Powder XRD diffractograms of Ca-bentonite leached in diluted Gipshut solution between pH 8.5 and 13 have a very similar appearance, featuring the same main peaks (Figure 3-4). Major identified phases are quartz (peaks at $2\theta = 20.8$, 26.6 and 50.2°) and the clay minerals montmorillonite (peaks at $2\theta = 5.7$, 19.8, 35.1 and 61.9°), illite and muscovite. Illite and muscovite have a similar diffraction behavior so that some peaks cannot be unambiguously attributed. No alteration of mineral composition (dissolution, precipitation, recrystallization) with increasing pH was detected up to pH 12.5. Additional peaks appear at $2\theta = 11.2°$ and 27.4° at pH 12.5 and 13. These are attributed to the mineral hydrotalcite, which has been reported to precipitate from alkaline fluids in contact with bentonite (Fernández et al., 2009).

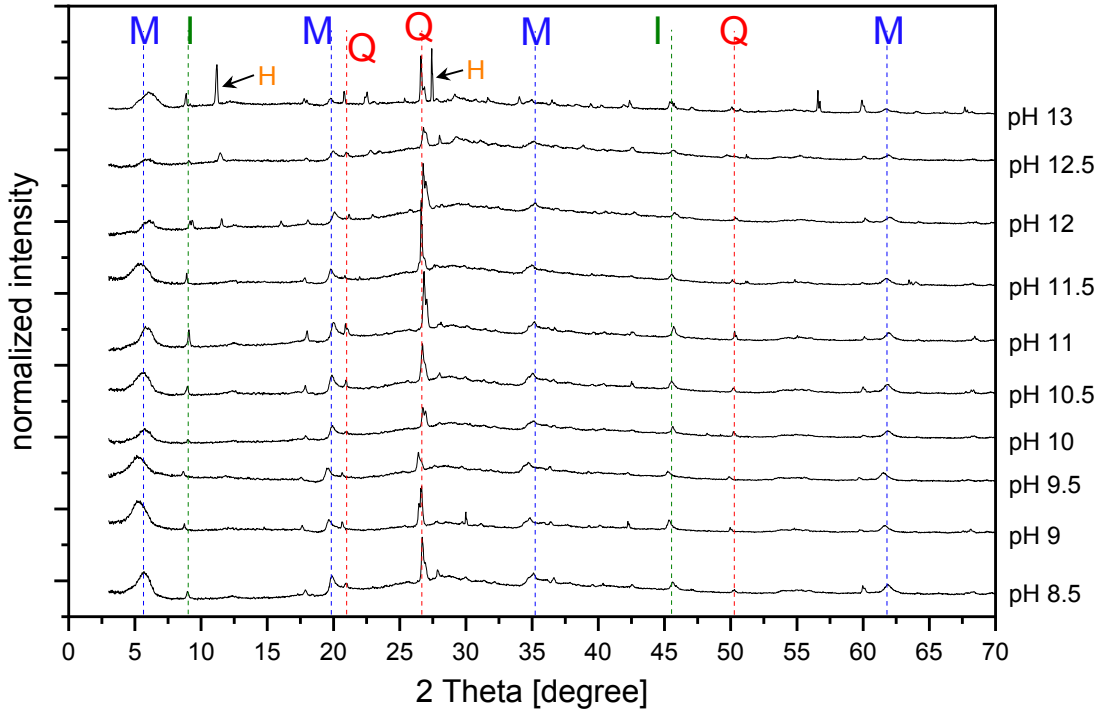

Figure 3-4: X-ray diffractograms of Ca-bentonite treated with diluted Gipshut solution for 3 weeks at pH 8.5-13. Mineral phases assigned to the peaks: M = montmorillonite, Q = quartz, I = illite or muscovite, H = hydrotalcite.

At pH 13 additionally portlandite $Ca(OH)_2$ precipitates, being responsible for the appearance of peaks at 56.6° and 60.0°. The results suggest a general stability of bentonite up to pH 12.5. This is in accordance with several studies where treatment with alkaline fluids of pH 12.5 only led to minimal alteration of smectites or left the bentonite virtually unchanged (Fernández et al., 2009; Milodowski et al., 2016; Vuorinen et al., 2006). Additionally, Schatz et al. (2013) found that Ca-montmorillonite is more stable towards chemical erosion than Na-montmorillonite. Severe alterations only occur at even higher pH values (>13), higher temperatures and over longer timespans. However, it has to be mentioned, that these studies investigated systems with much higher S/L ratios, making direct comparison difficult. Furthermore, PXRD is not sensitive for amorphous phases, such as calcium silicate hydrate (C-S-H). Consequently, partial mineral dissolution and precipitation of amorphous minerals is possible. This is discussed with the results of the leaching experiment in chapter 3.2.1.3.

3.2.1.3. Leaching

Ions leached out of the Ca-bentonite in 0.1 M NaCl and diluted Gipshut solution to noticeable amounts are Ca, Mg, Si and Al (Figure 3-5). The kinetic leaching experiment at pH 8 showed that the concentrations of dissolved elements reach equilibrium after short time. Concentrations can be regarded as stable after 1 week within the margin of error (Figure 3-5a). Concentrations of leached carbonate, resulting from the dissolution of small fractions of calcite contained in the bentonite were determined to be at maximum 2.9×10^{-4} M. The most strongly leached element is calcium, which is predominantly mobilized from the interlayers of Ca-montmorillonite. However, calcium is removed from the solution in the presence of

carbonate by precipitation of calcite above pH 8.5 (not shown). In the absence of carbonate in diluted Gipshut solution (where calcium concentrations exceed 0.02 M) Ca precipitates as portlandite ($Ca(OH)_2$) above pH 12 (not shown). This can be observed with the naked eye in samples at pH 12.5 and 13. In 0.1 M NaCl, leached calcium concentrations do not exceed the solubility limit with respect to portlandite (1.3 mM). Nevertheless, the amount of dissolved calcium decreases with increasing pH (Figure 3-5b). A possible explanation for this trend is the formation of calcium (aluminate) silicate hydrate (C-(A-)S-H) phases at hyperalkaline conditions. This would require the availability of silicon. Al and Si concentrations in the leachates are very low up to pH 12. Only at pH 12.5 and 13 a significant increase in concentration of both elements can be observed (Figure 3-5b). This would technically suggest a stability of the montmorillonite up to pH 12. However, in the light of calcium concentrations decreasing strongly in the solution at pH>10, Al and Si might be released from the montmorillonite already at lower pH but are immediately bound in the form of C-A-S-H. Both Al and Si appear then in solution at pH 12.5 and 13, when the availability of calcium becomes the limiting factor for C-(A-)S-H formation. In line with this hypothesis, significant release of Al and Si from kaolinite was observed already at pH>10 by Huittinen et al. (2012). C-(A-)S-H phases cannot be detected with PXRD as they have an amorphous structure.

The leaching experiments show an apparent stability of the Ca-bentonite up to pH 12.5. However, indirect proof for the release of Al and Si and formation of C-A-S-H phases at pH>10 arises from the decreasing calcium concentrations. Consequently, C-A-S-H has to be considered as an additional sorbing mineral in the sorption experiments. Nevertheless, in relation to the remaining clay mineral fraction this can be considered as a minor contribution. Also the results of the site-selective TRLFS measurements underpin the assumption that U(VI) sorption on clay minerals is still the dominating process (chapter 3.2.2.4).

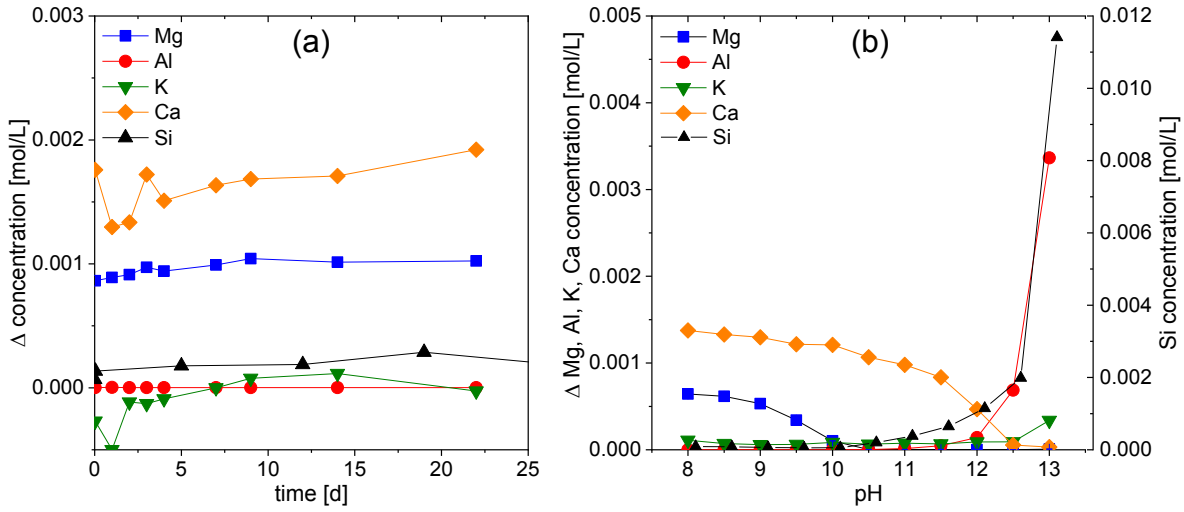

Figure 3-5: Concentration of ions leached out of Ca-bentonite (10 g/L) (difference to initial concentrations) in the absence of CO_2 in diluted Gipshut solution at pH 8 as a function of contact time (a) and in 0.1 M NaCl as a function of pH after three weeks of contact time (b).

3.2.2. Sorption of U(VI) on Ca-bentonite at (hyper)alkaline conditions

3.2.2.1. Batch sorption experiments

S/L ratio dependence

In the absence of CO_2, U(VI) sorption is independent of the S/L ratio in the probed range, both at pH 8 (3-20 g/L) and at pH 10.5 (0.1-5 g/L), with a sorption percentage of approx. 80% and close to 100%, respectively (Figure 3-6). The strong U(VI) retention at the lowest S/L ratio indicates a high excess of sorption sites in the bentonite in the absence of CO_2.

By contrast, at low carbonate concentration at pH 8, U(VI) sorption increases with increasing S/L ratio from 38% at 3 g/L to 64% at 20 g/L. Sites for uranyl adsorption in the presence of carbonate seem to be rather limited as an increase of solid fraction in the suspension caused a strong increase in sorption due to an increase of available sorption sites. This observation hints to different sorption processes in the absence and presence of carbonate at pH 8. Based on these results a S/L ratio of 10 g/L was chosen for all following batch sorption experiments with Ca-bentonite.

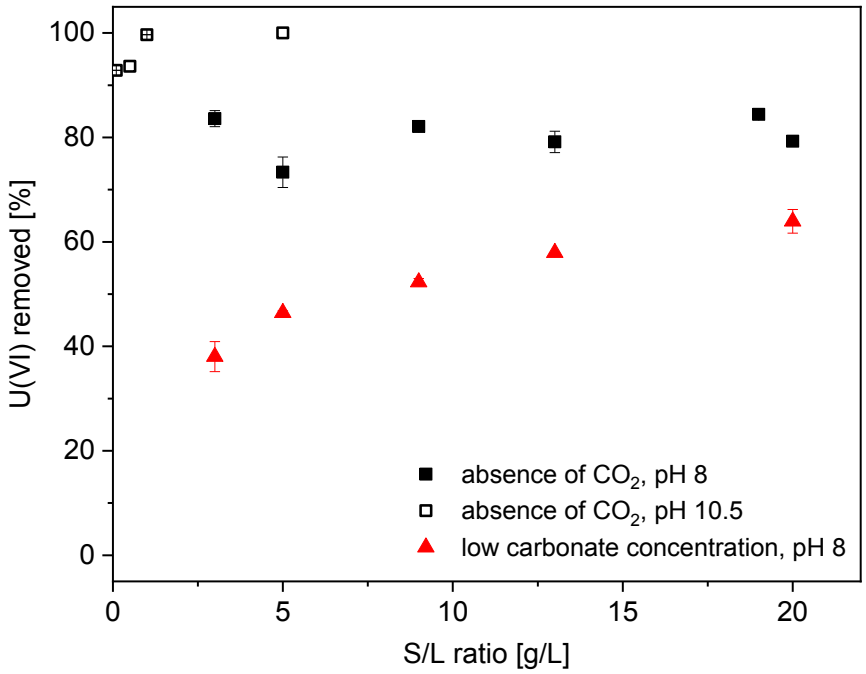

Figure 3-6: Percentage of U(VI) sorbed on Ca-bentonite in diluted Gipshut solution as a function of S/L ratio in the absence of CO_2 ([U(VI)] = 5×10^{-7} M) at pH 8 and 10.5 and at low carbonate concentration (1 mM) ([U(VI)] = 1×10^{-6} M) at pH 8.

Kinetic sorption experiments

All kinetic sorption experiments show that the U(VI) sorption process is fairly fast. At low carbonate concentration at pH 8 half of the maximum sorption of 62% is already reached after one hour and sorption is almost completed after two days. In the absence of CO_2 (pH 8, 10.5

and 12.5) and at high carbonate concentration at pH 12.5 the U(VI) sorption process is even faster. After one hour, sorption is already almost completed and it finally reaches a plateau after one day (Figure 3-7). The similarity between the kinetic behavior in the system without carbonate and the system with carbonate at pH 12.5 indicates that the underlying retention mechanisms under these conditions are similar. This will also be discussed in paragraph "pH dependency of sorption" and in chapter 3.2.2.2. To guarantee that the reaction has reached equilibrium, sorption time in all other experiments was chosen to be 7 days.

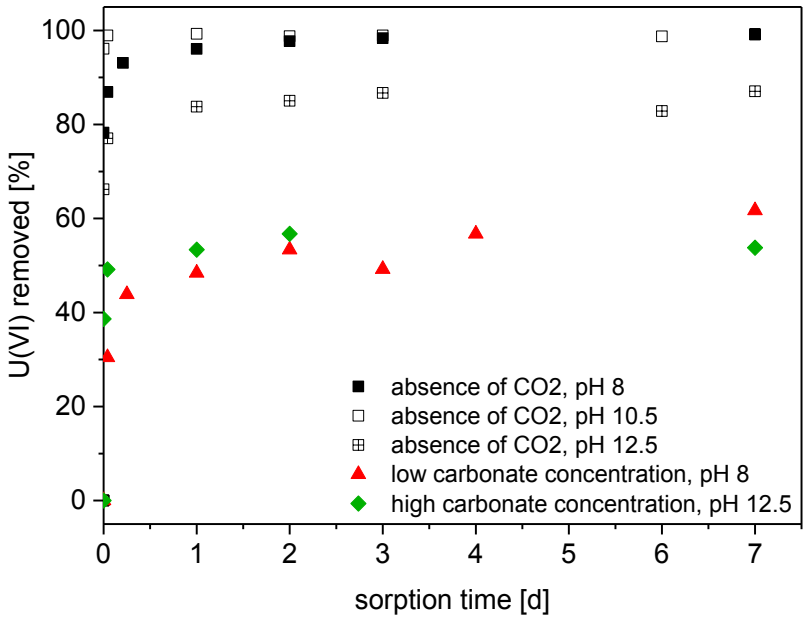

Figure 3-7: Percentage of U(VI) sorbed on Ca-bentonite in diluted Gipshut solution at different pH in the absence of CO_2 ([U(VI)] = 5×10^{-7} M) and at low and high carbonate concentrations ([U(VI)] = 1×10^{-6} M) as a function of sorption time.

Sorption isotherms

When plotting the logarithm of the equilibrium amount of uranium sorbed on the bentonite a_{eq} against the logarithm of the equilibrium uranium concentration in the solution c_{eq} (Figure 3-8), the slope of a linear fit represents the Freundlich exponent n (eq. (3.7)). If the slope of the fit is 1, the sorption behavior can be described as linear, as the Freundlich isotherm (eq. (3.5)) then equals the linear Henry isotherm (eq. (3.4)). In that special case, the y-intercept represents the log(K_d) value.

$$\log(a_{eq}) = n \times \log(c_{eq}) + \log(k_F) \qquad (3.7)$$

In the absence of CO_2, n was determined to be 0.99 at pH 8 and 1.03 at pH 12.5, indicating a linear sorption behavior (Figure 3-8a,b). On the contrary, at low carbonate concentration at pH 8 sorption cannot be described as linear since a Freundlich exponent of 0.89 was obtained. The K_d values were derived by forcing the fit through the data points to have a slope of 1. Resulting log(K_d) values were 2.19 log(L/kg) at low carbonate concentration at pH 8 and 3.03 and 3.06 log(L/kg) in the absence of CO_2 at pH 8 and 12.5, respectively. Consequently, U(VI)

sorption on Ca-bentonite at pH 8 is much weaker in the presence of carbonate, which is in accordance with literature studies.

Another sorption isotherm was recorded in the absence of CO_2 at pH 10.5. In the entire U(VI) concentration range of 1×10^{-9} M to 3.2×10^{-6} M the uranium was removed to 100%. As no uranium was left in solution after the experiment ($c_{eq} = 0$), irrespective of the initial concentration, no isotherm could be plotted. Nevertheless, this observation contains valuable information. The complete retention over the entire concentration range suggests that the U(VI) removal at high initial concentration (i.e. $\geq 1\times10^{-8}$ M) is probably not due to precipitation, because the same removal is observed when oversaturation can be ruled out (at $[U(VI)] \leq 1\times10^{-8}$ M). Therefore, a uniform retention mechanism can be assumed for the entire U(VI) concentration range studied - most probably adsorption (discussed in the following chapters).

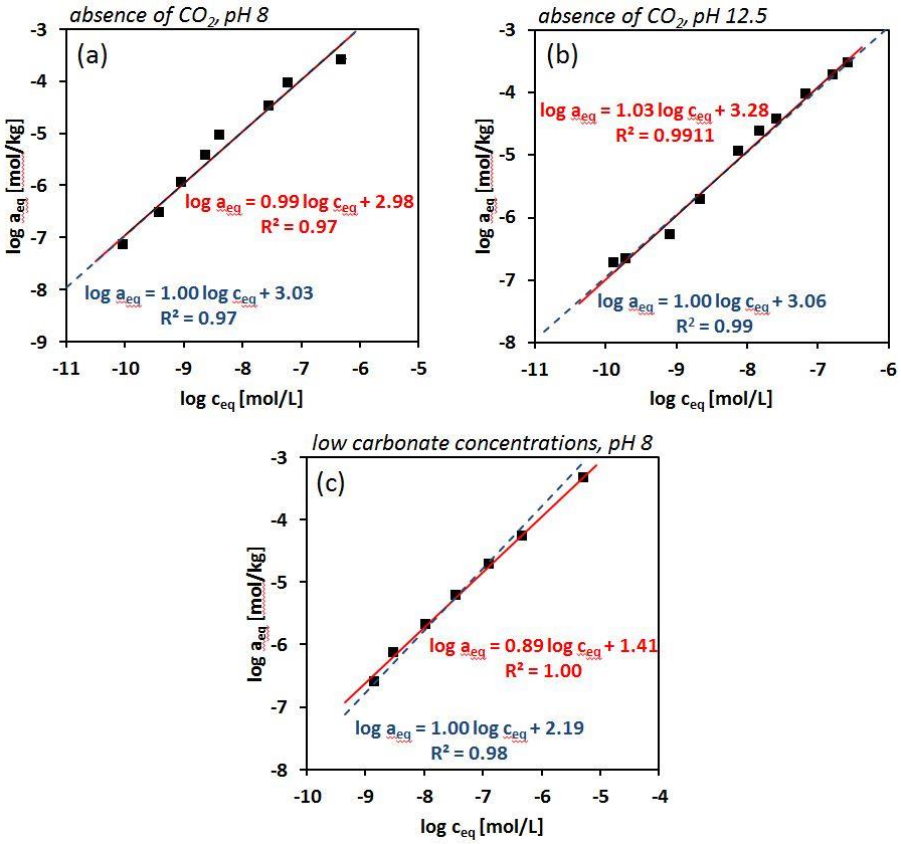

Figure 3-8: Sorption isotherms at pH 8 and pH 12.5. Red lines show a linear fit through the data points. Dashed blue lines represent a fit with a forced slope of 1. (a) Sorption isotherm in the absence of CO_2 at pH 8, (b) Sorption isotherm in the absence of CO_2 at pH 12.5. (c) Sorption isotherm at low carbonate concentration at pH 8.

The sorption isotherms reveal that at pH 8 the adsorption of uranyl in the presence and absence of carbonate follows different processes. The retention of U(VI) in the absence of CO_2 can be described as linear within the investigated concentration range. This indicates that enough sorption sites are available on the bentonite. This is in accordance with the sorption experiments as a function of the S/L ratio, showing that a very small solid fraction already provides enough sorption sites to reach maximum U(VI) sorption. By contrast, the removal of

U(VI) at low carbonate concentration at pH 8 is non-linear, meaning that not enough high affinity sites are available or that the complexes are generally hampered to occupy the sites. This also fits to the observation from the S/L ratio dependent sorption, where an increased amount of solid fraction caused a substantially increased retention (see paragraph "S/L ratio dependence"). The observed differences are attributed to differences in the aqueous speciation of U(VI) as a function of carbonate concentration, which is discussed in chapter 3.2.2.2.

pH dependency of sorption

Batch sorption experiments as a function of pH exhibit a complex U(VI) retention behavior depending on the amount of carbonate present in solution (Figure 3-9). In the absence of CO_2, U(VI) retention is approx. 90% at pH 8-9 (squares in Figure 3-9). At higher pH, sorption even increases, forming a plateau of complete retention from pH 9.5 to about pH 12. At pH ≥ 12, U(VI) sorption decreases again to only 50% at pH 13. At low carbonate concentration (1 mM), U(VI) retention is low (approx. 20%) at pH 8-9. Going to higher pH values, the retention increases drastically, following a similar pH-dependent trend as in the absence of CO_2. Also here a plateau of complete sorption is observed at pH 10-12, followed by a pronounced drop at pH ≥ 12 (triangles in Figure 3-9). When carbonate concentration is high (0.1 M), U(VI) retention remains on a very low level (< 10%) up to pH 11. Thereafter it increases, reaching 80% at pH 12 (diamonds in Figure 3-9), before dropping again, similar to the previously described series. The complete U(VI) retention in the absence of CO_2 and at low carbonate concentration corresponds to maximum log(K_d) values of approx. 5-6 log(L/kg), restricted by the detection limit of the ICP-MS measurements (0.1 μg/L). At high carbonate concentration, the maximum retention at pH 12 corresponds to a log(K_d) value of 2.6 log(L/kg) (Figure 3-10). The obtained log(K_d) values are generally in good agreement with those found in literature for U(VI) sorption by montmorillonite in the pH range 8-10. Boult et al. (1998b), Bradbury and Baeyens (2005), Marques Fernandes et al. (2012) and Fritsch (2018) reported distribution coefficients of 4-5 log(L/kg) in the absence of CO_2 and of 1-2 log(L/kg) in the presence of CO_2. In the absence of CO_2 at pH 8 the log(K_d) value determined in the present study is comparatively small with approx. 3 log(L/kg). An obvious explanation for this difference is that the main sorbing mineral phase, montmorillonite, only makes up 60–70% of the Ca-bentonite, while the aforementioned studies all investigated the sorption behavior of pure montmorillonite. Another reason could be the complexation of a minor fraction of U(VI) with carbonate which was released from the bentonite (see chapter 3.2.1.3).

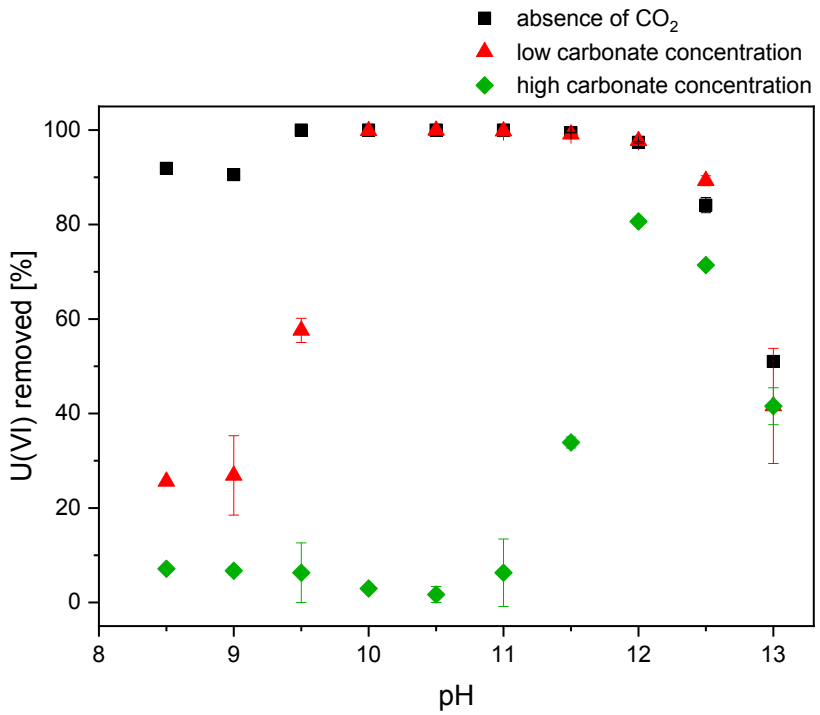

Figure 3-9: Percentage of U(VI) sorbed on Ca-bentonite (10 g/L) in dil. Gipshut solution (I = 2.63 M) as function of pH and carbonate concentration. Initial U(VI) concentrations were 5×10^{-7} M in the absence of CO_2 and 1×10^{-6} M at low (1 mM) and high (0.1 M) carbonate concentrations.

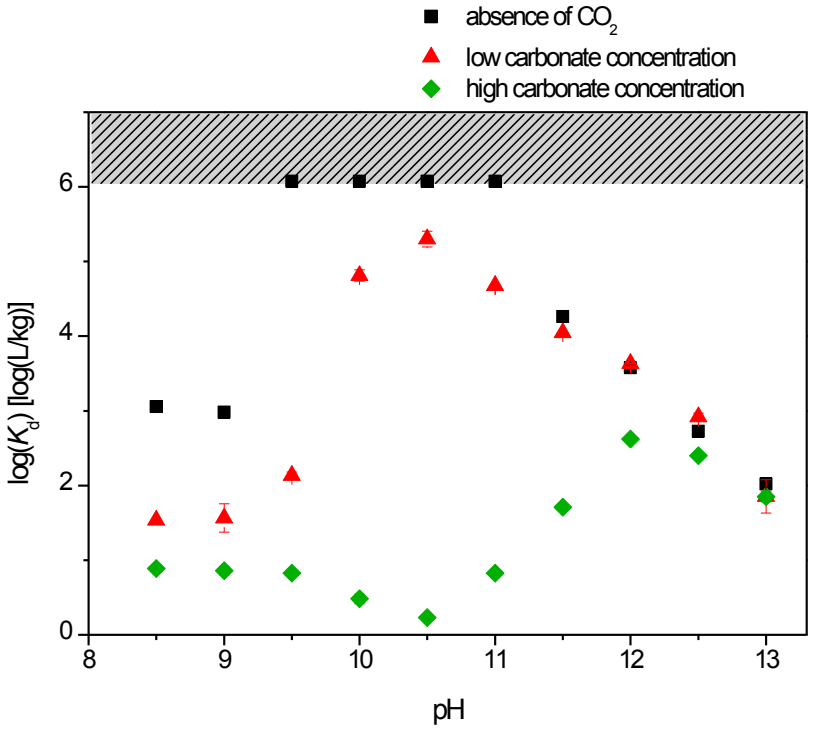

Figure 3-10: Logarithmized U(VI) distribution coefficients log(K_d) for U(VI) sorbed on Ca-bentonite (10 g/L) plotted as a function of pH and carbonate concentration. Initial U(VI) concentrations were 5×10^{-7} M in the absence of CO_2 and 1×10^{-6} M at low (1 mM) and high (0.1 M) carbonate concentrations.

The strong increase of the log(K_d) at pH around 9.5 from 3 to 5-6 log(L/kg), as it has been demonstrated in this study, has not yet been reported in literature, where sorption always reached its maximum at circumneutral pH. For pH > 10, no published data exist for comparison. The lower U(VI) retention in the presence of carbonate at pH 8 to 9.5 is in accordance with literature and is attributed to the predominant formation of weakly sorbing (calcium) uranyl carbonate complexes (Bachmaf et al., 2008; Joseph et al., 2013; Maher et al., 2013; Marques Fernandes et al., 2012; Richter et al., 2016; Schmeide et al., 2014; Tournassat et al., 2018). An increase in retention with further increasing pH has not been systematically reported for such carbonate-containing systems as none of the mentioned studies expands to the hyperalkaline regime.

Even without discussing the underlying retention mechanism on a molecular level, the presented batch results alone provide already substantial knowledge gain as they present for the first time a systematic study of the U(VI) retention by clay rock from weakly alkaline to hyperalkaline pH. The results show that sorption can be very effective up to pH 12, also in the presence of carbonate. The decreased U(VI) retention in the presence of carbonate, reported previously in the literature, does only apply up to a certain pH and is highly dependent on the amount of carbonate in the solution.

Reasons for the observed differences in sorption behavior as a function of pH and carbonate concentration are discussed in the following chapters based on U(VI) solubility experiments and spectroscopic investigations on the aqueous and surface speciation of U(VI).

Desorption

The stability and reversibility of the U(VI) retention at pH 11 in the absence of CO_2 was tested in batch desorption experiments. After performing sorption experiments exactly as described above, the background electrolyte was exchanged with different U(VI)-free solutions as described in chapter 3.1.3.5. After one week of reaction time the supernatant was analyzed for remobilized U(VI).

Exchanging the diluted Gipshut solution with exactly the same electrolyte did not lead to any remobilization of U(VI) (Figure 3-11). After having reached a steady distribution between the phases, no force exists that would drive the U(VI) towards the liquid phase again. Also contact with 5 M NaCl results in 0% desorption (Figure 3-11). Conventionally, an increase in ionic strength (as here from 2.63 to 5 M) causes a decrease of sorption in the case of outer-sphere complexation where the high density of solution ions near the surface prevents electrostatic attachment of U(VI). Consequently, conventional outer-sphere complexation can be excluded under the given conditions. This retention mechanism was considered unlikely, because the ionic strength was already very high in the initial sorption experiments (2.63 M). A change of pH from 11 to 13 of the diluted Gipshut solution resulted in a U(VI) remobilization of 50.5% (Figure 3-11). This corresponds to the observed amount of sorption

at pH 13 in the pH-dependent batch sorption experiment (paragraph "pH dependency of sorption") where approx. 50% U(VI) removal from solution was observed. Changing the pH of a solution is a strong alteration of the chemical system, which can cause even inner-sphere complexes to desorb. Desorption experiments with 1 M HNO_3 prove that all U(VI) was adsorbed to the Ca-bentonite in the first place and that theoretically 100% are recoverable.

Applying conventional criteria for inner- and outer-sphere surface complexation, the desorption experiments suggest that at pH 11 all U(VI) is retained in the form of inner-sphere sorption complexes, as it cannot be remobilized by a change of ionic strength, but only by a change of pH. However, in the special case of U(VI) sorption at hyperalkaline conditions, this classical concept has to be reassessed. Conventionally, outer-sphere complexation applies to cationic metal ions that adsorb to a negatively charged surface. By contrast, at pH 11 the prevailing U(VI) species are anionic (see also chapter 3.2.2.2). In that case the solution cations are no longer direct competitors for sorption sites and also do not electrostatically repel the metal ion. They rather attract the anionic U(VI), possibly even facilitating an adsorption. Hence, anionic metal ions could possibly form outer-sphere complexes on negatively charged clay mineral surfaces via bridging cations (such as Ca^{2+}). Such kind of outer-sphere complexes would then not be influenced negatively by increasing the ionic strength. Consequently, to unequivocally distinguish the underlying retention mechanisms, spectroscopic investigations are indispensable.

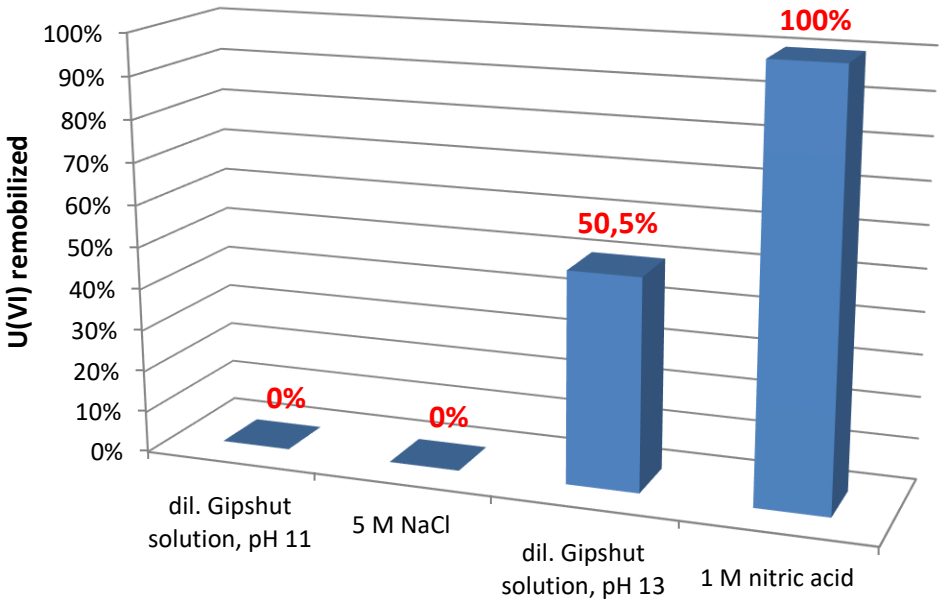

Figure 3-11: Percentage of U(VI) ([U] = 5×10^{-7} M) remobilized after one week of reaction time from Ca-bentonite (10 g/L) after exchanging the background electrolyte (diluted Gipshut solution at pH 11) with different solutions (as indicated in the diagram).

3.2.2.2. Aqueous speciation of U(VI) investigated with TRLFS

In the absence of CO_2, the luminescence spectra of U(VI) in diluted Gipshut solution measured at 153 K feature a low intensity with a poor spectral resolution (Figure 3-12a). Both phenomena are characteristic for uranyl hydroxide complexes at alkaline conditions. This has been reported by Moulin et al. (1998), Martínez-Torrents et al. (2013) and Drobot et al. (2016), where monomeric hydrolysis species $UO_2(OH)_2$, $UO_2(OH)_3^-$ were shown to exhibit broadened spectra with weak spectral splitting. In spite of the low signal to noise ratio (particularly up to pH 10), the positions of the first two main peaks could be identified, being at approx. 500 nm and 521 nm for the samples up to pH 12 (Table 3-5). Drobot et al. (2016) observed maxima at 499 and 520 nm for $UO_2(OH)_{2\,(aq)}$ and at 503 and 525 nm for $UO_2(OH)_3^-$. Moulin et al. (1998) and Martínez-Torrents et al. (2013) described peaks for $UO_2(OH)_3^-$ at 499 nm and 519 nm and at 503 and 521 nm, respectively. Luminescence lifetimes depend on the presence of quenchers and, to a large degree, on the temperature of the sample. Therefore, comparing lifetimes obtained in different studies is difficult. From the aforementioned studies only Martínez-Torrents et al. (2013) performed measurements at cryogenic conditions (10 K). The reported luminescence lifetime of 198 μs for $UO_2(OH)_3^-$ corresponds very well to the 208 µs obtained in the present work at pH 11 (measured at 153 K). At pH 13 the luminescence spectrum is shifted towards lower wavelength, having the first two maxima at approx. 490 nm and 511 nm (Table 3-5). These positions are in agreement with spectra measured by Tits et al. (2011) at very alkaline conditions (pH 13.3), which were assigned to the higher hydrolysis species $UO_2(OH)_4^{2-}$. In the present study, the luminescence lifetime at pH 13 was measured to be somewhat shorter than at lower pH. This observation is consistent with the works of Martínez-Torrents et al. (2013) and Kitamura et al. (1998) in which shorter lifetimes are reported for $UO_2(OH)_4^{2-}$ compared to $UO_2(OH)_3^-$. Consequently, based on analysis of peak positions and luminescence lifetimes, (anionic) uranyl hydroxides ($UO_2(OH)_2$, $UO_2(OH)_3^-$ and at very high pH $UO_2(OH)_4^{2-}$) dominate the aqueous speciation of U(VI) in the diluted Gipshut solution in the absence of CO_2 between pH 8 and 13.

In the presence of carbonate, the recorded luminescence emission spectra vary strongly within the investigated pH range 8-13. Up to pH 10 at low carbonate concentration and up to pH 11 at high carbonate concentration, the shape of the spectra is very similar, exhibiting a well-resolved spectral splitting (Figure 3-12b,c). Compared to the uranyl aquo ion, these spectra are shifted towards lower wavelengths, which is characteristic for uranyl carbonate complexes (Bernhard et al., 2001; Lee and Yun, 2013; Steudtner et al., 2011; Wang et al., 2004). The obtained peak positions (first two main peaks at approx. 480 and 500 nm) match very well with literature data for $UO_2(CO_3)_3^{4-}$ and the ternary calcium uranyl carbonate complexes $Ca_2UO_2(CO_3)_{3\,(aq)}$ and $CaUO_2(CO_3)_3^{2-}$ (Table 3-5). Luminescence lifetimes of these samples range between 700 and 1000 µs. As peak positions are very similar and the luminescence lifetimes depend on temperature and solution composition, it is not possible to distinguish between $UO_2(CO_3)_3^{4-}$ and ternary Ca-UO_2-CO_3 complexes here, based on the spectral

properties. However, given that the diluted Gipshut solution contains large amounts of calcium, the formation of ternary complexes with calcium is expected. Another plausible complex is $MgUO_2(CO_3)_3^{2-}$, which was described by Lee et al. (2017) with almost the same luminescence spectroscopic properties as $UO_2(CO_3)_3^{4-}$. The formation of this complex might be favored when calcium is removed successively from the solution with increasing pH due to calcite precipitation. Magnesium is then still available as brucite precipitation is initiated at somewhat higher pH. At pH 10.5 at low carbonate concentration and at pH 11.5 at high carbonate concentration, an abrupt change in speciation is visible. The well resolved emission bands are not detectable anymore. Instead, broad spectra with lower luminescence intensity are observed (Figure 3-12b,c). Peak positions and lifetimes compare very well to those that were obtained in the absence of CO_2 (Figure 3-13) and are therefore also interpreted as monomeric uranyl hydroxide complexes $UO_2(OH)_3^-$ and $UO_2(OH)_4^{2-}$. Consequently, uranyl carbonate complexes, which have been widely reported to dominate the aqueous U(VI) speciation at alkaline conditions, prevail only up to a certain pH, depending on the concentration of dissolved carbonate. At higher pH, the formation of uranyl hydroxides is favored.

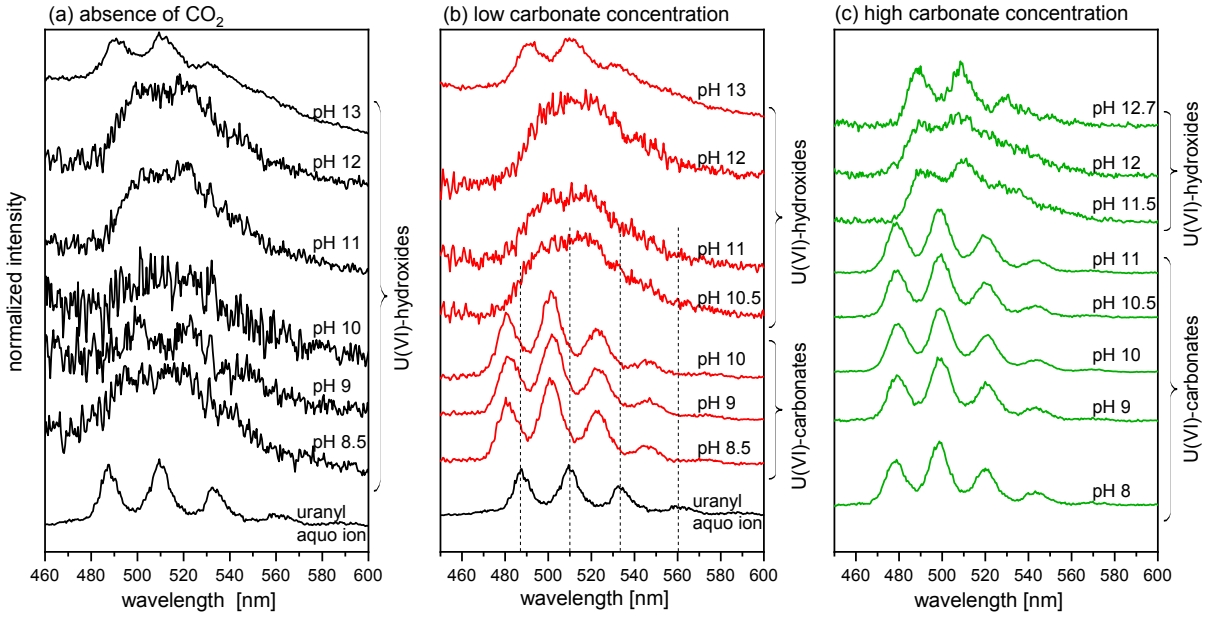

Figure 3-12: Luminescence spectra of uranyl ([U(VI)] = 5×10^{-7} M) in the diluted Gipshut solution as a function of pH in the absence of CO_2 (a), at low carbonate concentration (b) and at high carbonate concentration (c).

Table 3-5: Luminescence spectroscopic properties (peak positions and luminescence lifetimes) of U(VI) in the diluted Gipshut solution at different pH and carbonate concentrations (LC = low carbonate concentration, HC = high carbonate concentration). Literature data are given for comparison.

Series	pH	Peak positions [nm]				Lifetime [μs]	T [K]
N_2	8.5	497.4	517.3			-	153
	9.0	502.1	522.9			-	153
	11.0	499.3	521.0			208 ± 30	153
	12.0	500.2	521.5			130 ± 21	153
	13.0	490.4	510.7	531.6		74 ± 17	153
LC	9.0	481.2	502.1	523.4	546.9	877 ± 17	153
	9.5	481.2	501.6	523.4	546.9	995 ± 55	153
	10.0	480.8	501.1	522.9	546.0	882 ± 15	153
	10.5	495.6	518.3	546.2	567.0	193 ± 0	153
	11.0	497.0	519.2	542.8	569.6	149 ± 13	153
	12.0	496.5	523.8			166 ± 16	153
	13.0	490.4	510.3	532.5		89 ± 7	153
HC	8.0	477.4	498.3	520.0	544.1	851 ± 33	153
	9.0	478.8	499.6	521.4	544.1	804 ± 17	153
	9.5	478.8	499.2	521.4	544.1	727 ± 20	153
	10.0	479.3	499.6	521.4	544.5	704 ± 10	153
	10.5	478.8	499.2	520.5	543.1	792 ± 19	153
	11.0	477.9	499.2	520.5	544.1	808 ± 18	153
	11.5	489.9	511.2	533.4	557.5	123 ± 7	153
	12.0	489.0	508.4			133 ± 7	153
	12.5	488.1	509.4	530.2	556.3	146 ± 16	153
	12.7	488.1	508.9	530.2		112 ± 10	153
UO_2^{2+} [a]		488	509	533	560	0.9 - 2	293
$UO_2(CO_3)_3^{4-}$ [b]		480.7	499.9	520.3	542.5	834 ± 9	153
$UO_2(CO_3)_3^{4-}$ [c]		479.6	499.2	519.9	542.4	883	6
$Ca_2UO_2(CO_3)_{3\,(aq)}$ [c]		480.5	501.2	522.7	546.0	1282	6
$Ca_2UO_2(CO_3)_{3\,(aq)}$ [d]		484	504	524		0.036	293
$UO_2(OH)_3^-$ [e]		503.0	521.0	534.0	550.0	198 ± 8	10
$UO_2(OH)_3^-$ [f]		503	525	547	572	3.4 ± 0	274
$UO_2(OH)_3^-$ [a]		499	519	543	567	0.8	293
$UO_2(OH)_4^{2-}$ [g]		491.4	510.5			140 ± 30	153

[a] Moulin et al. (1998); [b] Steudtner et al. (2011); [c] Wang et al. (2004); [d] Bernhard et al. (2001); [e] Martínez-Torrents et al. (2013); [f] Drobot et al. (2016); [g] Tits et al. (2011)

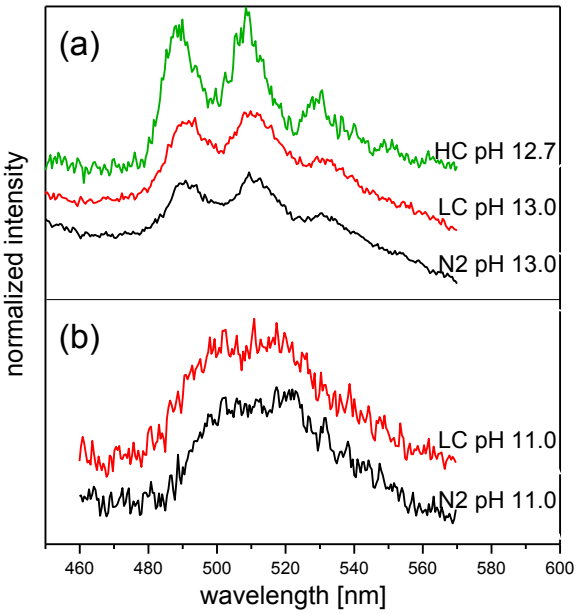

Figure 3-13: Comparison of luminescence spectra of uranyl ([U(VI)] = 5×10^{-7} M) in the diluted Gipshut solution at pH 13 (pH 12.7 at high carbonate concentration) (a) and pH 11 (b) at different carbonate concentrations. Similarity of spectra shows that the aqueous U(VI) speciation is independent of carbonate concentration at such elevated pH.

A clear correlation between changes in aqueous speciation and changes in the sorption behavior can be observed. U(VI) retention on Ca-bentonite is low in the pH range, where uranyl carbonate complexes dominate the aqueous speciation according to the TRLFS measurements. The observed increase in retention in the presence of carbonate above a certain pH coincides with the change in aqueous speciation from uranyl carbonates to uranyl hydroxides. Generally, it can be stated that U(VI) retention is very high in samples, where $UO_2(OH)_3^-$ dominates the aqueous speciation. At pH > 12 the decrease in retention correlates with the formation of the higher hydrolysis species $UO_2(OH)_4^{2-}$. In the light of electrostatic interactions, it has to be discussed if the very strong U(VI) retention at pH 10-12 can be attributed to adsorption of a negatively charged metal complex to the negatively charged bentonite surface, or if the retention under these conditions is rather caused by a precipitation of uranates. This is clarified by solubility tests (chapter 3.2.2.3) and direct spectroscopic investigation of U(VI) sorbed on the bentonite surface (chapter 3.2.2.4).

3.2.2.3. Solubility of U(VI)

Batch samples of U(VI) in leachates of Ca-bentonite in diluted Gipshut solution demonstrate that substantial amounts of the initial U(VI) (5×10^{-7} M) remained in solution over the entire pH range after one week of contact time and after ultracentrifugation (Figure 3-14). Hence, the complete removal of U(VI) observed for the sorption samples at pH 10-12 cannot exclusively be attributed to precipitation from the solution. This is in contrast to literature solubility studies, where U(VI) solubility is often described to induce nanomolar concentrations at alkaline conditions (Altmaier et al., 2017; Kitamura et al., 1998). The solubility limiting phase between pH 8 and 13 is sodium di-uranate ($Na_2U_2O_7 \cdot H_2O$) in pure

sodium chloride solutions (Altmaier et al., 2017) and calcium uranate ($CaUO_4$) in the presence of calcium (Bots et al., 2014; Moroni and Glasser, 1995; Smith et al., 2015; Tits et al., 2008; Tits et al., 2011; Tits and Wieland, 2018). Due to the high calcium concentration in the diluted Gipshut solution, the precipitation of Ca-uranates would be expected in the present study. However, the solubility data given in literature were determined from undersaturation experiments, consistently yielding lower equilibrium U(VI) concentrations compared to an oversaturation approach. Furthermore, most solubility studies (e.g. Altmaier et al. (2017)) were conducted over much longer time spans, so that kinetics have to be considered. Under the given conditions, precipitation of uranates might be a much slower process than U(VI) adsorption, making precipitation negligible within the one-week sorption experiments. Tits and Wieland (2018) also found that at least up to 2×10^{-6} M U(VI) is stable in Ca-rich alkaline solutions for a time span of seven days. The observed partial loss of U(VI) from the solution in the present experiment might be caused by a local supersaturation with respect to uranates upon addition of the highly concentrated acidic U(VI) stock solution. Formed colloids would dissolve only slowly with time.

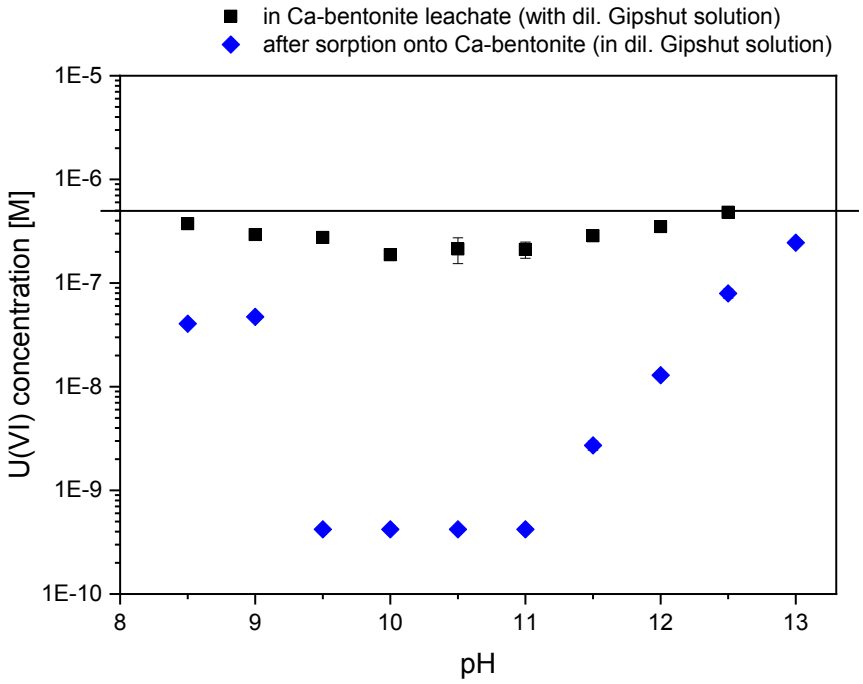

Figure 3-14: Solubility of U(VI) in Ca-bentonite leachate solution after 7 days contact time and ultracentrifugation in comparison to U(VI) concentrations measured after sorption experiments. The line indicates the initial U(VI) concentration of 5×10^{-7} M in the solubility and sorption experiments.

Having shown that precipitation from the solution does not play a major role, surface-mediated precipitation processes are still possible. Those could occur only when the Ca-bentonite is present, triggered by an increased U(VI) concentration near the surface. In order to unambiguously distinguish between surface precipitation and surface complexation, direct spectroscopic investigation of the U(VI) complexes sorbed to the Ca-bentonite surface is necessary (chapter 3.2.2.4).

3.2.2.4. U(VI) surface speciation

***In situ* ATR FT-IR spectroscopy**

The application of *in situ* ATR FT-IR allows the monitoring of U(VI) accumulation on the Ca-bentonite surface with time. As the obtained spectra are difference spectra (relative to a conditioning stage without sorptive) the appearance of signals can unequivocally be attributed to the sorption of U(VI). The wavenumber of the peaks corresponds to the asymmetric stretch vibration of the uranyl unit and is characteristic for the U(VI) speciation. Experiments were conducted at pH 6.8 in order to be able to compare the results with previous experiments with montmorillonite (Fritsch, 2018), furthermore at pH 8, as this is the lower boundary of the range of interest of this work, at which U(VI) retention is already well understood, and at pH 10.5, representative for the so far unstudied regime, where complete retention was observed in the present work in the absence of CO_2 as well as at low carbonate concentration. For the interpretation of the spectra it has to be taken into account that the initial U(VI) concentration was much higher compared to the batch sorption experiments described above (2×10^{-5} M instead of 5×10^{-7} M, due to the detection limit of the method), so that a direct comparison and deduction of analogous mechanisms is difficult.

At pH 6.8 and 8, a prominent absorption band appears at approx. 941 cm^{-1} (between 939 and 942 cm^{-1} at pH 8), evolving immediately from the onset of the sorption stage (Figure 3-15). Additionally, shoulders can be observed at lower wavenumbers, namely at 925 cm^{-1} at pH 6.8 and at 915 and 900 cm^{-1} at pH 8. This indicates the simultaneous presence of different U(VI) species on the Ca-bentonite surface. At pH 10.5 the main peak evolves with time between 927 and 929 cm^{-1}. Consequently, the structure of the retained U(VI) compound is fundamentally different from those at pH 6.8 and 8. Also here, small shoulders show the presence of multiple sorption species. In all three samples small negative absorption bands appear at the wavenumbers of the adsorption maxima during the flushing stage. However, these truncations only represent weak remobilization of U(VI) and therefore eliminate classical outer-sphere sorption as relevant retention mechanism at the given conditions.

As described in previous ATR FT-IR studies (Comarmond et al., 2016; Duff et al., 2002; Gückel et al., 2012; Lefevre et al., 2008; Lefevre et al., 2006; Müller et al., 2008; Müller et al., 2013; Müller et al., 2012; Tsushima, 2011; Wazne et al., 2003), the adsorption of U(VI) to the mineral film is accompanied by a red shift of absorption bands compared to the respective aqueous species. In the absence of CO_2 at pH between 6.8 and 10.5 and a U(VI) concentration of 20 μM, the predominant aqueous species are the uranyl hydrolysis species $(UO_2)_3(OH)_5^+$, $UO_2(OH)_2$ and $UO_2(OH)_3^-$ (Müller, 2010).

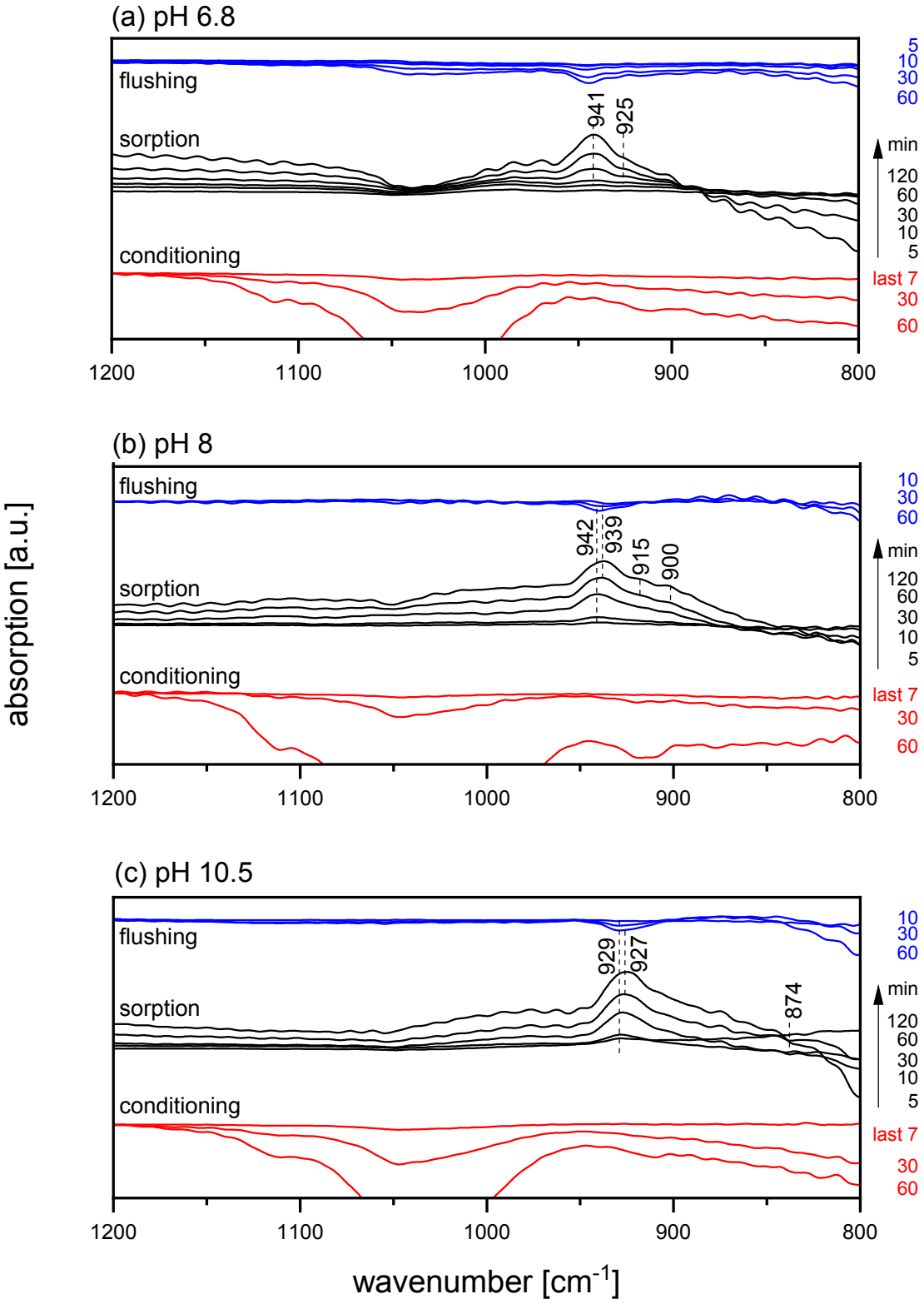

Figure 3-15: ATR FT-IR spectra of 2×10^{-5} M U(VI) sorbed on Ca-bentonite films at pH 6.8 (a), pH 8 (b) and pH 10.5 (c). Difference spectra show the time-dependent evolution of absorption with respect to the initiation of the conditioning (red), sorption (black) and flushing (blue) stage.

The asymmetric vibrational frequencies of these species decrease with increasing number of hydroxide ligands per U atom and were determined in previous studies to be 925, 922 and 895 cm^{-1}, respectively (Müller, 2010; Müller et al., 2008; Müller et al., 2013). The latter one was not determined experimentally but was derived from the underlying linear correlation. However, the obtained values of the main peaks in the present spectra are not red shifted compared to the respective aqueous species, but appear at higher wavenumbers. Hence, the formation of bidentate inner-sphere sorption complexes, as it has been described by Lefevre et al. (2006), Müller (2010), Foerstendorf et al. (2012), Müller et al. (2013) and Comarmond et al. (2016), is not the dominant retention mechanism in all three samples. Nevertheless, such inner-sphere complexes might form at least to some extent, inferred from the observed shoulders.

The observed absorption maximum at around 941 cm^{-1} at pH 6.8 and 8 fits very well to the asymmetric vibrational frequency reported for the oxyhydroxide mineral schoepite ($(UO_2)_8O_2(OH)_{12}\cdot 12(H_2O)$). Müller et al. (2013) determined the absorption band of synthetic schoepite to be at 939 cm^{-1} and found a schoepite-like surface precipitate on Al_2O_3 at 946 cm^{-1}. Furthermore, a colloidal U(VI) solution in 0.1 M NaCl at pH 7, measured by Müller et al. (2008) showed an asymmetric vibrational frequency of 940 cm^{-1}. While this comparison with literature data suggests a schoepite-like precipitate at pH 6.8 and 8, the retained U(VI) at pH 10.5 seems to be distinct from that. The precipitation of a different mineral phase than schoepite at pH higher than 8 has been shown in previous studies. Altmaier et al. (2017) identified the solubility limiting phase in NaCl solutions to be metaschoepite ($UO_3\cdot 2H_2O$) up to pH 6.5-8.5 (depending on NaCl concentration) and sodium diuranate ($Na_2U_2O_7\cdot H_2O$) at higher pH values. Consequently, the retained U(VI) compound at pH 10.5 could be sodium diuranate. Chernorukov et al. (2016) and Baran and Tympl (1966) measured infrared spectra of sodium diuranate compounds which were synthesized with variable number of H_2O molecules (water of crystallization) and Na/U ratio. The observed asymmetrical stretch vibration strongly depended on these two parameters and varied between 936 and 861 cm^{-1} and between 949 and 869 cm^{-1}, respectively. Therefore, in the present study, a clear assignment to this compound cannot be made. The observed band position of 927-929 cm^{-1} at pH 10.5 is somewhere in between the regions usually attributed to precipitation and to adsorbed species. The only U(VI) compound with a comparable asymmetric stretch vibration (927 cm^{-1}) described in literature is a oligomeric surface complex on Al_2O_3 (Müller et al., 2013). Presumably such oligomeric complexes also form here and display precursors for surface precipitates.

In general, it can be stated that in all three samples (pH 6.8, 8 and 10.5) precipitation (or at least formation of oligomeric surface complexes at pH 10.5) appears to be the predominant retention mechanism. Only minor contributions of inner-sphere adsorption could be observed. This finding is reasonable because with a U(VI) concentration of 2×10^{-5} M, alkaline NaCl solutions are supersaturated by several orders of magnitude according to Altmaier et al. (2017). However, this does not have to hold true for the much lower initial U(VI) concentrations of the batch sorption experiments (5×10^{-7} M). Consequently, due to the detection limit, ATR FT-IR spectroscopy is capable of identifying U(VI) speciation in super-micromolar systems but does not allow determination of different retention mechanisms at sub-micromolar concentrations. Thus, in order to resolve underlying processes at 5×10^{-7} M U(VI), where precipitation is less favored, more sensitive techniques such as site-selective TRLFS and EXAFS were applied.

Site-selective TRLFS

Figure 3-16a shows the excitation spectrum (black data points) of U(VI) sorbed on Ca-bentonite at pH 11 in the absence of CO_2 and a series of selected emission spectra (in color), obtained at different excitation wavelengths. The excitation spectrum does not contain much spectral information. The absence of distinct maxima is attributed to great variety of sorption sites within the sample, leading to an inhomogeneous broadening. This heterogeneity of sorption sites is not surprising as Ca-bentonite is a very complex, multi-mineral material, where already montmorillonite provides different complexation sites (e.g. edge sharing, corner sharing) and aluminol/silanol functionalities. The variety of sorption species can also be inferred from different emission spectra, which shift strongly, depending on the excitation energy. At low excitation wavelength (e.g. 472.8 nm) the emission spectra appear broadened and weakly resolved as the incident energy is high enough to excite all uranyl moieties within the sample. At higher excitation wavelengths (in Figure 3-16a exemplarily shown for λ_{ex} = 494.3, 499.7 and 505.2 nm), however, a clear luminescence line-narrowing can be observed due to resonant/direct excitation of single species. The occurrence of luminescence line-narrowing alone already indicates the presence of adsorbed U(VI) surface complexes and eliminates U(VI) precipitation as the predominant retention mechanism. In U(VI) precipitates, such as Na,Ca-uranates, the phenomenon of luminescence line-narrowing is suppressed by homo-resonance energy transfer between the U-atoms arranged in close distance to each other, leading to a mutual excitation and consequently to a broadening of the signal (Lakowicz, 2006; Tits et al., 2015). Such signal broadening is observed in the present batch sample prepared with an initial U(VI) concentration of 5×10^{-5} M to provoke U(VI) precipitation for comparison (Figure 3-16b). In fact, the obtained spectra show no luminescence line-narrowing, irrespective of the excitation energy. U(VI) precipitation at these conditions is in accordance with the *in situ* ATR FT-IR spectroscopy measurements at 2×10^{-5} M. Broad and unresolved maxima around 545 nm appear at all excitation wavelengths,

featuring luminescence lifetimes between 30 and 60 μs, depending on the excitation wavelength. Spectra with similar appearance and lifetimes have been identified as Ca-uranate in Tits et al. (2015) and (2011). No such features were observable in the sorption sample with 5×10^{-7} M uranium, implying that adsorption can be considered as the only relevant retention mechanism at these experimental conditions.

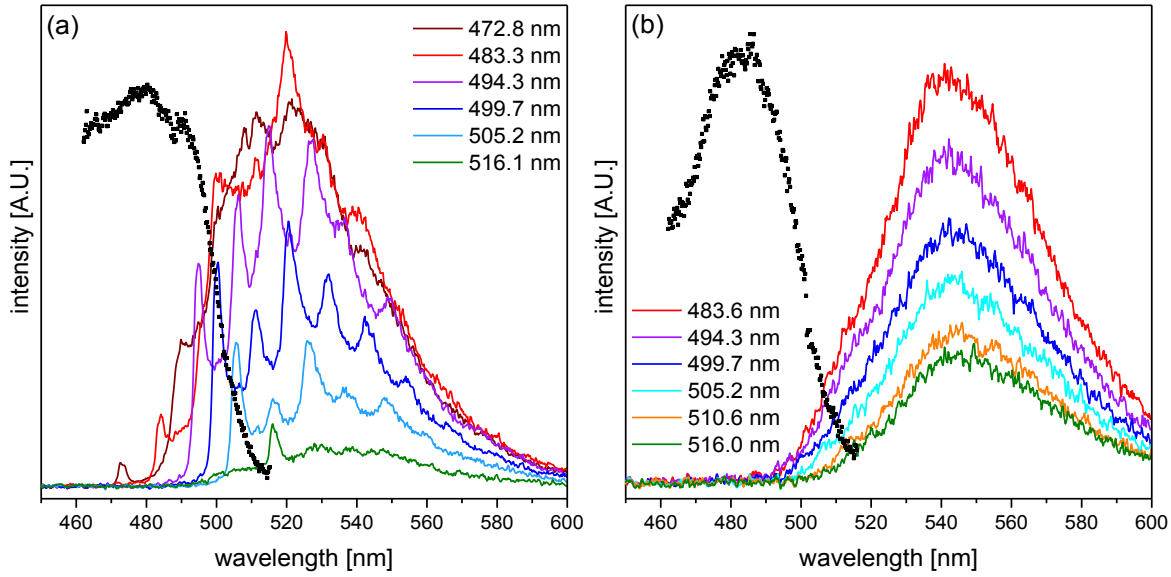

Figure 3-16: Excitation (black dots) and emission spectra (colored lines) of U(VI) sorbed on Ca-bentonite in the absence of CO_2 at pH 11 with [U(VI)] = 5×10^{-7} M (a) and [U(VI)] = 5×10^{-5} M (b) obtained with site-selective TRLFS at 10 K.

From the absolute positions of the narrowed peaks of the emission spectra alone, not much information about the U(VI) surface speciation can be deduced. However, the relative position of the maxima (i.e. the distance of the different electronic and vibronic transition lines) provides insight into the structure of the uranyl unit. For that purpose, electronic and vibronic transition events were assigned to the single emission lines, exemplarily shown for the emission spectrum obtained at 499.7 nm excitation wavelength (Figure 3-17). In phase with the incident laser energy, the resonant electronic transition line E_1 appears, followed by the lines of vibronic progression on E_1 ($S_{1,E1}$ and $S_{2,E1}$) caused by the vibronic degeneracy of the electronic ground state. Furthermore, a second (non-resonant) U(VI) species with the non-resonant electronic transition line E_2 can be identified. Also this species is superimposed by the first two lines of vibronic progression ($S_{1,E2}$ and $S_{2,E2}$). The spacing between the first two peaks of each species (i.e. between E_1 and $S_{1,E1}$ and between E_2 and $S_{1,E2}$, respectively) corresponds to the total symmetric stretch vibration (ν_s) of the uranyl ion in the ground state. The spacing of the first (resonantly excited) species $\nu_s(1)$ is 781 ± 5 cm^{-1} (Table 3-6). With 758 ± 12 cm^{-1}, the stretch vibration $\nu_s(2)$ of the second, non-resonantly excited, species noticeably differs from the first one. Both frequencies lie in the typical range found for U(VI) minerals and sorbed species (Wang et al., 2011; Wang et al., 2005a), and are significantly smaller than values found for aqueous species (Nguyen-Trung et al., 2000), such as

$UO_2(OH)_3^-$, which is dominating the aqueous speciation at pH 11 (Table 3-6). Especially for species 2, this strong weakening of the axial U-O bond implies strong bonding in the U(VI) equatorial plane upon adsorption (i.e. inner-sphere surface complexation). The comparatively higher frequency for species 1 could then hint towards outer-sphere sorption.

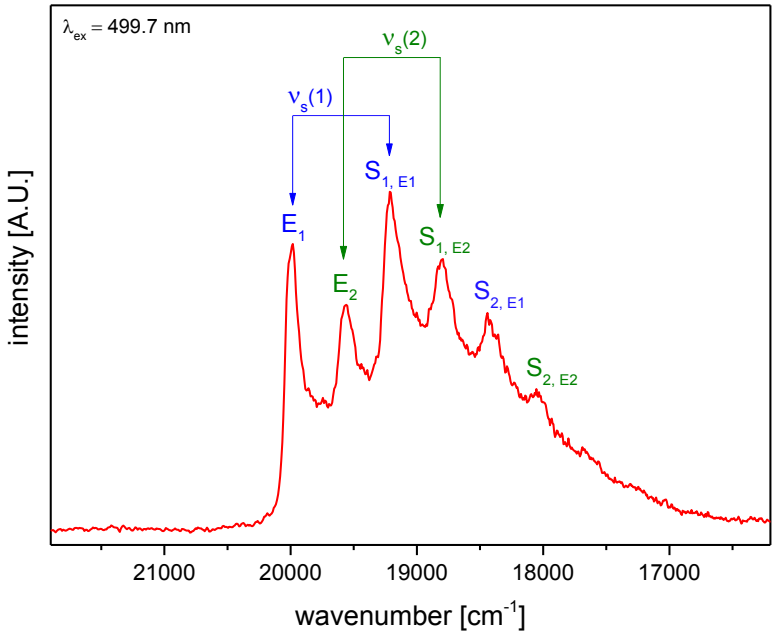

Figure 3-17: Luminescence emission spectrum of 5×10^{-7} M U(VI) sorbed on Ca-bentonite at pH 11 in the absence of CO_2 after laser excitation at 499.7 nm. Two U(VI) species could be identified based on their different electronic and vibronic transitions. Spacing between the first two main peaks of each species $\nu_s(1)$ and $\nu_s(2)$ are indicated.

Table 3-6: Frequencies of the total symmetric stretch vibration (ν_s) deduced from the spacing between the luminescence emission lines of U(VI) (5×10^{-7} M) sorbed on Ca-bentonite at pH 11 in comparison to literature values.

Uranyl species	ν_s [cm^{-1}]	Reference
1	781 ± 5	this study
2	758 ± 12	this study
UO_2^{2+}	870	Nguyen-Trung et al. (2000)
$UO_2(OH)_3^-$	804	Nguyen-Trung et al. (2000)
U(VI) minerals and sorbed species	700-800	Wang et al. (2011); Wang et al. (2005a)
Adsorbed on C-S-H	758	Tits et al. (2015)

Inner-sphere surface complexation of U(VI) at montmorillonite silanol and aluminol edge sites has been previously demonstrated at neutral pH by TRLFS (Chisholm-Brause et al., 2004; Chisholm-Brause et al., 2001; Kowal-Fouchard et al., 2004) and EXAFS (Catalano and Brown, 2005; Marques Fernandes et al., 2012). Between pH 8 and 13, no spectroscopic studies dealing with U(VI) surface complexation exist for comparison. The present study suggests that inner-sphere surface complexation at pH 10-12 can occur in a similar way as at

neutral pH. A couple of studies are available on U(VI) sorption by cementitious systems above pH 13. The total symmetric stretch vibration of species 2 of the present study compares very well to that of a surface complex detected on C-S-H phases at pH 13.3 by Tits et al. (2015). As $UO_2(OH)_3^-$ is the dominant aqueous U(VI) species at pH 11, electrostatic repulsion does not seem to prevent this anionic complex from adsorbing to the negatively charged clay surface. The general ability of $UO_2(OH)_3^-$ to form surface complexes (in contrast to $UO_2(OH)_4^{2-}$) might be a result of electrostatic inter-ligand repulsion. According to this concept, only a limited number of OH groups can fit in the first coordination sphere of any given actinide, depending on its oxidation state. For U(VI) the maximum number of OH groups in the equatorial plane is four (Fanghänel and Neck, 2002; Neck and Kim, 2000, 2001). Therefore, $UO_2(OH)_3^-$ with three hydroxyls in its first coordination sphere is still able to form an additional bond between the surface and the metal center, while in $UO_2(OH)_4^{2-}$ the equatorial plane is fully occupied. A possible role of cations (i.e. Ca^{2+}) mediating between the anionic hydrolysis complex and the mineral surface is investigated in chapter 4.

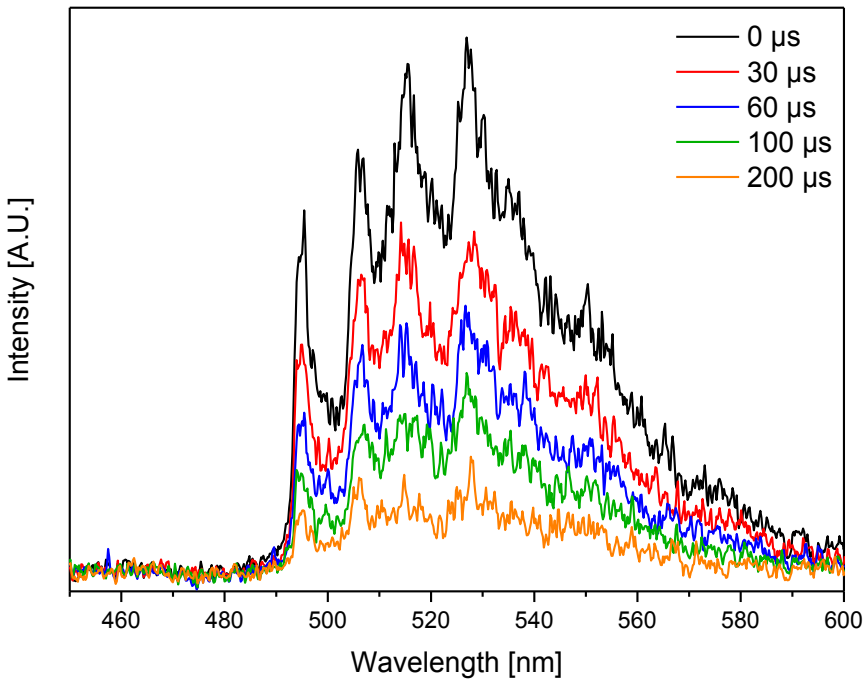

Figure 3-18: Luminescence emission spectra at λ_{ex}=494.3 nm of U(VI) ([U(VI)] = 5×10^{-7} M) sorbed on Ca-bentonite in the absence of CO_2 at pH 11 at different delay time (as indicated in the diagram). The intensity of all emission bands decreases uniformly with increasing delay time. Hence, coexisting species do not feature different luminescence lifetimes.

The luminescence signal decays biexponentially with a short lifetime $\tau_1 = 35.5 \pm 3.9$ µs and a long lifetime $\tau_2 = 148.7 \pm 13.5$ µs, seemingly reflecting the two species identified from the narrow lines in the emission spectra. However, when inspecting single emission spectra at different delay time it becomes evident that the intensity of all narrow lines decays with the same rate (Figure 3-18). None of the two species vanishes as a response to a shorter lifetime. That means that both adsorbed species 1 and 2 are represented by lifetime τ_2. Even though it

is not becoming apparent in the emission spectra, the shorter lifetime τ_1 is tentatively attributed to a small portion of U(VI) precipitates formed under these conditions.

EXAFS spectroscopy

Figure 3-19 shows the EXAFS spectra and Fourier transforms (FT) of the sorption samples with different pH and carbonate concentrations (N_2, LC, HC), including a reference spectrum of the aqueous $UO_2(OH)_4^{2-}$ complex. None of the spectra shows indications for U(VI) precipitation (i.e. no U-U backscattering paths detected). Consequently, as already deduced from site-selective TRLFS, the predominant retention mechanism of U(VI) in Ca-bentonite under the given conditions is adsorption. A trend of decreasing average equatorial oxygen (O_{eq}) distance with increasing pH is observed within each sample series. While the peaks for O_{eq} and axial oxygen (O_{ax}) are clearly separated at pH 8 and 9, at elevated pH only combined peaks for O_{eq} and O_{ax} can be observed in the Fourier transforms (FT).

The application of ITFA showed that all ten EXAFS spectra can be reproduced with two spectral components (Figure 3-19). The *IND* function reaches a minimum at $n = 2$ and only the first two eigenvectors show EXAFS spectral features above the noise level (Figure 3-20). Consequently, two structurally different sorption complexes are present in the system with different fractions in each sample, depending on the pH. According to the result of the iterative target test (ITT) component 1 is predominant at the lowest pH of each sample set (i.e. sample 1 (N_2, pH 8.0) or sample 5 (LC, pH 9)) and occurs independently of the presence or absence of carbonate. Conversely, the fraction of component 2 is highest in the samples prepared at high pH (Figure 3-21). According to the extracted single component spectra and the results of the ITFA, component 2 matches to the $UO_2(OH)_4^{2-}$ reference. Hence, for the samples with high pH, both the spectrum and the local atomic structure around U(VI) agree with those of the aqueous $UO_2(OH)_4^{2-}$ complex. Consequently, component 2 is a sorption species at the bentonite surface with a structure similar to the aqueous $UO_2(OH)_4^{2-}$ complex.

An interaction of U(VI) with carbonate would lead to the detection of a third component in the sample series LC and HC. However, only two components were detected. Consequently, no ternary U(VI) carbonate sorption complexes are present on the Ca-bentonite surface. This observation is in accordance with the work of Marques Fernandes et al. (2012), where no influence of carbonate on the surface complexation could be detected with EXAFS, also supporting the hypothesis of Tournassat et al. (2018) that uranyl carbonate complexes do not adsorb on montmorillonite surfaces to significant amounts.

Shell fitting of the ITT isolated spectrum of component 1 and of the spectrum of the aqueous $UO_2(OH)_4^{2-}$ complex was performed, while the latter was selected instead of the ITT isolated spectrum of component 2 in order to gain a higher resolution for the determination of radial distances due to the larger available *k*-range. The fit of the spectra and the corresponding EXAFS structural parameters are given in Figure 3-22 and Table 3-7.

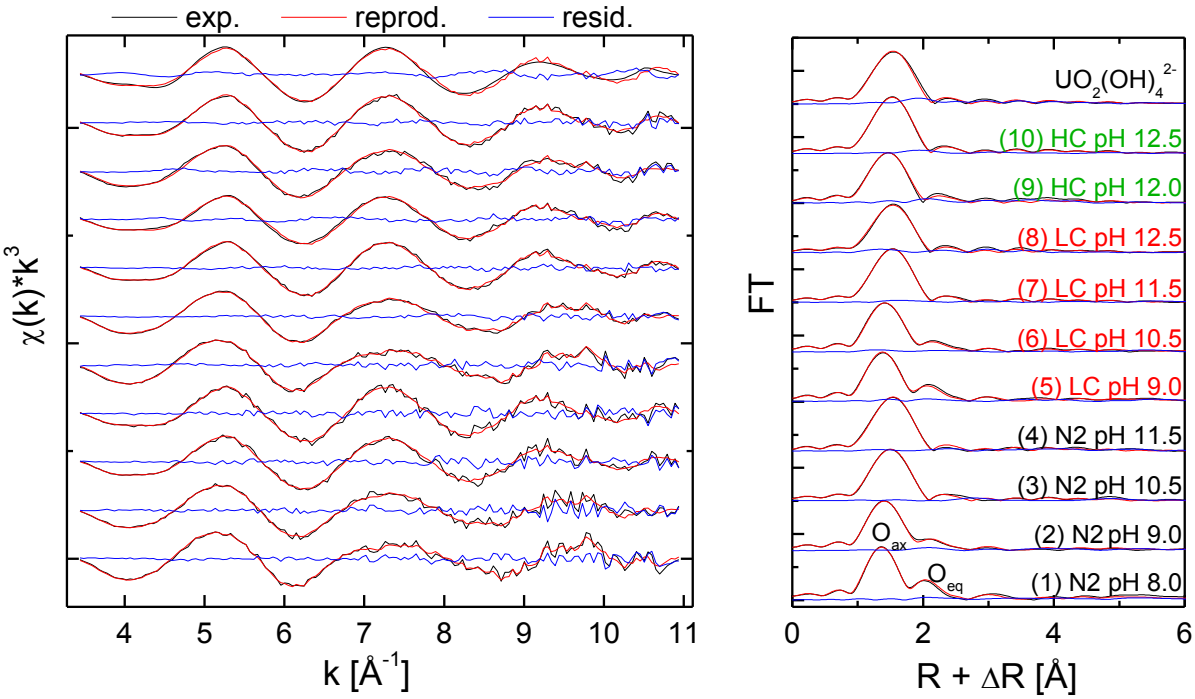

Figure 3-19: U L_{III}-edge EXAFS spectra (left, black) and corresponding Fourier transforms (right, black) with reproductions (red) and the residual (blue) of U(VI) sorption samples on Ca-bentonite in the absence of carbonate (N_2) and at low (LC) and high (HC) carbonate concentrations, including a reference spectrum of the aqueous $UO_2(OH)_4^{2-}$ complex (Moll et al., 2014).

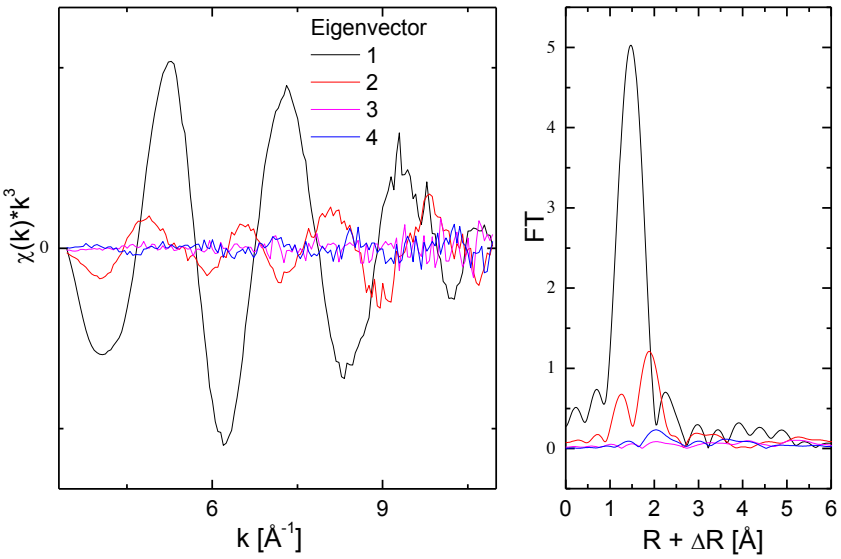

Figure 3-20: U L_{III}-edge EXAFS spectra of the first four eigenvectors (left) and their corresponding Fourier transforms (FT) (right).

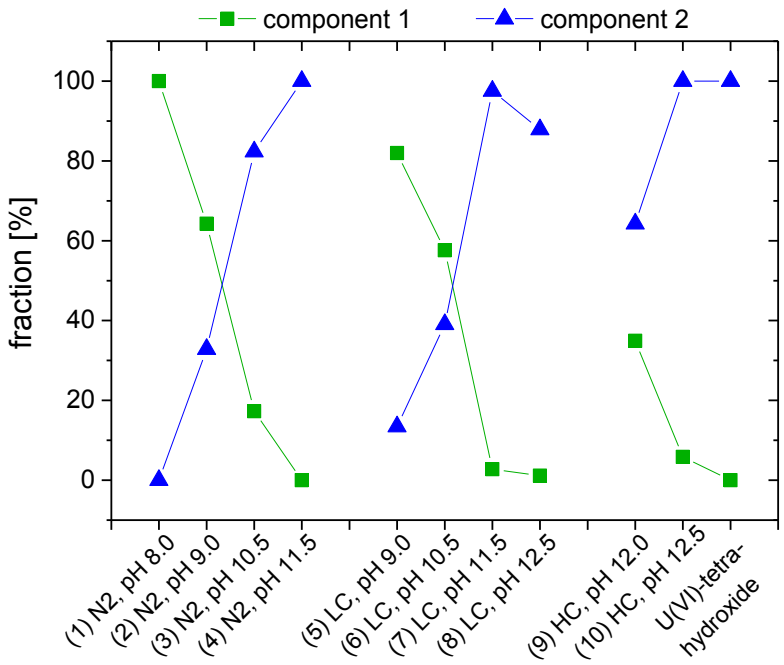

Figure 3-21: ITT calculated fractions of component 1 and component 2 for U(VI) sorption samples on Ca-bentonite in the absence of carbonate (N_2) and at low (LC) and high (HC) carbonate concentrations, including the reference of the aqueous $UO_2(OH)_4^{2-}$ complex (Moll et al., 2014).

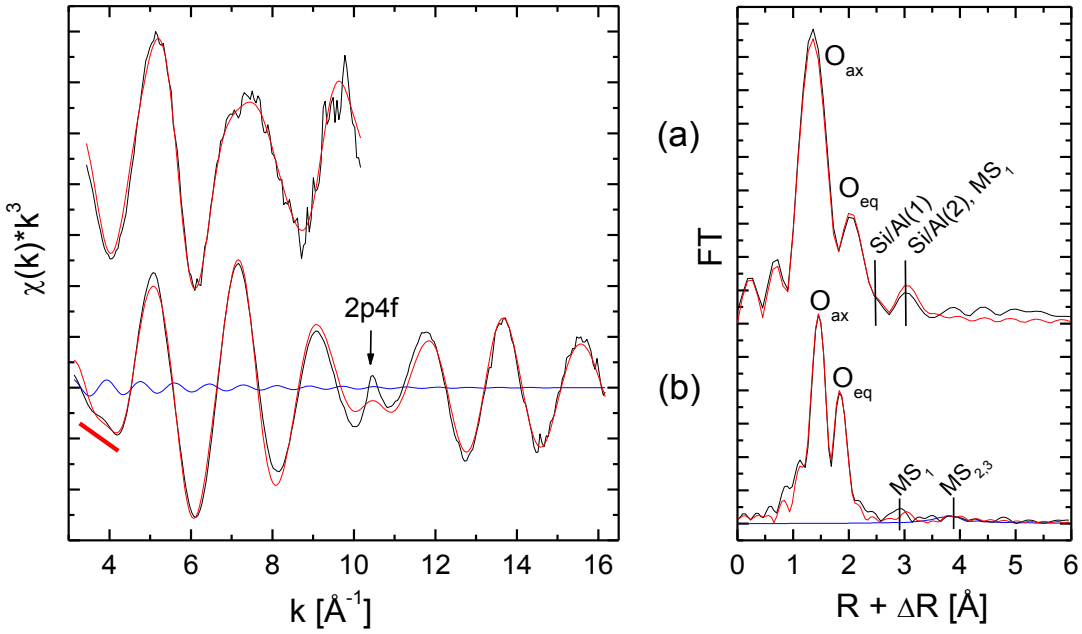

Figure 3-22: U L_{III}-edge EXAFS spectra of the ITFA isolated component 1 (a) and of the aqueous $UO_2(OH)_4^{2-}$ complex (b) (left) with corresponding Fourier transforms (FT) (right) together with the shell fit (red). Spectral contribution of MS_2 and MS_3 (blue). 2p4f multi-electron excitation assigned with arrow (Hennig, 2007).

For component 1 an equatorial oxygen shell (U-O_{eq}) at a distance of ~2.38 Å (*CN* fixed to 5) was obtained. This shortened distance in comparison to U-O_{eq} of hydrated outer-sphere sorption complexes on montmorillonite described in literature of ~2.43 Å (Chisholm-Brause

et al., 1994; Sylwester et al., 2000) suggests the formation of inner-sphere surface complexes. Marques Fernandes et al. (2012) observed a splitting of the equatorial oxygen shell in sorption samples at pH 8 and obtained U-O_{eq} distances of ~2.3 Å and ~2.48 Å. Such a splitting cannot be resolved in the present study due to lower resolution in radial distances. However, when averaging the reported distances of Marques Fernandes et al. (2012), weighted by the coordination numbers (3.1 and 2.9), a mean U-O_{eq} distance of 2.387 Å can be derived, which is in excellent agreement with the results of the present study. Furthermore, two Si/Al shells could be fitted in radial distances of 3.11 Å and 3.32 Å. Those are in good agreement with the Si/Al distances of 3.09 Å and 3.28 Å for the bidentate inner-sphere sorption complexes on montmorillonite at pH 8 described by Marques Fernandes et al. (2012). Therefore, the same type of U(VI) surface complex is proposed for component 1.

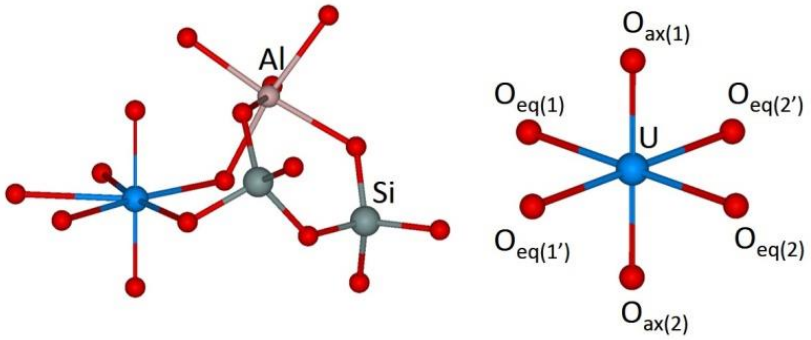

Figure 3-23: Arbitrary structural model of the sorption complex and of the aqueous $UO_2(OH)_4^{2-}$ complex used for the calculation of theoretical phase and amplitude functions by FEFF8.20. O_{ax}: axial oxygen, O_{eq}: equatorial oxygen.

Representative for component 2, the high symmetry of the $UO_2(OH)_4^{2-}$ complex leads to the appearance of a spectral feature at k = 3.5 – 4.3 Å^{-1} (Figure 3-22, highlighted with red line) which originates from the multiple scattering (MS) paths MS_2 (U-$O_{eq(1)}$-U-$O_{eq(2)}$) and MS_3 (U-$O_{eq(1)}$-U-$O_{eq(1)}$) (Figure 3-23). The scattering contribution of these inherent MS paths is strongly enhanced due to the linear arrangement of the involved atoms, comparable with the arrangement in the linear 'yl' chain of U(VI) for which the MS_1 (U-$O_{ax(1)}$-U-$O_{ax(2)}$) shows a significant spectral contribution. Note that the 4-fold degenerated 3-legged MS path U-$O_{eq(1)}$-$O_{eq(2)}$ was also tested, but no further improvement of the fit was obtained. The sum of the MS_2 and MS_3 scattering contributions causes a truncation of the negative maximum of the EXAFS oscillation in this k-region (Figure 3-22). The distance of 4.55 Å measured for MS_2 and MS_3 matches, within the common error in determination of distances probed by EXAFS (Li et al., 1995), the theoretically expected distance of 4.54 Å which would be twice the O_{eq} distance of 2.27 Å (Table 3-7). The O_{ax} and O_{eq} distances and the corresponding Debye-Waller factors (σ^2) are in good agreement with published data (Table 3-7) where the MS feature was not explored so that only the coordination number (*CN*) and/or the O_{eq} distance could be used for the structural interpretation of the aqueous $UO_2(OH)_4^{2-}$ complex (Moll et al., 2000; Moll et al., 2014). However, the error in determination of the *CN* is approximately 20% (Li et al., 1995), hence the EXAFS determined *CN* is not reliable enough to be used as a proof for the

presence of a 4-fold coordinated U(VI) complex. Thus, only the presence of the MS feature at k = 3.5 – 4.3 Å^{-1} indicates univocally a symmetric 4-fold coordination of U(VI). Due to the appearance at low k-values, the MS feature is visible in the X-ray absorption near edge structure (XANES) at 17,240 eV. Therefore, XANES can be also used for the identification of a 4-fold coordination, as exemplary shown for the aqueous complexes of the 5- and 4-fold coordinated U(VI)-hydrate ($UO_2(H_2O)_5^{2+}$) and $UO_2(OH)_4^{2-}$, respectively (Figure 3-24).

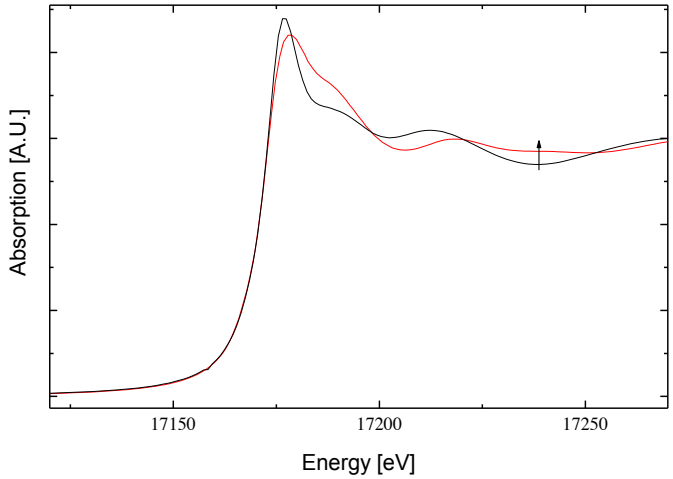

Figure 3-24: U L_{III}-edge XANES spectrum of $UO_2(H_2O)_5^{2+}$ (black) and $UO_2(OH)_4^{2-}$ (red). Arrow marks position of the multiple scattering (MS) feature at 17,240 eV resulting from U-$O_{eq(1)}$-U-$O_{eq(2)}$ and U-$O_{eq(1)}$-U-$O_{eq(1)}$ MS paths.

The MS feature at k = 3.5 – 4.3 Å^{-1} is also present in case of the high pH sorption samples (Figure 3-19, which is in line with the ITFA result (Figure 3-21) pointing to the prevalence of a sorption complex with a $UO_2(OH)_4^{2-}$ like structure. In the case of 5-fold coordinated U(VI) the $O_{eq(1)}$-U-$O_{eq(2)}$ angles are not straight, so that the spectral contribution of MS_2 and MS_3 diminishes as observed for component 1 which covers the lower pH sorption samples. Thus, beside the fractions of the two sorption complexes the ITT shows also the transition from a 5-fold to a 4-fold coordination of U(VI) with increasing pH.

Despite the strong similarity with the aqueous $UO_2(OH)_4^{2-}$ complex according to the shell fit, it can be ruled out that component 2 corresponds to an aqueous species, as U(VI) was almost completely removed from solution and the EXAFS samples were prepared as wet pastes with only a minor amount of aqueous solution present. An aqueous species could therefore be present in the samples only as a minor fraction, while component 2 accounts for up to 100% in some of the samples. Consequently, component 2 can definitely be assigned to an adsorbed species. Furthermore, $UO_2(OH)_4^{2-}$ is expected to be the dominant aqueous species only at pH > 12, as confirmed by the TRLFS measurements. In the EXAFS samples between pH 10 and 12, $UO_2(OH)_3^-$ is the dominant aqueous species prior to sorption. Owing to the difficulty to obtain $UO_2(OH)_3^-$ as a single, isolated species, no EXAFS reference spectra exist for this complex. Its structure, especially the coordination number of equatorial oxygen, is not clarified. While sometimes referred to be 5-fold coordinated (3 OH and 2 H_2O), the DFT

study of Ingram et al. (2006) proposed a 4-fold coordination (3 OH and 1 H_2O). The finding of the present study of a 4-fold coordination of component 2 supports this hypothesis. Apparently, this geometry is then preserved upon sorption, indicating relatively weak interaction with the substrate. Also the fact that it was not possible to fit U-Si/Al scattering paths for component 2 indicates a larger distance to the mineral surface. The complex could be bound via mediating cations such as Ca^{2+}, located between the negatively charged surface and the anionic uranyl hydroxide unit. Sorption of negatively charged uranyl species would then be realized by initial adsorption of Ca^{2+} to the clay mineral surface (Gascó and Méndez, 2005; Missana and García-Gutiérrez, 2007; Pointeau et al., 2004; Viallis-Terrisse et al., 2001), leading to a local charge inversion and facilitating attachment of anionic uranyl hydroxides. Also the formation of aqueous ternary Ca-uranyl-hydroxides is possible, which would have a neutral or even positive net charge and would be therefore capable of interacting with the negatively charged bentonite surface. The existence of such ternary Ca-uranyl-hydroxide complexes at (hyper)alkaline conditions is hypothesized but has not been explored yet in detail. The influence of calcium on U(VI) sorption on clay minerals is systematically and comprehensively investigated in chapter 4.

Table 3-7: Shell fit EXAFS structural parameters for component 1 and the aqueous $UO_2(OH)_4^{2-}$ complex.

Shell	*CN*	*R* [Å]	σ^2 [Å^2]	ΔE_0 [eV]
		Component 1		
O_{ax}	2*	1.797(3)	0.0010(2)	11.0(5)
MS_1	/2	/3.594	/0.002	/11.0
O_{eq}	5*	2.382(8)	0.0154(8)	/11.0
Si/Al(1)	1.5(2)	3.11(1)	0.003[a]	/11.0
Si/Al(2)	1.2(2)	3.32(1)	0.003[a]	/11.0
		aqueous $UO_2(OH)_4^{2-}$ complex		
O_{ax}	2*	1.8254(9)	0.00176(6)	3.6(3)
		1.83[b], 1.82[c]	0.001[b], 0.0015[c]	
MS_1	/2	/3.6508	/0.00352	/3.6
O_{eq}	4*	2.271(1)	0.0040(1)	/3.6
		2.25[b],	0.0043[b],	
		2.26[b], 2.27[c]	0.0046[b], 0.004[c]	
MS_2	/4	4.55(2)	0.005(3)	/3.6
MS_3	/4	/4.55	/0.005	/3.6

* - fixed parameter, / - linked parameter, *CN* − coordination number, *R* − radial distance, σ^2 − Debye-Waller factor, ΔE_0 − shift in energy threshold. The standard deviation of the fitted parameters is given in parentheses. Amplitude reduction factor $S_0^2 = 1.0$. Multiple scattering paths MS_1 (U-$O_{ax(1)}$-U-$O_{ax(2)}$), MS_2 (U-$O_{eq(1)}$-U-$O_{eq(2)}$), MS_3 (U-$O_{eq(1)}$-U-$O_{eq(1)}$). [a] - σ^2 fixed at value taken from literature (Hennig et al., 2002; Marques Fernandes et al., 2012), [b] - (Moll et al., 2000), [c] - (Moll et al., 2014).

Based on the knowledge obtained from EXAFS, also an assignment of the two species detected with site-selective TRLFS to the structurally different surface complexes is possible. Assuming a $UO_2(OH)_4^{2-}$ like structure for component 2, a theoretical frequency for the symmetric stretch vibration can be calculated according to an empirical relationship for

aqueous uranyl hydroxide complexes found by Nguyen-Trung et al. (2000). With four equatorial oxygens a ν_s of 782 cm^{-1} is obtained, which is almost identical to the ν_s of TRLFS-species 1 (781 cm^{-1}, Table 3-6). Accordingly, TRLFS-species 2, with a lower ν_s of 758 cm^{-1}, has to correspond to the 5 fold-coordinated bidentate surface complex (EXAFS-component 1). This assumption is reasonable as a decrease of ν_s (as a consequence of a weakening of the axial U-O bonds) is a response to an increased electron density and increased ligand bond strength in the equatorial plane (Di Pietro and Kerridge, 2016; McGlynn et al., 1961; Nguyen-Trung et al., 2000; Tsushima, 2011). For EXAFS-component 1 this is a result of the bidentate binding and the close proximity to substrate atoms (Si/Al) in contrast to EXAFS-component 2, where no backscattering contributions from the substrate could be detected. Due to extensive σ donation from the surface, Tsushima et al. (1998) and Morris et al. (1994) obtained similar values for ν_s for inner-sphere surface complexes on silver nanoparticles (750 cm^{-1}) and smectite edge sites (751 cm^{-1}), respectively.

CTR/RAXR

CTR and RAXR were performed in order to gain further information about the spatial distribution of U(VI) at clay mineral surfaces at hyperalkaline conditions. As the X-ray reflectivity measurements require a single crystal, the mica (001) surface was used as a structural analogue for clay minerals. The idea was to test the hypothesis that calcium is mediating between the negatively charged surface and anionic uranyl hydroxides in solution. This could not be directly proven with EXAFS, as EXAFS-component 2, prevailing at hyperalkaline conditions, did not feature any backscattering contribution from the substrate, possibly due to an increased distance of adsorbed U(VI). As CTR/RAXR is a surface sensitive technique, it uncovers the distance of the resonant U(VI) to the mineral surface as well as the electron density between U(VI) and the surface, possible influenced by the presence of calcium.

Fitting of the integrated CTR data yields the total electron density above the surface. In Figure 3-25 the normalized electron density profiles of the U(VI) sorption samples at pH 11 in the presence and absence of 0.02 M $CaCl_2$, as well as a blank muscovite sample (absence of U(VI)) in 0.1 M NaCl + 0.02 M $CaCl_2$ are plotted. It is clearly visible that the peaks of the U(VI) sorption samples feature higher electron densities compared to the blank muscovite sample, meaning that U(VI) definitely approaches the crystal to some extent. However, the overall electron density is comparably low in all samples, indicating that the amount of sorbed U(VI) must be relatively small.

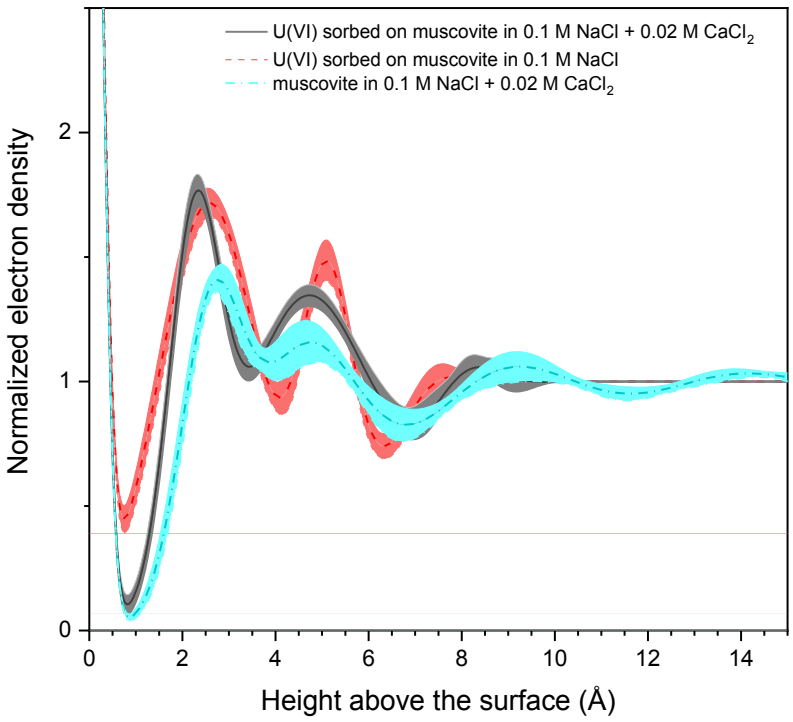

Figure 3-25: Electron density profile (normalized to the electron density of water) above the surface of the muscovite crystal of the U(VI) sorption samples ([U(VI)] = 5×10^{-5} M) in 0.1 M NaCl (grey solid line) and in 0.1 M NaCl + 0.02 M CaCl$_2$ (red dashed line). The blank sample without U(VI) (only muscovite crystal in 0.1 M NaCl + 0.02 M CaCl$_2$, blue dashed-dotted line) is included for comparison. Envelopes around the graphs indicate the margins of uncertainty.

Slight differences in the electron density of the sorption samples with and without calcium suggest the adsorption of calcium to the muscovite surface. In the presence of calcium, the first maximum at approx. 2.6 Å is noticeably narrowed in the presence of calcium, while the second maximum at approx. 5.1 Å is broadened. Both peaks are slightly shifted toward the surface. Compared to a muscovite sample in 0.03 M NaCl from Lee et al. (2012) especially the second maximum of both samples containing calcium (U(VI) sorption sample and blank) is closer to the surface, suggesting that the solution cation has greatest influence on the region at 4.7-5.1 Å above the surface. Without clearly associating the peaks of bulk electron density to adsorbed water or solution cations Na^+ or Ca^{2+}, it can be stated that the presence of different ions in the solution alters the electron density at the surface due to their adsorption. Depending on the adsorbed cation also the contribution of water to the electron density is influenced, caused by the different hydration behavior of sodium and calcium.

Integrated RAXR data, elucidating the contribution of the resonant U(VI) to the electron density, exhibit small but clear modulations around the L_{III} absorption edge in both U(VI) sorption samples at pH 11 (in the presence as well as in the absence of calcium). Representative for both, as the obtained data is very similar, in Figure 3-26a only the spectra of the sample in 0.1 M NaCl + 0.02 M $CaCl_2$ are shown. Noticeable modulations only appear at very low momentum transfer of 0.14, 0.19 and 0.24 Å^{-1}. This indicates a very broad distribution of U(VI) above the surface, i.e. a very variable adsorption height.

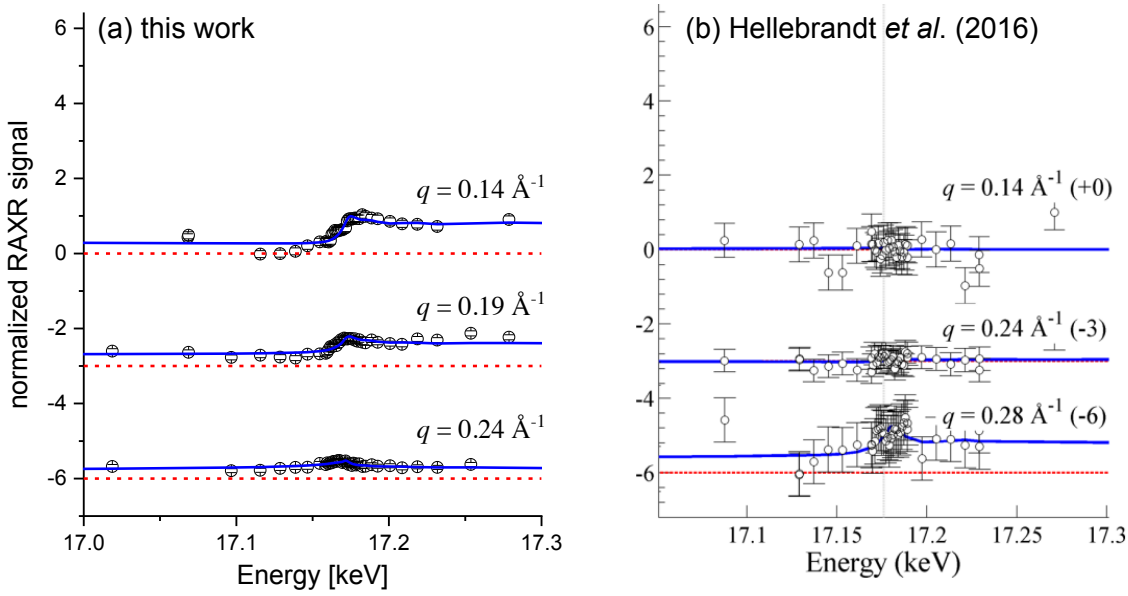

Figure 3-26: Selected RAXR data measured at the muscovite (001) basal plane at different fixed momentum transfer for the U(VI) sorption sample ([U(VI)] = 5×10^{-5} M) at pH 11 in 0.1 M NaCl + 0.02 M $CaCl_2$ of this work (a) and for a U(VI) sorption sample ([U(VI)] = 1×10^{-3} M) at pH 3.2 measured by Hellebrandt et al. (2016) (b). The deviation of the RAXR signal from the U(VI) free baseline (dashed red lines) is a result of adsorbed resonant U(VI). The blue lines display the model-independent fit of the data points and are included to guide the eye.

In a previous CTR/RAXR study of U(VI) sorption on the muscovite basal plane at acidic conditions and with a significantly higher concentration of U(VI) ([U(VI)] = 1×10^{-3} M) by Hellebrandt et al. (2016) (Figure 3-26b) no U(VI) was found to adsorb on the surface. This behavior is somewhat counterintuitive as at the chosen experimental conditions (pH 3.2) the cationic uranyl aquo ion dominates the aqueous speciation and should adsorb much better to a negatively charged surface than the anionic solution species prevailing at the very alkaline conditions (pH 11) of the present study. Hellebrandt et al. (2016) presumed that the size or the complex charge distribution of uranyl hindered its adsorption in comparison to other divalent cations. Alternatively, U(VI) sorption could be suppressed due to competition with an excess of sodium in solution. Experiments with plutonium revealed that a reduction to the tetravalent oxidation state was necessary for an effective interaction with the muscovite (001) surface. Possible reasons for the increased U(VI) retention in the present work could be the lower U(VI) solubility at alkaline conditions but also the fact that solution cations (Na^+, Ca^{2+}) at high pH do not act as competitors for anionic uranyl hydroxides, but maybe even as mediators.

A first approximation of the distribution of the resonant ions above the surface is provided by model-independent fitting of the RAXR data. Based on the output data of the model-independent fit (position, distribution width and integral area of the peaks in the electron density profile) it was attempted to build a model which reproduces the amplitude and phase of the modulations at different momentum transfer (Figure 3-27a). The corresponding electron density profile is depicted in Figure 3-27b. It should not be understood as definite structure but only represents one possible solution with satisfactory fit to the data points. The

real distribution of U(VI) above the surface could be different from that (e.g. exact height of the different species) but is expected to be similar. Refining the fit with model-dependent approaches is complicated by the very small number of measurements (data points for the fitting) with significant modulation. This is due to the particular spatial distribution of U(VI) in the samples. Moreover, additional optimization of the model is not worthwhile, as this would not affect the general outcome. U(VI) is very broadly distributed on the surface, resulting in a sharp drop in amplitude already at low momentum transfer (Figure 3-27a top). The corresponding flat and extremely broad peak of electron density is most likely a representation of U(VI) nanoparticles or surface precipitates. This is in line with the results from ATR FT-IR spectroscopy, where also predominantly surface precipitates or oligomeric U(VI) species were observed at a comparable initial U(VI) concentration (2×10^{-5} M). However, the phase of the RAXR modulations can only be satisfactory reproduced when introducing a second peak (species) to the model. This second peak is small, sharp, located in close proximity to the surface and supposedly represent adsorbed U(VI). Consequently, next to the predominant precipitation of U(VI) due to oversaturation at high pH at such 'high' initial U(VI) concentrations, also a small portion of U(VI) is adsorbed to the surface. Due to the overall low surface coverage, the exact configuration of the small amount of adsorbed U(VI) cannot be resolved. Therefore, CTR/RAXR also does not allow to observe differences between the U(VI) adsorption in the presence and in the absence of calcium at very low U(VI) concentrations. Nonetheless, the measurement confirmed the retention mechanisms occurring when applying super-micromolar U(VI) concentrations. Furthermore, for the first time U(VI) was measured on a muscovite (001) surface with CTR/RAXR.

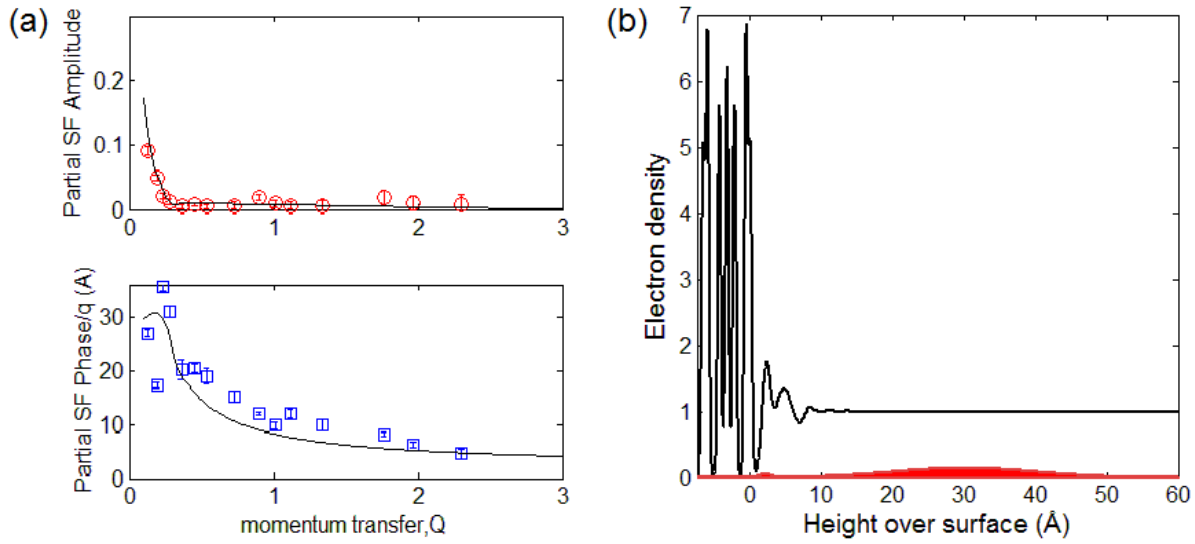

Figure 3-27: Based on the model-independent fitting of the RAXR data of the U(VI) sorption sample at pH 11 in 0.1 M NaCl + 0.02 M $CaCl_2$ the data points for amplitude and phase (a) were approximated with a model for the resonant part of electron density (normalized to the electron density of water) above the surface (b).

4. Influence of Ca(II) on U(VI) and Np(VI) sorption on clay minerals at (hyper)alkaline conditions

The groundbreaking outcome of the experiments on U(VI) sorption on Ca-bentonite at (hyper)alkaline conditions (chapter 3.2.2) was that the predominant retention mechanism between pH 10 and 12 under the given conditions was adsorption despite the anionic character of prevailing aqueous species. It was hypothesized that the attachment to the negatively charged mineral surface could be mediated by calcium, of which large amounts were present in the background electrolyte. Possible mechanisms involve the formation of aqueous ternary Ca-U-OH complexes, which do not feature a negative net charge, allowing for interaction with the mineral surface. The existence of such complexes was so far only hypothesized but has never been investigated. Another plausible mechanism is the adsorption of calcium to the mineral surface in the first place, creating local positively charged sites, where the actinyl hydroxides can attach. In order to prove this hypothesis, this chapter is dedicated to the careful evaluation of the effect of calcium on An(VI) sorption on clay minerals. It encompasses the study of calcium sorption on Ca-bentonite (and its effect on the surface charge of Ca-bentonite), the influence of calcium on batch sorption of U(VI) and Np(VI) on different clay minerals, and the spectroscopic identification of such calcium-induced U(VI) sorption complexes with site-selective TRLFS.

4.1. Experimental

The experimental conditions related to these specific experiments are compiled in chapter 3.1.

4.2. Results and discussion

4.2.1. Ca(II) sorption on Ca-bentonite at (hyper)alkaline conditions

The sorption of calcium on Ca-bentonite was investigated in batch sorption experiments as a function of S/L ratio and pH. The initial calcium concentration of 2×10^{-4} M, spiked with 1×10^{-12} M ^{45}Ca was chosen based on estimations for a monolayer saturation of the bentonite surface with calcium cations according to literature values for montmorillonite surface site density of 2×10^{-5} mol/g (Wieland et al., 1994). The amount of calcium removed from the solution was determined by LSC of ^{45}Ca.

The batch experiments as a function of S/L ratio prove that calcium strongly adsorbs to the Ca-bentonite surface, when sufficient sorption sites (i.e. high enough mineral mass) are provided (Figure 4-1a). Calcium sorption increases rapidly from 34% at 0.2 g/L to more than 90% at 2 g/L, reaching a plateau of approx. 95% sorption. A maximum surface capacity for calcium of 3.41×10^{-4} mol/g can be derived from the sorption at 0.2 g/L. Assuming that adsorbed Ca^{2+} occupies two surface sites, this corresponds to a surface site density of 6.82×10^{-4} mol/g, being considerably higher than the value given by Wieland et al. (1994), but

very close to the cation exchange site density of MX-80 bentonite of 6.96×10^{-4} mol/g, assumed by Grambow et al. (2006). Based on these results, a S/L ratio of 10 g/L (also used for the U(VI) sorption experiments with Ca-bentonite) was chosen for the pH-dependent sorption experiments, in order to provide enough sites for unrestricted calcium adsorption. Under these conditions sorption of calcium was very high in the whole investigated pH range 8-13 (Figure 4-1b). A weak dependency on pH can be observed, as sorption is increasing with increasing pH from 88% at pH 8 to a maximum of 97% at pH 11. This corresponds to a maximum log(K_d) value of 3.47 log(L/kg). The slight decrease to 86% sorption at pH 13 could be due to beginning dissolution of minerals, as described in chapter 3.2.1.3.

Strong sorption of Ca^{2+} or Sr^{2+} (which can be regarded as chemical analogue) has been observed previously already on bentonite (Cherian et al., 2018; He et al., 2016; Missana and García-Gutiérrez, 2007; Missana et al., 2008), muscovite (Fenter et al., 2007; Schlegel et al., 2006) and kaolinite (Chen et al., 2014). Predominant retention mechanism is cation exchange, which is largely independent of pH, but highly sensitive to ionic strength, according to the reaction

$$z_B A \equiv X + z_A B = z_A B \equiv X + z_B A \tag{4.1}$$

where B is a cation (i.e. Ca^{2+}) with charge z_B, which exists in the aqueous phase, and A is a cation (e.g. H^+ or Na^+), with charge z_A, at the clay surface (≡X) (Missana and García-Gutiérrez, 2007). A contribution of surface complexation to the retention of calcium was only significant at pH>8. Missana and García-Gutiérrez (2007) were only able to model an increase in calcium (M^{z+}) sorption from pH 8 to 10 by the introduction of a surface complex on the amphoteric edge sites (SOH) of the clay mineral according to the following reaction

$$SOH + M^{z+} \leftrightarrow SOM^{z-1} + H^+ \tag{4.2}$$

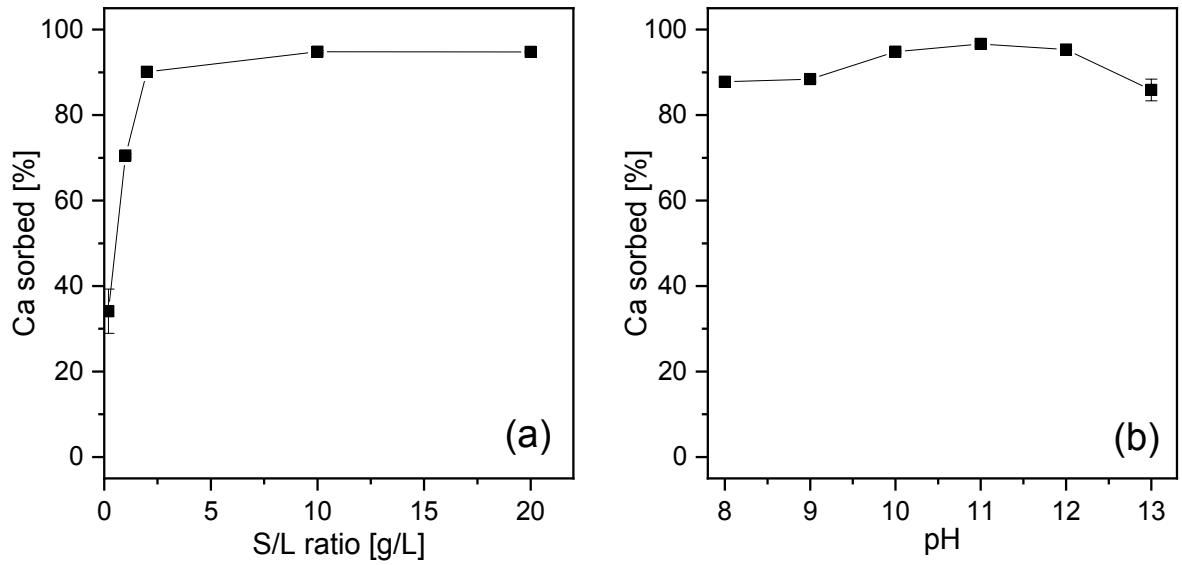

Figure 4-1: Sorption of calcium (2×10^{-4} M spiked with 1×10^{-12} M ^{45}Ca) on Ca-bentonite in the absence of CO_2 as a function of S/L ratio (pH 10) (a) and as a function of pH (S/L ratio = 10 g/L) (b).

At high pH, surface complexation is promoted due to the successive deprotonation of the clay mineral surface ($SOH \leftrightarrow SO^- + H^+$). Accordingly, Schlegel et al. (2006) and Fenter et al. (2007) also observed a contribution of surface complexation to calcium and strontium adsorption on the mica 001 surface, expressed in the fact that the hydration shell was partly removed. Based on these findings, surface complexation is also assumed to contribute significantly to the strong calcium retention at pH 8-13 observed in the present study.

Further evidence for the adsorption of calcium on the Ca-bentonite surface arises from the measurement of zeta potential with added $CaCl_2$. Compared to the measurement in 0.1 M NaCl (chapter 3.2.1.1), the addition of 0.02 M calcium results in a much less negative surface charge over the entire investigated pH range 7-13 (Figure 4-2). Even though the presence of calcium does not result in a complete reversal of surface charge, negative surface charge is partly compensated, leading to potentials of approx. -15 mV at pH 7-11 and between -15 and +2 mV at pH 11-13. As the measurement of zeta potential is a bulk technique, measuring the average charge of all existing surface sites, partial compensation of negative surface charge implies the existence of locally positively charged sites where calcium is adsorbed. Beside the effect of calcium, also the influence of strontium on the surface charge was tested. Assuming that the charge of the cation is the main driving factor, the adsorption of Sr^{2+} should be similar to the one of Ca^{2+}. In fact, in 0.1 M NaCl + 0.02 M $SrCl_2$, the surface charge at pH 7-13 is almost identical to that in 0.1 M NaCl + 0.02 M $CaCl_2$ (Figure 4-2). That means, both divalent cations Ca^{2+} and Sr^{2+} obviously have the same charge compensating effect.

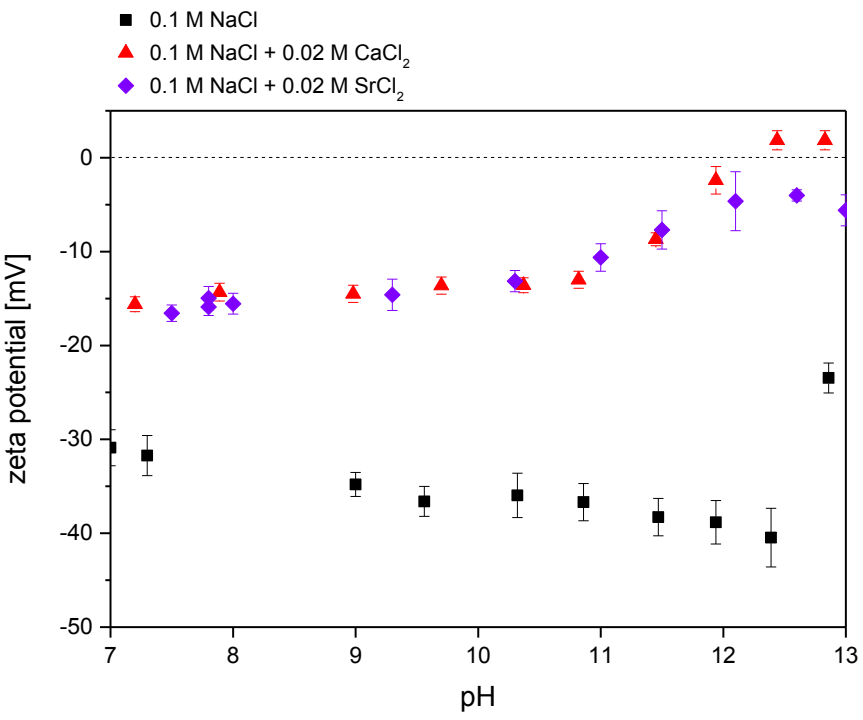

Figure 4-2: Surface potential of Ca-bentonite (0.1 g/L) as a function of pH and background electrolyte.

Similar impact on surface charge due to adsorption of calcium at alkaline conditions has been previously reported for different types of bentonite (Cherian et al., 2018; Ho and Handy, 1963), kaolinite (Atesok et al., 1988; Farooq et al., 2011) and cementitious material (Pointeau et al., 2006; Viallis-Terrisse et al., 2001), where even an reversal of charge was observed.

Both zeta potential measurements and Ca batch sorption experiments have shown that calcium adsorbs strongly to the Ca-bentonite surface and consequently, potentially generates alternative sorption sites for anionic actinyl hydroxides. The resulting calcium-induced changes in U(VI) and Np(VI) sorption behavior are investigated in the following chapters.

4.2.2. Effect of Ca(II) on U(VI) sorption on montmorillonite, kaolinite and muscovite

As all previous U(VI) sorption experiments (on Ca-bentonite in diluted Gipshut solution) were conducted in the presence of calcium, the aim was to perform similar experiments, but with the exclusion of calcium. For that purpose, suspensions were prepared in NaCl background solutions and the minerals Na-montmorillonite, synthetic kaolinite and muscovite were chosen, which supposedly do not contain any calcium that could be leached during the experiment. Assuming that calcium is responsible for enabling sorption of anionic uranyl hydroxide complexes, U(VI) retention is expected to be radically decreased in these experiments between pH 10 and 12 compared to the results presented in chapter 3.2.2.1.

4.2.2.1. Batch sorption experiments

U(VI) sorption on Na-montmorillonite

Figure 4-3 shows the batch sorption of U(VI) on Na-montmorillonite between pH 8 and 13 in the absence of CO_2 (a) and at low carbonate concentration (1 mM) (b), both in 0.1 and 2.6 M NaCl. The pH-dependent sorption on Ca-bentonite in diluted Gipshut solution is included in the diagrams for comparison. In the absence of CO_2 the U(VI) sorption on Na-montmorillonite is extremely high up to pH 12, followed by a sharp decrease (Figure 4-3a). This behavior is very similar to the U(VI) sorption on Ca-bentonite. The slightly lower retention at pH 8-9 in the experiments with Ca-bentonite could be a result of small fractions of (calcium) uranyl carbonate complexes which might be forming due to release of minimal amounts of carbonate from the Ca-bentonite. Most significant difference between the sorption curves is the earlier decrease in retention with increasing pH in the series with 0.1 M NaCl. While sorption at pH 12 in 2.6 M NaCl is still at 95%, it has dropped to 52% in 0.1 M NaCl. This behavior can be explained with the ionic strength dependency of U(VI) hydrolysis. With increasing ionic strength, the formation of highly charged species is hampered, meaning that at I = 2.6 M the 1:4 hydrolysis species $UO_2(OH)_4^{2-}$, to which the decrease in U(VI) retention is attributed, gains predominance over the 1:3 complex only at higher pH, compared to the low ionic strength case. The U(VI) retention at pH 10-12 remains virtually unchanged

compared to the experiments with Ca-bentonite in diluted Gipshut solution, so that it has to be stated, that the intended reduction of calcium concentration (in solution as well as in the mineral) caused no effect. However, ICP-MS measurements revealed the presence of 3.6×10^{-5} M calcium at pH 11 in the supernatant after the experiments. This must arise from calcium impurities in the structure of Na-montmorillonite due to insufficient Ca-removal in the purification process. Chemical analysis of the purified clay still showed a CaO fraction of 1.00±0.24 weight-% (Fritsch, 2018). Apparently, such low calcium concentrations are sufficient to sustain a complete U(VI) sorption between pH 10 and 12.

Similarly, also at low carbonate concentration no significant deviations from the U(VI) sorption on Ca-bentonite in diluted Gipshut solution could be observed at pH>10 at reduced amount of dissolved calcium. However, at pH 8-9.5, clear differences appear (Figure 4-3b). Sorption on Na-montmorillonite in NaCl solutions is much higher in this pH range, ranging between 59 and 68% at pH 9, compared to 27% on Ca-bentonite in diluted Gipshut solution. The reason for this increased U(VI) retention is most probably that the formation of ternary calcium uranyl carbonate complexes is strongly suppressed at very low calcium concentrations. Such ternary calcium uranyl carbonate complexes have even a weaker tendency to adsorb to mineral surfaces compared to $UO_2(CO_3)_3^{4-}$ (Meleshyn et al., 2009; Richter et al., 2016).

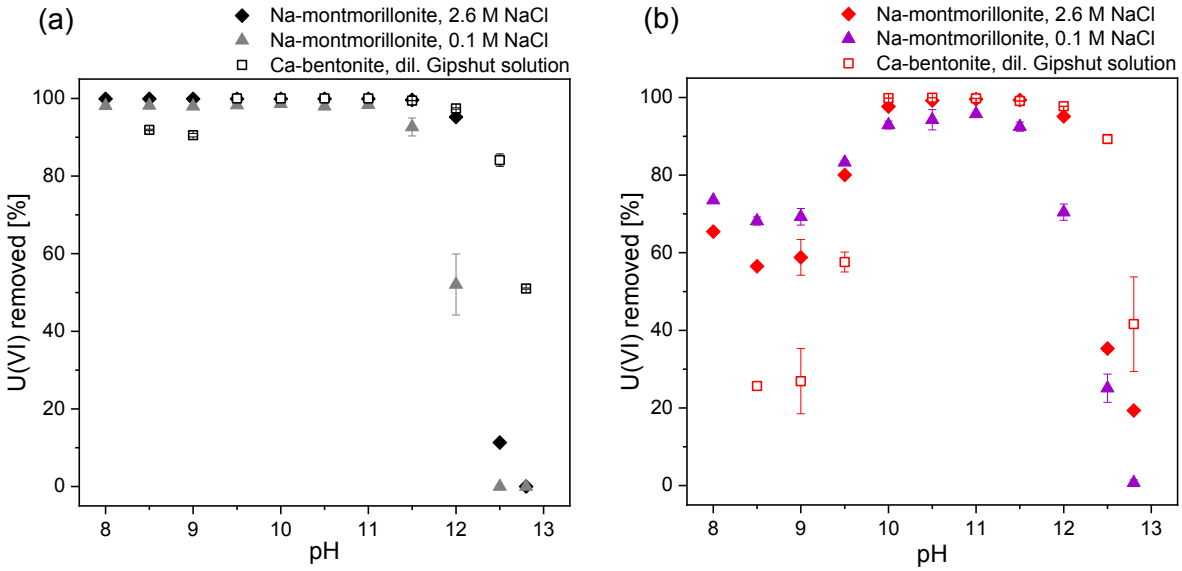

Figure 4-3: Percentage of U(VI) sorbed on Na-montmorillonite (10 g/L) in 2.6 M and 0.1 M NaCl as function of pH in the absence of CO_2 ([U(VI)] = 5×10^{-7} M) (a) and at low carbonate concentration (1 mM) ([U(VI)] = 1×10^{-6} M) (b). The U(VI) sorption on Ca-bentonite is shown for comparison (see chapter 3.2.2.1, paragraph "pH dependency of sorption").

U(VI) sorption on kaolinite

The U(VI) retention was tested on selected samples of synthetic kaolinite, of which only a very limited amount of sample material was available. Experiments were performed at pH 10, 11, 12 and 12.7 both in 0.1 M NaCl and 0.1 M NaCl + 0.02 M $CaCl_2$ (Figure 4-4a). In contrast to the experiments with Na-montmorillonite, the sorption of U(VI) on kaolinite is decreasing

dramatically at pH≥10 in the absence of calcium, compared to the experiments on Ca-bentonite in diluted Gipshut solution. At pH 12 sorption reaches 0%, supporting the hypothesis that high U(VI) retention at pH 10-12 cannot be sustained in the absence of calcium. Measured calcium concentrations in the supernatant after the sorption experiment were as low as 4×10^{-6} M. This seems to be sufficiently low to prevent U(VI) sorption to the mineral surface at hyperalkaline conditions due to Ca-mediation. Technically, according to SEM-EDX the synthetic kaolinite did not contain any calcium at all (Huittinen et al., 2010). However, trace amounts are beyond the sensitivity of the method. Alternatively, the origin of calcium in the supernatant (close to ICP-MS detection limit) could be due to contamination of laboratory equipment such as the pH electrode, or impurity of the NaCl electrolyte.

Experiments with added $CaCl_2$ serve to check if the decreased U(VI) retention is really associated to the lower calcium concentration or rather to the different mineral structure of kaolinite compared to montmorillonite. In 0.1 M NaCl + 0.02 M $CaCl_2$, U(VI) sorption on kaolinite is very high up to pH 12.7 (Figure 4-4a). No drop in retention with increasing pH can be observed. Therefore, it can be unequivocally concluded that the presence of calcium significantly enhances U(VI) retention between pH 10 and 13 by mediating between anionic aqueous uranyl hydroxide complexes and the negatively charged mineral surface.

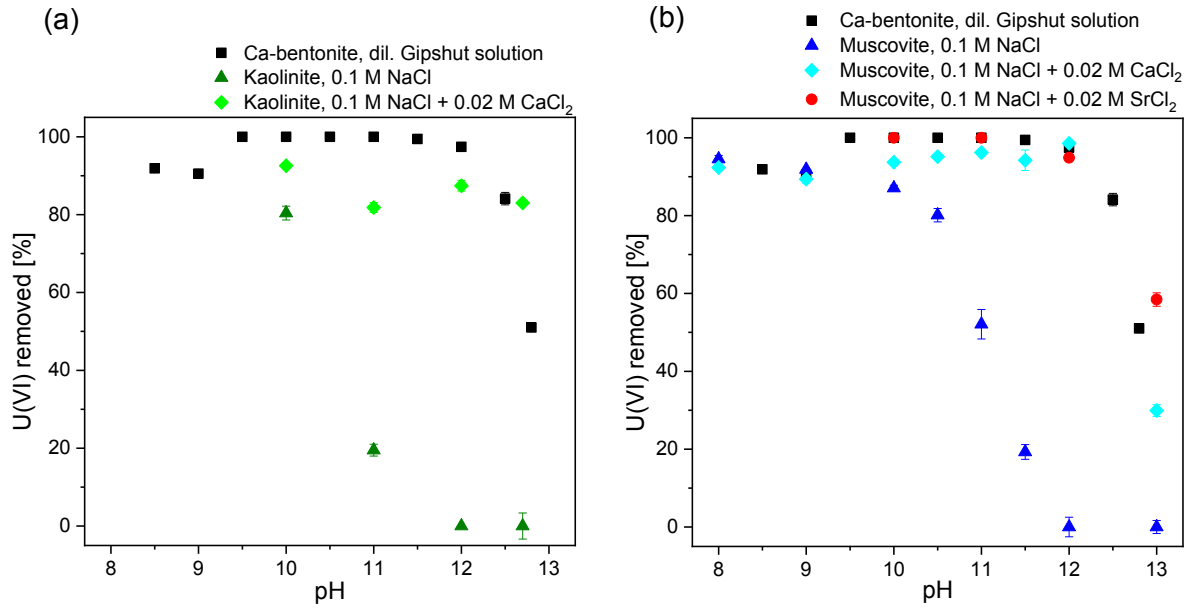

Figure 4-4: Percentage of U(VI) ([U(VI)] = 5×10^{-7} M) sorbed on synthetic kaolinite (0.5 g/L) (a) and muscovite (3 g/L) (b) in 0.1 M NaCl, 0.1 M NaCl + 0.02 M $CaCl_2$ and 0.1 M NaCl + 0.02 M $SrCl_2$ as function of pH in the absence of CO_2. The U(VI) sorption on Ca-bentonite is shown for comparison (see chapter 3.2.2.1, paragraph "pH dependency of sorption").

U(VI) sorption on muscovite

As a clay mineral analogue, also muscovite was studied regarding its retention potential towards U(VI) at pH 8-13 in 0.1 M NaCl and in 0.1 M NaCl + 0.02 M $CaCl_2$. Figure 4-4b shows that the sorption behavior is indeed comparable to the one on kaolinite. In 0.1 M NaCl U(VI) sorption decreases first slowly at pH>8 and then rapidly at pH≥10, until reaching 0% at

pH 12. Measured calcium concentrations in the solution were approx. 6.3×10^{-6} M. Although being slightly higher than in the experiments with kaolinite, they are still low enough to not allow substantial U(VI) mediation to the mineral surface.

The experiments with addition of $CaCl_2$ exhibit an extremely high U(VI) sorption up to pH 12 and follow essentially the same trend as sorption experiments on Ca-bentonite and Na-montmorillonite (Figure 4-4b). Again, as for kaolinite, this suggests that the low retention at pH≥10 in 0.1 M NaCl is not a consequence of the different mineral structure but merely of the lack of calcium availability.

As zeta potential measurements (chapter 4.2.1) have shown that strontium adsorbs to Ca-bentonite exactly as calcium, a complementary pH-dependent U(VI) sorption experiment was conducted in 0.1 M NaCl + 0.02 M $SrCl_2$, in order to investigate if strontium can have the same sorption mediating effect on U(VI). Indeed in the presence of strontium an almost identical U(VI) sorption behavior was observed, with very high retention up to pH 12 (Figure 4-4b). Consequently, the effect of enabling U(VI) adsorption is not attributed to exclusive properties of calcium but to the charge of divalent cations in general.

Effect of calcium concentration on U(VI) sorption & discussion of underlying mechanisms

The batch sorption experiments with Ca-bentonite, Na-montmorillonite, synthetic kaolinite, and muscovite in different background electrolytes demonstrate that certain amounts of dissolved calcium are sufficient to enable U(VI) sorption at pH 10-12, while others are not. Figure 4-5 summarizes measured calcium concentrations in the supernatant after the sorption experiment and respective percentage of U(VI) sorption of the different previously described batch sorption experiments at pH 11. More reasonable measures for the role of calcium would be the calcium concentration in solution prior to sorption, or even better, the amount of calcium that adsorbed to the surface, displaying possible sorption sites. However, both cannot be determined independently as leached calcium readily adsorbs to the mineral surface. As demonstrated by Figure 4-5 the concentration of calcium in the supernatant after the experiment is a good enough measure for its availability during the experiment and the connected potential to enhance U(VI) sorption. It is evident that fairly low calcium concentrations are sufficient to obtain very strong U(VI) sorption. While retention is only at 19% in the presence of 4×10^{-6} M calcium, it is already quantitative at 3.6×10^{-5} M calcium. The minimum calcium concentration that is required to achieve complete U(VI) retention under the given conditions lies somewhere between 6.3×10^{-6} M (on muscovite in 0.1 M NaCl) and 3.6×10^{-5} M (on Na-montmorillonite in 0.1 M NaCl). At higher calcium concentrations (up to 0.022 M) U(VI) sorption remains at a constantly high level close to 100%. It has to be mentioned that the experiments summarized in Figure 4-5 are not perfectly comparable because the various minerals have different specific surface areas and also applied S/L ratios were different. Nevertheless, the correlation between sorption percentage and calcium

detected in the supernatant is striking, implying that the calcium concentration can be assumed to be the dominating factor.

Bridging of a metal to a mineral surface is known from so called type B ternary surface complexes (Bradl, 2005; Hubbard, 2002). Such ternary type B surface complexes have the configuration surface ≡ ligand − metal and form by coordination of a metal to a sorbed ligand. In the present study, the mechanism is similar but the configuration is different. In contrast to type B surface complexes, the metal (U(VI)) is not bridged via the ligand (OH) but via an additional metal cation (Ca^{2+}). This could be described as quaternary surface complex (surface ≡ Ca^{2+} − $UO_2(OH)_3^-$). Due to their complexity, quaternary systems have not been studied thoroughly so far and very few studies are published dealing with similar systems. Commonly accepted textbook knowledge about surface complexation is restricted to simple coordination of the metal to the surface and to ternary surface complexation. Moreover, conventionally the adsorption of ions to surfaces of opposite charge is studied. Sorption of anionic actinide complexes to a negatively charged surface, as observed in the present work, displays a rarely considered scenario.

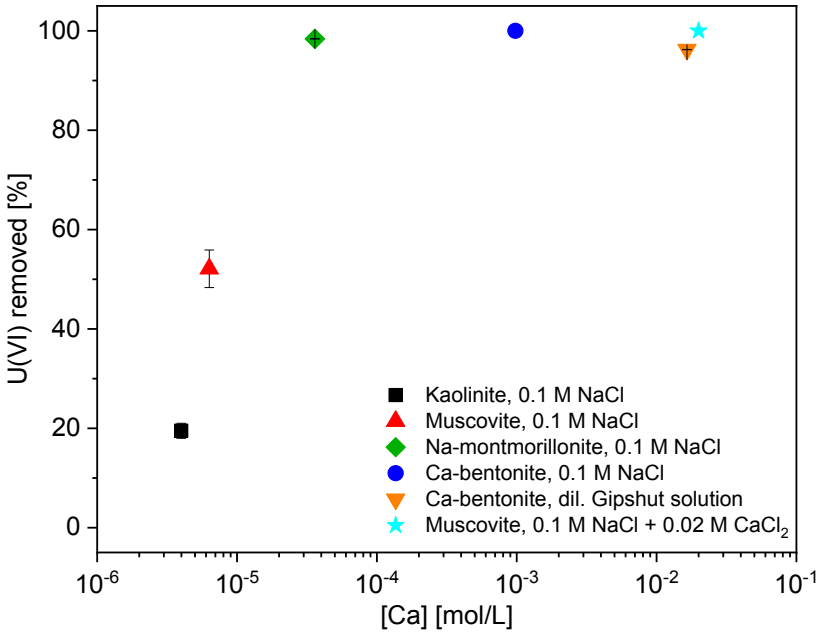

Figure 4-5: Percentage of U(VI) ([U(VI)] = 5×10^{-7} M) sorbed on Ca-bentonite (10 g/L), Na-montmorillonite (10 g/L), muscovite (3 g/L) and kaolinite (0.5 g/L) at pH 11 as a function of calcium concentration measured in the supernatant after the sorption experiments in the absence of CO_2.

A small number of studies already pointed out the potential of calcium to enhance anion retention. Allen et al. (2019) and Griffin et al. (2016) described a calcium bridging between the anionic surfactant bis(2-ethylhexyl) sulfosuccinate and mica surfaces. The bridging effect was achieved with low concentrations of divalent cations and was absent in monovalent electrolyte solutions. Arnarson and Keil (2000) found an increased sorption of natural organic matter to montmorillonite due to calcium bridging. For Np(V) and Np(VI) Tits et al. (2014)

obtained higher retention on TiO_2 in the presence of calcium at pH 13.3. The K_d value of Np(VI) increased by two orders of magnitude upon introduction of 10^{-5} M calcium. As possible explanations, the authors suggested neutralization of negative surface charge or formation of very strong surface stabilized Ca-neptunate complexes, and stated that additional experiments, especially spectroscopic measurements, are necessary to draw conclusions about the retention mechanisms.

No peer-reviewed publication exists about a potential bridging effect of calcium on U(VI) adsorption. However, in the batch sorption data of the PhD theses of both Andreas Schnurr (Schnurr, 2015) and Natalia Mayordomo (Mayordomo, 2017) an increased U(VI) sorption at very alkaline conditions in the presence of calcium is visible. Schnurr (2015) noticed a difference between U(VI) sorption on Illite du Puy in NaCl and $CaCl_2$ at pH 10-12. Mayordomo (2017) was able to model high U(VI) sorption on smectite at pH 9.5-10 only by introduction of a calcium mediated surface complex $S^WO\text{-}Ca\text{-}UO_2(OH)_3$. The batch sorption results of the present study also suggest such calcium-mediated surface complexes. However, no spectroscopic evidence for the existence of such complexes exists so far. Therefore, site-selective TRLFS measurements on sorption samples were performed.

4.2.2.2. Site-selective TRLFS of Ca-induced U(VI) surface complexes

Solids of muscovite and kaolinite with sorbed U(VI) were investigated at different pH and in different electrolyte solutions in order to be able to detect different sorption species, which either form in the absence or exclusively in the presence of calcium. For muscovite at pH 11 and kaolinite at pH 10, both in 0.1 M NaCl, 'regular' surface complexes are expected, as U(VI) batch sorption was still sufficiently high in the absence of calcium (chapter 4.2.2.1). For muscovite at pH 11 in 0.1 M NaCl + 0.02 M $CaCl_2$ a combination of 'regular' and calcium-induced sorption complexes is supposed. Finally, both for muscovite and kaolinite at pH 12 in 0.1 M NaCl + 0.02 M $CaCl_2$ it is assumed that only calcium-induced sorption species can be observed, as U(VI) was not sorbing under these conditions in the absence of calcium (chapter 4.2.2.1).

Irrespective of the chosen excitation wavelength, in none of the five samples (3 on muscovite and 2 on kaolinite) a characteristic luminescence line-narrowing similar to the one on Ca-bentonite could be observed. All spectra feature comparatively broad emission bands, suggesting homo-resonance energy transfer from excited uranyl ions to neighboring uranyl ions with slightly different bonding environments (Figure 4-6). As described previously, this phenomenon is observed for precipitates, where the uranium atoms are in close distance to each other. However, a broad maximum shifted to high wavelengths, as it is characteristic for uranates, can only be observed in the kaolinite sample at pH 12 in the presence of calcium. In all other samples no such feature can be found in the spectra at high excitation wavelength (Figure 4-6a,b,c,). Hence the broadening of the spectra cannot be attributed to the formation

of U(VI) precipitates, except for the kaolinite sample at pH 12 in the presence of calcium. The same observation (inhomogeneous line broadening in the absence of precipitate-like spectral features) has been made by Tits et al. (2015) for U(VI) sorbed on TiO_2 under comparable conditions. The authors stated that they could not find a reason for the absence of luminescence line-narrowing. Combining the findings of the present study and of the one by Tits et al. (2015) (the only two existing studies applying site-selective TRLFS to U(VI)), line-narrowing was observed for Ca-bentonite (this study) and C-S-H but was absent on muscovite, kaolinite (both this study) and TiO_2. Hence, it has to be questioned whether the absence of line-narrowing is really a peculiar exception or rather the rule. Apparently, for the observation of line-narrowing certain preconditions have to be met, which are provided by Ca-bentonite (or rather montmorillonite) and C-S-H phases. These preconditions possibly derive from their mineral structure (and associated uranium immobilization processes) which is distinct from the one in muscovite, kaolinite and TiO_2.

Both montmorillonite and C-S-H have a sheet like structure, with two tetrahedral silicon-oxygen layers, sandwiching aluminum octahedra or calcium polyhedra, respectively. However, this is also the case for muscovite for which no line-narrowing could be observed. A major difference between these minerals is how the above described units are stacked and held together. Montmorillonite and C-S-H are swellable, being able to accommodate variable amounts of water next to counterions in the interlayers between the negatively charged sheets. In contrast to that, in muscovite the layers are bonded via potassium, resulting in a much smaller interlayer distance and absence of swelling properties. As a consequence, in montmorillonite and C-S-H radionuclides could possibly enter the interlayers and interact with the basal planes of the mineral, while the interlayer space is inaccessible in muscovite. A large part of its specific surface area is virtually blocked by the potassium. Also kaolinite does not possess expandable interlayer space. The weakly charged layers are connected via hydrogen bonds, inhibiting interactions of radionuclides with most of the basal planes. Consequently, the possibility to observe luminescence line-narrowing could be related to the ability of U(VI) to adsorb to the basal planes of the minerals and not only to the edge sites. Especially calcium-mediated species which are bound electrostatically could be associated to these sites. In case that the basal planes are not accessible for U(VI), the actual reactive surface area is much lower than the measured BET surface area. All uranium ions then accumulate at the edge sites, which could cause the distance between the uranium atoms to approach the critical Förster distance, at which homo-resonance energy transfer occurs. Knowing the specific surface area of the minerals and the U(VI) loading of 1.67×10^{-3} mol/kg, it can be calculated that approx. 1.3, 10.1 and 4.5 uranium atoms are adsorbed on a 10 nm^2 surface area of Ca-bentonite, muscovite and kaolinite, respectively. Assuming homogeneous distribution and a model where a square area is attributed to each atom, the distance between the single adsorbed U(VI) atoms would be approx. 2.76 nm on Ca-bentonite, 0.99 nm on muscovite and 1.49 nm on kaolinite. Compared to Ca-bentonite, where a line-narrowing could

be observed, the distance between the U atoms on muscovite and kaolinite is much closer to the critical Förster distance of 0.7 nm calculated by Tits et al. (2015). When additionally large parts of the surface of muscovite and kaolinite are not reactive, U(VI) is not distributed homogeneously, but accumulates on a smaller area. As a consequence, interatomic distances are further reduced, so that homo-resonance energy transfer can occur. Heterogeneous adsorption of U(VI) in very close distance to each other is also a good explanation for the line broadening on TiO_2 observed by Tits et al. (2015). With a U(VI) loading of 1×10^{-3} mol/kg and a specific surface area of 5 m^2/g the theoretical distance of the U atoms is 0.91 nm and therefore also close to the critical Förster distance.

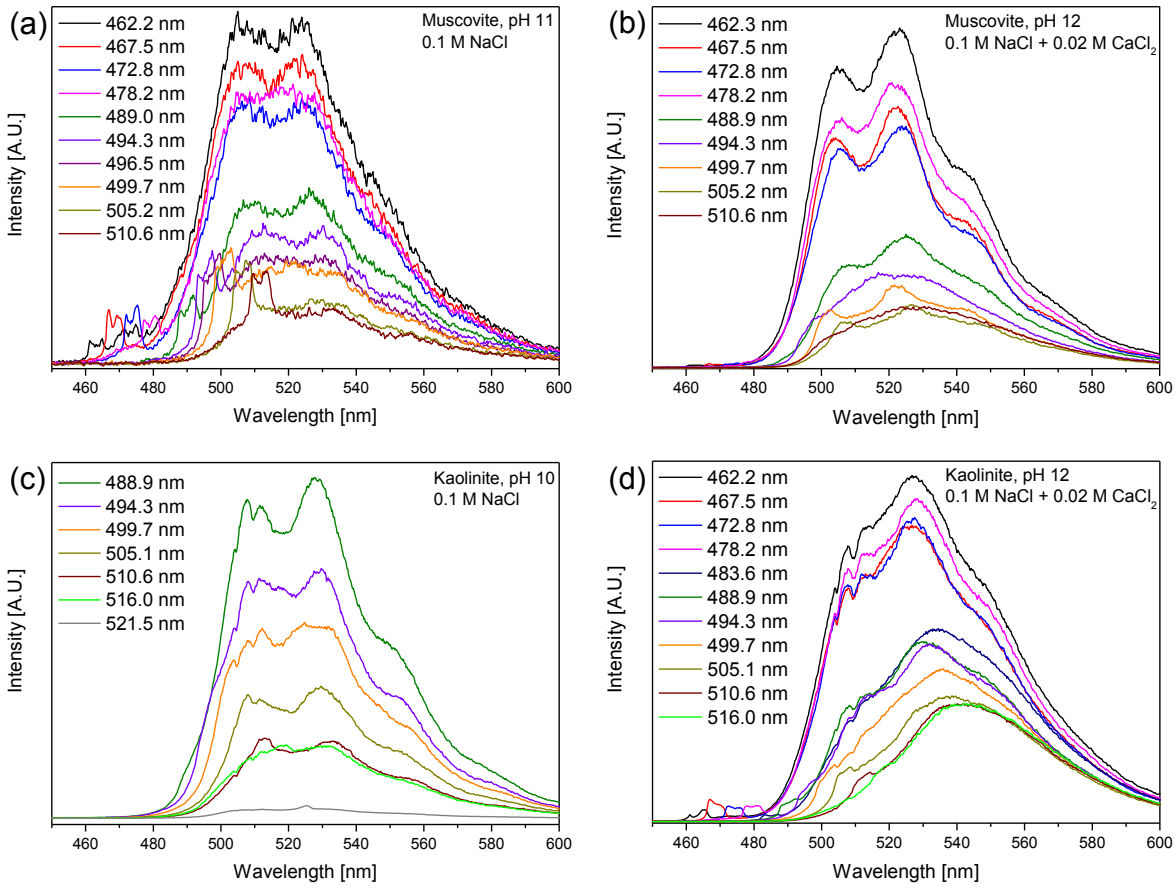

Figure 4-6: Emission spectra of U(VI) ([U(VI)] = 5×10^{-7} M) sorbed on muscovite at pH 11 in 0.1 M NaCl (a), muscovite at pH 12 in 0.1 M NaCl + 0.02 M $CaCl_2$ (b), kaolinite at pH 10 in 0.1 M NaCl (c) and kaolinite at pH 12 in 0.1 M NaCl + 0.02 M $CaCl_2$ (d) at different excitation wavelengths in the absence of CO_2.

The attribution of a reduced reactive surface area and resulting luminescence line-narrowing to the accessibility of interlayer space and availability of sorption sites on the basal plane is only a working hypothesis so far, which has to be confirmed by repeating comparable measurements on further solids.

Despite the absence of luminescence line-narrowing the static emission spectra still contain sufficient spectral information to identify different U(VI) species on both muscovite and kaolinite. Especially the comparison with the U(VI) sorption on Ca-bentonite (in diluted

Gipshut solution, pH 11), where emission spectra at λ_{ex} = 499.7 nm revealed the presence of one inner-sphere and one outer-sphere sorption species (chapter 3.2.2.4), allows to draw some conclusions regarding the influence of pH and calcium concentration on the formation of these two different species. Figure 4-7 shows the normalized emission spectra at λ_{ex} = 499.7 nm of all samples, including U(VI) sorbed on Ca-bentonite and U(VI) precipitated on Ca-bentonite as references. Least information yields the spectrum of U(VI) sorbed on muscovite at pH 11 in the absence of calcium. Here one would expect the presence of one species, which does not involve calcium cations. However, no clear emission bands can be identified. Luminescence intensity is very weak, resulting in a low signal to noise ratio. The poor spectral quality can be explained by the fact that a much smaller amount of U(VI) is retained on the muscovite surface (approx. 50%) compared to the other samples. Direct comparison with the sample in the presence of calcium (otherwise identical experimental conditions) unequivocally reveals the impact of calcium on the static emission spectrum (dark blue spectrum in Figure 4-7). In the presence of calcium the spectrum is significantly intensified, mainly in the wavelength region around 521 nm. A transition band at this wavelength has been attributed to the first line of vibronic progression of TRLFS-species 1 (not to confuse with EXAFS-component 1) on Ca-bentonite. Additionally, in between the maxima attributed to TRLFS-species 1, slight shoulders appear which fit to the electronic and vibronic transition lines of TRLFS-species 2 on Ca-bentonite. This confirms the hypothesis that under these conditions both species are present – the 'regular' inner-sphere sorption complex and the calcium-mediated species. By contrast, the muscovite sample at pH 12 in the presence of calcium shows exclusively maxima which were attributed to TRLFS-species 1 on Ca-bentonite (light blue spectrum in Figure 4-7). The absence of shoulders between the emission bands of TRLFS-species 1 is in line with the hypothesis that under these conditions only the calcium-induced species is formed, as U(VI) sorption was at 0% in the absence of calcium. The overlap of the maxima with those from TRLFS-species 1 on Ca-bentonite proves that TRLFS-species 1 is a calcium-induced sorption complex. This was already hypothesized in chapter 3.2.2.4 but could not be proven, because no isolated samples in the absence and presence of calcium could be prepared with Ca-bentonite. The conclusion from the measurements on muscovite that TRLFS-species 1 is the calcium-induced species (and not TRLFS-species 2) is in accordance with the values obtained for the total symmetric stretch vibration of both sorption species (chapter 3.2.2.4). TRLFS-Species 1 has a greater spacing of the transition bands, indicating weaker interaction with the mineral surface. Retention is realized via calcium which is situated between the mineral surface and the bound anionic uranyl hydroxide. The resulting larger distance of U(VI) from the substrate in the presence of calcium is also reflected in the EXAFS analysis of EXAFS-component 2 (chapter 3.2.2.4), corresponding to TRLFS-species 1, lacking backscattering paths from the substrate.

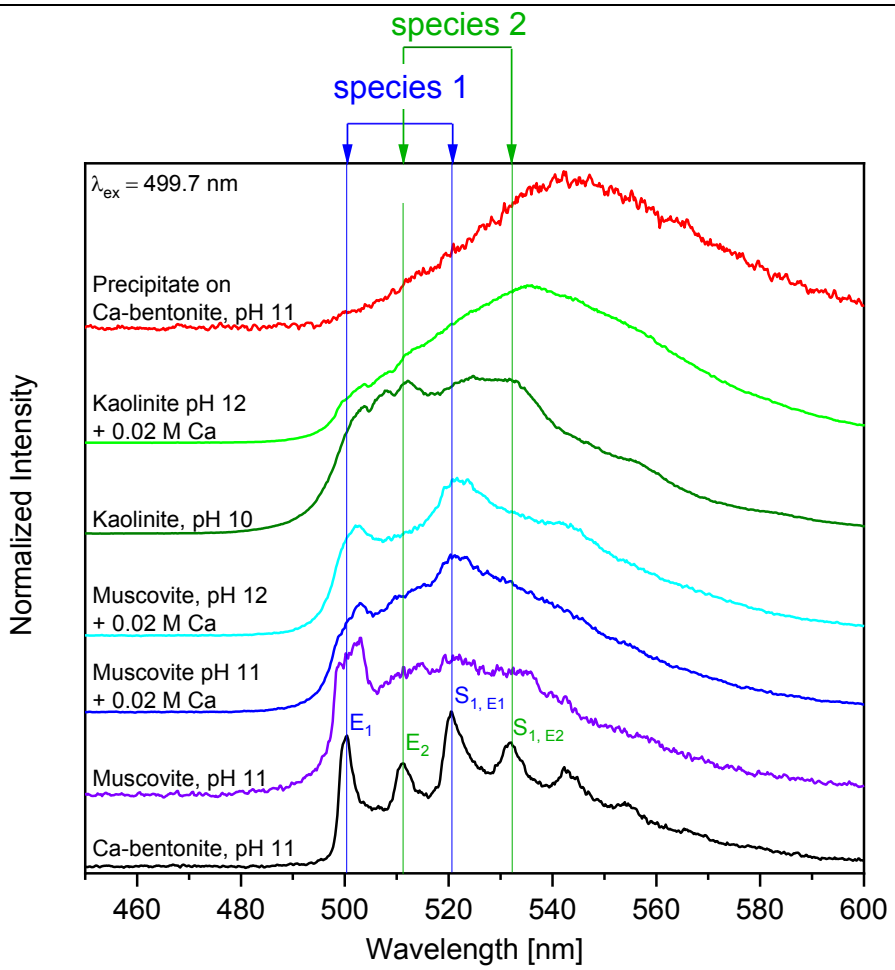

Figure 4-7: Comparison of single emission spectra at λ_{ex} = 499.7 nm of U(VI) ([U(VI)] = 5×10^{-7} M) sorbed on muscovite and kaolinite in the absence of CO_2 at different pH in 0.1 M NaCl or 0.1 M NaCl + 0.02 M $CaCl_2$. Spectra of U(VI) sorbed on Ca-bentonite and of a uranate-like precipitate on Ca-bentonite (both at pH 11) are included for comparison. Vertical lines in the graph attribute different emission lines to two independent species (presented in chapter 3.2.2.4).

The spectrum of U(VI) sorbed on kaolinite at pH 10 in the absence of calcium shows several small maxima of which the most prominent ones coincide with the electronic transition line and first line of vibronic progression of TRLFS-species 2 (dark green spectrum in Figure 4-7). In the light of the findings from the measurements on muscovite this makes sense, because TRLFS-species 2 is the one which is not calcium-induced. Conversely, at pH 12 in the presence of calcium, one would expect to observe the calcium-induced TRLFS-species 1 exclusively, as on muscovite. However, at these conditions the spectrum lacks spectral resolution. No single emission bands can be observed (light green spectrum in Figure 4-7). Additionally, the broad emission spectrum is shifted to higher wavelengths. Both characteristics, inhomogeneous broadening of the spectrum and the shift to higher wavelengths, indicate U(VI) precipitation as Ca-uranate (see chapter 3.2.2.4). The spectrum resembles the one of U(VI) precipitated on Ca-bentonite. However, the shift to higher wavelengths is not as pronounced as in the reference sample. This can be explained by the fact, that the U(VI) precipitate is not the only U(VI) component in the sample, but that the obtained spectrum is a result of superimposition of single component spectra of both adsorbed and precipitated U(VI). The simultaneous presence of adsorbed U(VI) becomes evident when

looking at emission spectra at different delay. As the Ca-uranate precipitate has a shorter luminescence lifetime than the adsorbed U(VI) species (Tits et al., 2011; Tits et al., 2015), with increasing delay time the portion of the spectrum at lower wavelength gains relative importance compared to the region characteristic for U(VI) precipitation (Figure 4-8). Even though adsorbed U(VI) is present in the sample, the dominance of U(VI) precipitation makes a spectral evaluation of the adsorbed U(VI) (and therefore also a comparison with the calcium-induced U(VI) species on muscovite) impossible.

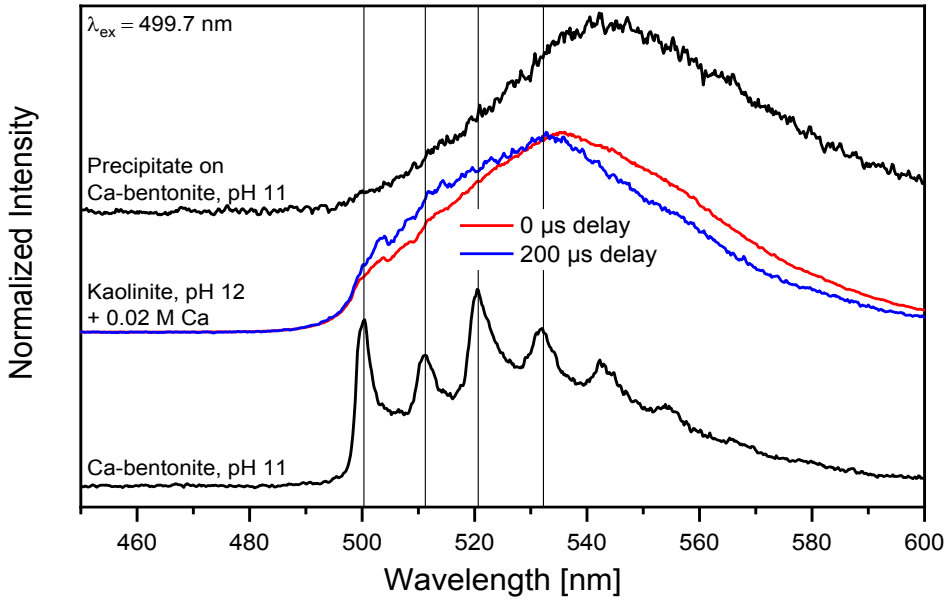

Figure 4-8: Luminescence emission spectra at λ_{ex}=499.7 nm of U(VI) ([U(VI)] = 5×10^{-7} M) sorbed on kaolinite in the absence of CO_2 at pH 12 in 0.1 M NaCl + 0.02 M $CaCl_2$ at 0 and 200 µs delay time. Spectra of U(VI) sorbed on Ca-bentonite and of a uranate-like precipitate on Ca-bentonite (both at pH 11) are included for comparison. Vertical lines in the graph attribute different emission lines to two independent species (presented in chapter 3.2.2.4).

The TRLFS results obtained in the presence of 0.02 M calcium at pH 12 show that under equal experimental conditions U(VI) predominantly precipitates on kaolinite, while it does not on muscovite. It can be assumed that U(VI) would also precipitate as Ca-uranate on muscovite and Ca-bentonite with time, if it was not removed from the solution by faster adsorption in the first place. Therefore, the precipitation of U(VI) on kaolinite can be related to its inability to adsorb U(VI) to the mineral surface, which can have different reasons. First of all a general lack of sorption sites could arise from disaggregation and dissolution of kaolinite with increasing pH. As described above, the accessible surface area for U(VI) on the intact kaolinite is already very small, leading to high adsorption density of U(VI). If the surface area is further reduced by mineral dissolution, not all of the U(VI) can be adsorbed anymore. Based on the elemental composition of the synthetic kaolinite given in Huittinen et al. (2010) as well as Al and Si concentrations measured in the supernatant after sorption, 2.9% of Al and 11.9% of Si were released from the mineral under these conditions. For muscovite mineral dissolution was weaker, with 2.8% of Al and 3.1% Si leached at pH 12, derived from leaching tests and digestion of the mineral. Hence, it is well possible, that the remaining kaolinite is not capable to accommodate all U(VI) from solution at its surface, forcing the

excess U(VI) to precipitate. Alternatively, it is possible that the reduced ability for U(VI) to adsorb is not a result of a general degradation of the mineral but due to the absence of a very specific type of sorption sites in kaolinite, which is necessary for the formation of calcium-mediated sorption complexes. One hypothesis is that this kind of sorption complex requires strongly negatively charged basal planes as they are present in montmorillonite and muscovite, but not in kaolinite. Under chemical conditions where calcium-bridging is the only possible mechanism for U(VI) adsorption, U(VI) would precipitate in the samples with kaolinite in case that this mechanism is hindered due to the different kaolinite structure. The hypothesis that the U(VI) retention mechanism in kaolinite differs from the ones in Ca-bentonite and muscovite is supported by differences in luminescence lifetime.

For all samples U(VI) luminescence shows a biexponential decay (Figure 4-9 and Table 4-1). This indicates the presence of two independent U(VI) species on muscovite and kaolinite irrespective of pH and the presence or absence of calcium. As described in chapter 3.2.2.4 for U(VI) sorption on Ca-bentonite, the two adsorbed TRLFS-species 1 and 2 identified from the emission bands, cannot be distinguished based on their lifetimes. Both are represented by the longer lifetime τ_2. The short lifetime τ_1 is attributed to a Ca-uranate precipitate. All samples comprise both adsorbed and precipitated U(VI) but distinguish themselves dramatically by the proportion which these mechanisms add to the luminescence signal. The shape of the luminescence decay curve provides qualitative information about these relative contributions. Figure 4-9a shows that the three samples with U(VI) sorbed on muscovite exhibit very similar luminescence decay, suggesting that all contain similarly small amounts of precipitated U(VI). In contrast to that, for U(VI) sorbed on kaolinite the luminescence decay at pH 10 in the absence of calcium is fundamentally different to that at pH 12 in the presence of calcium (Figure 4-9b). At pH 10 in the absence of calcium, the adsorbed U(VI) has a much longer lifetime of $\tau_2 = 394 \pm 15\ \mu s$, compared to 109-167 μs in the case of muscovite (Table 4-1). Therefore, a different process for U(VI) sorption has to be assumed. These strong differences in luminescence lifetime could be explained by sorption on different sites, i.e. on aluminol (Al-OH) or silanol (Si-OH) edge sites. Chisholm-Brause et al. (2004) and Kowal-Fouchard et al. (2004) observed considerably longer luminescence lifetimes for U(VI) inner-sphere complexes on silanol compared to aluminol functionalities at circumneutral pH. Chisholm-Brause et al. (2004) obtained lifetimes of 120 and 302 μs for inner-sphere sorption of uranyl hydroxides on gibbsite and silica, respectively. Kowal-Fouchard et al. (2004) measured lifetimes of 120 and even 400 μs for sorption of such complexes on corundum and silica. Direct comparison of the absolute values with the results of the present study is difficult, since the mentioned lifetimes in literature were not obtained at cryogenic conditions. Nevertheless, already the qualitative information about the strong difference in luminescence lifetime between U(VI) sorption on aluminol and silanol sites justifies the assumption, that U(VI) forms inner-sphere sorption complexes on silanol sites in the kaolinite sample at pH 10, while U(VI) predominantly adsorbs on aluminol sites in the montmorillonite and muscovite

samples. However, it has to be noted that no sample at pH 10 exists for direct comparison in the montmorillonite or muscovite system due to lack of time. Alternatively the long-lived species on kaolinite could represent ternary uranyl silicate surface complexes, promoted by the stronger dissolution of kaolinite compared to the other minerals. Such complexes with silicate have been identified for Cm by Huittinen et al. (2012) and Schnurr et al. (2015). Additional experiments with all three minerals at various pH could offer more detailed insight. At pH 12 on kaolinite in the presence of calcium the course of the decay curve is shifted towards the one of U(VI) precipitated on Ca-bentonite, indicating greater contribution of U(VI) precipitates. This is in line with the unresolved and red-shifted luminescence spectrum in Figure 4-7.

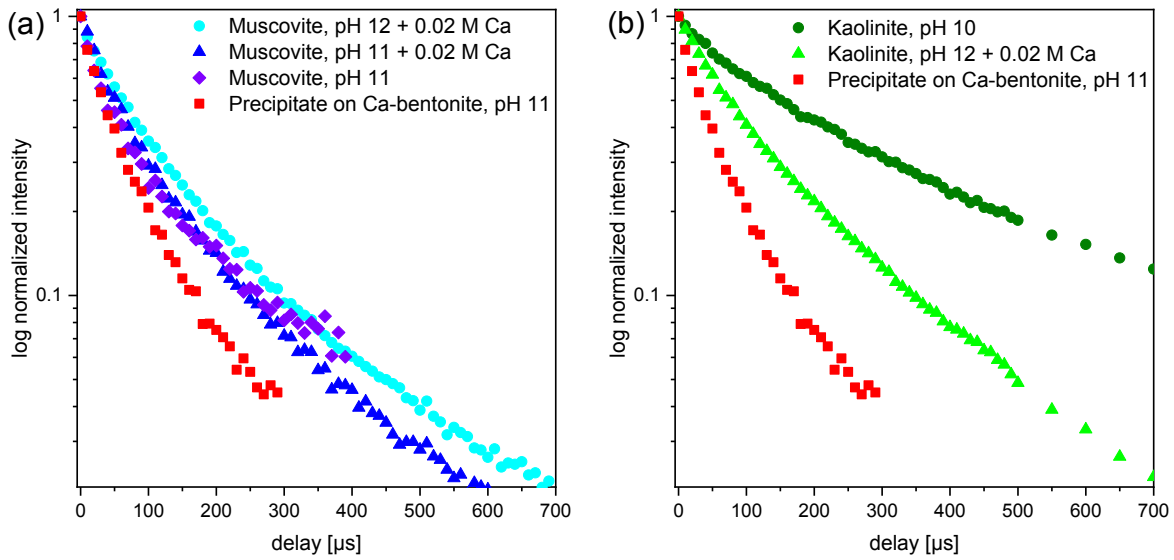

Figure 4-9: Logarithmized normalized luminescence intensity as function of delay time at λ_{ex} = 499.7 nm of U(VI) sorbed on muscovite (a) and kaolinite (b) at different pH and in 0.1 M NaCl or 0.1 M NaCl + 0.02 M $CaCl_2$. A uranate-like precipitate on Ca-bentonite at pH 11 is included for comparison. For experimental details of these samples please refer to Figure 4-6 and Figure 3-16.

Table 4-1: Luminescence lifetimes at λ_{ex} = 499.7 nm of U(VI) sorbed on muscovite and kaolinite at different pH in the presence and absence of calcium. A uranate-like precipitate on Ca-bentonite at pH 11 is included for comparison.

Sample	τ_1 [µs]	τ_2 [µs]
Muscovite, pH 11	21 ± 3	109 ± 9
Muscovite, pH 11 + 0.02 M $CaCl_2$	45 ± 2	157 ± 5
Muscovite, pH 12 + 0.02 M $CaCl_2$	52 ± 3	167 ± 6
Kaolinite, pH 10	99 ± 6	394 ± 15
Kaolinite, pH 12 + 0.02 M $CaCl_2$	60 ± 2	210 ± 3
Precipitate on Ca-bentonite, pH 11	58 ± 2	

Despite the absence of line-narrowing due to U(VI) adsorption in close proximity to each other and resulting homo-resonance energy transfer, calcium induced sorption species could

be detected with site-selective TRLFS and conclusions regarding the nature of such complexes can be drawn. The species observed on muscovite at pH 12 in the presence of calcium corresponds to TRLFS-species 1, identified in Ca-bentonite (chapter 3.2.2.4), which is interpreted to be an outer-sphere sorption species, based on its frequency of the total symmetric stretch vibration. This leads to the conclusion, that the calcium-mediated attachment of U(VI) on clay minerals observed in the batch sorption experiments is realized by outer-sphere complexation based on electrostatic interactions and not by ternary or quaternary inner-sphere surface complexation. While there was no experimental indication for the formation of Ca-U(VI)-OH complexes, Ca(II) sorption experiments, zeta-potential measurements, site-selective TRLFS and EXAFS all support the hypothesis that calcium adsorbs to the clay minerals in the first place, locally compensating negative surface charge and enabling electrostatic attachment of anionic uranyl hydroxides. Unfortunately, it was not possible to observe this kind of sorption species on kaolinite since the signal of adsorbed U(VI) was superimposed by the one of Ca-uranate, which precipitated due to an insufficient number of sorption sites on the mineral surface. The spectra obtained for muscovite, kaolinite and Ca-bentonite also prove that U(VI) predominantly sorbs on the respective clay minerals and not on C-(A-)S-H which might form as a secondary phase during the experiments (cf. chapter 3.2.1.3). If the mineral composition was altered severely and U(VI) sorption predominantly happened on C-(A-)S-H, the recorded spectra would all appear to be the same. However, spectral features which are characteristic for the different clay minerals are preserved within the different samples, such as presence or absence of line-narrowing and sorption on aluminol or silanol sites. Especially in the kaolinite sample at pH 12 in the presence of calcium, where mineral dissolution is noticeable, the formation of C-(A-)S-H should be favored. However, instead of adsorbing on C-(A-)S-H, the U(VI) rather appeared to precipitate.

4.2.3. Effect of Ca(II) on Np(VI) sorption on muscovite

Batch sorption experiments with Np(VI) on muscovite were conducted in order to evaluate whether the findings for U(VI) sorption at (hyper)alkaline conditions and especially the strong effect of calcium can be transferred to other hexavalent actinides. Comparable behavior is expected for Np(VI), as the aqueous speciation at alkaline conditions is very similar to the one of U(VI), with a prevalence of anionic actinyl hydroxides. However, studies about the Np(VI) sorption on clay minerals or muscovite are not existent in literature. In order to be able to apply very low initial Np(VI) concentrations, inhibiting precipitation of neptunates, experiments were performed with the highly active isotope ^{239}Np, produced at the TRIGA research reactor of the JGU Mainz as described in chapter 3.1.1.

The results of the two experimental series in 0.1 M NaCl and in 0.1 M NaCl + 0.02 M $CaCl_2$ at pH 8-13 show a strong dependency of Np(VI) sorption on muscovite on both the pH and the availability of calcium (Figure 4-10). At pH 8-9 Np(VI) retention increases with

increasing pH from ~20% to ~50%, irrespective of the presence of calcium. At higher pH, sorption reaches a maximum of 65% at pH 10.5 in the absence of calcium, before decreasing to almost 0% at pH 13.2. By contrast, in the presence of 0.02 M calcium Np(VI) sorption increases to 99%, forming a plateau of almost complete retention between pH 10.5 and 12, followed by a rapid drop to 9% at pH 12.5 and a sudden re-increase to 59% at pH 13.2. Consequently, the presence of calcium strongly enhances the Np(VI) sorption on muscovite at pH>9.

Even though the effect of calcium on Np(VI) sorption on muscovite was the same as on U(VI) sorption, the pH-dependent sorption diagrams differ significantly, namely in the pH region 8-10. While sorption of U(VI) in this pH region was >90% both in the presence and absence of calcium, it is very low for Np(VI). This strongly decreased retention is surprising as Np(VI) was expected to behave exactly as U(VI), based on the similarities in aqueous speciation. U(VI) sorption on many materials, particularly clay minerals, is generally known to be highest at circumneutral pH so that the observed 15% of Np(VI) sorption at pH 7.9 are especially unexpected. A mechanism that could explain this low retention is reduction of Np(VI) to Np(V). Indeed, the measured E_h values for the sample series in 0.1 M NaCl + 0.02 M $CaCl_2$ at pH ≤ 9 lie within the stability field for Np(V) (red circles in Figure 4-11).

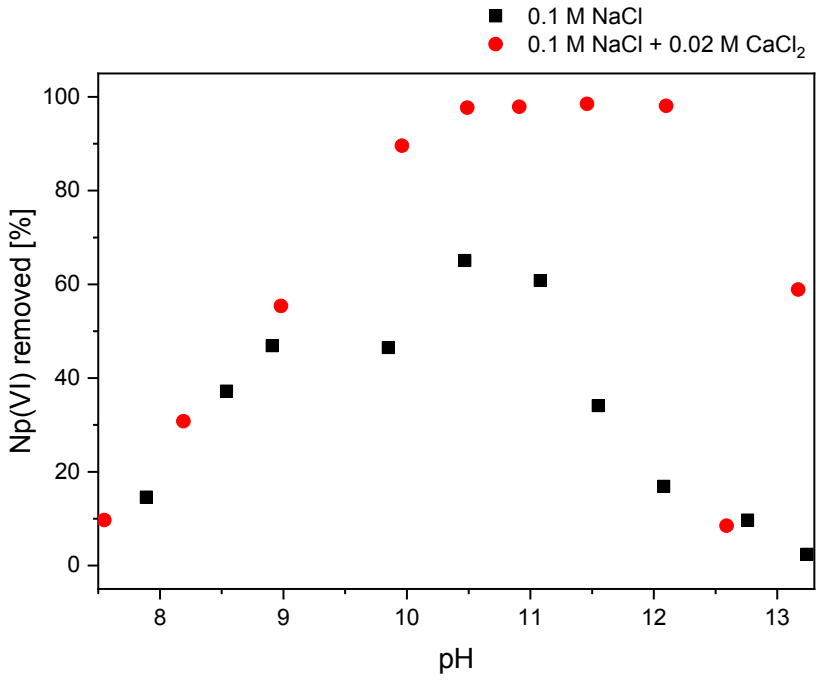

Figure 4-10: Percentage of Np(VI) ([Np(VI)] = 1×10^{-11} M) sorbed on muscovite (3 g/L) in 0.1 M NaCl and 0.1 M NaCl + 0.02 M $CaCl_2$ as a function of pH in the absence of CO_2.

The observed lowered, but increasing, Np-retention in this pH range fits to the sorption behavior of Np(V) reported in literature. In various studies it was found that the adsorption edge of Np(V) located between pH 6 and 10. However, the presence of Np(V) can only explain the low Np-retention at pH ≤ 9 in the samples containing calcium. The measured E_h

values for the sorption series in the absence of calcium clearly plot within the stability field for Np(VI) (black squares in Figure 4-11). Here, apparently, the well-studied process of formation of strong inner-sphere sorption complexes of hexavalent actinides on amphoteric edge sites for some reason does not apply to the investigated system Np(VI)/muscovite. The observed increase in Np(VI) retention at pH>8 seems to coincide with the formation of the anionic aqueous neptunyl hydroxide species $NpO_2(OH)_3^-$, which gain predominance over $NpO_2(OH)_2$ at pH > 8 (see Figure 4-12). This behavior is counterintuitive as usually cationic and neutral species are expected to sorb better to negatively charged surfaces than anionic species. In the present experiment, however, the known mechanisms for surface complexation at circumneutral conditions seem to not apply but anionic species are required to enable a sorption of Np(VI) to muscovite. As shown for U(VI), the sorption of these anionic species is facilitated by calcium cations (which are also released from the muscovite in minor amounts, see chapter 4.2.2), which mediate between the actinide complex and the mineral surface. No literature data exist for the sorption of Np(VI) on muscovite or clay minerals for comparison. Hence, it has also never been demonstrated or postulated that Np(VI) strongly sorbs on muscovite at pH 8-10. This assumption, and the resulting peculiarity of the low retention in the present study, only arises from the fact that U(VI) has been shown to sorb strongly on muscovite under equal conditions. The reason for the different behavior of Np(VI) in the absence of calcium remains unclear for the time being.

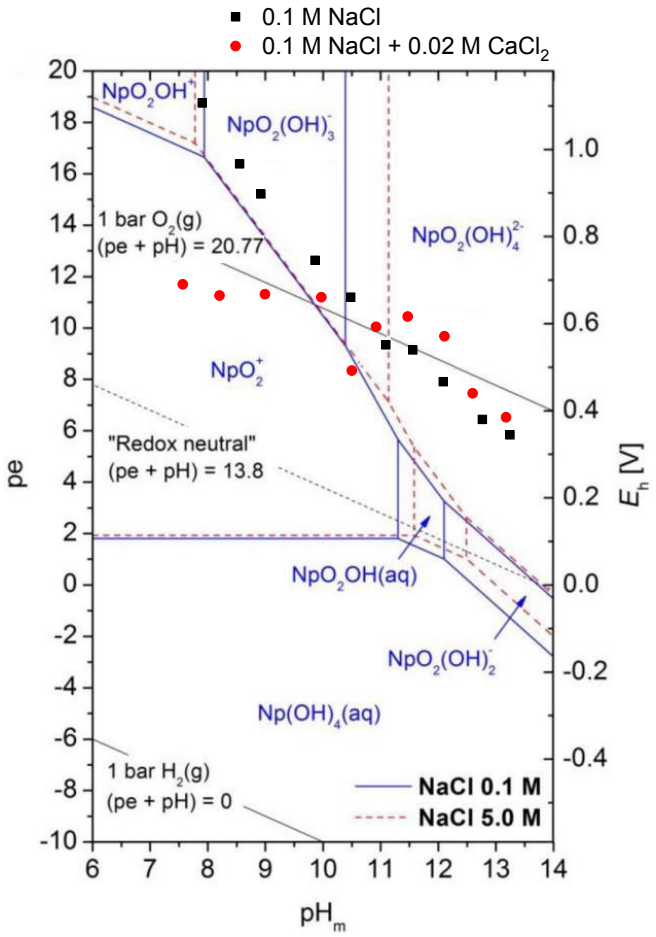

Figure 4-11: Predominance diagram of aqueous neptunium as a function of redox potential and pH modified after Gaona et al. (2013). Stability constants were recalculated to I=0. Measured E_h values of the sorption samples of the two experimental series (in 0.1 M NaCl and in 0.1 M NaCl + 0.02 M $CaCl_2$) are included in the diagram (black squares and red circles).

At pH>10 the Np(VI) sorption on muscovite is as expected, as the pH-dependent sorption diagram resembles the one obtained for U(VI) sorption (see Figure 4-4b). In the presence of calcium Np(VI) retention is very high up to pH 12 due to adsorbed calcium, locally compensating the negative surface charge of muscovite. In the experimental series without calcium addition this mediation cannot be achieved and Np(VI) sorption decreases at pH>10.5. Tits et al. (2014) studied the Np(VI) sorption on TiO_2 at pH 10-14. In the absence of calcium they found high retention at pH 10 and, in accordance to the present study, a decrease of sorption with increasing pH. They were also able to observe a positive correlation between calcium concentration and distribution ratio R_d at pH 12, 13.3 and 14. As possible underlying mechanisms they identified the formation of ternary Ca-Np(VI)-hydroxide complexes or charge compensation at the mineral surface due to calcium adsorption. As already discussed in chapter 4.2.2, the latter theory is favored based on results from calcium sorption on Ca-bentonite, as well as from zeta potential, site-selective TRLFS and EXAFS measurements in the U(VI) system.

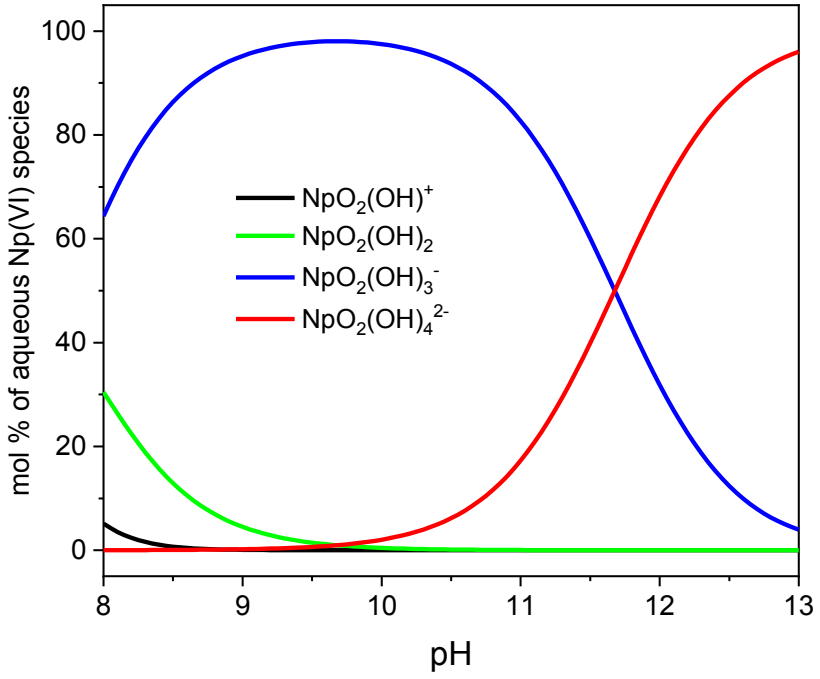

Figure 4-12: Aqueous speciation of Np(VI) (1×10^{-11} M) in 0.1 M NaCl in the absence of CO_2 calculated with the geochemical modelling software PHREEQC (Parkhurst and Appelo, 2013), based on thermodynamic data of the PSI/Nagra Chemical Thermodynamic Database 12/07 (Thoenen et al., 2014b). Stability constant for $NpO_2(OH)_2$ from Gaona et al. (2013).

The observed unexpected re-increase of Np(VI) retention from pH 12.5 to pH 13.2 in the presence of calcium might be not due to adsorption on muscovite but could be caused by incorporation into or co-precipitation with newly formed mineral phases. In the presence of 0.02 M $CaCl_2$, the solution is supersaturated with respect to $Ca(OH)_2$ at pH>12.5. Additionally, the formation of C-(A-)S-H phases could be triggered by the partial dissolution of muscovite at very high pH (both discussed in chapter 3.2.1.3 and 4.2). However, this hypothesis has to be assessed with spectroscopic measurements in the future. Owing to the low initial Np(VI) concentrations, it can be generally ruled out that precipitation of Np(VI) minerals contributes to the observed retention. Solubility studies showed that Np(VI) solubility is higher than 1×10^{-7} M in the presence of calcium at pH 9-12 (Fellhauer et al., 2017).

5. Influence of isosaccharinic acid (ISA) on U(VI) sorption on Ca-bentonite at (hyper)alkaline conditions

5.1. Experimental

The experimental conditions related to these specific experiments are compiled in chapter 3.1.

5.2. Results and discussion

Goal of the work was to investigate the ability of small organic molecules, i.e. isosaccharinic acid (ISA) (chemical structure of α-D-isosaccharinic acid shown in Figure 5-1) to increase the mobility of U(VI) in an alkaline repository environment. This could be realized by complexation of ISA with U(VI), forming stable aqueous species, thus, preventing U(VI) to adsorb to mineral surfaces. Therefore, U(VI) batch sorption experiments at different ISA concentrations were complemented with spectroscopic investigations (i.e. TRLFS) on the aqueous speciation of U(VI) in the presence of ISA.

At U:ISA ratios of 1:10, 1:100 (both not shown) and 1:1,000 (Figure 5-1) no effect of ISA on U(VI) retention could be observed. The pH-dependent U(VI) sorption on Ca-bentonite follows the same trend as described in chapter 3.2.2.1, with very strong sorption at pH 8-12, followed by a decrease in U(VI) retention at pH > 12. This is in contrast to existing studies at lower pH, where a lower excess of ISA already led to U-ISA complexation and to an associated decrease of U(VI) retention. At pH 7 Baston et al. (1994) observed significant reduction of U(VI) sorption on tuff rock at a U:ISA ratio of 1:250 and Warwick et al. (2006) described the formation of aqueous U-ISA complexes even at an ISA excess smaller than 1:20. At acidic conditions also Brinkmann et al. (2019) found different aqueous U-ISA complexes at very small excess of ISA (U:ISA = 1:16). However, in the alkaline pH range investigated in this study (pH 8-13) uranyl hydrolysis seems to be too strong for readily allowing interaction between U(VI) and ISA. This was confirmed by TRLFS measurements (not shown), where at a U:ISA ratio of 1:1000 no deviation from reference system without ISA could be observed.

Even at a U:ISA ratio of 1:10,000 the sorption behavior was still the same as in the experiment without ISA (see Dullies (2019)). Only at a U:ISA ratio of 1:100,000 (which was the highest excess of ISA achievable with the available stock solutions) a significant effect on U(VI) retention could be detected (Figure 5-1). Sorption is only at 52% and 41% at pH 8 and 9, respectively. At pH 10, the sorption maximum, U(VI) is retained to 83%, which is still a significant reduction compared to the complete retention in the absence of ISA. At pH>10, retention decreases gradually, consistently exhibiting smaller values than in the absence of ISA.

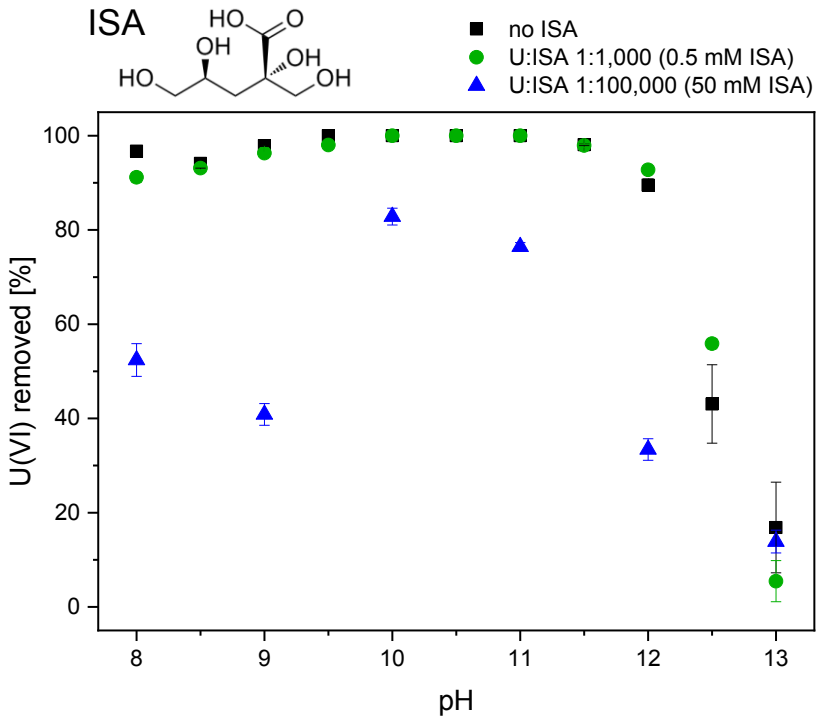

Figure 5-1: Percentage of U(VI) ([U(VI)] = 5×10^{-7} M) sorbed on Ca-bentonite (10 g/L) in 0.1 M NaCl as function of pH and U:ISA ratio in the absence of CO_2. Above the graph, the chemical structure of α-D-isosaccharinic acid is depicted.

TRLFS measurements of the supernatant solutions of the sorption experiments with an U:ISA ratio of 1:100,000 prove, that the decrease of U(VI) retention is caused by complexation of U(VI) with ISA. All luminescence spectra obtained between pH 8 and 13 (Figure 5-2) differ from the spectra obtained for the uranyl hydroxide complexes in the absence of ISA (not shown). Based on the position of the peaks, two species can be distinguished within the investigated pH range: One at pH 8-10 and another one at pH 11-13. The peak positions of species 1 (approx. 481, 502 and 523 nm) fit very well to the 1:2 U-ISA complex $UO_2(ISA)_2$ (Table 5-1). By combination of UV-Vis, ATR FT-IR, EXAFS and ESI-MS Brinkmann et al. (2019) showed that this complex forms in aqueous solution, provided ISA is present in excess of U(VI). A TRLFS spectrum of this complex was recorded and serves as a reference. So far $UO_2(ISA)_2$ was only observed in acidic solutions. The present work suggests, that it also occurs at up to pH 10 at extreme excess of ISA (U:ISA = 1:100,000). Species 2, which was observed at pH 11-13, is significantly shifted to lower wavelength and could not be assigned to a specific U-ISA species within the scope of this work. Due to an increased concentration of OH^- in hyperalkaline solutions, species 2 might be a mixed U-ISA-OH complex. Warwick et al. (2006) proposed the formation of $UO_2ISA(OH)_4$ at pH 13.3 based on the solubility product method (Warwick et al., 2004).

Even though it was shown that U(VI) retention on Ca-bentonite is significantly reduced between pH 8 and 13 at an U:ISA ratio of 1:100,000 due to aqueous complexation of U(VI) and ISA, it can be concluded that U(VI) mobilization by the introduction of ISA is not a major threat at alkaline repository conditions. Justification for this assumption arises from the

great improbability of encountering such a high excess of ISA in deep geological repository environments. The maximum concentration of ISA that might be present in such a repository is estimated to be 3×10^{-6} M (Wieland and Van Loon, 2003). This conclusion is in accordance with results on mobilization of other radionuclides by the introduction of cellulose degradation products. Th(IV), Eu(III) and Am(III) were found to sorb less on calcite at pH 13.3 only at ISA concentrations above 1×10^{-5} M (Tits et al., 2005). This corresponded to very high excess ratios of Th:ISA = 1:1,000,000, Eu:ISA = 1:10,000 and Am:ISA = 1:1,000,000.

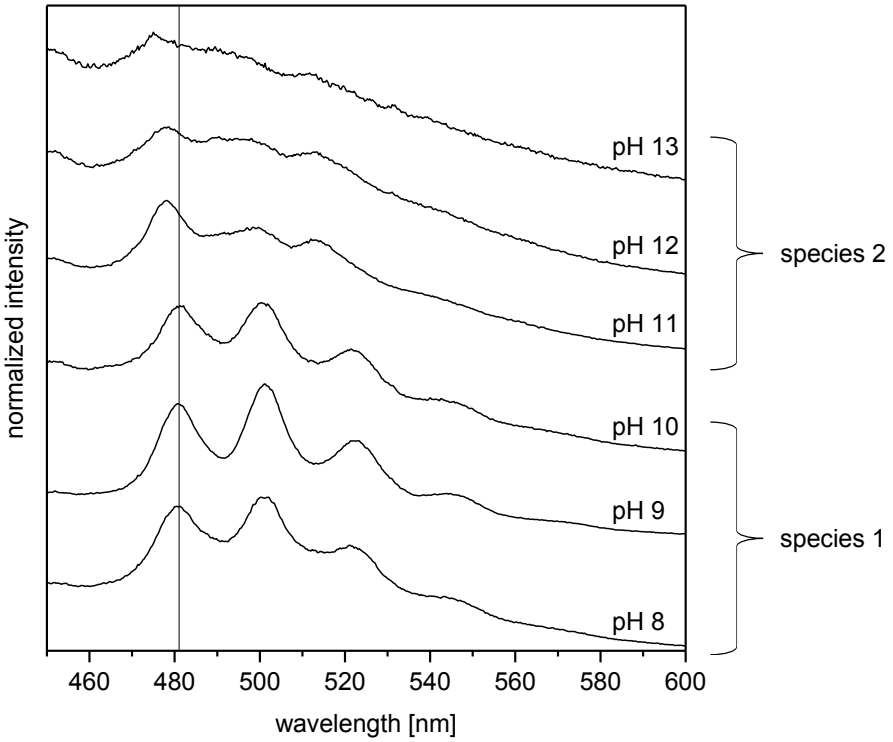

Figure 5-2: Luminescence spectra of uranyl ([U(VI)] = 5×10^{-7} M) in the supernatant of the sorption experiment with a U:ISA ratio of 1:100,000 in 0.1 M NaCl as a function of pH in the absence of CO_2.

Table 5-1: Positions of the first three main peaks of the luminescence spectra of uranyl in the supernatant of the sorption experiment with a U:ISA ratio of 1:100,000. [$UO_2(ISA)_2$], measured by Hannes Brinkmann, is included as a reference.

Experiment	pH	Peak positions [nm]		
Supernatant after	8	480.6	501.5	523.4
sorption experiment	9	480.9	501.2	523.4
with U:ISA 1:100,000	10	481.5	501.8	522.2
	11	478.1	499.7	514.5
	12	477.5	496.3	513.5
	13	473.2	499.7	512.9
[$UO_2(ISA)_2$]		482	502	523

6. Influence of polymeric cement additives on Eu(III) mobility at (hyper)alkaline conditions

Cement as a construction and backfill material in repository systems contains polymeric additives (so-called superplasticizers) at amounts of ~ 1% to reduce the viscosity of the grout. The required percentage is higher in low-pH cement due to the content of SiO_2 nanoparticles. Today, mostly polycarboxylate ethers (PCE) are in use, which are comparable to humic substances regarding the ability to form strong metal complexes. Therefore, they have been identified as one class of potential mobilizing agents among the organic inventory of a final repository (Hakanen, 2006). In leaching tests with freshly prepared hardened cement or concrete, 2% of the total amount of PCE was set free already after 2 months (Dransfield, 2004; Herterich et al., 2004; Young, 2012). In case of release together with radionuclides, adsorption barriers may be subverted. The respective conditions (pH, ionic strength) need to be identified.

There are only few pertinent studies so far, part of them leading to contradictory conclusions. Solubility of radionuclides was found to be increased by orders of magnitude in the presence of superplasticizers (Boult et al., 1998a; Butcher, 2008; Clacher and Cowper, 2009; Clacher et al., 2013; Greenfield et al., 1998; Young, 2012). In several studies, a mobilizing effect was also observed in respect of adsorption on cement (Dario et al., 2004; Glaus et al., 2004; Young, 2012). Other investigations did not arrive at such findings (Glaus and Van Loon, 2004; Wieland et al., 2014). Studies on adsorption to other relevant solid phases (buffer materials, host rock etc.) are missing, and the influence of parameters like pH value and electrolyte content has not yet been systematically investigated. So far, the extent of metal complexation with superplasticizers was only estimated from solubility enhancements.

In the present work, complexation was studied directly for the first time, using ultrafiltration as a separation method. ^{152}Eu(III) was employed as a tracer analogue of trivalent actinides such as Am(III) or Cm(III). The effect of PCE on adsorption of Eu(III) to Ca-bentonite as a buffer material was examined over a broad range of ionic strengths (up to 4 M NaCl, $CaCl_2$) and pH values in the alkaline region. Investigations with pristine PCE are certainly to be considered as worst-case studies since degradation by alkaline hydrolysis is likely to occur in the long term. In short-term tests, PCE proved to be amazingly stable (Butcher, 2008; Glaus and Van Loon, 2004; Hakanen, 2006; Young, 2012). In particular for low-pH cement, it must be taken into consideration that PCE may be persistent over extended time periods.

6.1. Experimental

6.1.1. Materials

^{152}Eu was purchased as [^{152}Eu]$EuCl_3$ in 0.1 M HCl from Radioisotope Centre Polatom (Poland). Ca-bentonite (*Calcigel*®, Clariant, Munich, Germany) was used. The

superplasticizer MasterGlenium 51® (shortly referred to as Glenium in the following) was supplied as a 35% aqueous solution by BASF. All other chemicals were of analytical grade and used without further pretreatment. Solutions were prepared using ultrapure Milli-Q water that was sonicated and flushed with argon for 15 min in order to remove CO_2.

6.1.2. Complexation experiments

For recording an isotherm of Eu(III) binding to Glenium, solutions of $Eu(NO_3)_3$ at a range of concentrations (10^{-7} - 10^{-2} mol/L) were spiked with ^{152}Eu at an activity of 0.6 kBq. The superplasticizer was added as last component, resulting in a concentration of 100 mg/L. A pH value of 6 was attained by using pH-adjusted stock solutions. Separation of bound and non-bound Eu was carried out after 24 h of contact time by ultrafiltration through polyethersulfone membrane centrifuge filters (Vivaspin, Sartorius) with an MWCO of 3 kDa, using a Hettich Universal 32 centrifuge operated at 7000 rpm. Concentrations of Eu in the filtrates were determined relative to reference samples with a 1480 Wallac Wizard 3" gamma counter (Perkin Elmer) in an energy window of 0 - 2 MeV. Wall adsorption during equilibration in 4 mL PP centrifuge tubes was found to be negligible. The amount of Eu complexed to Glenium was calculated from the difference between the concentrations of Eu in reference and filtrates.

To determine the carboxyl group content of the superplasticizer, a direct potentiometric titration with 0.1 M NaOH was performed under a N_2 atmosphere, using a SenTix 41 combination electrode (WTW). The proton exchange capacity was calculated according to Young et al. (1981) from the NaOH consumption at the equivalence point. 0.1 M $NaClO_4$ was used as a background electrolyte.

6.1.3. Sorption experiments

A 4×10^{-7} M stock solution of $Eu(NO_3)_3$ in 1 mM HNO_3 was spiked with ^{152}Eu, and a 20 g/L stock solution of Glenium was freshly prepared for every experimental series. Stock suspensions of 5.05 g/L Ca-bentonite with no salts, with 4.5 M NaCl or with 4.5 M $CaCl_2$ were adjusted to pH 9, 11 or 13 using NaOH while working under N_2 in a glove box. Conditioning required many steps over a period of two months until the pH was constant for two consecutive days. For pH measurements, the pH electrode was calibrated for high ionic strength by establishing a correction value. For this, appropriate amounts of NaOH were added to aqueous 4.5 M NaCl or $CaCl_2$ solutions, and the measured pH was recorded. From the comparison of this measured pH to the pH of a similarly prepared solution without salts, an averaged constant correction value of 0.356 for 4.5 M NaCl and 2.992 for 4.5 M $CaCl_2$ was obtained and applied to all pH measurements in suspensions with high ionic strength (Figure 6-1).

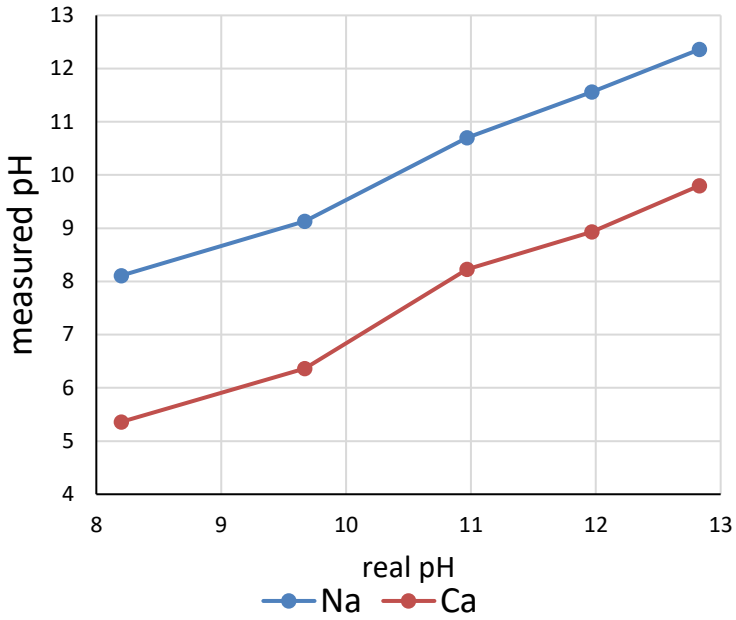

Figure 6-1: Calibration of the pH electrode for ionic strengths of 4.5 M NaCl and 4.5 M $CaCl_2$, respectively.

Table 6-1: Sample preparation scheme.

Final salt concentration in sample [M]	Volume of 4.5 M salt suspension added to sample [μL]	Volume of salt-free suspension added to sample [μL]	+ 20 μL 20 g/L Glenium stock solution (for Glenium samples) + 20 μL Milli-Q water (for Glenium-free samples)
4	3556	404	
3	2667	1293	+ 10 μL 4×10^{-7} M $[^{152}Eu]Eu(NO_3)_3$ (pH 3)
2	1778	2182	
1	889	3071	+ 10 μL 10^{-3} M NaOH
0.8	711	3249	
0.6	533	3427	work in N_2-filled glove box
0.5	444	3516	
0.4	356	3604	
0.3	267	3693	
0.2	178	3782	
0.1	89	3871	
0	0	3960	

The adsorption experiments were conducted by adding appropriate amounts of the pH-adjusted salt-free and salt-containing dispersions, Glenium stock solution or water and europium stock solution to 5 mL Simport PP cryo-vials to yield 4 mL samples of 0 - 4 M NaCl or $CaCl_2$, 100 mg/L Glenium and 10^{-9} M $[^{152}Eu]Eu(NO_3)_3$ (Table 6-1). The vials were

flushed with Ar before transfer into the N_2-filled glove box. Each sample was replicated twice. Additionally, a range of control experiments in the absence of bentonite were conducted to gain knowledge about wall effects.

The samples prepared under N_2 in a glove box were then closed and put into a Rotatherm overhead shaker working at 20 rpm for 24 h. Afterwards, the samples were centrifuged for 15 min at 7000 rpm, and 2 mL of the supernatant were transferred into another cryo-vial. The samples of the residue and of the supernatant were then measured for the ^{152}Eu activity using a 1480 Wallac Wizard 3" gamma counter (Perkin Elmer). The measured values were corrected by subtraction of the background value plus ten times the standard deviation of the background. This allowed for calculation of the fractions of Eu sorbed to the clay/vial and Eu remaining in solution from the ^{152}Eu activity A_R measured in the residue and the activity A_S measured in the supernatant according to the following equations:

$$\mathrm{Eu_{sorbed}} = \frac{(A_R - A_S)}{(A_R + A_S)} \tag{6.1}$$

$$\mathrm{Eu_{in\ solution}} = \frac{2\,A_S}{(A_R + A_S)} \tag{6.2}$$

Additionally, to exclude vial sorption effects, the residue sample was redispersed, and the dispersion was transferred to a new vial which was then analyzed for europium.

6.2. Results and discussion

6.2.1. Complexation of Eu(III) with PCE

The Charge Neutralization Model (Kim and Czerwinski, 1996), which has been widely used to quantify metal complexation with humic substances, was chosen as a basis to parameterize complexation with the PCE Glenium, allowing a direct comparison. In principle, the model represents the Langmuir isotherm equation with an equilibrium constant normalized to the ion charge (stability constant β) and a maximum adsorption normalized to the ion charge and to the proton exchange capacity of the polyelectrolyte (loading capacity *LC*). For the present system, the stability constant is given by the following equation:

$$\beta = \frac{[\mathrm{Eu_{bound}}]}{[\mathrm{Eu_{free}}]\left(\frac{1}{3}PEC \times LC - [\mathrm{Eu_{bound}}]\right)} \tag{6.3}$$

The proton exchange capacity *PEC* of the plasticizer was determined by direct titration. Figure 6-2 shows the derivative of the inverted titration curve, fitted by a Gaussian function to define the equivalence point.

With the equivalence point, taken from the maximum at pH 9.3, the total content of COOH groups was calculated to be 1.17 meq/g. The relatively sharp profile of the titration curve

indicates that the dispersity of the polymer mixture is notably low, i.e., the macromolecules are comparatively uniform.

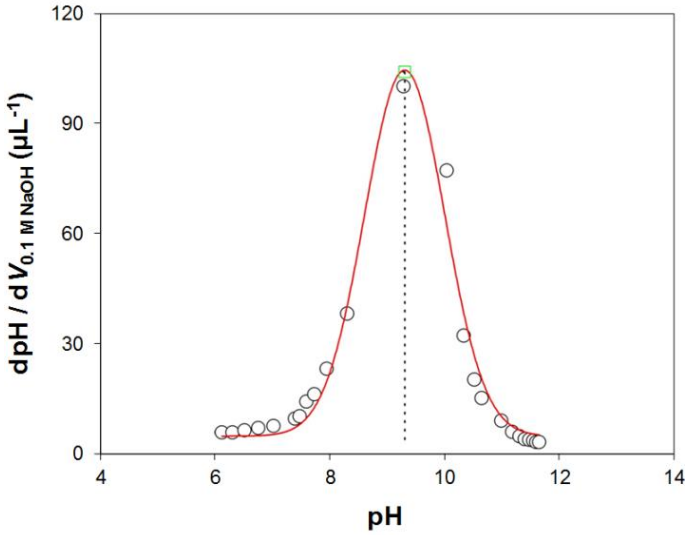

Figure 6-2: Titration curve for Glenium with Gaussian fit.

Figure 6-3 shows the binding isotherm for the Eu(III) / Glenium system at pH 6. The curve was calculated according to the Charge Neutralization Model with the parameters β and *LC* obtained from a linearization plot as suggested by Kim and Czerwinski (1996).

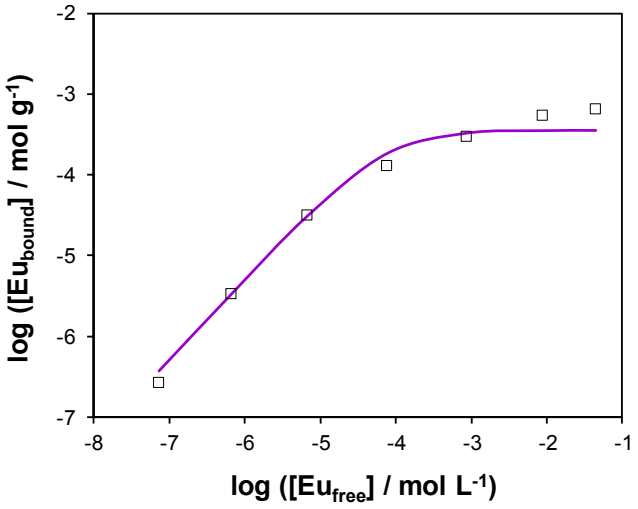

Figure 6-3: Isotherm of binding of Eu(III) to Glenium at pH 6 with curve fit according to the Charge Neutralization Model.

The parameter values are given in Table 6-2, along with the parameter values of the original Langmuir equation

$$\Gamma = \frac{\Gamma_{max} K_L [Eu_{free}]}{1 + K_L [Eu_{free}]} \tag{6.4}$$

where Γ is the bound amount of Eu per unit mass of PCE, and K_L is the Langmuir constant.

Table 6-2: Interaction parameters for binding of Eu(III) to Glenium at pH 6.

Charge Neutralization Model		**Langmuir equation**	
log (β_{LC} / L mol^{-1})	LC	K_L	Γ_{max}
4.62	92.4%	1.56×10^{4} L mol^{-1}	3.20×10^{-4} mol g^{-1}

The parameter values are comparable to those of humic substances, which are known for their ability to act as carriers of radionuclides. A mobilizing potential of PCE is thus evident. It must be noted, however, that the binding isotherm was recorded in the absence of electrolytes at a pH value in the circumneutral range – conditions that are not present in the environment of cement systems in a repository after water influx. Experiments at higher pH were carried out, but did not yield reliable data because of considerable adsorption of Eu to the filter material; a problem that was also encountered in the adsorption studies described below.

6.2.2. Vial sorption effects

Initial control experiments using 10^{-6} M [^{152}Eu]Eu(NO$_3$)$_3$ at pH 11 showed a high propensity of the europium for sorption on the vial wall. In order to rule out interfering effects of vial sorption in the experimental series, several series of control experiments were conducted. First, a time-dependent series of sorption experiments revealed that with 10^{-6} M [^{152}Eu]Eu(NO$_3$)$_3$ at pH 11 100% of the europium sorbed to the vial wall after about 6 h (Figure 6-4, top left). This effect can most likely be attributed to the formation of polynuclear neutral europium species that easily sorb to the PP material of the cryo-vials. To minimize such effects, the concentration of [^{152}Eu]Eu(NO$_3$)$_3$ was decreased in three steps down to 10^{-9} M [^{152}Eu]Eu(NO$_3$)$_3$.

The data for the experiments at reduced concentrations show a similar trend with a sorption process that levels off after about 6 h of contact time (Figure 6-4). However, the fraction of europium sorbed to the vial is reduced to about 40% at a concentration of 10^{-9} M [^{152}Eu]Eu(NO$_3$)$_3$ (Figure 6-4, bottom right). This suggests a possible strong interference of vial sorption effects at concentrations above 10^{-7} M europium with over 80% of vial sorption (Figure 6-5). A complete mitigation of the effect can be expected by extrapolation of the data at concentrations as low as 10^{-10} M [^{152}Eu]Eu(NO$_3$)$_3$. Such low concentrations, however, cannot be analyzed even with the low detection limit of the radiotracer method. To minimize vial sorption effects, all consecutive experiments were conducted at a concentration of 10^{-9} M [^{152}Eu]Eu(NO$_3$)$_3$. Additionally, the amount of europium sorbed to the vial surface in clay sorption experiments was determined by redispersion and transfer of the residual clay suspension to a new vial. These control experiments indicated that for the clay-containing systems, vial sorption effects could be neglected as the clay surface dominates the sorption of the europium. Nevertheless, control experiments were conducted for all test series.

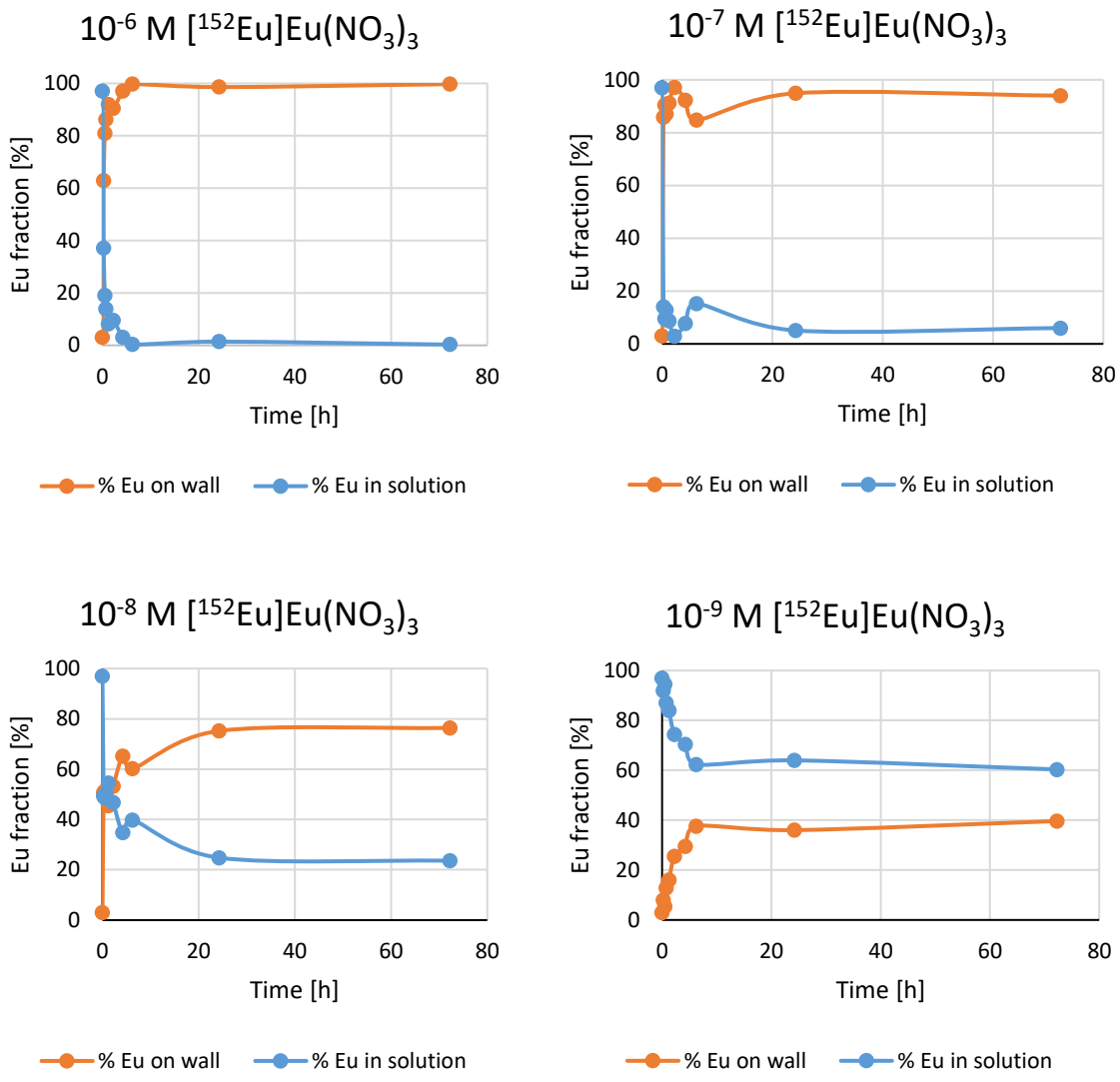

Figure 6-4: Time-dependent vial wall sorption of Eu(III) at pH 11 for different concentrations.

The results of these control experiments reveal several effects on the vial sorption of the europium (Figure 6-6). First, a pH effect, where more europium is sorbed to the wall with increasing pH. Second, an effect of the ionic strength, with high wall sorption at low ionic strength, decreasing at higher ionic strengths, down to a negligible effect at very high ionic strengths. This could hint at a trade-off effect between the out-salting of polynuclear neutral europium species at low ionic strengths and a competing ion effect at higher ionic strengths. Third, the addition of Glenium shows a mobilizing effect, decreasing the amount of europium sorbed to the vial wall. This effect is most pronounced at pH 11 and less significant at pH 9 and pH 13. This can likely be attributed to the complexation power of the Glenium that depends on the pH and is influenced by competing ion effects at higher ionic strengths.

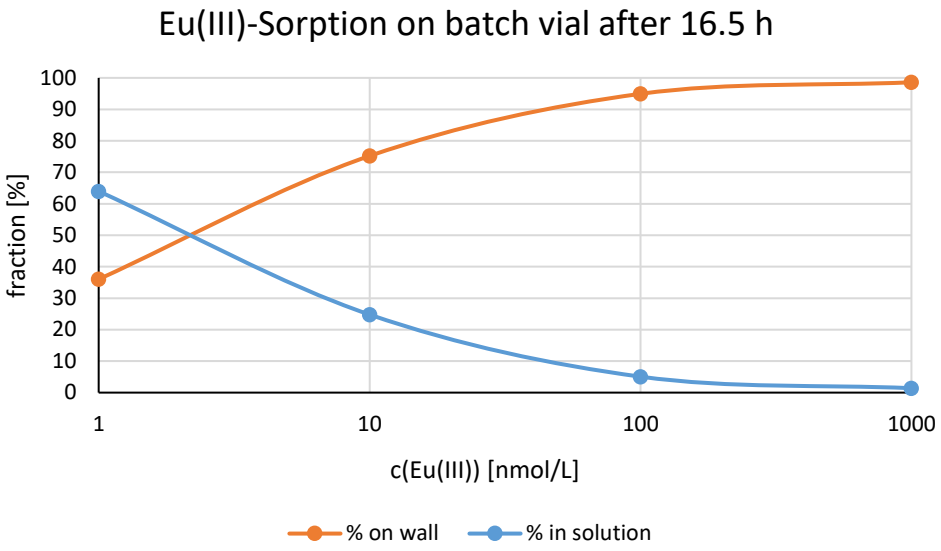

Figure 6-5: Concentration-dependent sorption of Eu(III) on the vial wall after 16.5 h of contact time.

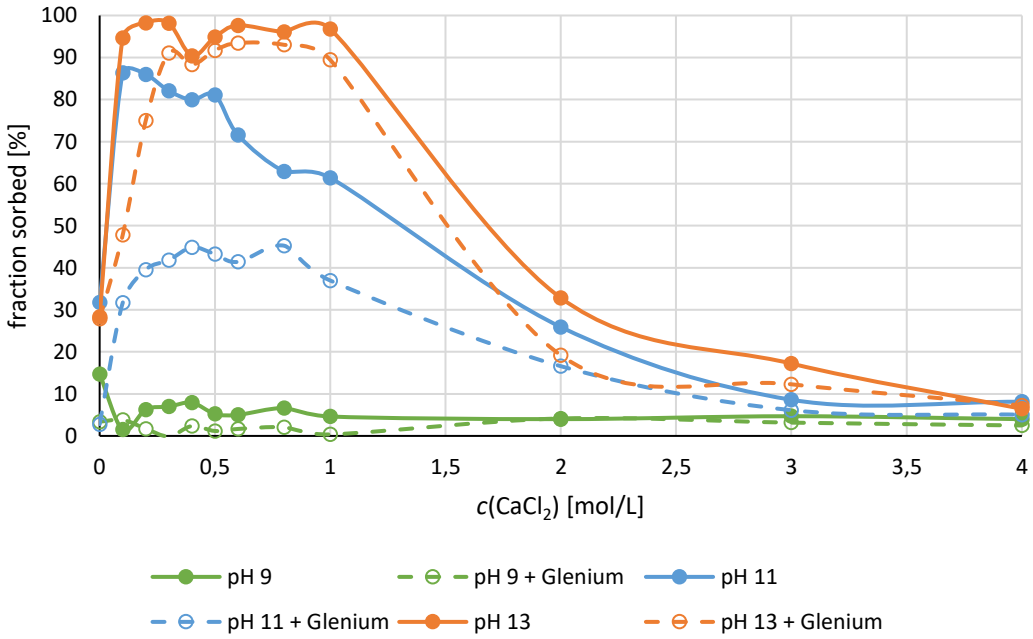

Figure 6-6: Sorption of Eu(III) on the vial wall after 24 h for samples without Glenium (solid lines) and with Glenium (dashed lines) at pH 9, 11 and 13.

6.2.3. Sorption of Eu(III) on Ca-bentonite

Several series of experiments were conducted to investigate the sorption of Eu(III) to Ca-bentonite at ionic strengths of NaCl or $CaCl_2$ ranging from 0 - 4 M at a pH between 9 and 13 in the presence or absence of Glenium. No pronounced differences between samples with and without superplasticizer were found for added NaCl at pH 11 with 100% of the added europium sorbed to the clay at all conditions except for the sample without NaCl (Figure 6-7). Only in this case, a slight mobilization effect of Glenium can be observed.

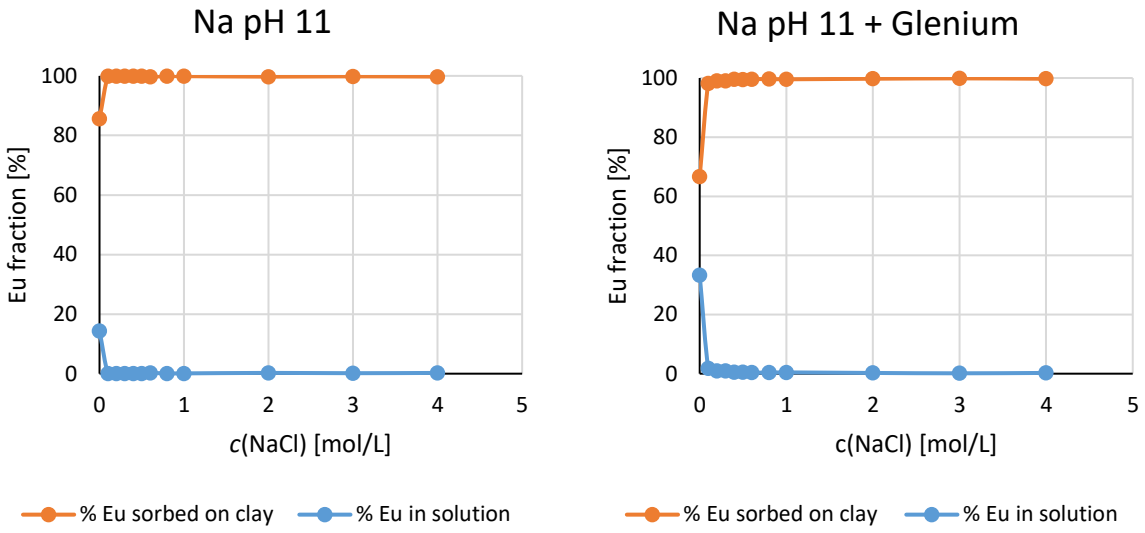

Figure 6-7: Sorption of Eu(III) on Ca-bentonite at pH 11 after 24 h in dependence on NaCl concentration for samples without Glenium (left) and with Glenium (right).

This picture does not change much if $CaCl_2$ is added instead of NaCl (Figure 6-8). Again, at pH 11 100% of the europium is sorbed to the clay except for the zero ionic strength condition. Extending the investigated pH range to 9 and 13 does not reveal a significant effect of Glenium addition. However, an increasing mobilization of europium with increasing concentration of $CaCl_2$ was observed for pH 9. This can be attributed to competition and/or charge screening effects of the electrolyte. A mobilization was also found at a $CaCl_2$ content of 4 M for pH 13. Considering the absence of such effect at pH 11, this is likely to be an artefact due to $Ca(OH)_2$ precipitation during the preparation of the original 4.5 M $CaCl_2$ clay stock suspension.

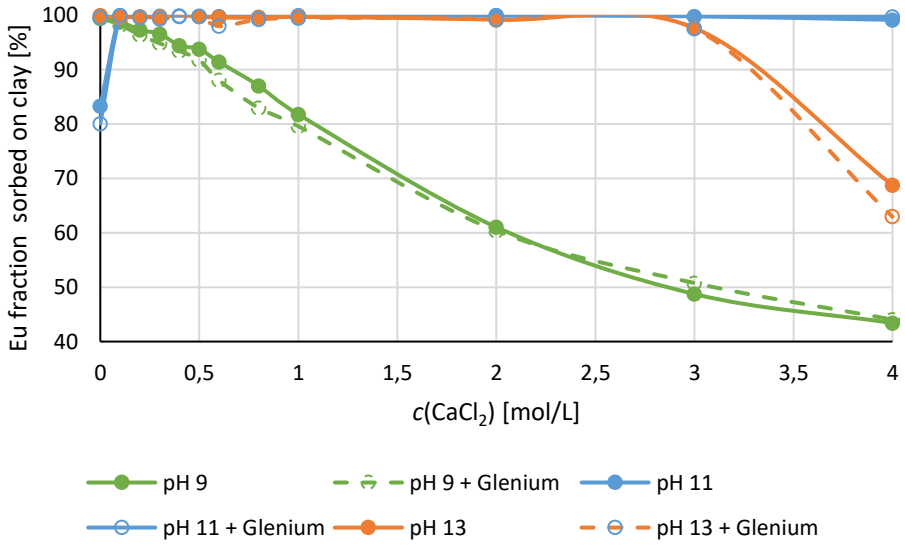

Figure 6-8: Sorption of Eu(III) on Ca-bentonite after 24 h in dependence on $CaCl_2$ concentration for samples without Glenium (solid lines) and with Glenium (dashed lines) at pH 9, 11 and 13.

The results have shown that superplasticizer do not have significant mobilizing effects on the europium / clay system at high pH and high ionic strength. Only for vial sorption, an effect of the superplasticizer was seen, most pronounced at pH 11. Here, the sorption process reached equilibrium after about 6 h. The pronounced mobilizing effects of high ionic strengths on the vial sorption could not be reproduced in the clay systems as the large sorption capacity of the clay mitigates any other effects. The different experiments indicate that any effect on actinide mobility will likely be limited to scenarios of very high ionic strength, low actinide concentrations and surfaces with very low availability of sorption sites. Future experiments on actinide mobility at very low concentrations ($< 10^{-8}$ M) may shed further light on the measured effects, however with the setback that spectroscopic information is currently not available at such low concentrations. In summary, it can be stated that carrier effects of PCE are not to be expected under the aqueous conditions present in cement systems since the high complexing power is obviously suppressed already at moderate ionic strengths.

7. Stability of U(VI) doped C-S-H phases at high ionic strength conditions

7.1. Experimental

7.1.1. Material, device and technique descriptions (relates to chapters 7, 8 and 9)

All samples were synthesized in an inert gas box (N_2 atmosphere, $O_2 < 2$ ppm), using degassed deionized water (18 MΩ cm^{-1}; mod. Milli-RO/Milli-Q-System, Millipore, Schwalbach, Germany), NaOH (p. a., Roth, Karlsruhe, Germany), KOH (ACS reagent, Roth, Karlsruhe, Germany), carbonate-free CaO (anhydrous, 99.99%, heated for 24 h at 900 °C) (Sigma-Aldrich, Missouri, USA), fumed silica (AEROSIL 300, Evonik, Essen, Germany), Al_2O_3 (metals basis, Alfa Aesar, Massachusetts, USA) and $Al(NO_3)_3 \cdot 9H_2O$ (p. a., Merck, Darmstadt, Germany).

Before usage, NaOH and KOH surface carbonate was removed from the NaOH and KOH pellets by washing the pellets several times with degassed deionized water in a Büchner funnel under inert gas atmosphere. Total inorganic carbonate concentrations of the prepared NaOH and KOH solutions were determined with a multi-N/C 2100 S (Analytik Jena, Jena, Germany) and was below 100 μM.

For sample shaking, an end-over-end rotator (SB2, Stuart, Staffordshire, UK) was used. Centrifugations were carried out either with an Avanti J-20 XP (Beckman Coulter, Krefeld, Germany) at 6,800×*g* or an EBA 280 (Hettich Lab Technology, Tuttlingen, Germany) at 3,059×*g* when not stated otherwise. The supernatant solutions after synthesis were analyzed for Na, K, Ca, Si, U or Al with inductively coupled plasma mass spectrometry (ICP-MS) (KED-mode, He gas, mod. NexION 350X/Elan 9000, PerkinElmer, Waltham, MA, USA) and for Cm(III) with liquid scintillation counting (LSC) using a TriCarb 3100TR counter (Perkin Elmer, Freiburg, Germany) and Ultima Gold™ (Perkin Elmer) as scintillation cocktail.

After sample decomposition in hydrofluoric acid, the elemental compositions of solid phases were determined by analyzing the supernatants for Na, K, Ca, Si, U or Al concentrations with ICP-MS. For drying, wet samples were frozen in liquid nitrogen and then, dried at 1 mbar and -40 °C for 1 d in a freeze-drying system (mod. ALPHA 1-4 LSCplus, Christ, Osterode am Harz, Germany).

The pH values of solutions were measured with a pH meter (inoLab pH 720, WTW, Weilheim, Germany) with a SenTix®Mic pH microelectrode (WTW) calibrated against standard pH buffers (pH: 6.865, 9.180 and 12.454) (WTW). The pH values of solutions with high ionic strengths were corrected using a method reported by Altmaier et al. (2008) ($pH_m = pH_{exp} + 0.3$ at 2.5 M NaCl).

For non-selective U(VI) TRLFS investigations, samples were suspended in deionized water and transferred into polystyrene single use cuvettes (Roth, Karlsruhe, Germany) or Boro 5.1 (ASTM type 1 class B glass, 5 mm) tubes (Deutero, Kastellaun, Germany) and shock-frozen in liquid N_2. For measurements, the cuvettes were placed in a cryogenic cooling system (mod. TG-KKK, KGW-Isotherm, Karlsruhe, Germany) and further cooled with N_2 vapor to a constant temperature of (153 ± 2) K. The laser set-up was optimized for high intensities and good signal-to-noise ratios of the spectra: front entrance of 500 µm, gate width of 2 ms and a delay time between 0.1 µs and 2 ms. To generate the excitation wavelength of 266 nm, a Nd:YAG laser (mod. Minilite, Continuum, Santa Clara, CA, USA) with an average pulse energy of 0.3 mJ was used. Emission wavelengths were detected between 369 nm and 669 nm by accumulating 75 or 100 laser pulses with a spectrograph (mod. iHR 550, HORIBA Jobin Yvon, Unterhaching, Germany) and an ICCD camera (mod. ICCD-3000, HORIBA Jobin Yvon). Positions of luminescence bands were determined by calculating the minima of the second derivative. For the time-resolved measurements a camera delay profile with 51 steps was used calculated via equation (7.1) (y: camera delay time [μs], x: steps, y_0: offset [μs]).

$$y = y_0 + ax + x^n = 0.1 + 0.05x + x^{4/3000} \tag{7.1}$$

For the site-selective Cm(III) TRLFS, Cm(III) doped C-S-H gel samples were investigated by varying the excitation wavelength in 0.1 or 0.2 nm steps between 600 and 630 nm. The emission signal obtained at each chosen wavelength was integrated and plotted against the applied wavelengths. High-resolution emission spectra were thereafter collected at the excitation peak maxima, corresponding to individual Cm-species (or hot bands), associated with the C-S-H structure or their alteration products. In this work, for TRLFS measurements the dried solid samples were transferred into an Al sample holder and covered with a quartz plate (Qiopitq, Göttingen, Germany). The site-selective TRLFS measurements were performed with a pulsed Nd:YAG (Continuum Surelite II, USA) pumped dye laser set-up (Radiant Dyes Narrow Scan K). A combination of laser dyes such as sulforhodamine B, rhodamine B, and rhodamine 101 were used to enable tuning of the excitation wavelength between 600 and 630 nm. To improve the resolution of the spectra, the samples were cooled with a helium-refrigerated cryostat below a temperature of 12 K. The emission signal was collected by a fiber coupled optical multi-channel system consisting of a polychromator with 600 and 1200 lines/mm gratings and an intensified CCD camera model iStar (Andor, Belfast, Ireland). Emission measurements were accumulated over 5,000 spectra while excitation and time-resolved measurements were accumulated over 100 spectra. Luminescence lifetimes were monitored as a function of delay time between 10 and 1,570 μs in 40 μs steps. The excitation spectra were energy corrected for each wavelength using the average energy collected with an optical power meter (Newport 1918-R).

XRD diffractograms were collected with a MiniFlex 600 diffractometer (Rigaku, Tokyo, Japan) equipped with a Cu Kα X-ray source (40 keV/15 mA operation for X-ray generation) and the D/teX Ultra 1D silicon strip detector in the Bragg-Brentano *θ-2θ* geometry at a scanning speed of 0.6° per min. The samples were mounted as wet pastes on a zero-background Si sample holder and stored for several minutes in an inert gas atmosphere to remove excess water from the samples and thus, to minimize carbonation of the samples during measurements. The subsequent phase analysis of diffractograms was done with the program PDXL 2 (Rigaku) and the ICDD PDF-4+ 2016 database (C-S-H phase (database card number 00-033-0306), portlandite (database card number 01-083-4600), calcite (database card number 01-083-4601), aragonite (database card number 01-075-9985), vaterite (database card number 04-017-8634), halite (database card number 00-005-0628), aluminum tobermorite (database card number 00-019-0052), tobermorite, aluminian, syn. (database card number 01-074-2878), and laumontite (database card number 04-015-7175)).

Immediately after removing the C-S-H phases from N_2 atmosphere, IR samples were prepared under ambient conditions by mixing approximately 1 mg of the freeze-dried samples with 300 mg dried KBr and subsequently pressing for 2 min at 1×10^9 Pa until clear pellets were obtained. IR samples were measured with a Vertex 70/v spectrometer (Bruker, Billerica, Massachusetts, USA) equipped with a D-LaTGS-detector (Lalanine doped triglycine sulfate), over a range of 4,000 to 400 cm^{-1} in the transmittance mode, with a spectral resolution of 4 cm^{-1}. Each spectrum was averaged over 64 scans.

Raman spectra were recorded using a LabRAM ARAMIS instrument (HORIBA, Jobin Yvon) equipped with an optical Olympus BX 41 microscope, a Peltier cooled detector and coupled with an external 633 nm He-Ne laser (50 mW power at the source). An objective of 50X magnification was applied for spectrum acquisition. The outer surface of dried samples was investigated under ambient conditions. The scattered light was collected in backscattering configuration. The slit width of the spectrometer was set at 155 μm. A holographic grating having 300 grooves/mm was used resulting in a spectral resolution of about 22 cm^{-1}.

For TGA and DSC investigations, C-S-H phases (sample E (freeze-dried), samples A-C (wet pastes), sample C (dried under N_2 atmosphere) were transferred in an Al_2O_3 crucible and measured between 25 and 1000 °C at 20 K min^{-1} in an Ar atmosphere with a STA 449 F5 Jupiter thermal analysis instrument (Netzsch, Selb, Germany).

Solubility calculations were performed with the geochemical speciation code Geochemist's Workbench (GWB), Module React (vers. 11.0.6) (Bethke, 2008) using the Pitzer ion-ion interaction model. The thermodynamic database was "THEREDA". U(VI) speciations in the supernatant solution were also calculated with GWB using the "PSI/Nagra Chemical Thermodynamic Database 12/07" (Thoenen et al., 2014a).

7.1.2. Synthesis of U(VI) doped C-S-H phases

7.1.2.1. Direct synthesis of U(VI) doped C-S-H phases

U(VI) doped C-S-H phases (A-D, Table 7-1) were prepared applying a direct U(VI) incorporation method. For this, a U(VI)-containing artificial cement pore water (ACW) was prepared according to Berner et al. (1992) by adding an excess of solid UO_3 to a solution of 0.18 M KOH and 0.114 M NaOH (pH 13.3) and stirring for a week. Subsequently, the ACW was separated from remaining solid UO_3 by centrifugation and analyzed for U(VI) by ICP-MS after adjusting the pH of an aliquot to 2 with concentrated HNO_3. The resulting ACW contained 19.5 μM U(VI). This U(VI)-containing ACW was added to a mixture of fumed silica and carbonate-free CaO in centrifuge tubes (polypropylene, Greiner bio-one, Kremsmünster, Austria). While the S/L ratio was 24 g/L, the CaO to SiO_2 ratio was varied depending on the targeted C/S ratio (0.6, 1.0, 1.6, 2.0). Suspensions were shaken end-over-end for 14 d and then centrifuged to analyze the supernatant for U with ICP-MS. Subsequently, the samples were re-suspended and filtered through a Whatman ashless 541-grade filter (22 μm cut-off). The U(VI) doped C-S-H samples were washed with deionized water and stored moist in sealed tubes for leaching experiments (see chapter 7.1.3) or dried for spectroscopy.

7.1.2.2. Sorption of U(VI) onto C-S-H phases

An additional C-S-H phase (sample E, Table 7-1) was synthesized at a S/L ratio of 24 g/L in U(VI)-free ACW for sorption experiments. For a comparison of samples A–D with U(VI)-containing C-S-H phases synthesized by Tits et al. (2011), a further U(VI)-containing C-S-H sample (sample E/U, Table 7-1) with a C/S ratio of 1.3 was prepared. For this, sample E was exposed to a $UO_2(NO_3)_2$ solution which contained 19.5 μM U(VI) for 14 d (S/L ratio: 24 g/L, pH after 14 d: 11.7) resulting in sample E/U. Subsequently, the U(VI)-containing C-S-H phase was centrifuged to analyze the supernatant for U with ICP-MS. Then the samples were re-suspended and filtered off, washed with deionized water, and stored moist.

7.1.3. Batch leaching of U(VI) doped C-S-H phases

For batch leaching experiments, wet pastes of U(VI) doped C-S-H samples (A-C), prepared by direct synthesis, were equilibrated in 2.5 M NaCl, 2.5 M NaCl/0.02 M Na_2SO_4, 2.5 M NaCl/0.02 M $NaHCO_3$ or 0.02 M $NaHCO_3$ at S/L ratios of 1.2 (sample A), 1.5 (sample B) and 2.3 g/L (sample C) by shaking the samples end-over-end. After different time intervals, up to 768 h, samples were centrifuged and each supernatant solution was analyzed for Ca, Si and U by ICP-MS as well as for the pH value. Solid and liquid phases after leaching were characterized by spectroscopic and further analytical methods (TRLFS, XRD and IR). All leaching experiments mentioned above were performed as triplicates.

Additionally, sample B was leached in 2.5 M NaCl/0.075 M $NaHCO_3$ for 768 h to visualize changes in the TRLFS spectrum of U(VI) doped C-S-H phases after leaching in solutions with high concentrations of carbonate. To determine the influence of increasing carbonate concentrations on the pH evolution and U(VI) release from U(VI) doped C-S-H phases, sample A was exposed to solutions containing 1, 2, 10, 20, 50, and 75 mM $NaHCO_3$ for 768 h. Subsequently, the supernatants were separated by centrifugation and analyzed for the pH value and released U. To get a detailed understanding about the Ca and Si release in dependence on NaCl concentrations, sample E was exposed to solutions containing 0, 0.5, 1.0, 1.5, 2.0, and 2.5 M NaCl at an actual S/L ratio of 1.5 g/L for 7 d. Subsequently, the supernatants were analyzed for Ca and Si with ICP-MS.

7.2. Results and discussion

7.2.1. Composition of U(VI) doped C-S-H phases

U(VI) doped C-S-H phases, synthesized by the direct incorporation method (samples A-D in Table 7-1), possess molar C/S ratios between 0.6 and 2.0 and U/S ratios between 74.5−157 ppm. The retardation coefficients, log(R_d) [log(L/kg)], increase from 3.1 to 4.1 with increasing C/S ratios.

Compared to the retardation coefficients reported by Tits et al. (2011) (3.8−4.9 for U(VI) sorbed on C-S-H in ACW and 4.7−5.9 for U(VI) sorbed on C-S-H in alkali-free water) the log(R_d) values in the present study are on the lower end. Tits et al. (2011) also found that log(R_d) values increase with the C/S ratio and that the values are one order of magnitude lower in ACW compared to water.

*Table 7-1: Composition of U(VI) doped C-S-H phases synthesized by direct incorporation as described in chapter 7.1.2.1. Sample E/U was prepared from sample E (chapter 7.1.2.2). * Values are higher due to presence of bulk and gel water in sample E before sorption which decreased the amount of solid exposed to the dissolved U(VI). ** Determined after centrifugation at 40,000×g for 1 h.*

Sample	C/S ratio	Ca [mmol/g]	Si [mmol/g]	Na [mmol/g]	K [mmol/g]	U [nmol/g]	U/S ×10^6	log(R_d) [log(L/kg)]
A	0.99	1.17	1.18	0.29	0.44	134.0	114	3.1/4.3**
B	1.55	1.87	1.21	0.17	0.24	156.7	129	3.7
C	2.02	2.94	1.46	0.10	0.14	229.0	157	4.1
D	0.59	1.38	2.25	0.47	0.67	167.6	74.5	n.d.
E	1.35	1.09	0.81	0.06	0.07	–	–	–
E/U	1.25	0.98	0.79	0.01	0.02	769*	975*	3.3

Tits et al. (2003) observed a high uncertainty in log(R_d) values due to an extremely strong sorption of Eu(III) on the C-S-H phase and a possible incomplete phase separation during centrifugation at low *g* values due to the presence of colloids in the supernatant. Since in the present study samples were centrifuged at 6,800×*g*, it is possible that the low log(R_d) values are also caused by an incomplete phase separation. To verify this assumption, sample A was

additionally centrifuged at 40,000×*g* for 1 h. Subsequently, the supernatant was analyzed for U(VI) with ICP-MS, resulting in a higher log(R_d) value of 4.3 (Table 7-1). Thus, an incomplete phase separation at 6,800×*g* can be assumed. The log(R_d) value determined at 40,000×*g* is in line with log(R_d) values from Tits et al. (2011) reported for U(VI) sorbed on C-S-H in ACW.

A comparison of the log(R_d) values with the C/S ratios reveals an increased U(VI) retention at high C/S ratios, similar as observed by Tits et al. (2011) and by Pointeau et al. (2004). Tits et al. ascribed this trend to an ion exchange mechanism between Ca^{2+} from the interlayer and UO_2^{2+}. The log(R_d) value of sample E/U is similar to those of samples A-C.

To identify mineral phases formed in the samples A-D powder XRD was applied (Figure 7-1, l.). The phase identification of the reflection patterns with the program PDXL 2 (Rigaku) and the ICDD PDF-4+ 2016 database (C-S-H database card number 00-033-0306) verifies the presence of C-S-H phases due to reflections at 29.1 (220), 32 (222), 50 (240) and 55°2θ (Grangeon et al., 2013b). Most of the diffraction peaks are broad and asymmetrical, characteristic for synthetic C-S-H.

For sample C, the additional reflections of portlandite at 18.1, 28.7, 34.2, 47.2, 50.9, 54.5, 56.2 and 59.6°2θ were observed (portlandite database card number 01-083-4600). TGA and DSC investigations of sample C showed the co-existence of 18 mass-% portlandite (related to dry weight) in sample C (Figure 7-2, l.). For samples A-C, (001) basal reflections around 8.2°2θ were observed while no basal reflection is observed for sample D. This implies that the crystallite size (amount of stacked layers in c direction) of samples A-C is larger compared to sample D (Grangeon et al., 2013b). The reflection pattern of sample D (C/S 0.59) shows a diffuse background peak that could be caused due to the co-formation of amorphous SiO_2. The IR spectra and the corresponding band positions of samples A-D dried in an N_2 atmosphere are shown in (Figure 7-1, r.) and Table 7-2. Characteristic bands observed in the C-S-H system are compiled in Table 7-3. Bands between 3,000 and 4,000 cm^{-1} are present in all samples and are caused by O-H vibrations of remaining interlayer and bulk water, while only sample C shows a band at 3,644 cm^{-1} which is characteristic for portlandite. In the literature, a co-formation of portlandite and synthetic C-S-H was detected for C/S ratios above 1.7 (Yu et al., 1999). Consistent with this literature value of 1.7, portlandite is not detectable in sample B (C/S 1.55) by IR measurements, therefore this sample should not contain portlandite. Please note that in HCP systems portlandite can be detected at lower C/S ratios compared to synthetic C-S-H phases (Auroy et al., 2018).

Since all samples were measured under ambient conditions, a surface carbonation could not be prevented completely, only minimized by drying the U(VI) doped C-S-H samples before exposure to air, as recommended in (Black et al., 2007). Therefore, carbonate doublets were observed in the IR spectra at about 1,410 and 1,480 cm^{-1} in the spectra of samples A-C, probably caused by vaterite on the surface that possesses a doublet around 1,420 and 1,490 cm^{-1} as mentioned by Sato and Matsuda (1969).

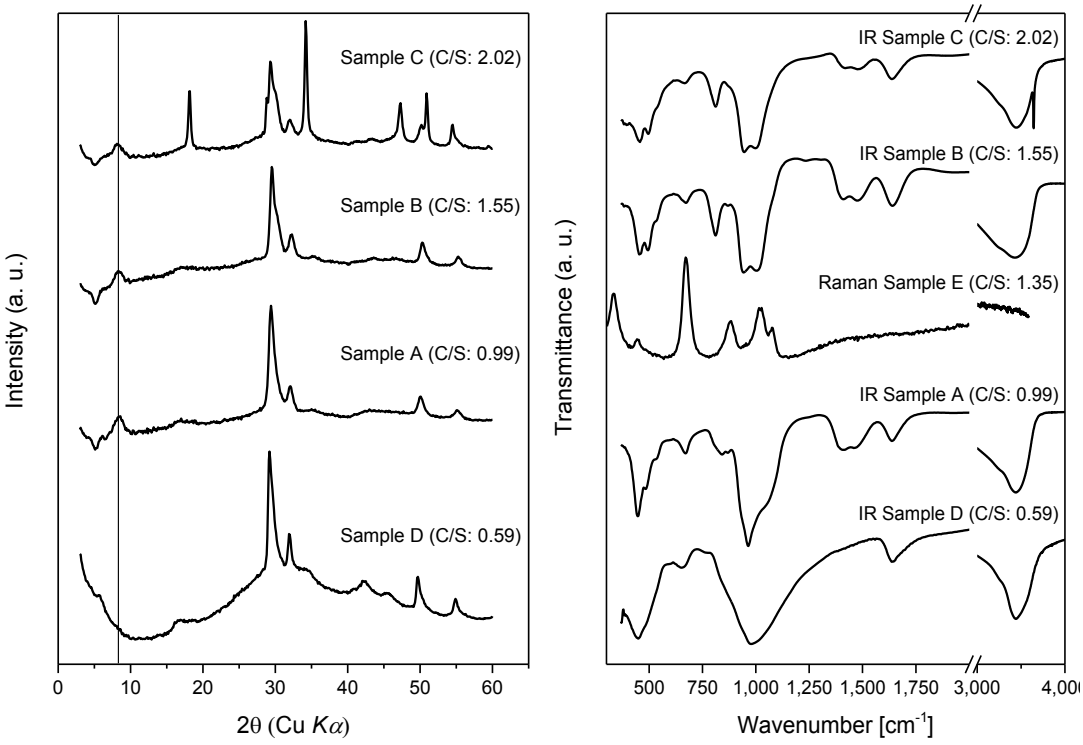

Figure 7-1: Powder XRD patterns of samples A-D (l.) (Cu Kα X-ray source). IR spectra of samples A-D and Raman spectrum of sample E before leaching (r.).

Table 7-2: Band positions of samples A-E in their IR and Raman spectra (cf. Figure 7-1, r.).

Sample	Band positions [cm^{-1}]
C	459; 497; 673; 814; 937; 1,012; 1,390; 1,410; 1,481; 1,633; 3,441; 3,644
B	453; 498; 538; 675; 812; 868; 933; 1,024; 1,232; 1,387; 1,406; 1,477; 1,635; 3,438
A	451; 494; 546; 669; 806; 904; 964; 1,043; 1,386; 1,431; 1,458; 1,631; 3,444
D	445; 661; 972; 1,639; 3,429
E	337; 452; 672; 884; 1,021; 1,075

The Raman spectrum of sample E shows a $\nu[CO_3]$ band at 1,075 cm^{-1} similar to observations from Garbev et al. (2007). The absence of these bands in the spectrum of sample D is probably caused by the lower pH of its bulk water and thus, slower carbonation.

In the IR spectra the most pronounced vibrations are observed between 930 and 960 cm^{-1}, caused by Si-OH vibrations of the bridging silanol tetrahedra and ν_{as} Si-O-Si vibrations of the C-S-H "dreierketten" (Kapeluszna et al., 2017; Yu et al., 1999). The IR spectra of samples A-C show a band at about 810 cm^{-1}. With increasing C/S ratio the "dreierketten" are losing their bridging silica tetrahedra causing bands of isolated Si-O Q^1 pairing tetrahedral (Drits and Tchoubar, 1990; Yu et al., 1999) vibrations at 810 cm^{-1}. Thus, the band at 810 cm^{-1} is more pronounced in the spectra of sample B and C compared to sample A, while it is missing in the spectrum of sample D that possesses an almost completely polymerized silica chain.

Table 7-3: Band positions characteristic for the C-S-H system.

Wavenumber [cm^{-1}]	IR band assignments (Kapeluszna et al., 2017; Yu et al., 1999)	Raman band assignments (Garbev et al., 2007)
320		Ca-O lattice vibration
445		ν_2 (SiO_4), O_{non}-Si-O_{non} bending
525	Internal Si-O tetrahedra deformation	
660	Si-O-Si bending vibrations	Si-O-Si symmetrical bending
~810	Q^1 sites of Si[4]	
870	ν_2 C-O in calcium carbonate	Symmetrical ν_1 (SiO_4) of Q^1
850-1,300	ν_{as} Si-O-Si in C-S-H	Symmetrical ν_1 (SiO_4) of Q^2
1,420	ν_1 C-O in calcium carbonate	
3,664	O-H vibration in $Ca(OH)_2$	

An expected U-O stretching vibration at 925 cm^{-1} could not be observed due the low U(VI) loadings and an overlap with the Si-OH and Si-O-Si stretching vibration around 960 cm^{-1}. Further features observed in all IR spectra are the Si–O–Si bending vibration around 660 cm^{-1} and the Si-O tetrahedra deformation vibrations between 400 and 500 cm^{-1}. The Raman spectrum of sample E (Figure 7-1, r.) shows many vibrations that were observed in the IR spectra. The symmetrical Si-O-Si bending vibration at 660 cm^{-1} is very pronounced compared to the IR spectra suggesting that this vibration possesses a high symmetry.

The bands at 450 and 960 cm^{-1} show an increase in resolution with increasing C/S ratios for all samples. An increased C/S ratio results in more ordered Si-O-Si angles and Si-O tetrahedra orientations (Yu et al., 1999) and less structural deformations which explains the increase in the band resolution for samples B and C. An increased band resolution was also observed in the IR spectrum of 14 Å tobermorite (Yu et al., 1999), which is an ordered version of the C-S-H structure.

The TRLFS spectra and luminescence properties of U(VI) doped C-S-H samples are compiled in Figure 7-2 (r.) and Table 7-4, respectively. Observed luminescence emission bands of U(VI) dissolved in ACW (Figure 7-2, r.) are in good agreement with bands reported by Tits et al. (2011) for the uranyl hydroxide complex, $UO_2(OH)_4^{2-}$, occurring in ACW under comparable conditions (Table 7-4). The 0-0 band of sample C is located at 500.2 nm, thus between the 0-0 bands of the U(VI)/C-S-H surface complex (496.3 nm) and the U(VI)/C-S-H incorporated species (503.9 nm), reported by Tits et al. (2011) for U(VI) containing C-S-H phases with a C/S ratio of 1.07. Compared to the further emission lines of samples A-C, the 0-0 band is weakly pronounced. Since the 0-0 band is located in higher proximity to the 0-0 band of U(VI) coordinated by hydroxide in ACW, it is concluded that the 0-0 band in samples A-C and E/U is mainly caused by a U(VI) species located on the C-S-H surface where OH^- and SiO_4^{4-} ligands are present.

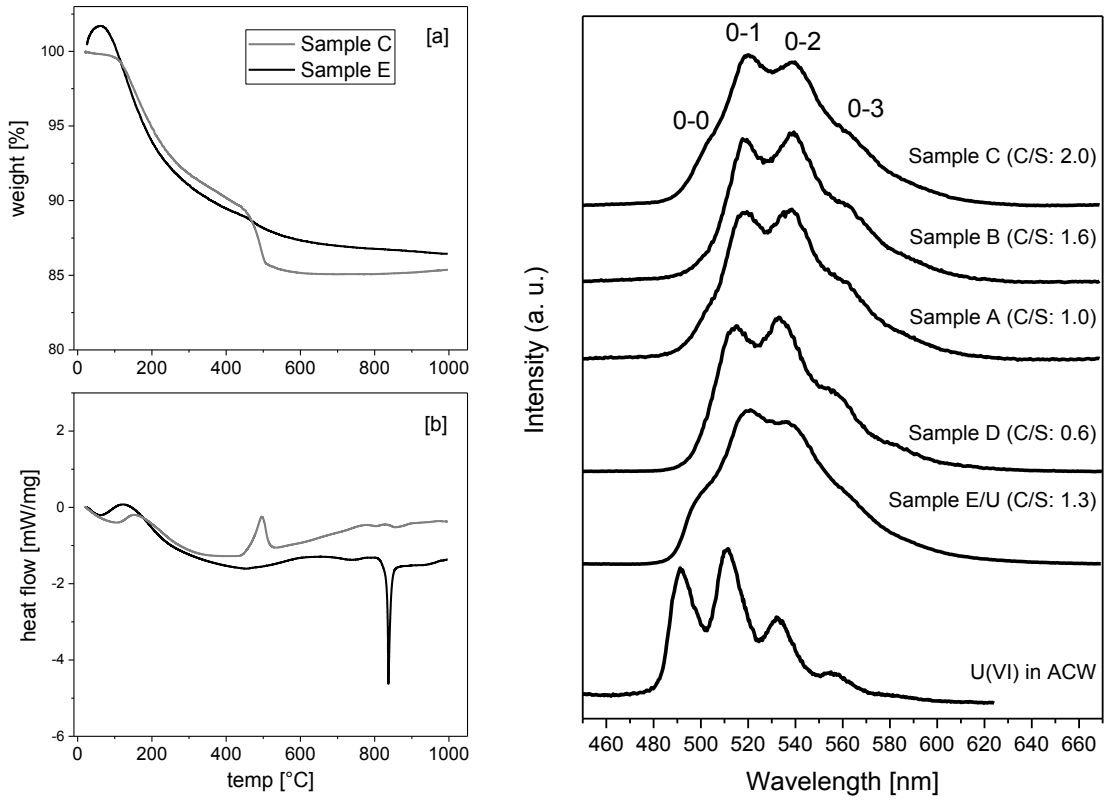

Figure 7-2: TGA [a] and DSC [b] (l.) of freeze-dried sample E (C/S 1.35) and dried sample C (C/S 2.02) before leaching. TRLFS spectra (r.) of samples A-D (direct U(VI) incorporation) and E/U (U(VI) sorption) before leaching as well as U(VI)(aq) (19.5 µM) in ACW.

Table 7-4: Luminescence band positions and lifetimes of samples A-D and E/U in comparison to data reported in the literature determined at 153 K unless stated otherwise.

Type	Band maxima [nm] 0-0; 0-1; 0-2; 0-3	$\tau \pm 2\sigma$ [µs]
Sample C (C/S 2.02)	500.2, 519.0, 540.7, 565.5	103 ± 12, 521 ± 34
Sample B (C/S 1.55)	–, 517.7, 539.8, 564.4	119 ± 8, 592 ± 18
Sample A (C/S 0.99)	497.1, 517.2, 538.9, 562.5	118 ± 14, 604 ± 28
Sample D (C/S 0.59)	–, 512.6, 534.9, 558.9	109 ± 64, 468 ± 46
Sample E/U (C/S~1.35)	493.7, 514.1, 535.4, 559.4	68 ± 26, 251 ± 30
$UO_2(OH)_4^{2-}$ in ACW (Figure 7-2)	490.9, 511.3, 532.8	129 ± 10
$UO_2(OH)_4^{2-}$ in ACW (Tits et al., 2011)	491.4	140 ± 30
$UO_2(OH)_4^{2-}$ (Meca, 2009; Torrents, 2014)	495.0, 513.6, 533.6	5.9 (40 K)
U(VI) on C-S-H surface (Tits et al., 2011)	496.3, 516.8	(205–293) ± 50
U(VI) in C-S-H interlayer (Tits et al., 2011)	503.9, 525.4	(546–647) ± 50

Note that the 0-0 band of the reference sample E/U, synthesized according to the procedure reported by Tits et al. (2011), is more distinct than in samples A-D. Due to the surface exposure of sample E to uranyl nitrate during the synthesis of sample E/U, U(VI) is probably first sorbed on the C-S-H surface before it is incorporated in the C-S-H interlayer by recrystallization. This was also described by Tits et al. (2011) who observed an ongoing incorporation of U(VI) in the C-S-H crystal structure over a time period of 6 months after U(VI) surface sorption on C-S-H samples. Due to the shorter synthesis time of 14 d compared to 6 months, sample E/U probably possesses a higher amount of surface sorbed U(VI) which is also higher compared to samples A-D where more U(VI) should be located in the C-S-H interlayers.

The positions of the 0-1 bands of samples A-D range between 512.6 and 519.0 nm, and most probably belong to uranyl incorporated in the C-S-H interlayer. An increase in red shift of the 0-1 band with increasing C/S ratios in samples A-D suggests that the U(VI) bond to the C-S-H phases is stronger at high C/S ratios, which corresponds well to the observed increased log(R_d) values as previously discussed.

Thus, during the 14 d of synthesis of the U(VI) doped C-S-H phases the direct incorporation method ensures a fast incorporation of U(VI) in the C-S-H phase whereas the U(VI) sorption procedure requires longer time periods (up to 6 months) to acquire a high ratio of U(VI) incorporated in the C-S-H interlayer. Thus, for the preparation of U(VI) doped C-S-H phases, representative for cement encapsulated nuclear waste, within short times (14 d) the direct incorporation method is preferable.

Luminescence decay lifetime analyses of samples A-D show the presence of two U(VI) species, one with short lifetimes of 103–119 μs and one with long lifetimes of 468–604 μs (Table 7-4). These lifetimes are in the same range as the lifetimes determined for the U(VI)/C-S-H surface complex ((205–293) ± 50 μs) and the U(VI)/C-S-H incorporated species ((546–647) ± 50 µs) reported by Tits et al. (2011). However, it should be noted that the lifetimes of U(VI) species in solid C-S-H phases are influenced by sample preparation, C/S ratio, moisture of the sample, and presence of quenchers. Thus, a species identification based on the lifetime is only reasonable to a limited extent (Chisholm-Brause et al., 2004; Chisholm-Brause et al., 2001).

All in all, the analyses of the samples A-D by XRD and IR (Figure 7-1) as well as TGA/DSC and TRLFS (Figure 7-2) are entirely consistent with the formation of tobermorite-like C-S-H phases with the co-existence of 18 mass-% portlandite for sample C.

The U(VI) in samples A-C is predominantly incorporated into the interlayer structure of C-S-H gel and to a much smaller degree sorbed on the C-S-H gel surface.

7.2.2. Leaching of U(VI) doped C-S-H phases

7.2.2.1. Leaching in water, 2.5 M NaCl and 2.5 M NaCl/0.02 M Na_2SO_4

The contact of samples A-C with a 2.5 M NaCl leaching solution leads to a Ca concentration in solution of about 1.0–6.6 mM (Figure 7-3, Table 7-5). Consequently, the pH value of the leaching solution increased from 7 to 11.7–12.2.

Hill et al. (2006), who monitored the Ca release from radionuclide-free C-S-H phases into 0 to 1 M NaCl solutions over 1 month ([Ca]: 2–29 mM leached, C/S: 1.0–2.0, S/L: 10–77 g/L), showed that the presence of 1 M NaCl increased the amount of Ca leached from C-S-H phases compared to pure water. The authors suggested an ion exchange mechanism between Na and Ca which increased the Ca release from C-S-H phases in the presence of 1 M NaCl. They also found a good agreement of the Ca release from portlandite and C-S-H phases with a high C/S ratio in 1 M NaCl.

Compared to this study, the results of the present study show a lower Ca mobilization into solution which is attributed to the lower S/L ratios (1.2 to 2.3 g/L) and salting in/salting out effects that have an impact on the Ca solubility. To study the C-S-H solubility behavior at low S/L ratios, sample E (C/S 1.35) was exposed to salt solutions between 0 and 2.5 M NaCl at a S/L ratio of 1.5 g/L over 7 d. Between 0 and 1.5 M NaCl, an increase of the Ca release from 1.1 mM towards 2.7 mM (Figure 7-3, r.) was observed. At higher NaCl concentrations, the Ca release stagnated around 2.7 mM. The Si release of sample E reached a maximum of 0.95 mM between 0.5 and 1 M NaCl (Figure 7-4, l.).

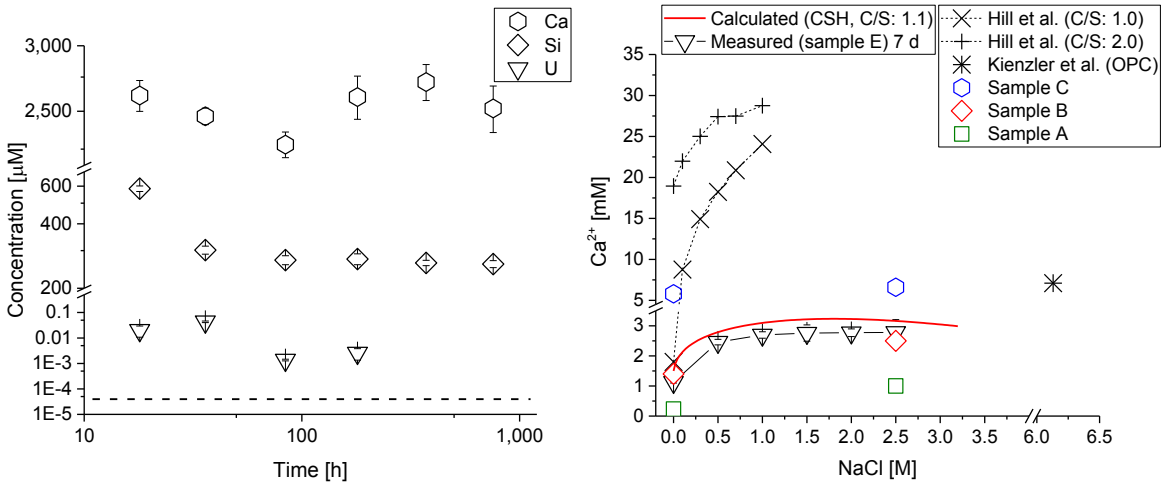

Figure 7-3: Calcium, silicon and uranium concentration in the supernatant solution after leaching of sample B in 2.5 M NaCl as a function of time (ICP-MS detection limit for U is 4.2×10^{-5} µM (dashed line)) (l.). Calculated solubility of a C-S-H phase with a C/S ratio of 1.1 in NaCl solutions between 0 and 3.2 M at a S/L ratio of 1.5 g/L (r.) (calculation cf. chapter 7.1.1). Measured calcium release from sample E (S/L 1.5 g/L) between 0 and 2.5 M NaCl and from samples C (S/L 2.3 g/L), B (S/L 1.5 g/L) and A (S/L 1.2 g/L) in water and 2.5 M NaCl in comparison to literature data of Hill et al. (2006) (S/L 50 g/L) and Kienzler et al. (2010) (OPC = ordinary Portland cement) (r.).

Leaching results of samples A–C in pure water were in good agreement with these observations and showed a lower release of Ca, especially at a low C/S ratio, compared to the leaching in 2.5 M NaCl (Figure 7-3, r.). Additionally, the Ca release from a C-S-H phase with a C/S ratio of 1.1 was calculated at a S/L ratio of 1.5 g/L for 0 to 3.2 M NaCl solutions (Figure 7-3, r.). The calculations showed an increase of the Ca release from the C-S-H phase up to a maximum at 1.5 M NaCl and a slight decrease at higher NaCl concentrations. This is in good agreement with the leaching results of samples B and E. Therefore, in terms of Ca release from C-S-H phases the effect of a 2.5 M NaCl solution is comparable to a 1 M NaCl solution.

The Si release of sample B into the 2.5 M NaCl solution amounts to 2.1% of total Si (0.26 mM) after 768 h (Figure 7-3, l.). Please note that due to the release of Ca and Si from the C-S-H phases, the final C/S ratios of the C-S-H samples after leaching are decreased in dependence on the initial C/S ratios and the composition of the leaching solutions (cf. Table 7-5). To ease the recognition of the various samples, however, C/S ratios before leaching will be used in the following text. Generally, an increased Ca and Si release from concrete at higher ionic strength would be equivalent to a faster chemical degradation of HCP in a nuclear waste repository.

Only 2.7% (4.3×10^{-2} μM) of the total U(VI) of sample B was released in the first 36 h of leaching (Figure 7-3, l.). After 186 h, the U(VI) concentration decreased below the ICP-MS detection limit of 4.2×10^{-5} μM, indicating a reincorporation of U(VI) into the C-S-H phases or into a secondary phase formed.

Kienzler et al. (2016) investigated the U(VI) release from U(VI)-containing cementitious material prisms submerged in highly saline salt solutions (5.98 M NaCl, 0.02 M $CaSO_4$, 0.02 M $MgSO_4$) over 32 years and observed an increase of uranium concentrations from 2×10^{-3} μM towards 5×10^{-1} μM over that time period. Despite the differences in solution composition, mineral assemblages and S/L ratios, both experiments showed only small amounts of mobilized uranium due to the presence of saline solutions.

To clarify the U(VI) speciation for the leached solids in the present study, TRLFS was applied (Figure 7-4, r.). The spectrum of sample B leached in 2.5 M NaCl is broadened and shifted towards lower wavelengths indicating the presence of a uranophane-like phase with a maximum around 520.0 nm (Figure 7-4, r.). The presence of a diuranate-type U(VI) mineral would shift the maximum of the spectrum towards higher wavelengths around 552.5 nm (Tits et al., 2011) and was therefore excluded.

These findings correspond well with the observations of Kienzler et al. (2010) who characterized concrete drill dust after leaching by XRD, TRLFS and EXAFS and reported the presence of a uranophane-like phase.

Table 7-5: Calcium, silicon and uranium concentrations and pH values of supernatant solutions as well as C/S ratios determined after 768 h leaching of sample C (C/S 2.02, S/L 2.3 g/L), sample B (C/S 1.55, S/L 1.5 g/L) and sample A (C/S 0.99, S/L 1.2 g/L). Values in brackets give the percentage dissolution of the ions present in the respective samples.

	Leaching solutions				
	Water	*2.5 M NaCl*	*2.5 M NaCl/ 0.02 M Na_2SO_4*	*2.5 M NaCl/ 0.02 M $NaHCO_3$*	*0.02 M $NaHCO_3$*
Ca [mM]					
Sample C	5.8 (13.0)	6.6 (14.8)	7.4 (16.6)	0.21 (0.5)	0.034 (0.1)
Sample B	1.4 (7.5)	2.5 (13.4)	2.4 (12.8)	0.16 (0.9)	0.062 (0.3)
Sample A	0.23 (2.4)	1.0 (10.3)	1.9 (19.6)	0.18 (1.9)	0.17 (1.8)
Si [mM]					
Sample C	0.029 (0.1)	0.11 (0.5)	0.068 (0.3)	3.8 (17.1)	5.3 (23.9)
Sample B	0.13 (1.1)	0.26 (2.1)	0.26 (2.1)	2.4 (19.8)	8.4 (69.4)
Sample A	0.48 (4.9)	0.64 (6.5)	0.48 (4.9)	2.6 (26.5)	8.6 (87.8)
U [μM]					
Sample C	7.8×10^{-4}	$< 4.2\times10^{-5}$	$< 4.2\times10^{-5}$	0.16 (4.6)	0.022 (0.6)
Sample B	8.7×10^{-4}	$< 4.2\times10^{-5}$	$< 4.2\times10^{-5}$	0.20 (12.5)	0.64 (40.0)
Sample A	1.1×10^{-3}	$< 4.2\times10^{-5}$	$< 4.2\times10^{-5}$	0.18(16.4)	0.24 (21.8)
pH					
Sample C	12.0	12.2	12.0	10.4	10.3
Sample B	11.7	11.9	11.7	10.1	9.6
Sample A	11.4	11.7	11.5	9.9	9.3
C/S ratio after leaching					
Sample C	1.75	1.57	1.69	–	–
Sample B	1.45	1.37	1.38	–	–
Sample A	1.01	0.96	0.84	–	–

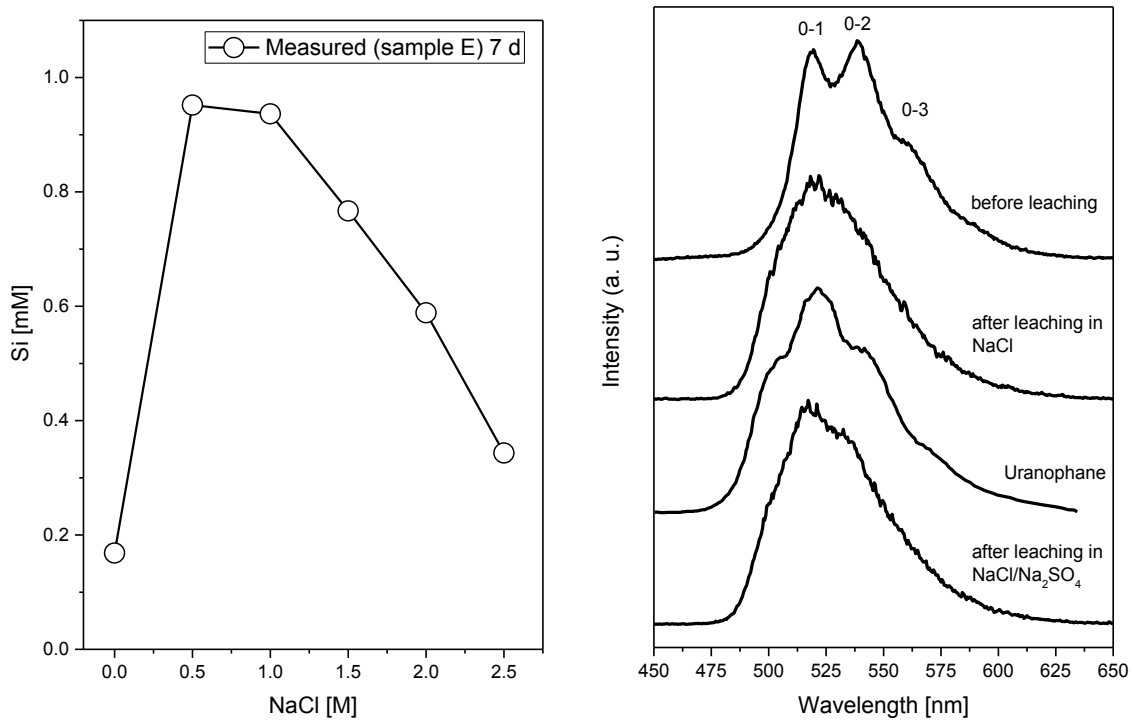

Figure 7-4: Measured silicon release from sample E (C/S 1.35, S/L 1.5 g/L) between 0 and 2.5 M NaCl (l.). TRLFS spectra of sample B (C/S 1.55) before and after 768 h of contact with different leaching solutions (2.5 M NaCl, 2.5 M NaCl/0.02 M Na_2SO_4) in comparison to the spectrum of uranophane (Kienzler et al., 2010)(r.).

The IR spectrum of sample B leached in 2.5 M NaCl shows a decrease of band resolution due to a reduction of the C/S ratio and crystallinity due to leaching (Figure 7-5). The Si–OH vibration at 960 cm^{-1} was not shifted which indicates that the silanol (Si-OH) groups with bridging tetrahedra of the C-S-H structure remained intact after leaching in 2.5 M NaCl.

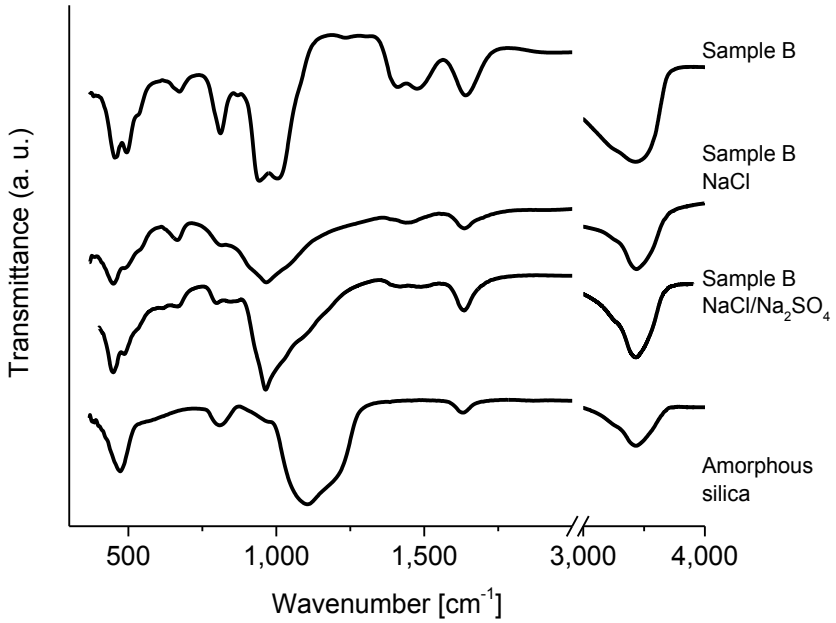

Figure 7-5: IR spectra of sample B (C/S 1.55) before and after 768 h of contact with different leaching solutions (2.5 M NaCl, 2.5 M NaCl/0.02 M Na_2SO_4) in comparison to the spectrum of amorphous silica (AEROSIL 300).

In summary, due to increased ionic strength (2.5 M NaCl) the Ca and Si release from C-S-H phases increased compared to pure water while the U(VI) environment partially changed from C-S-H towards a uranophane-like phase. Nonetheless, the structure of the C-S-H phase remained mostly stable and almost no U(VI) was released into the aqueous phase.

With regard to safety assessment of HCP barriers in deep geological waste disposals for actinides, after contact with about 2.5 M NaCl solutions, a uranophane-like phase becomes the mobility controlling phase for U(VI) on the HCP suface.

The Ca, Si and U release of sample B in 2.5 M NaCl/0.02 M Na_2SO_4 after 768 h was similar to the Ca, Si and U release in 2.5 M NaCl (Table 7-5). Moreover, TRLFS and IR investigations of U(VI) doped C-S-H phases leached in 2.5 M NaCl/0.02 M Na_2SO_4 show no further changes compared to the leaching in 2.5 M NaCl (Figure 7-4 (r.), Figure 7-5). Conclusively, 0.02 M Na_2SO_4 does not have any negative effects on C-S-H stability or U(VI) retention by C-S-H phases.

7.2.2.2. Leaching in 0.02 M $NaHCO_3$ and 2.5 M NaCl/0.02 M $NaHCO_3$

The presence of carbonate increased the amount of leached Si for samples A-C to 17.1-26.5% (2.4−3.8 mM) in 2.5 M NaCl/0.02 M $NaHCO_3$ and to 23.9-87.8% (5.3−8.6 mM) in 0.02 M $NaHCO_3$ (Table 7-5, Figure 7-6, l.). Thus, for all samples a partial destabilization of the silicate chains of the C-S-H structure leading to the formation of SiO_2(am) can be assumed. This was confirmed by IR spectroscopy due to the appearance of a shoulder at 1,234 cm^{-1} which is also present in the IR spectrum of SiO_2(am) (Figure 7-6, r.). For sample C leached in carbonate-containing solutions, the SiO_2(am) band was only weakly pronounced (Figure 7-6, r.), suggesting that a part of the $NaHCO_3$ preferentially reacted with portlandite, consequently, less SiO_2(am) was formed. However, the IR spectrum of sample C leached in 2.5 M NaCl/0.02 M $NaHCO_3$ shows a distinct carbonate band around 1,400 cm^{-1} (Figure 7-6, r.) that probably belongs to calcite (Sato and Matsuda, 1969) formed by reaction of portlandite and carbonate. In contrast, only a weak carbonate band around 1,400 cm^{-1} is observed in the IR spectrum of sample B leached in 2.5 M NaCl/0.02 M $NaHCO_3$, indicating a low amount of solid $CaCO_3$. This implies that, compared to $Ca(OH)_2$, a C-S-H phase reacts slower with carbonate while the $CaCO_3$ solubility is increased at lower pH values (10.4 vs. 10.1, Table 7-5).

Compared to carbonate-free leaching experiments, the leaching of sample B in 2.5 M NaCl/0.02 M $NaHCO_3$ causes a lower Ca concentration (0.9%, 0.16 mM) as well as a lower pH (10.1) in the leaching solution (Table 7-5, Figure 7-6, l.). Under carbonate-free conditions, the pH in a concrete system is buffered by dissolved $Ca(OH)_2$. In the presence of HCO_3^-, the precipitation of $CaCO_3$ removes Ca^{2+} and OH^- from the solution, thus, lowering the pH and Ca concentrations compared to carbonate-free solutions. Final C/S ratios of leached samples

were not determined since the Ca contents of U(VI) doped C-S-H phases after leaching are distributed between C-S-H and $CaCO_3$.

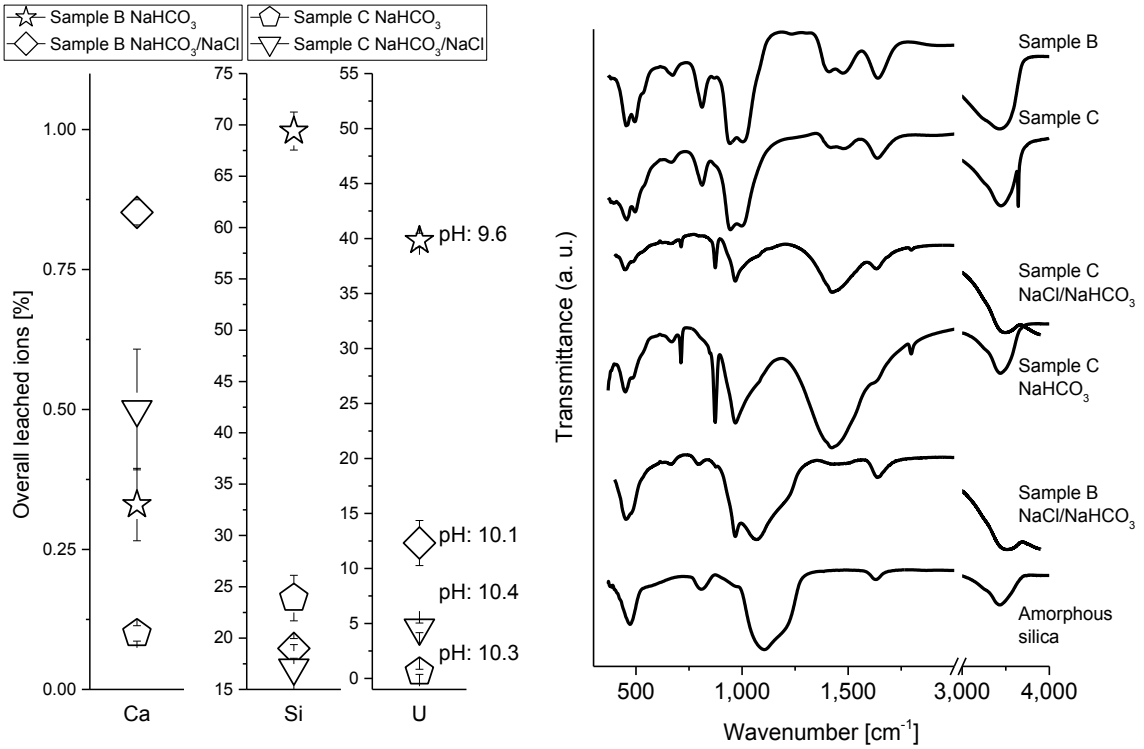

Figure 7-6: Percentage amount of leached calcium, silicon and uranium with corresponding pH values after leaching of sample B (C/S 1.55) and sample C (C/S 2.02) in 0.02 M $NaHCO_3$ or 2.5 M NaCl/0.02 M $NaHCO_3$ for 768 h (l.). IR spectra of sample B (C/S 1.55) before and after 768 h of contact with 2.5 M NaCl/0.02 M $NaHCO_3$ and sample C (C/S 2.02) before and after 768 h of contact with 2.5 M NaCl/0.02 M $NaHCO_3$ and 0.02 M $NaHCO_3$ in comparison to the spectrum of amorphous silica (AEROSIL 300) (r.).

The U(VI) release of sample B due to leaching in 2.5 M NaCl/0.02 M $NaHCO_3$ is strongly increased to 12.5% (0.2 μM, pH 10.1) of the overall U(VI) (rhombus in Figure 7-6, l., Table 7-5). This effect is even more distinct in the absence of 2.5 M NaCl where the 0.02 M $NaHCO_3$ leaching solution mobilizes 40% of the U(VI) of sample B (star in Figure 7-6, l., Table 7-5). In contrast, sample C shows a lower amount of released U(VI) of 4.6% (0.16 μM, pH 10.4) in 2.5 M NaCl/0.02 M $NaHCO_3$ and 0.6% in 0.02 M $NaHCO_3$ (triangle/pentagon in Figure 7-6, l., Table 7-5). These results are a clear indication for an increased U(VI) mobility in the presence of carbonate and a reduction of the pH which influences the U(VI) speciation in the leaching solution.

Under hyperalkaline (pH > 12) conditions, U(VI) hydroxide complexes such as $UO_2(OH)_4^{2-}$ or $UO_2(OH)_3^-$ dominate U(VI) speciation and solubility (Torrents, 2014), whereas at lower pH (8 < pH < 10.6) soluble uranyl carbonate complexes (e.g., $UO_2(CO_3)_3^{4-}$) can occur in carbonate-containing aqueous systems (Wang et al., 2004). In the presence of 0.034-0.21 mM Ca, determined in solution in the current study, ternary calcium uranyl carbonate complexes, $Ca_2UO_2(CO_3)_3(aq)$ and $CaUO_2(CO_3)_3^{2-}$, would likely form (Bernhard et al., 2001). These

ternary species impede the U(VI) sorption onto solids as shown, for instance, for ferrihydrite and quartz (Fox et al., 2006), clay (Joseph et al., 2013) and granite (Schmeide et al., 2014).

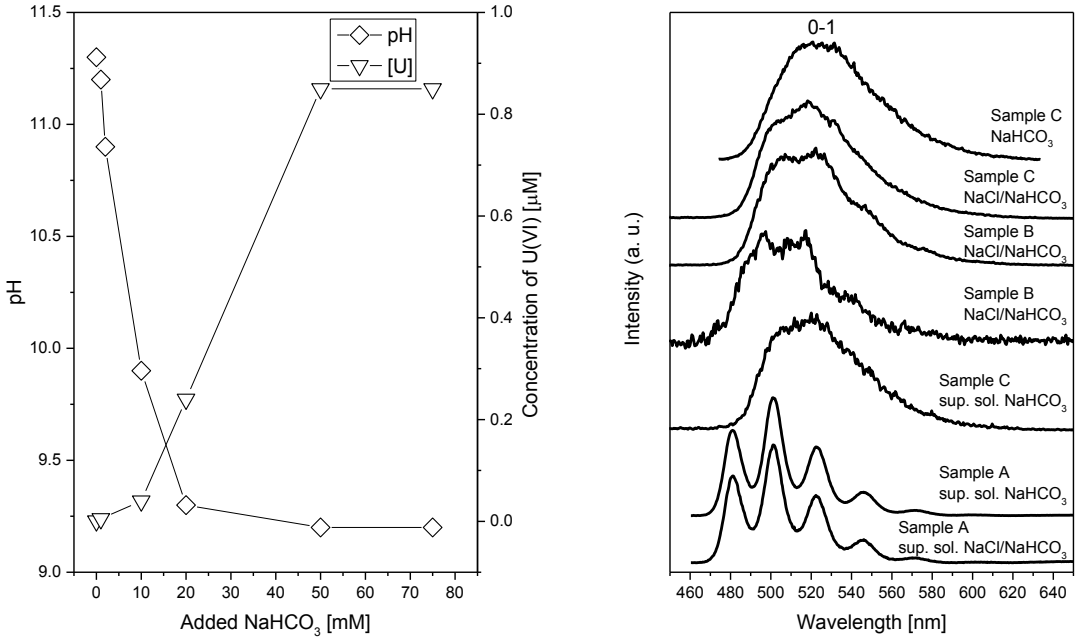

Figure 7-7: Evolution of pH value and U concentration of the supernatant solution of sample A as function of added $NaHCO_3$ (768 h leaching, S/L 1.2 g/L) (l.). TRLFS spectra of sample C leached in 0.02 M $NaHCO_3$, sample C leached in 2.5 M NaCl/0.02 M $NaHCO_3$, sample B leached in 2.5 M NaCl/0.02 M $NaHCO_3$, sample B leached in 2.5 M NaCl/0.075 M $NaHCO_3$, supernatant solution of sample C leached in 0.02 M $NaHCO_3$, supernatant solution of sample A leached in 0.1 M $NaHCO_3$, supernatant solution of sample A leached in 2.5 M NaCl/0.075 M $NaHCO_3$ (768 h leaching) (r.).

To investigate U(VI) speciation changes in the leaching solution from $UO_2(OH)_4^{2-}$ or $UO_2(OH)_3^-$ towards aqueous calcium uranyl tricarbonate in dependence on pH and amount of $NaHCO_3$, a leaching series of sample A in solutions containing up to 75 mM $NaHCO_3$ was performed (Figure 7-7, l.). The leaching solutions of sample A show a non-linear decrease of the pH value coupled with increasing amounts of released U in dependence on the $NaHCO_3$ contents. TRLFS investigations confirmed the predominance of aqueous calcium uranyl tricarbonate (Figure 7-7, r.) for $NaHCO_3$ concentrations ≥ 75 mM which corresponds to pH 9.3. This complex possessed well-defined emission bands at 480.7, 500.9, 522.0 and 545.0 nm and a lifetime of 750 μs (at 153 K) similar to the data reported by Wang et al. (2004) (cf. Table 7-6). This complex was also observed in the presence of 2.5 M NaCl when the pH and carbonate content were similar (Figure 7-7, r.).

Speciation calculations performed for the composition determined in the supernatant solution of sample B after leaching in 2.5 M NaCl/0.02 M $NaHCO_3$ ([Ca]: 0.159 mM, [Si]: 2.4 mM, [U]: 0.2 μM, [carbonate]: 14 mM, pH: 10.1), supported the formation of aqueous calcium uranyl tricarbonate complexes.

Table 7-6: Band positions and lifetimes of U(VI) species in relevant reference systems.

Type	Band maxima [nm] 0-0; 0-1; 0-2; 0-3	$\tau \pm 2\sigma$ [µs]
$Ca_2UO_2(CO_3)_{3(aq)}$, present work	480.7, 500.9, 522.0, 545.0	750 ± 24 (153 K)
$Ca_2UO_2(CO_3)_{3(aq)}$ (Wang et al., 2004)	480.5, 501.2, 522.7, 546.0	1282 (6 K)
$Ca_2UO_2(CO_3)_{3(aq)}$ (Bernhard et al., 2001)	467.0, 484.0, 504.0, 524.0	0.036 (298 K)
U-rich natural calcite (Wang et al., 2005b)	481.0, 500.0, 520.9, 543.7	339 (6 K)

At higher pH values, the high concentration of OH^- suppresses the formation of calcium uranyl tricarbonate, and spectra with low intensities and without any band resolution are detected (sample C sup. sol. $NaHCO_3$, Figure 7-7, r.).

Nonetheless, further factors such as formation of secondary $CaCO_3$ phases like calcite, vaterite and aragonite and their solubility in dependence on ionic strength may also influence the U(VI) mobility due to sorption of U(VI) on these $CaCO_3$ polymorphs. To investigate the influence of the secondary phase formation, TRLFS spectra of leached samples A-C were recorded. The TRLFS spectra of sample B leached in 2.5 M NaCl/0.02 M $NaHCO_3$ or 2.5 M NaCl/0.075 M $NaHCO_3$ (Figure 7-7, r.) show a shift of the 0-1 band towards lower wavelengths from 517.1 nm to 505.5 nm and 494.2 nm, respectively. These shifts towards lower wavelengths can be explained by an increased amount of U(VI) sorbed or incorporated in calcite formed as secondary phase as reported in the literature (Elzinga et al., 2004; Geipel et al., 1997; Smith et al., 2015).

TRLFS investigations of a natural U(VI)-containing calcite showed 0-0 and 0-1 bands at 481.0 and 500.0 nm, respectively (Wang et al., 2005b). Since the leached samples contain a mixture of U(VI) sorbed on calcite and U(VI) remaining in the C-S-H phase, the recorded spectra after leaching in carbonate-containing solutions are caused by an overlap of both U(VI) coordination environments.

The phase identification with the PDXL-2 program of the XRD patterns of sample C and A leached in 2.5 M NaCl/0.02 M $NaHCO_3$ (Figure 7-8[a, b]) show, that U(VI) doped C-S-H phases and portlandite are partly converted to $CaCO_3$ whereby exclusively calcite was detected.

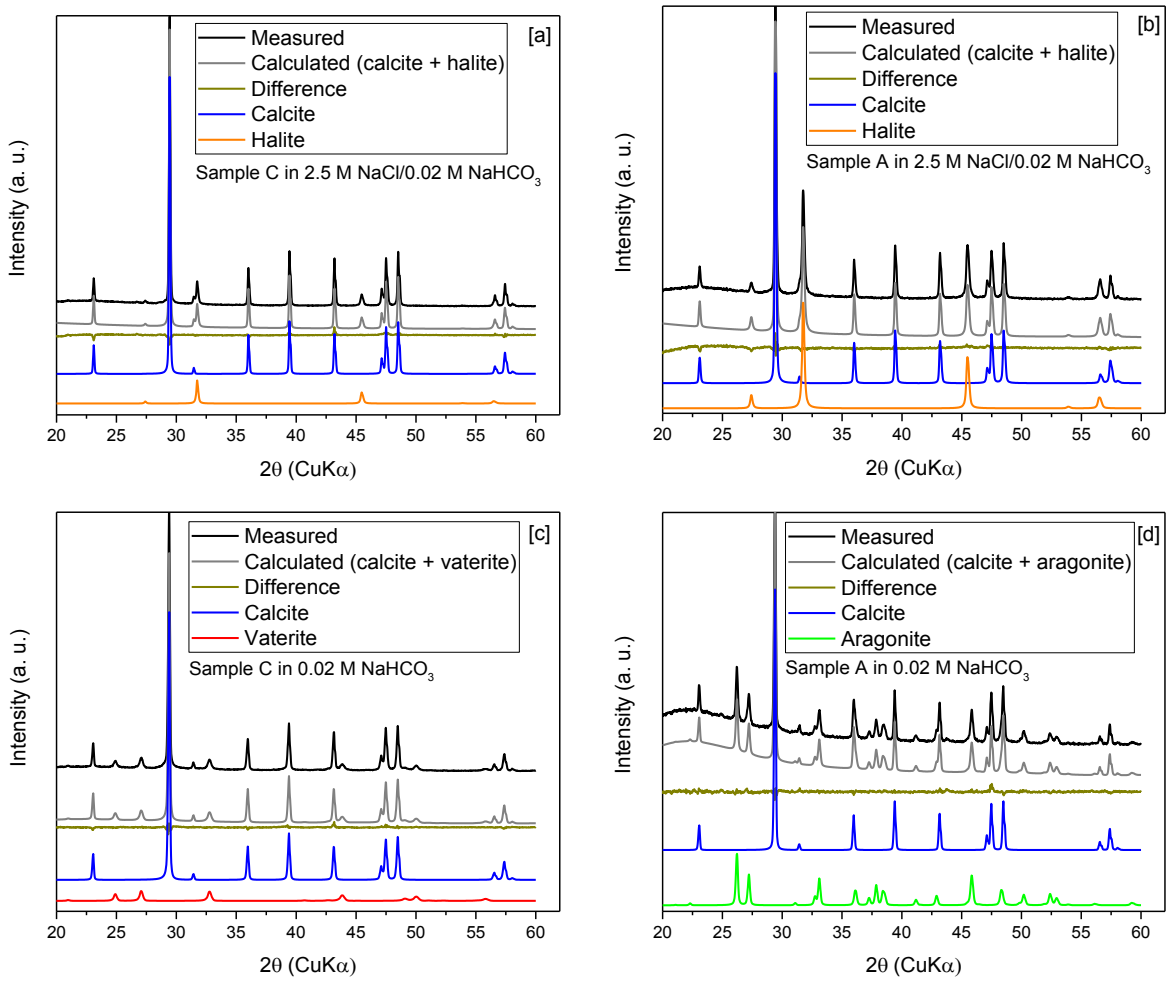

Figure 7-8: Powder XRD patterns of sample C (C/S 2.02) after leaching in 2.5 M NaCl/0.02 M $NaHCO_3$ [a] and 0.02 M $NaHCO_3$ [c] (768 h leaching), and sample A (C/S 0.99) after leaching in 2.5 M NaCl/0.02 M $NaHCO_3$ [b] and 0.02 M $NaHCO_3$ [d] (768 h leaching), calcite (database card number 01-083-4601), halite (database card number 00-005-0628), vaterite (database card number 04-017-8634), aragonite (database card number 01-075-9985), (Cu Kα X-ray source).

XRD patterns of samples C and A leached in 0.02 M $NaHCO_3$ but absence of NaCl (Figure 7-8[c, d]) also suggest that these samples are partly converted into secondary $CaCO_3$ phases: A part of sample A is converted into 70% calcite and 30% metastable aragonite while sample C, that consists of U(VI) doped C-S-H phases and portlandite, is partly converted into 80% calcite and 20% metastable vaterite. A comparison with data from Black et al. (2007), who investigated carbonation effects in mechanochemically prepared C-S-H phases with C/S ratios between 0.2 and 1.5 under ambient conditions, revealed the occurrence of predominantly vaterite for samples with C/S ratios ≥0.67 while in C-S-H samples with C/S ratios ≤0.5 mainly aragonite was detected. Although this trend is similar to that of the present study, the absence of calcite and the lower C/S boundary for the vaterite formation confirm differences between both studies. This can probably be attributed to different preparation methods and carbonation techniques of both studies. Further studies where similar cementitious systems were exposed to carbonate detected either the simultaneous presence of calcite, vaterite and aragonite (Chang and Fang, 2015; Ibanez et al., 2007) or a reversed trend where aragonite was observed at higher and vaterite at lower C/S ratios (Auroy et al., 2018).

These findings suggest that the formation of the various $CaCO_3$ modifications depends on the cement system and the carbonation method. The results of the present study also suggest that high amounts of NaCl suppress the formation of metastable $CaCO_3$ modifications such as vaterite and aragonite. This is tentatively attributed to an increased recrystallization rate of these phases as suggested by Takita et al. (2007).

TRLFS investigations of sample C leached in exclusively 0.02 M $NaHCO_3$ showed a broad spectrum without any band resolution that is less blue-shifted than the spectrum of sample B leached in 0.02 M $NaHCO_3$ (Figure 7-7, r.). Due to the higher amount of portlandite in sample C, combined with the higher solubility of portlandite compared to C-S-H, most of the carbonate is precipitated as calcite and vaterite (Figure 7-8[c]). Thus, the amount of carbonate in solution, which could contribute to a decomposition of the U(VI) doped C-S-H structure, is reduced. Simultaneously, a higher pH value in solution after $CaCO_3$ precipitation is maintained. Since portlandite does not contain U(VI) its dissolution does not contribute to a U(VI) mobilization. Calcite, however, acts as a U(VI) sink as implied by the TRLFS investigations (Figure 7-7, r.). Compared to metastable $CaCO_3$ phases like vaterite, better U(VI) retention properties were reported for calcite (Noubactep et al., 2006).

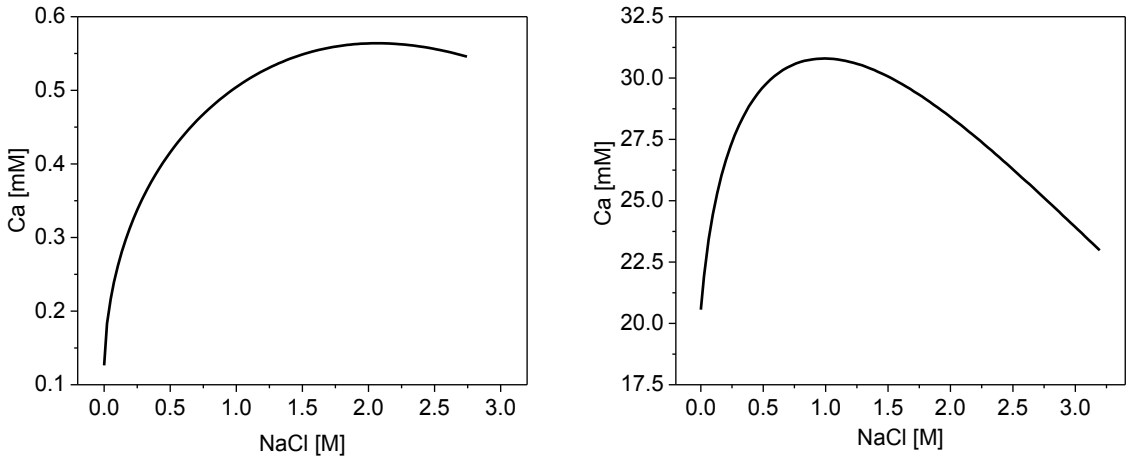

Figure 7-9: Calculated solubilities of calcite in 0–2.75 M NaCl solutions at pH 10 (l.) and of portlandite in 0–3.2 M NaCl solutions (r.). Details of calculations are given in chapter 7.1.1.

Compared to the leaching of sample C in 0.02 M $NaHCO_3$ solution, the additional presence of 2.5 M NaCl increased the amounts of released U(VI) and Ca from 0.6 to 4.6% and from 0.1 to 0.5%, respectively (pentagon/triangle, Figure 7-6, l.), although the pH values were with 10.3 and 10.4 very similar. Solubility calculations showed that the calcite solubility increases with increasing NaCl concentrations between 0 and 2.5 M NaCl (Figure 7-9, l.). Also the solubility of portlandite increases between 0 and 1 M NaCl, but decreases afterwards (Figure 7-9, r.). If, in turn, less calcite precipitates, which also leads to somewhat higher Ca^{2+} and CO_3^{2-} concentrations in the supernatant, less U(VI) can be immobilized on the calcite surface. Thus, the formation of aqueous calcium uranyl tricarbonate is favored against the formation of U(VI) hydroxide complexes at a pH around 10.4.

8. Stability of Cm(III) doped C-S-H phases at high ionic strength conditions

8.1. Experimental

For material, device and technique descriptions see chapter 7.1.1.

8.1.1. Direct synthesis of Cm(III) doped C-S-H phases

For the synthesis of Cm(III) doped C-S-H phases, 3.6 mL of a 4×10^{-6} M Cm(III) stock solution and 1.4 mL of deionized water were added in 15 mL centrifuge tubes (polypropylene, Greiner bio-one, Kremsmünster, Austria) to 120 mg of a mixture of carbonate-free CaO and fumed silica, resulting in an initial Cm(III) concentration of 2.88×10^{-6} M. The ratios of CaO and fumed silica were varied according to the targeted C/S ratios 1.0 and 2.0 (sample M and N, Table 8-1). Immediately, the suspensions were homogenized and carbonate-free NaOH was added to achieve a NaOH concentration of 0.294 M. After 14 d of shaking the samples end-over-end, the phases of the suspensions were separated via centrifugation at 3,059×*g* for 1 h (EBA 280, Hettich Lab Technology, Tuttlingen, Germany). Then, the supernatant solutions were analyzed for Cm(III) with LSC. The synthesized Cm(III) doped C-S-H samples were stored as wet pastes.

8.1.2. Batch leaching of Cm(III) doped C-S-H phases

Wet pastes of Cm(III) doped samples were equilibrated in 0.02 M $NaHCO_3$ or in 2.5 M NaCl/0.02 M $NaHCO_3$ at a S/L ratio of 10 g/L by shaking the samples end-over-end for 14 or 60 d. Then, the phases of the suspensions were separated by centrifugation at 3,059×*g* for 1 h. Each supernatant solution was analyzed for Cm(III) concentration with LSC and final pH values were determined. Leached C-S-H samples were stored as wet pastes for TRLFS investigations. All leaching experiments were performed as duplicates.

8.2. Results and discussion

8.2.1. Composition of Cm(III) doped C-S-H phases

*Table 8-1: Amount of Cm(III) incorporated into C-S-H phases in dependence on C/S ratios. * Determined with Eu(III) after centrifugation at 40,000×g.*

Sample	C/S	Cm(III) [%]	Cm(III) [ppm]	Cm(III) [mol/kg]	log(R_d) [log(L/kg)]
M	1.0	98.5	28.5	1.15×10^{-4}	3.4/6.2*
N	2.0	97.1	28.1	1.13×10^{-4}	3.1/6.2*

The exposure of CaO and fumed silica to the alkaline Cm(III) solution led to the formation of C-S-H phases having C/S ratios of 1.0 and 2.0 and a Cm(III) uptake of 98.5 and 97.1% into the solid C-S-H phases. This corresponds to log(R_d) values of 3.4 and 3.1 (Table 8-1).

As observed for the U(VI) uptake by C-S-H, the log(R_d) values resulting from the Cm(III) uptake in C-S-H are low compared to literature (Häußler et al. (2018): log(R_d) value of 5.6 for the sorption of Am(III) on C-S-H, Pointeau et al. (2001) and Tits et al. (2003): log(R_d) 4.4−5.7 for Eu(III) sorbed on C-S-H phases). Similar as discussed in chapter 7.2.1 the low log(R_d) values may be caused by a strong sorption of Cm(III) on the C-S-H phase and a possible incomplete phase separation during centrifugation at 3,059×*g*, resulting in the presence of colloids in the supernatant. To verify this assumption, Eu(III) doped C-S-H phases with C/S ratios of 1.0 and 2.0 were synthesized under conditions identical to the Cm(III) doped C-S-H phases. These samples were centrifuged at 40,000×*g* for 1 h. Subsequently, the supernatants were analyzed for Eu(III) with ICP-MS resulting in a log(R_d) value of 6.2 for both C/S ratios. This shows that the low log(R_d) values for Cm(III) in the present study were indeed caused by an incomplete phase separation.

Since the synthesis of Cm(III) doped C-S-H phases was performed under similar conditions and with similar C/S ratios compared to samples A and C, it is concluded that sample M (C/S 1.0) consists of C-S-H phases while sample N consists of C-S-H phases and 18 mass-% portlandite.

For the identification of Cm(III) species in the formed solids, site-selective TRLFS was applied. The luminescence spectra of samples M and N are compiled in Figure 8-1.

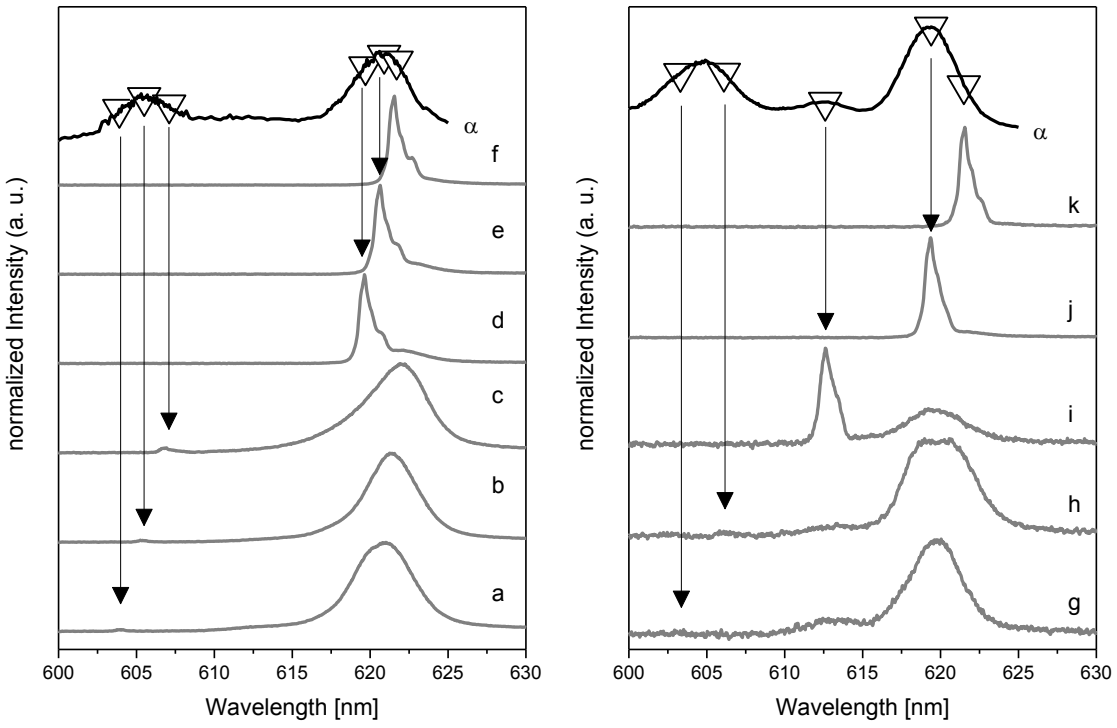

Figure 8-1: Excitation spectra (α, top black lines) of sample M (C/S 1.0, l.) and sample N (C/S 2.0, r.) and recorded emission spectra (a-k, gray lines) after excitation at different wavelengths: a (604.1 nm), b (605.5 nm), c (606.9 nm), d (619.6 nm), e (620.9 nm), f (621.5 nm), g (603.4 nm), h (606.1 nm), i (612.6 nm), j (619.3 nm), k (621.5 nm).

Sample M (C/S 1.0) provides a broad excitation spectrum with maxima at 605.5 and 620.9 nm (Figure 8-1, l., α) which are in good agreement with results obtained in nonselective TRLFS studies at 10 K of the Cm(III) incorporation in the C-S-H structure by Tits et al. (2003). The authors identified a Cm(III) hot band in C-S-H at 606 nm and a main band around 620 nm that shifted with increasing delay time towards lower energies. A peak deconvolution of the main band was performed and two bands at 618.9 and 620.9 nm with lifetimes of (289 ± 11) μs and (1482 ± 200) μs, respectively, were identified. The twofold split main band was attributed to Cm(III) located in the C-S-H interlayer substituted against Ca^{2+} with 1.4 water molecules in the hydration sphere and Cm(III) incorporated in the polyhedral CaO plane of the C-S-H structure substituted against Ca^{2+} with a total loss of its hydration sphere.
In the present TRLFS study, the excitation of sample M (C/S 1.0) between 604.1 and 606.9 nm yields emission lines only in the region around 620.5 nm (Figure 8-1, l., a-c). This implies that the broad peak in the excitation spectrum around 605.5 nm (Figure 8-1, l., α) is a hot band of the main band transition ($^8S_{7/2} \rightarrow {}^6D_{7/2}$) and not a second non-equivalent Cm(III) species. The obtained emission spectra upon excitation in the hot band region (Figure 8-1, a-c) are rather broad and asymmetric, pointing towards the presence of more than one species.

After selectively exciting around 620 nm, multiple narrow emission spectra with two visible shoulders at slightly longer wavelengths (red-shifted) become visible (Figure 8-1, l., d-f). The magnitude of the red-shift of these two shoulders is 0.5 nm and 1.2 nm from the main peak, independent of the excitation wavelength used. Thus, these shoulders can be ascribed to a partially resolved splitting of the $^8S_{7/2}$ ground state. The shifting of the emission lines d-f with the applied excitation wavelength is known as luminescence line narrowing and is visualized in Figure 8-2.

For Cm^{3+}, line narrowing effects have been reported for Cm^{3+} incorporation in amorphous grain boundaries in bioapatite (Holliday et al., 2012) and for Cm^{3+} incorporation in $La_{1-x}Gd_xPO_4$ monazite solid solutions (Huittinen et al., 2018). In both studies the line narrowing was explained by a continuum of related environments arising from the lack of long-range order in the solid structure. Thus, in agreement with these studies, the observed emission line narrowing in the present study is assigned to variations of the local surrounding of the Cm(III) cation in the semi-crystalline C-S-H structure. A clear distinction between two different species cannot be made, but as already mentioned, indications for the presence of at least two species can be seen in the collected spectroscopic data. This can be confirmed by the averaged luminescence lifetimes of the hot and main band, which follow a bi-exponential decay with averaged lifetimes of (163 ± 111) μs which corresponds to 3.1 water or OH^- molecules in the first coordination sphere and (977 ± 51) μs equivalent to a total loss of the hydration sphere. The substantial error of 111 µs on the calculated lifetime of one species most probably originates from the low contribution of this species to the composite spectra. These lifetimes imply the presence of a Cm(III) species inside the C-S-H interlayer with 3.1 water or OH^- molecules in the first coordination sphere and Cm(III) incorporated into the polyhedral CaO

plane with a total loss of the hydration sphere as schematically illustrated in Figure 8-3. These results correspond to the findings of Tits et al. (2003).

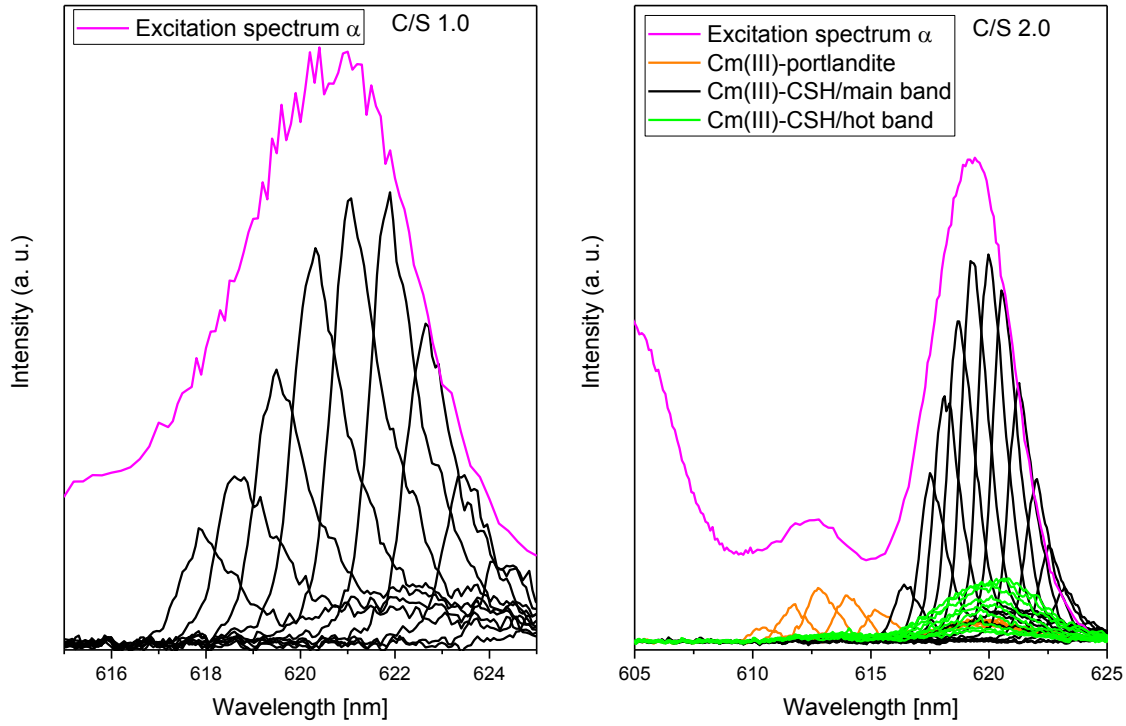

Figure 8-2: Excitation spectra with associated emission bands (100 accumulations) of sample M (C/S 1.0) (l.) and sample N (C/S 2.0) (r.). Emission bands due to direct excitation of the Cm(III)/C-S-H main band between 618 and 624 nm (l., black). Emission bands due to direct excitation of the Cm(III)/C-S-H hot band (r., 603-608 nm, green), Cm(III)/C-S-H main band (r., 618-624 nm, black) and Cm(III) sorbed on portlandite (r., 610-615 nm, orange).

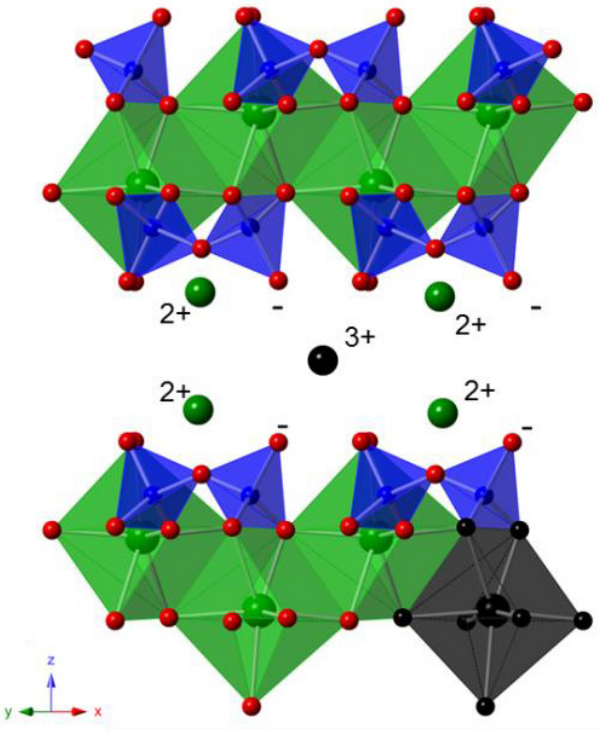

Figure 8-3: Assumed positions of Cm(III) in the crystal structure of calcium silicate hydrate (calcium (green), silicon (blue), oxygen (red), curium (black)).

The site-selective luminescence study of sample N (C/S 2.0) shows a similar excitation spectrum as recorded for sample M with the lower C/S ratio (Figure 8-1, r.). However, in addition to the hot band signal around 604.5 nm and the corresponding main band for Cm(III) associated with the C-S-H structure (~619 nm), a weak signal around 613 nm can be discerned in the excitation spectrum, which was not observed in sample M (C/S 1.0). Excitation at this peak maximum (612.6 nm) yields an emission signal with a shoulder on the red side (~613.5 nm) (Figure 8-1, r., i) and a lifetime of (155 ± 15) μs which corresponds to 3.3 water molecules in the Cm(III) coordination sphere. Please note that these emission lines are strongly red-shifted compared to emission lines of the Cm^{3+} aquo ion (593.8 nm) and the Cm(III) hydroxo complexes ($Cm(OH)^{2+}$ 598.7 nm (Moulin et al., 1992), $Cm(OH)_2^+$ 603.5 nm (Fanghänel et al., 1994), and $Cm(OH)_{3(aq)}$ 607.1 nm (Tits et al., 2003)) suggesting the formation of a Cm(III)/OH^- inner-sphere complex. As previously shown by XRD (Figure 7-1, l.) and TGA (Figure 7-2, l.) investigations, sample C (C/S 2.0) contains around 18 mass-% portlandite in addition to the C-S-H phase. Thus, the additional peak observed for sample N is assumed to arise from Cm(III) association with portlandite. TRLFS investigations of Cm(III) sorbed on HCP/portlandite by Stumpf et al. (2004) showed the formation of an inner-sphere Cm(III)/portlandite complex with an emission spectrum at 613.6 nm and a lifetime of (66 ± 1) μs which corresponds to 9 OH^- molecules in the first coordination sphere. The peak position corresponds well with that observed in the present study even though the lifetimes are different. This may be due to the different experimental conditions employed in the two studies (here site-selective excitation of Cm(III) in a mixture of dried C-S-H and portlandite at 10 K in comparison to Cm(III) exposed to a portlandite suspension for 30 d excited with 395 nm at room temperature by Stumpf et al. (2004)). Thus, it is assumed that the amount of H_2O and OH^- in portlandite was higher in the study of Stumpf et al., which explains the longer lifetimes observed in the present study. Nonetheless, in agreement with the study by Stumpf et al. (2004) the signal at ~613 nm is assigned to a Cm(III) inner-sphere complex incorporated in the formed portlandite phase.

As already indicated for sample M (C/S 1.0), the emission spectra of sample N obtained after selective excitation in the hot band region, especially at λ_{ex} = 606.1 nm (Figure 8-1, r., h), shows a very asymmetric emission peak with two clear maxima, corroborating the presence of two non-equivalent Cm(III) species in the C-S-H structure. Furthermore, the lifetime decay analyses after excitation of the C-S-H hot- and main bands of this sample show a bi-exponential decay behavior with averaged lifetimes of (214 ± 28) μs and (928 ± 109) μs, corresponding to Cm(III) species with 2 and 0 water molecules, respectively, in the first coordination sphere of the actinide cation.

8.2.2. Leaching of Cm(III) doped C-S-H phases

8.2.2.1. Leaching in 0.02 M $NaHCO_3$ and 2.5 M NaCl/0.02 M $NaHCO_3$

The exposure of sample M (C/S 1.0) to solutions that contain either 0.02 M $NaHCO_3$ or 2.5 M NaCl/0.02 M $NaHCO_3$ over a time period of 14 or 60 d led to a negligible Cm(III) mobilization between 0.01 and 0.5% of the previously incorporated Cm(III) (Table 8-2).
Comparable leaching experiments performed with U(VI) doped C-S-H samples A-C showed a much higher U(VI) release (up to 40%) which was attributed to the formation of $Ca_2UO_2(CO_3)_3$ in solution at pH values ≤ 10.4. Since samples A-C were leached at lower S/L ratios (1.2−2.3 g/L) compared to samples M and N (10 g/L) the pH of the leaching solutions for sample M was higher (cf. Table 7-5 and Table 8-2). Thus, the formation of Cm(III) hydroxide complexes is favored against Cm(III) carbonate complexes. Furthermore, Cm(III) carbonate complexation studies performed in solutions containing 0 to 6 M NaCl by Fanghänel et al. (1999) indicated the presence of $Cm(CO_3)_n^{3-2n}$ complexes at pH < 10 and carbonate concentrations ≥ 10^{-4} M. A comparison of the stability constants at infinite dilution ($\log \beta^0$) reveals lower stability constants for $Cm(CO_3)_n^{3-2n}$ ($\log \beta^0_{101} = 8.1 \pm 0.3$, $\log \beta^0_{102} = 13.0 \pm 0.6$, $\log \beta^0_{103} = 15.2 \pm 0.4$, and $\log \beta^0_{104} = 13.0 \pm 0.5$ (Fanghänel et al., 1999)) compared to $Ca_2UO_2(CO_3)_3(aq)$ ($\log \beta^0_{213} = 30.45 \pm 0.35$ (Bernhard et al., 2001)). Therefore, comparable $NaHCO_3$ concentrations should lead to a stronger complexation of U(VI) by carbonate compared to Cm(III). Furthermore, differences in the S/L ratio and a higher pH after leaching contribute to the lower Cm(III) release compared to U(VI).

Table 8-2: Amount of Cm(III) leached from sample M (C/S 1.0) and final pH values of 0.02 M $NaHCO_3$ or 2.5 M NaCl/0.02 M $NaHCO_3$ leaching solutions.

Conditions	Cm(III) leached [M]	Cm(III) leached [%]	pH
$NaHCO_3$, 14 d	3.8×10^{-10}	0.014	10.9 ± 0.2
$NaHCO_3$, 60 d	2.4×10^{-9}	0.086	10.9 ± 0.1
NaCl/$NaHCO_3$, 14 d	2.2×10^{-10}	0.008	10.6 ± 0.3
NaCl/$NaHCO_3$, 60 d	1.4×10^{-8}	0.498	10.7 ± 0.3

To investigate the influence of the portlandite phase on the stability of the Cm(III) doped C-S-H system, sample N (C/S 2.0) was leached in either 0.02 M $NaHCO_3$ or 2.5 M NaCl/0.02 M $NaHCO_3$. Comparable to sample M, the leaching of sample N leads only to a very low Cm(III) release between 0.05 and 0.7% of the previously incorporated Cm(III) (Table 8-3).

To identify factors such as secondary phase formation that might be responsible for the low Cm(III) releases, site-selective TRLFS spectra of samples M and N were recorded and discussed in comparison to the XRD patterns of samples A (C/S 1.0) and C (C/S 2.0) after leaching in 0.02 M $NaHCO_3$ or 2.5 M NaCl/0.02 M $NaHCO_3$ (Figure 7-8[a-d]).

Table 8-3: Amount of Cm(III) leached from sample N (C/S 2.0) and final pH values of 0.02 M $NaHCO_3$ or 2.5 M NaCl/0.02 M $NaHCO_3$ leaching solutions.

Conditions	Cm(III) leached [M]	Cm(III) leached [%]	pH
$NaHCO_3$, 14 d	1.2×10^{-9}	0.045	12.1 ± 0.01
$NaHCO_3$, 60 d	2.0×10^{-9}	0.075	12.2 ± 0.01
NaCl/$NaHCO_3$, 14 d	4.6×10^{-9}	0.170	12.0 ± 0.01
NaCl/$NaHCO_3$, 60 d	2.0×10^{-8}	0.737	12.1 ± 0.01

The results of the XRD study revealed that a part of the C-S-H phase with a C/S ratio of 1.0 is converted into secondary $CaCO_3$ phases such as calcite (70%) and aragonite (30%) while the C-S-H phase with a C/S ratio of 2.0 is partly converted into an average of 80% calcite and 20% vaterite after leaching in 0.02 M $NaHCO_3$ (Figure 7-8[c, d]). The additional presence of 2.5 M NaCl led to the exclusive formation of calcite, independent of the C/S ratio (Figure 7-8[a, b]). At a S/L ratio of 10 g/L, a 0.02 M $NaHCO_3$ solution could convert a maximum of 23 mol-% of sample M and 18 mol-% of sample N into $CaCO_3$.

Despite the clear transformation of a part of the C-S-H structure into secondary phases, the very low Cm(III) release from C-S-H phases points towards either incongruent leaching of the samples, where Cm(III) remains in the C-S-H structure, or a Cm(III)-re-immobilization into the formed secondary $CaCO_3$ phases. To trace the association of Cm(III) in the solid mixtures, site-selective TRLFS analyses of the solids after leaching were performed.

The excitation spectrum of sample M (C/S 1.0) leached in 0.02 M $NaHCO_3$ for 14 d shows a new broad peak between 607.7 and 612.8 nm (Figure 8-4, l., α and γ) in addition to the Cm(III)/C-S-H hot and main bands at 606 and 620 nm, respectively (Figure 8-4, l., α and β).

After selective excitation in the region where the new Cm(III) species is detected, threefold split emission spectra (Figure 8-4, l., b, c) with lifetimes of (734 ± 55) μs are obtained which corresponds to a total loss of the hydration sphere. In order to assign the new Cm(III) species, the obtained data in terms of emission peak position and lifetime are compared to published data for Cm(III) association with the $CaCO_3$ polymorphs calcite, vaterite and aragonite (Table 8-4). Marques Fernandes et al. (2008) investigated the association of Cm(III) with calcite at a pH value of 12.5. At these solution conditions, the authors found a $Cm(OH)^{2+}$ species incorporated within the calcite structure with an emission band at 608.2 nm and a lifetime of (477 ± 25) μs. Other calcite species were reported with emission peak maxima at 606.2 nm and 620.3 nm (Marques Fernandes et al., 2008).

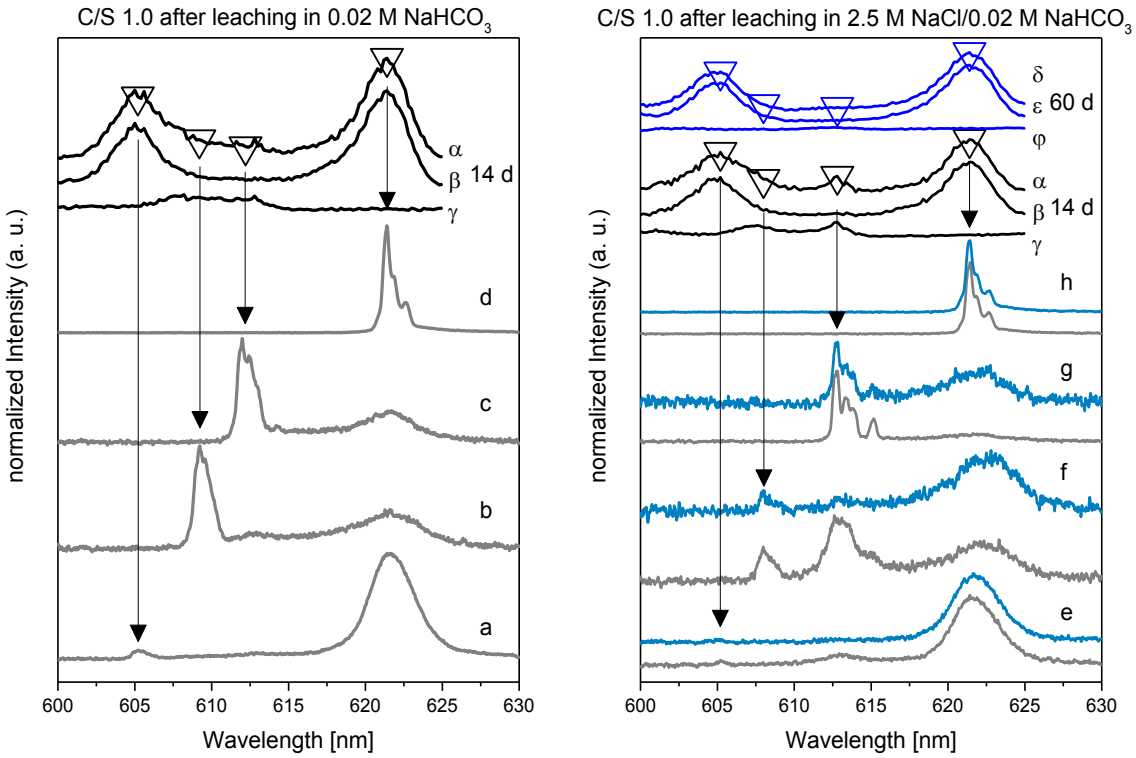

Figure 8-4: TRLFS spectra of sample M (C/S 1.0) after leaching in 0.02 M $NaHCO_3$ (l.) for 14 d and in 2.5 M NaCl/0.02 M $NaHCO_3$ (r.) for 14 d (gray lines) and 60 d (blue lines). α-γ: Excitation spectra after 14 d (black lines); δ-φ: Excitation spectra after 60 d (blue lines); α, δ: Integrated over the complete emission spectrum; β, ε: Integrated over the C-S-H main band (~615-625 nm); γ, φ: Integrated between the C-S-H hot and main band (~605-615 nm). Recorded emission spectra after excitation at different wavelengths: a (605.2 nm), b (609.2 nm), c (612.2 nm), d (621.4 nm), e (605.2 nm), f (608.0 nm), g (612.8 nm), h (621.4 nm).

These peak positions overlap with the hot and main band transitions of the Cm(III)/C-S-H species in the present study and thus, no assignment to Cm(III)/calcite species in this emission wavelength range can be made. Cm(III) incorporated in aragonite was found by Schmidt et al. (2009) to result in a main band transition at 612.7 nm, a corresponding hot band transition at 607.5 nm and a lifetime of (637 ± 77) μs (Table 8-4). Even though the signal obtained in the present study for the presumed Cm(III)/$CaCO_3$ species is very broad, the two local maxima at 607.7 nm and 612.8 nm can be distinguished in the excitation spectrum integrated between 605 and 615 nm (Figure 8-4, l., γ). Thus, it is likely that Cm(III) indeed is incorporated within the formed aragonite phase as a result of the C-S-H phase conversion. However, the broad nature of the excitation peak recorded in the present study implies that other sorption/incorporation processes may contribute to the Cm(III) speciation after leaching in 0.02 M $NaHCO_3$ solutions which cannot be conclusively assigned based on the recorded luminescence data.

Excitation spectra of sample M (C/S 1.0) leached for 14 and 60 d in 2.5 M NaCl/0.02 M $NaHCO_3$ are presented in Figure 8-4, r., as black lines α-γ and blue lines δ-φ, respectively. Although XRD confirmed the exclusive presence of calcite, TRLFS shows multiple low-intensity emission lines between 608.0 and 612.8 nm (Figure 8-4, r., f, g, gray lines).

Table 8-4: Band positions and lifetimes of Cm(III) species in system relevant phases.

Cm(III) species	Band position [nm]	$\tau \pm 2\sigma$ [µs]
Cm(III) surface sorbed on calcite, pH 8−12.5 (Marques Fernandes et al., 2008)	606.2	386 ± 40 (298 K)
$CmOH^{2+}$ incorporated in calcite, pH 12.5 (Marques Fernandes et al., 2008)	608.2	477 ± 25 (298 K)
Cm(III) incorporated in calcite, pH 8−12.5 (Marques Fernandes et al., 2008)	620.3	1874 ± 200 (298 K)
Cm(III) incorporated in vaterite (Schmidt et al., 2010)	612.1	1802 ± 216 (< 20 K)
	619.1	2569 ± 308 (< 20 K)
Cm(III) incorporated in aragonite (Schmidt et al., 2009)	607.5	637 ± 77 (< 20 K)
	612.7	637 ± 77 (< 20 K)
Cm(III) incorporated in portlandite ($Ca(OH)_2$) (Stumpf et al., 2004)	613.6	62 ± 8 (298 K)
Cm(III) in C-S-H interlayer (Tits et al., 2003)	618.9	289 ± 11 (10 K)
Cm(III) in C-S-H polyhedral CaO plane (Tits et al., 2003)	620.9	1482 ± 200 (10 K)

After excitation at 612.8 nm, a splitting of the emission line in four separated peaks is observed (Figure 8-4, r., g, gray line). This fourfold splitting was also observed by Schmidt et al. (2009) after excitation of Cm(III)-containing aragonite at 612.7 nm caused by a fourfold ground state splitting of the $^8S_{7/2}$ state. The decreased intensity of these emission lines after 60 d of leaching in 2.5 M NaCl/0.02 M $NaHCO_3$ (Figure 8-4, r., f, g, blue lines) at 608.0 and 612.8 nm indicates that these emission lines are caused by Cm(III) incorporation into aragonite that is probably present in amounts below the XRD detection limit. The aragonite phase is converted into calcite over time due to its metastable nature, thus, causing the decrease of the Cm(III)/aragonite emission lines. However as discussed above, due to the overlap of the signals of Cm(III) incorporated in calcite with those of Cm(III) in C-S-H, this species cannot be detected in the current system.

In contrast to the leached sample M (C/S 1.0), sample N (C/S 2.0) leached in 0.02 M $NaHCO_3$ shows no emission line between 608 and 609 nm (Figure 8-5, l., b), but a weak emission line around 612.0 nm (Figure 8-5, l., c). This emission line differs from the emission lines of Cm(III) incorporated into aragonite, observed for sample M (C/S 1.0) after leaching in 0.02 M $NaHCO_3$ (cf. Figure 8-4, b).

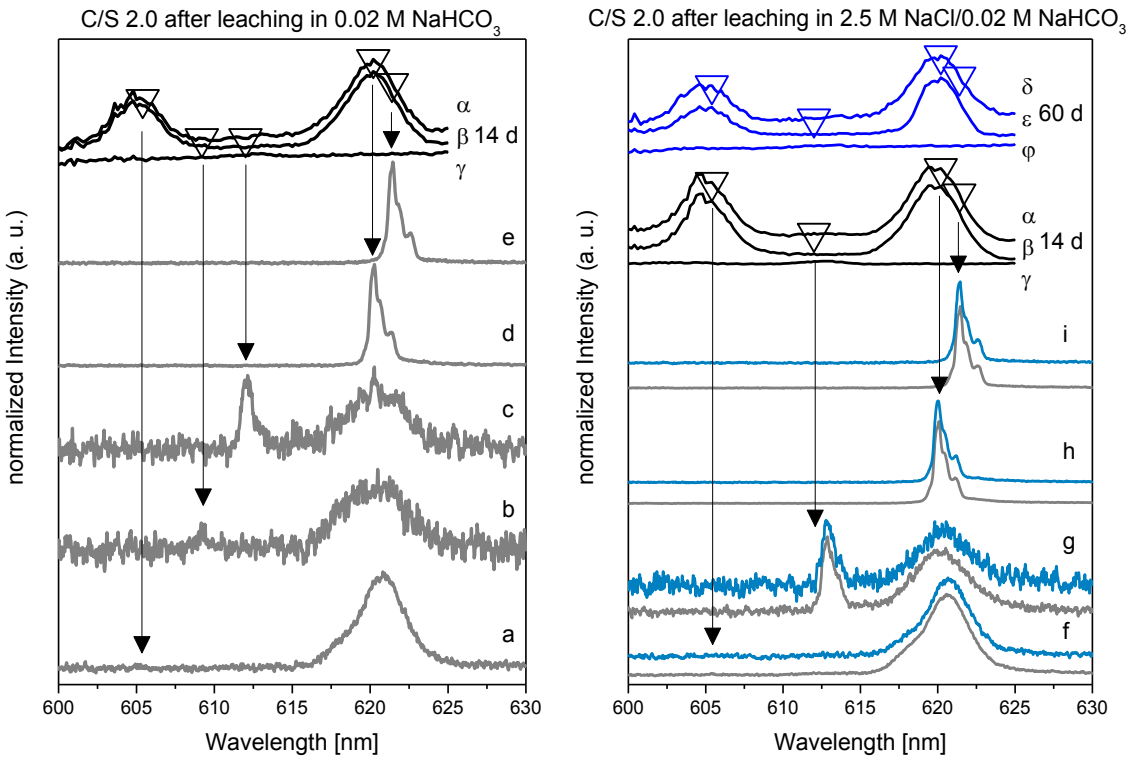

Figure 8-5: TRLFS spectra of sample N (C/S 2.0) after leaching in 0.02 M $NaHCO_3$ (l.) for 14 d and in 2.5 M NaCl/0.02 M $NaHCO_3$ (r.) for 14 d (gray lines) and 60 d (blue lines). α-γ: Excitation spectra after 14 d (black lines); δ-φ: Excitation spectra after 60 d (blue lines); α, δ: Integrated over the complete emission spectrum; β, ε: Integrated over the C-S-H main band (~615-625 nm); γ, φ: Integrated between the C-S-H hot and main band (~605-615 nm). Recorded emission spectra after excitation at different wavelengths: a (605.4 nm), b (609.2 nm), c (612.0 nm), d (620.2 nm), e (621.4 nm), f (605.4 nm), g (612.8 nm), h (620.0 nm), i (621.4 nm).

The new emission line at 612.0 nm is either caused by Cm(III) that is still incorporated into portlandite (612.6 and 613.5 nm, τ: 155 μs) or Cm(III) incorporated into the secondary phase vaterite (612.1 nm, τ: 1,802 μs (Schmidt et al., 2010)). Since the intensity of the emission line at 612.0 nm (Figure 8-5, l., c) is near the noise level after 5,000 accumulations, a lifetime analysis with the applied 100 accumulations was not feasible. Since Cm(III) incorporated into vaterite would possess a very long lifetime of 1,802 μs as observed by Schmidt et al. (2010), it is concluded that the band at 612.0 nm (Figure 8-5, l., c) is caused by Cm(III) remaining in portlandite. The excitation and emission spectra of sample N (C/S 2.0), recorded after 14 and 60 d of leaching in 2.5 M NaCl/0.02 M $NaHCO_3$, are shown in Figure 8-5 (r.). The presence of the emission line around 612.8 nm (Figure 8-5, r., g, gray line) that also possesses a low intensity and a rather short lifetime (τ: (312 ± 39) μs) indicates that this band is caused by Cm(III) incorporated in portlandite instead in metastable vaterite. Furthermore, the persistence of this emission line after 60 d of leaching (Figure 8-5, r., g, blue line) underlines this assumption.

Combined results of TRLFS and XRD investigations suggest that the majority of Cm(III) remains in the C-S-H and portlandite phases after leaching in saline carbonate-containing solutions. A minor incorporation or sorption of Cm(III) in calcite can neither be excluded nor verified due to the main band overlap of the Cm(III)/calcite and Cm(III)/C-S-H system.

9. Stability of U(VI) doped C-A-S-H phases at high ionic strength conditions

9.1. Experimental

For material, device and technique descriptions see chapter 7.1.1.

9.1.1. Synthesis of U(VI) doped C-A-S-H and Al-tobermorite

While the targeted molar aluminum-to-silicon (A/S) ratio was varied (0.05-0.16), the targeted molar calcium-to-silicon (C/S) ratio was fixed at 1.0. The S/L ratios were either 24 g/L for samples F-J or 31 g/L for samples K-L. An overview about the used amounts of CaO, SiO_2, Al compounds and water as well as the composition of the supernatant solution after synthesis can be found in Table 9-1 and Table 9-2, respectively.

Table 9-1: Overview of weighing for C-A-S-H samples.

Sample	CaO [mg]	SiO_2 [mg]	$Al(NO_3)_3 \cdot 9H_2O$ [mg]	Al_2O_3 [mg]	H_2O [ml]	C/S	A/S
F	224	240	–	24	20	1.00	0.051
G	398	426	137	–	40	1.00	0.059
H	398	426	137	–	40	1.00	0.059
J	398	426	137	–	40	1.00	0.059
K	199	213	216	–	20	1.00	0.16
L	199	213	216	–	20	1.00	0.16

9.1.1.1. Sample synthesis at room temperature

Sample G (Table 9-3 and Table 9-4) was prepared at room temperature by mixing water, carbonate-free CaO, fumed silica, and $Al(NO_3)_3 \cdot 9H_2O$ in 50 ml centrifuge tubes (polypropylene, Greiner bio-one, Kremsmünster, Austria). To the resulting suspensions carbonate-free NaOH was added to achieve a NaOH concentration of 0.294 M. Subsequently, the suspensions were shaken end-over-end for 14 or 120 d, centrifuged at 6,800×*g* and freeze-dried to remove the bulk water.

9.1.1.2. Sample synthesis under hydrothermal conditions

Samples F, J, K and L (Table 9-3 and Table 9-4) were synthesized under hydrothermal conditions. For this, water, carbonate-free CaO, fumed silica, Al_2O_3 or $Al(NO_3)_3 \cdot 9H_2O$ were mixed in Teflon lined hydrothermal synthesis autoclave reactors. To these suspensions carbonate-free NaOH was added to achieve a NaOH concentration of 0.294 M. Subsequently, the reactors were left in an oven at 200 °C for 3 d. After this time, the suspensions were transferred into centrifuge tubes, shaken end-over-end for further 14 or 120 d, centrifuged at 6,800×*g* for phase separation and freeze-dried to remove the bulk water.

Table 9-2: Composition of the supernatant solutions of C-A-S-H samples.

Sample	Ca [mg/L]	Si [mg/L]	Al [mg/L]	U [μg/L]
J	1.6	1360	9.2	5.9
K	10	6.9	79.4	< 0.5
L	2.2	15.4	19.8	64.2
G/U	33.4	2.4	1.3	< 0.5

9.1.1.3. U(VI) incorporation into C-A-S-H and Al-tobermorite

For a direct incorporation of U(VI) into samples H, J and L (Table 9-3 and Table 9-4) at room temperature or under hydrothermal conditions a 2.2×10^{-3} M $UO_2(NO_3)_2$ solution was added to the suspensions of carbonate-free CaO, fumed silica, $Al(NO_3)_3{\cdot}9H_2O$ and NaOH in water resulting in a U(VI) concentration of 15.0 μM U(VI). Subsequently, samples were treated as mentioned in chapters 9.1.1.1 and 9.1.1.2.

For the U(VI) sorption experiment, sample G was synthesized accordingly as aforementioned. The freeze-dried U(VI)-free sample G was than exposed to a $UO_2(NO_3)_2$ solution at a S/L ratio of 24 g/L which contained 15.0 μM U(VI) for 14 or 120 d (pH after 14 d: 11.8). Subsequently, the new sample G/U was then separated from the supernatant by centrifugation at 6,800×*g* and freeze-dried.

9.1.2. Batch leaching of U(VI) doped C-A-S-H and Al-tobermorite

For batch leaching experiments, freeze-dried samples J and L were equilibrated in 2.5 M NaCl or 2.5 M NaCl/0.02 M $NaHCO_3$ at a S/L ratio of 1.8 g/L by shaking the samples end-over-end for up to 35 d. After time intervals of 1, 4, 11 and 35 d samples were centrifuged at 6,800×*g* and the supernatant solutions were analyzed for Ca, Si, Al and U with ICP-MS as single determinations due to time reasons as well as for their pH values.

9.2. Results and discussion

9.2.1. Composition of U(VI) doped C-A-S-H and Al-tobermorite phases

An overview about synthesized samples in the calcium aluminate silicate hydrate (C-A-S-H) system is given in Table 9-3 and Table 9-4. Since the humidity in the samples can vary and is difficult to unify, C/S, A/S and U/S ratios are given in Table 9-3. These molar ratios are independent of the sample humidity since all elements present in one sample are diluted by an equal factor due to the bulk and gel water.

*Table 9-3: Overview of synthesized samples with respective Ca, Si, Al, and U contents, C/S, A/S and U/S ratios and log(R_d) values. *Samples are from chapter 7.2.1. **Determined after centrifugation at 40,000×g for 1 h.*

Sample	C/S	A/S	Ca [mmol/g]	Si [mmol/g]	Al [mmol/g]	U [nmol/g]	U/S ×10^6	log(R_d) [log(L/kg)]
A*	0.99	–	1.17	1.18	–	134	114	3.1/4.3**
E*	1.35	–	1.09	0.81	–	–	–	–
F	0.85	0.17	5.41	6.41	1.11	–	–	–
G	1.14	0.06	5.71	5.02	0.29	–	–	–
H	1.29	0.06	5.76	4.46	0.28	533.6	119.6	–
J	0.49	0.06	0.41	0.83	0.05	25.6	30.8	4.5
K	1.00	0.18	4.92	4.91	0.87	–	–	–
L	0.83	0.14	4.54	5.52	0.77	334.9	60.7	5.6
G/U	1.04	0.05	2.25	2.17	0.11	80.3	37.0	5.6

*Table 9-4: Overview of synthesized samples with respective descriptions of synthesis conditions and U(VI) introduction techniques. RT: room temperature, HT: hydrothermal conditions (200 °C). *Samples are from chapter 7.2.1.*

Sample	Synthesis	U(VI) introduction
A*	RT	direct U incorporation
E*	RT	-
F	HT/Al_2O_3	-
G	RT/$Al(NO_3)_3$	-
H	RT/$Al(NO_3)_3$	direct U incorporation
J	HT/$Al(NO_3)_3$	direct U incorporation
K	HT/$Al(NO_3)_3$	-
L	HT/$Al(NO_3)_3$	direct U incorporation
G/U	RT/$Al(NO_3)_3$	U sorption

A comparison of the U/S ratios of samples A, H, J, L and G/U suggests that samples prepared at RT conditions possess higher U/S ratios compared to the samples prepared at HT. The additional presence of low amounts of Al (sample H in comparison to sample A) seems to have no significant influence on the U/S ratio.

The XRD patterns of samples F, G and K in comparison to that of Al-free sample A are compiled in Figure 9-1 and Table 9-5. Sample A, prepared at room temperature, shows a XRD pattern representative of C-S-H phases. The (001) reflection of sample A is around 8.3° 2θ Cu Kα equivalent to a basal layer-to-layer spacing of 10.6 Å. Furthermore, the prominent C-S-H (220), (222) and (240) reflections at 29, 30 and 50° 2θ Cu Kα are present, indicative of a turbostratic disordered 11 Å tobermorite structure (Drits and Tchoubar, 1990; Grangeon et al., 2013a; Grangeon et al., 2013b).

Table 9-5: Literature data of reflection angles with respective (abc) interpretations observed for the Al-tobermorite system (Grangeon et al., 2013b; Qu et al., 2018) (l.).

2θ (Cu *Kα*) angle [°]	d spacing [Å]	(abc)
7	12.6	(001)
15	5.9	(101)
25	3.6	(105)
27	3.4	(111)
29	3.2	(220) + (020)
30	3.1	(222) + (022)
33	2.8	(200)
39	2.4	(206)
50	2.0	(240)

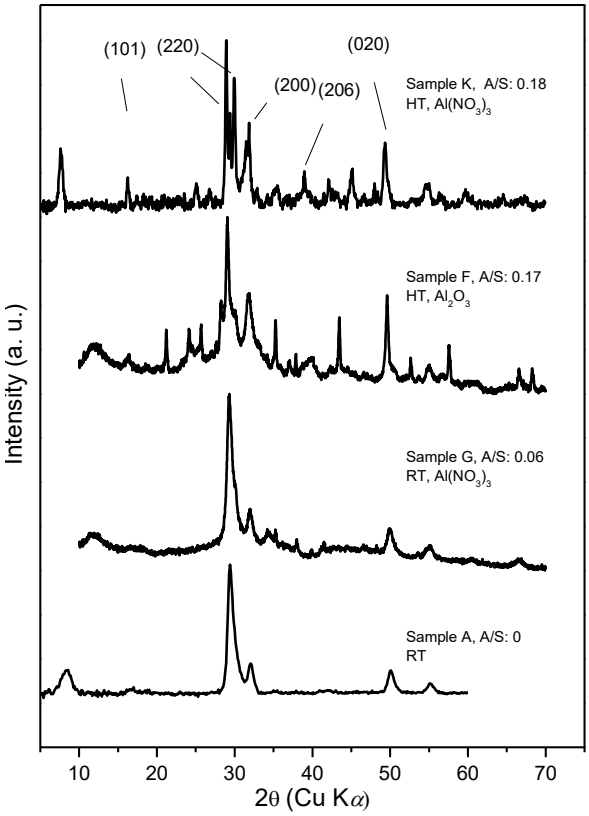

Figure 9-1: XRD patterns of samples A, G-F and K. RT: room temperature, HT: hydrothermal conditions (200 °C) (r.).

Sample G shows a reflection pattern with minor differences to that of sample A. Thus, only a small influence of the Al additive on the C-S-H structure can be assumed for sample G.
In contrast, the increased A/S ratio of sample F has a strong impact on the XRD pattern. New reflections can be observed throughout the complete spectrum. The phase identification (with the PDXL-2 program) suggests that sample F consists of 83% Al-tobermorite and 17% of a secondary phase with a reflection pattern similar to laumontite ($Ca(AlSi_2O_6)_2 \cdot 4H_2O$). Since the figure of merit for the laumontite phase identification was close to other Ca-Al-Si-H_2O phases it is somewhat uncertain which secondary Al-phases were formed. Additionally, the reflection pattern of sample F shows an increased distance between the 220 and 200 reflections which indicates an increased basal spacing (Grangeon et al., 2013b). This could be an indication of Al entering the bridging positions in the "dreierketten" arrangement which increases the mean chain length (MCL). The increase in MCL and structural order can both increase the basal spacing of tobermorite and C-S-H (Garbev et al., 2008; Grangeon et al., 2013b).

The XRD pattern of sample K, prepared in the presence of $Al(NO_3)_3$ and under hydrothermal conditions, suggests the formation of Al-tobermorite (tobermorite, aluminian, syn., database card number 01-074-2878). The (001) reflection is located at 7.6° 2θ Cu Kα, thus, a layer-to-layer spacing of 11.6 Å can be assumed. Compared to sample F that was prepared with Al_2O_3 the (200) reflection around 33° 2θ Cu Kα is strongly increased in intensity and distance to the (220) reflection at 29° 2θ Cu Kα. This indicates that sample K should have a high MCL for

tobermorite with a C/S ratio of 1.0, which suggests that Al entered the bridging positions in sample K. Under alkaline conditions, the Al additive has to undergo a transition from the starting Al component via $Al(OH)_3(s)$ to dissolved $Al[OH]_4^-$ before it can be incorporated into the cementitious material. It is assumed that $Al(NO_3)_3$ undergoes this transition faster than Al_2O_3 which explains the differences in the XRD pattern of samples F and K.

The ^{29}Si NMR spectra of samples E, G and K are shown in Figure 9-2. Literature data about ^{29}Si NMR spectra of relevant cementitious phases can be found in Table 9-6. Several solid state ^{29}Si MAS NMR studies of Al-rich cementitious materials showed the influence of Al on the "dreierketten" arrangement of the C-S-H and tobermorite structure. In summary ^{29}Si NMR provides information about the amount of bridging Si neighbors in the C-S-H structure. A Q^1 arrangement where every Si tetrahedron is connected to one Si neighbor (Si-O-Si, Q^1Si (0Al)) can be found in C-S-H phases with high C/S ratios where most of the silicate chain is depolymerized (Irico et al., 2017; Sun et al., 2006).

Table 9-6: Literature data of Si sites with corresponding chemical shifts present in cementitious phases (l.).

Chemical shift [ppm]	Si site
−97 to −92	Q^3Si (0Al) in C-S-H (Cong and Kirkpatrick, 1996; Qu et al., 2018)
−94 to −88	Q^3Si (1Al) in C-S-H (Komarneni et al., 1987; Komarneni et al., 1985b; Qu et al., 2018)
−86.7	Stratlingite (Kwan et al., 1995)
−84.5 to −84	Q^2Si (0Al) in C-S-H (Irico et al., 2017; Sun et al., 2006)
−82	Q^2Si (1Al) in C-S-H (Irico et al., 2017)
−79.7 to −79	Q^1Si (0Al) in C-S-H (Irico et al., 2017; Sun et al., 2006)
−74 to −72	Q^0Si (Irico et al., 2017; Qu et al., 2018)

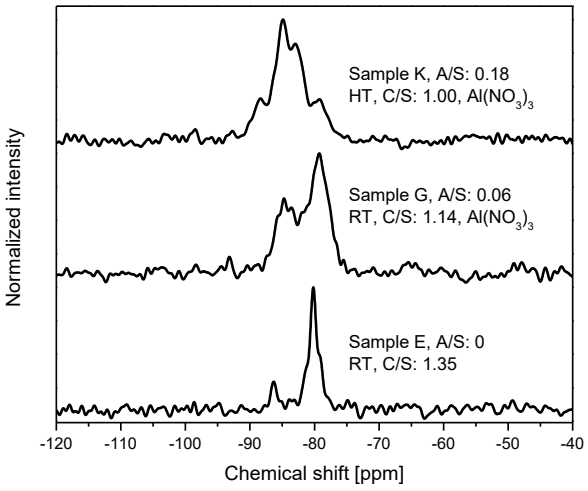

Figure 9-2: Solid state ^{29}Si MAS NMR spectra of samples E, G and K. RT: room temperature, HT: hydrothermal conditions (200 °C) (r.).

In C-S-H phases with lower C/S ratios, more bridging Si tetrahedra link the pairing dimers, which increases the MCL. Thus, the amount of Q^1 sites decreases while the occurrence of Q^2 (-Si-O-Si-O-Si-, Q^2Si (0Al)) arrangements can be observed.

With regard to Al, it was reported that Al tetrahedra can occupy the positions of bridging Si tetrahedra, increasing the silicate chain length, thus, reducing Si Q^1 peaks and increasing Q^2 peaks (Q^2Si (1Al)). At very high Al contents in cementitious materials even a cross-linking between C-S-H layers was observed, resulting in the occurrence of Q^3 sites (Q^3Si (1Al)) (Komarneni et al., 1987; Komarneni et al., 1985b).

From the Q^{1-3} integrals of a ^{29}Si NMR spectrum MCL and cross-linking quotients (CLQ) of a sample can be determined according to equations (9.1) and (9.2) developed by Coleman (2006) and applied by Qu et al. (2018).

$$MCL = \frac{2(Q^1+Q^2+Q^2(1Al)+Q^3+2Q^3(1Al))}{Q^1} \quad (9.1)$$

$$CLQ = \frac{(Q^3+2Q^3(1Al))}{(Q^1 + Q^2 + Q^2(1Al) + 2Q^3(1Al))} \quad (9.2)$$

Sample E (C/S 1.35) shows a typical ^{29}Si NMR spectrum for Al-free C-S-H phases with a medium to high C/S ratio. Its Q^1 peak is located around −80 ppm which accounts roughly to 85% of the observed signal area, indicating a low degree of silica chain polymerization. The small signal around −86 ppm has to be caused by a Q^2Si (0Al) site since sample E is Al-free. The MCL calculation results in a MCL of 2.3 silica units supporting the assumption that the silica chain in sample E is nearly depolymerized.

Sample G, that was prepared at RT similar to sample E but in the additional presence of $Al(NO_3)_3$ (A/S: 0.06), shows a pronounced reduction of the Q^1 peak at −80 ppm to 50% of signal area. The peak at −84.7 ppm, caused by the Q^2Si (0Al) site, amounts to 34% of the signal area and results from the lower C/S ratio of sample G (C/S: 1.14). The signal at −81.6 ppm, caused by (Q^2Si (1Al)) shows that 17% of the bridging positions in sample G are occupied by Al. Thus, the MCL of sample G is increased to 4.1 indicating a higher degree of (alumino)silicate chain polymerization (Qu et al., 2018).

The reduction of Q^1 peaks is even more pronounced in the Al-rich hydrothermally prepared sample K that consists of tobermorite as shown by XRD. The Q^1 peak is reduced to only 11% of the total peak area, while high intensity Q^2Si (1Al) and Q^2Si (0Al) peaks become visible at −82.6 and −85 ppm, respectively. Thus sample K shows a high degree of (alumino)silicate chain polymerization by bridging Si (47%) and bridging Al (31%). Additionally, a peak at −88.7 ppm was observed that could be either caused by stratlingite (−86.7 ppm) or by layer cross-linking Q^3Si (1Al) sites (−94 to −88 ppm). Therefore, sample K shows the highest MCL of 18.5 and a CLQ of 0.128. No Q^3Si (0Al) peaks between −97 and −94 ppm could be observed, implying that only alumina units occupy the cross-linking positions. Qu et al. (2018) synthesized Al-rich tobermorite samples with Al/(Si+Al) ratios between 0.01 and 0.12 at 180 °C and 7 h of synthesis times. The authors found a decrease of the MCL at Al/(Si+Al)>0.03. At an Al/(Si+Al) ratio of 0.12 they found a MCL of 11.4 and CLQ of 0.13. Thus, the CLQ is comparable while the MCL in the present study is higher, probably due to

the slightly higher synthesis temperature of 200 °C and longer synthesis time of 3 d. This assumption is supported by findings of Ortaboy et al. (2017) that showed that high synthesis temperatures provide the formation of long-range ordered chain structures. This shows that it is possible to archive long chain lengths and cross-linked sheets in the tobermorite structure using aluminum nitrate additive under hydrothermal conditions.

Information about the ^{27}Al NMR spectra of samples F-G and K are compiled in Figure 9-3 and Table 9-7. ^{27}Al MAS NMR allows to obtain an insight into the coordination environment like fourfold Al[4] (tetrahedral), fivefold Al[5], sixfold Al[6] (octahedral) coordination in cementitious materials. Several ^{27}Al MAS NMR studies showed that Al can be found in an Al[4] coordination inside the silica chain of C-S-H and tobermorite (Irico et al., 2017; Klimesch and Ray, 1998; Komarneni et al., 1985a; Komarneni et al., 1985b; Qu et al., 2018) occupying bridging and cross-linking positions. The presence of Al[5] in the interlayer and Al[6] in the Ca-O sheet in C-S-H and tobermorite was suggested (Faucon et al., 1999; Stade and Wieker, 1982). More recent studies, however, showed that only Al[4] exists in the tobermorite interlayer (Andersen et al., 2003; Sun et al., 2006) while Al[6] might be present on the C-S-H surface. Additionally, the formation of secondary Al[5] and Al[6] phases in cementitious systems such as hydrogarnet (Qu et al., 2018) under hydrothermal conditions or AFm and AFt phases in concrete (Irico et al., 2017; Kapeluszna et al., 2017) or Al[5] and Al[6] (calcium) aluminate hydrate phases (Ortaboy et al., 2017) in high C/S ratio C-S-H phases was observed.

Table 9-7: Literature data of Al sites with corresponding chemical shifts present in cementitious materials (l.).

Chemical shift [ppm]	Al site
69.5 and 72.3	Al[4] in C-S-H (Andersen et al., 2003)
65	Q^2Al[4] site in tobermorite (Guo et al., 2017)
57	Q^3Al[4] site in tobermorite (Guo et al., 2017)
60.2 and 10	Al[4] and Al[6] in stratlingite (Sun et al., 2006)
35	Al[5] (Sun et al., 2006)
0-10	Al[6] secondary phases (Andersen et al., 2003; Dai et al., 2014; Sun et al., 2006)

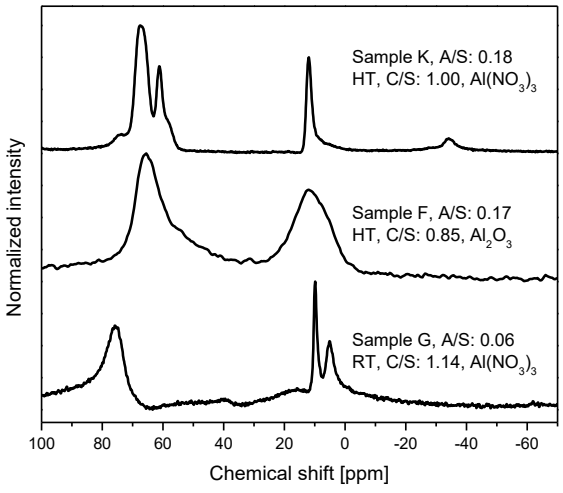

Figure 9-3: Solid state ^{27}Al MAS NMR spectra of samples F-G and K. RT: room temperature, HT: hydrothermal conditions (200 °C) (r.).

The ^{27}Al NMR spectrum of sample G shows peaks at 76, 9.9 and 5 ppm. Andersen et al. (2003) reported the presence of Al[4] in the C-S-H structure similar to tobermorite with a chemical shift between 69.5 and 72.3 ppm, while Dai et al. (2014) detected Al[6] on the C-S-H surface around 10 ppm. Thus, the peaks at 76 and 9.9 ppm can be attributed to Al incorporated into the C-S-H silica chain and sorbed on the C-S-H surface. The XRD study of sample G suggested some minor reflections of an unidentified phase. Since the ^{27}Al NMR spectrum shows an Al[6] peak at 5 ppm, this unidentified secondary phase probably contains Al.

Sample F shows a spectrum with a very broad Al[4] peak between 60 and 65 ppm as well an Al[6] peak at 10 ppm that probably belongs to secondary Al[6] phase with a XRD pattern similar to laumontite ($Ca(AlSi_2O_6)_2 \cdot 4H_2O$) that amounted to 17% of sample F. Although the ^{27}Al NMR peak positions are comparable to those of stratlingite (Lothenbach et al., 2011), no stratlingite was detected in the XRD patterns.

Sample K shows main peaks at 67.6, 58.3 and 11 ppm in its ^{27}Al NMR spectrum. This indicates that sample K possesses Al[4] in Q^2 and Q^3 sites in the tobermorite structure as already detected in its ^{29}Si NMR spectrum. Additionally, the band positions are in agreement with those reported for stratlingite (Sun et al., 2006). Since also the ^{29}Si NMR spectrum of sample K suggested the presence of stratlingite it could be present in small quantities below the XRD detection limit. The additional minor peaks at 74.0 and −34.6 ppm are rotation side bands originating from a too low MAS frequency. This shows that the static line width (tensor without MAS) of sample K is greater than the chosen MAS frequency of 20 kHz. The high amounts of Al seem to increase the line width which makes NMR investigations of Al containing cementitious materials technically challenging.

TRLFS measurements were applied to identify the U(VI) incorporation into the formed Al-tobermorite phases. In Figure 9-4 the luminescence spectra of samples A, H, J, L and G/U are compiled. Determined band positions and lifetimes are compiled in Table 9-8. The U(VI) luminescence spectrum of sample A (Al-free C-S-H phase) shows a luminescence of U(VI) sorbed on the C-S-H surface (37.1%) and incorporated (62.9%) in the C-S-H interlayer with lifetimes of 118 and 604 μs, respectively. U(VI)/C-S-H spectra were discussed in the previous chapter 7.2.1. An incorporation of U(VI) in the C-S-H interlayer resulted in an increased red shift compared to U(VI) exclusively sorbed on the C-S-H surface (Tits et al., 2011). The incorporation of U(VI) from the C-S-H surface into the interlayer took longer time periods due to C-S-H re-crystallization compared to a direct U(VI) incorporation.

For sample H, a luminescence spectrum comparable to sample A with luminescence lifetimes of 118 and 604 μs was recorded and assigned to a U(VI)/C-S-H surface complex and U(VI) incorporated in the C-S-H structure.

Table 9-8: Band positions and lifetimes of samples A, H, J, L and G/U determined in TRLFS investigations (l.).

Sample (days)	Band positions [nm]	Lifetimes [μs]
L (120)	505.5, 525.3, 545.3	
L (14)	505.4, 522.3, 542.3	7/202
J (120)	517.1, 538.8, 562.0	260/720
J (14)	516.2, 537.5, 560.2	
H (14)	516.3, 539.6, 563.2	
G/U (120)	501.4, 522.3, 546.7	188/601
G/U (14)	501.6, 522.9, 547.0	
A (14)	497.1, 517.2, 538.9	118/604

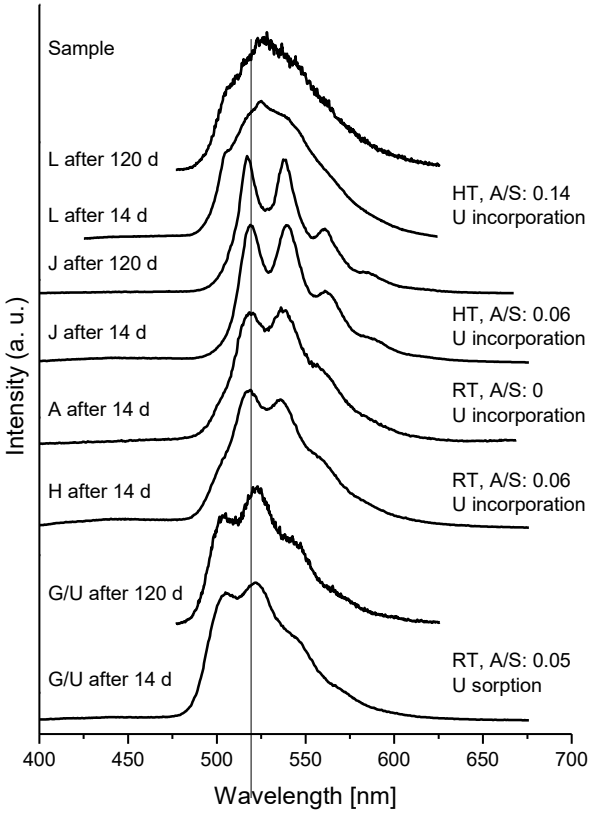

Figure 9-4: TRLFS spectra of samples A, H, J, L and G/U after 14 or 120 d of equilibration time. RT: room temperature, HT: hydrothermal conditions (200 °C) (r.). The decrease in line resolution for samples L and G/U after 120 d was caused by malfunctions of the spectrograph.

This indicates that C-S-H with low to moderate amounts of Al remains capable of incorporating U(VI) in its interlayer. The luminescence spectrum of sample J shows a close resemblance to U(VI) incorporated into C-S-H structure, but with a better band resolution. Since the hydrothermal synthesis conditions of sample J leads to the formation of tobermorite, which is a crystalline form of C-S-H, the increase in band resolution can be explained by a more defined chemical environment of U(VI) in the tobermorite interlayer. The Al-additives seem to have no major influence on the chemical environment of U(VI) in the tobermorite interlayer at low A/S ratios. With increasing equilibration time the spectrum of sample J remains unchanged. Two U(VI) luminescence lifetimes of 260 (81.4%) and 720 μs (18.6%) were determined for sample J suggesting that some U(VI) is also located in the tobermorite interlayer but to a larger amount on the tobermorite surface.

If the amount of Al in hydrothermally prepared tobermorite is increased to a A/S ratio of 0.14 changes in the U(VI) luminescence spectrum become visible (sample L in Figure 9-4). The band resolution decreases drastically while the lifetime analysis provides lifetimes of 7 and 202 μs. This implies that U(VI) is only located on the tobermorite surface but not in the tobermorite interlayer. It is possible that the Al distorts the tobermorite structure to a point that no further U(VI) can be incorporated in the interlayer. This could be caused by the Q^3Si (1Al) sites which are present at high A/S ratios and cross-link single layers which could result

in a decreased U(VI) retention capability for Al-saturated tobermorite which should be reflected in the leaching experiments.

The sorption of U(VI) on C-S-H with small amounts of Al (G/U after 14 d, Figure 9-4) leads to a spectrum similar to U(VI) sorbed on the C-S-H surface as shown for sample E/U in Figure 7-2 or reported by Tits et al. (2011). With increasing sorption time the spectrum becomes slightly red shifted due to the ongoing incorporation of U(VI) in the C-S-H interlayer caused by C-S-H re-crystallization (G/U after 120 d, Figure 9-4). Such a time-dependent effect was also observed by Tits et al. (2011). This shows that C-A-S-H remains its sorption and incorporation capabilities for U(VI).

9.2.2. Leaching of U(VI) doped Al-tobermorite

9.2.2.1. Leaching in 2.5 M NaCl

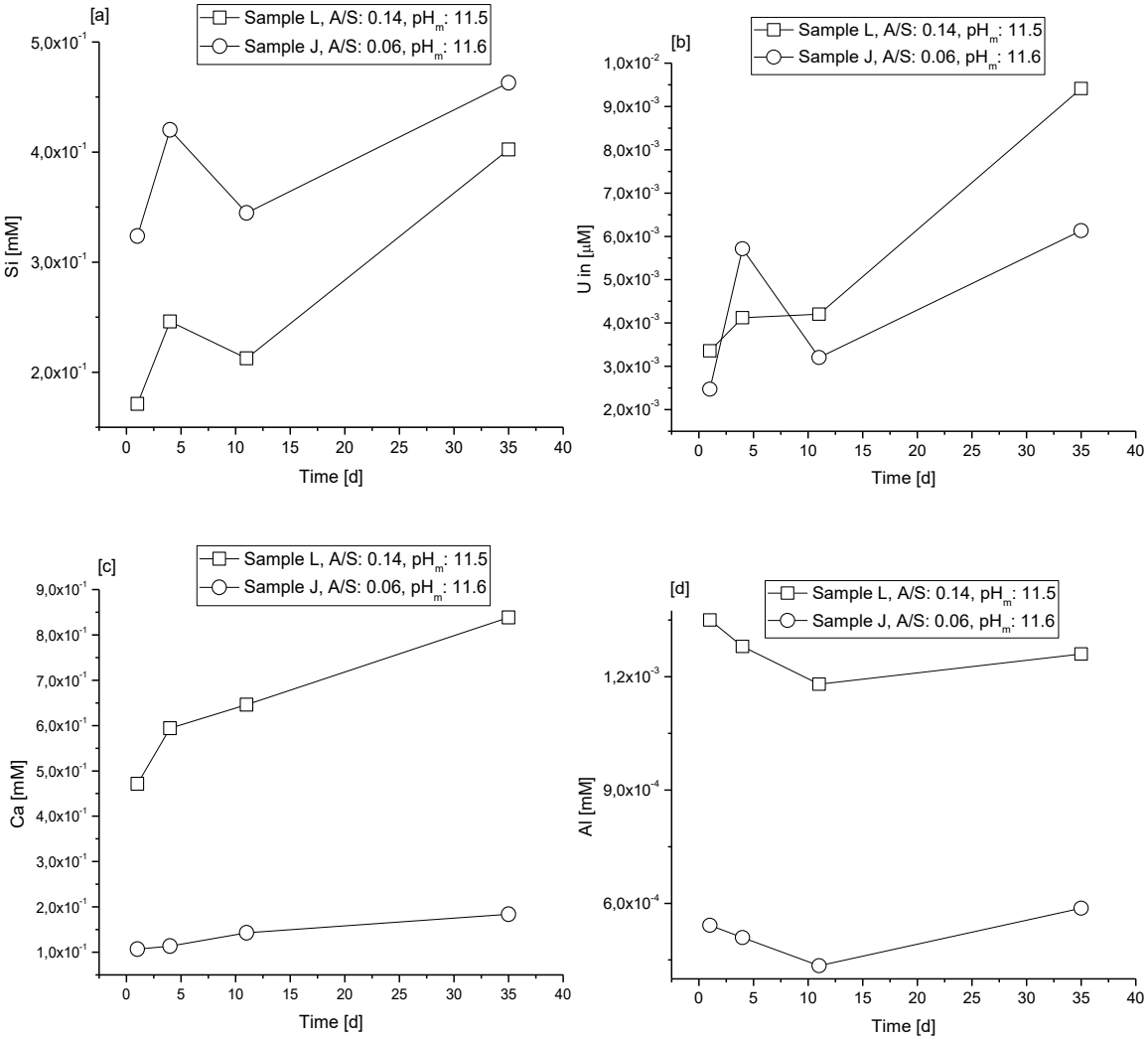

Figure 9-5: Silicon [a], uranium [b], calcium [c] and aluminum [d] concentration in the supernatant solution after leaching of samples J (C/S 0.49, A/S 0.06) and L (C/S 0.83, A/S 0.14) (HT, $Al(NO_3)_3$) in 2.5 M NaCl as a function of time.

The leaching of sample J (C/S 0.49, A/S 0.06) in 2.5 M NaCl at a S/L of 1.8 g/L leads to the release of 0.32−0.46 mM Si (Figure 9-5[a]) and 0.10−0.18 mM Ca (Figure 9-5[c]). Compared to the leaching of sample A (C/S 1.0) in 2.5 M NaCl (0.64 mM Si, Table 7-5) the Si release of sample J is slightly lower. Thus, tobermorite seems to be more stable in saline solutions probably caused by its higher crystallinity.
Sample L (C/S 0.83, A/S 0.14) shows a decreased Si release (0.17−0.40 mM) compared to sample J which is probably caused by the higher C/S ratio of sample L.
The U(VI) release from samples J and L after 35 d ranges between $6.1-9.3\times10^{-3}$ μM U comparable (Figure 9-5[b]). Although the TRLFS investigation showed that sample J possesses U(VI) in the interlayers and at the surface while the U(VI) in sample L is exclusively located on the tobermorite surface, the U(VI) retention for sample L remains high in 2.5 M NaCl. It was reported that even the inner-sphere surface sorption of U(VI) complex provides a strong U(VI) retention by C-S-H at high pH values (Tits et al., 2011). This shows that a 2.5 M NaCl solution is not capable of removing the uranyl inner-sphere complex from a C-S-H and tobermorite surface at high pH values.

9.2.2.2. Leaching in 2.5 M NaCl/0.02 M $NaHCO_3$

For samples L and J the Al concentration in the leaching solution was near the ICP-MS detection limit (Figure 9-6[d]). This could be caused by the pH decrease from 11.5−11.6 to 9.6 due to the presence of carbonate in solution.

Thus, the Al speciation in the liquid phase should change from $Al[OH]_4^-$ to $Al(OH)_3$ which is highly insoluble (0.02 mM). The Ca concentration in solution (Figure 9-6[c]) is around one order of magnitude lower (8.0×10^{-2} mM) compared to the carbonate-free leaching because of the precipitation of $CaCO_3$.

Nonetheless, samples L and J show an increased Si release into 2.5 M NaCl/0.02 M $NaHCO_3$ which is around one order of magnitude higher (1.3−3.5 mM, Figure 9-6[a]) compared to the leaching in 2.5 M NaCl (0.17−0.46 mM, Figure 9-5[a]). This indicates a stronger dissolution of Al-tobermorite in the presence of 2.5 M NaCl/0.02 M $NaHCO_3$ compared to 2.5 M NaCl.

The U(VI) release from sample A into 2.5 M NaCl/0.02 M $NaHCO_3$ amounted to 0.18 μM (Table 7-5). The U(VI) release from sample J (C/S 0.49, A/S 0.06) was with 0.16 μM (Figure 9-6[b]) almost identical, which shows that at low A/S ratios Al-tobermorite possesses a similar U(VI) retention capability than Al-free C-S-H phases. At a high A/S ratio the U(VI) release increased from 0.16 to 0.41 μM (sample L in Figure 9-6[b]). TRLFS measurements already suggested a reduced U(VI) retention capability of sample L due to an inaccessibility of the tobermorite interlayers for U(VI). The U(VI) of sample L is located on the surface of Al-rich tobermorite were it is easily accessible for the carbonate ions that enhance the U(VI) mobility in this pH range.

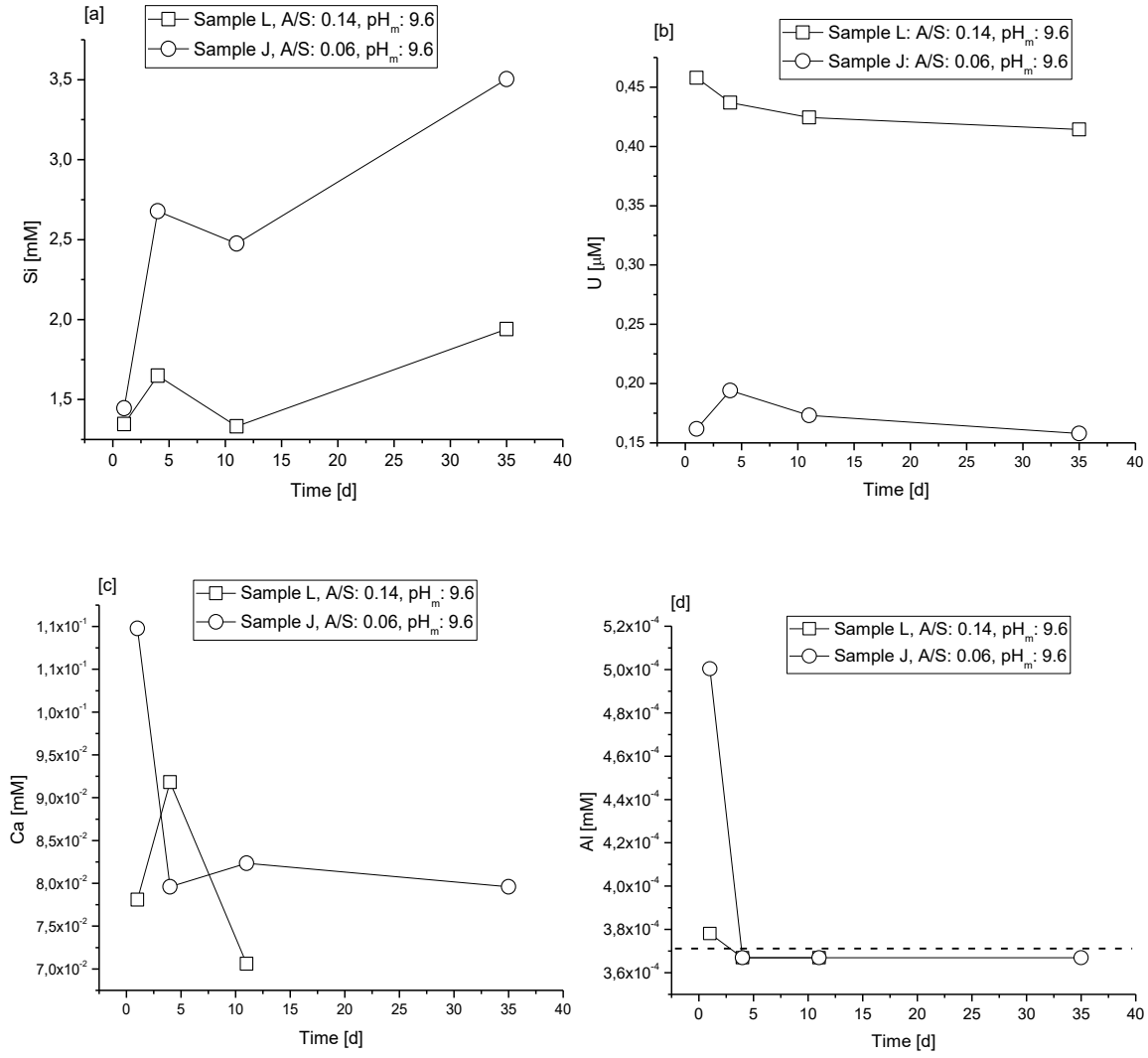

Figure 9-6: Silicon [a], uranium [b], calcium [c] and aluminum [d] concentration in the supernatant solution after leaching of sample J (C/S 0.49, A/S 0.06) and L (C/S 0.83, A/S 0.14) (HT, $Al(NO_3)_3$) in 2.5 M NaCl/0.02 M $NaHCO_3$ as a function of time (ICP-MS detection limit for Al is 3.7×10^{-4} mM (dashed line)).

10. References

THEREDA - Thermodynamic Reference Database, https://www.thereda.de, Release No. 6.

Allen F.J., Truscott C.L., Gutfreund P., Welbourn R.J.L. and Clarke S.M. (2019) Potassium, Calcium, and Magnesium Bridging of AOT to Mica at Constant Ionic Strength. Langmuir 35, 5753-5761.

Allen P.G., Shuh D.K., Bucher J.J., Edelstein N.M., Reich T., Denecke M.A. and Nitsche H. (1996) EXAFS Determinations of Uranium Structures: The Uranyl Ion Complexed with Tartaric, Citric, and Malic Acids. Inorg. Chem. 35, 784-787.

Altmaier M., Metz V., Neck V., Müller R. and Fanghänel T. (2003) Solid-liquid equilibria of $Mg(OH)_{2(cr)}$ and $Mg_2(OH)_3Cl{\cdot}4H_2O_{(cr)}$ in the system Mg-Na-H-OH-Cl-H_2O at 25°C. Geochim. Cosmochim. Acta 67, 3595-3601.

Altmaier M., Neck V. and Fanghänel T. (2008) Solubility of Zr(IV), Th(IV) and Pu(IV) hydrous oxides in $CaCl_2$ solutions and the formation of ternary Ca-M(IV)-OH complexes. Radiochim. Acta 96, 541-550.

Altmaier M., Yalçıntaş E., Gaona X., Neck V., Müller R., Schlieker M. and Fanghänel T. (2017) Solubility of U(VI) in chloride solutions. I. The stable oxides/hydroxides in NaCl systems, solubility products, hydrolysis constants and SIT coefficients. J. Chem. Thermodyn. 114, 2-13.

Amayri S., Jermolajev A. and Reich T. (2011) Neptunium(V) sorption on kaolinite. Radiochim. Acta 99, 349-357.

Andersen M.D., Jakobsen H.J. and Skibsted J. (2003) Incorporation of aluminum in the calcium silicate hydrate (C-S-H) of hydrated Portland cements: A high-field Al-27 and Si-29 MAS NMR Investigation. Inorg. Chem. 42, 2280-2287.

Ankudinov A.L., Ravel B., Rehr J.J. and Conradson S.D. (1998) Real-space multiple-scattering calculation and interpretation of X-ray-absorption near-edge structure. Phys. Rev. B 58, 7565-7576.

Arnarson T.S. and Keil R.G. (2000) Mechanisms of pore water organic matter adsorption to montmorillonite. Marine Chem. 71, 309-320.

Atesok G., Somasundaran P. and Morgan L.J. (1988) Adsorption properties of Ca^{2+} on Na-kaolinite and its effect on flocculation using polyacrylamides. Colloid Surface 32, 127-138.

Auroy M., Poyet S., Le Bescop P., Torrenti J.-M. and Charpentier T. (2018) Comparison between natural and accelerated carbonation (3% CO_2): Impact on mineralogy, microstructure, water retention and cracking. Cement Concrete Res. 109, 64-80.

Bachmaf S., Planer-Friedrich B. and Merkel B.J. (2008) Effect of sulfate, carbonate, and phosphate on the uranium(VI) sorption behavior onto bentonite. Radiochim. Acta 96, 359-366.

Baran V. and Tympl M. (1966) Infrared Spectra of Sodium Uranates. Z. Anorg. Allg. Chem. 347, 175-183.

Barone V. and Cossi M. (1998) Quantum Calculation of Molecular Energies and Energy Gradients in Solution by a Conductor Solvent Model. J. Phys. Chem. A 102, 1995-2001.

Basile M., Unruh D.K., Gojdas K., Flores E., Streicher L. and Forbes T.Z. (2015) Chemical controls on uranyl citrate speciation and the self-assembly of nanoscale macrocycles and sandwich complexes in aqueous solutions. Chem. Commun. 51, 5306-5309.

Baston G.M.N., Berry J.A., Bond K.A., Boult K.A., Brownsword M. and Linklater C.M. (1994) Effects of cellulosic degradation products on uranium sorption in the geosphere. J. Alloy Compd. 213-214, 475-480.

Becke A.D. (1993) Density-functional thermochemistry. III. The role of exact exchange. J. Chem. Phys. 98, 5648-5652.

Berner U.R. (1992) Evolution of pore water chemistry during degradation of cement in a radioactive waste repository environment. Waste Manage. 12, 201-219.

Bernhard G., Geipel G., Reich T., Brendler V., Amayri S. and Nitsche H. (2001) Uranyl(VI) carbonate complex formation: Validation of the $Ca_2UO_2(CO_3)_{3(aq.)}$ species. Radiochim. Acta 89, 511-518.

Berto S., Crea F., Daniele P.G., De Stefano C., Prenesti E. and Sammartano S. (2012) Potentiometric and spectrophotometric characterization of the UO22+-citrate complexes in aqueous solution, at different concentrations, ionic strengths and supporting electrolytes. Radiochim. Acta 100, 13-28.

Bethke C. (2008) Geochemical and Biogeochemical Reaction Modeling. Cambridge University Press, pp. 565.

Binstead R.A., Zuberbühler A.D. and Jung B. (2005) SPECFIT Global Analysis System, Version 3.0.37 ed. Spectrum Software Associates, Marlborough, MA, USA.

Black L., Breen C., Yarwood J., Garbev K., Stemmermann P. and Gasharova B. (2007) Structural features of C-S-H(I) and its carbonation in air - A Raman spectroscopic study. Part II: Carbonated phases. J. Am. Ceram. Soc. 90, 908-917.

Bots P., Morris K., Hibberd R., Law G.T., Mosselmans J.F., Brown A.P., Doutch J., Smith A.J. and Shaw S. (2014) Formation of stable uranium(VI) colloidal nanoparticles in conditions relevant to radioactive waste disposal. Langmuir 30, 14396-14405.

Boult K., McCrohon R. and Williams S.J. (1998a) Further experiments on the effects of Sikament 10 and Sikament N on plutonium solubility, AEA Technology Report RWMD (97) P95.

Boult K.A., Cowper M.M., Heath T.G., Sato H., Shibutani T. and Yui M. (1998b) Towards an understanding of the sorption of U(VI) and Se(IV) on sodium bentonite. J. Contam. Hydrol. 35, 141-150.

Bradbury M.H. and Baeyens B. (2005) Modelling the sorption of Mn(II), Co(II), Ni(II), Zn(II), Cd(II), Eu(III), Am(III), Sn(IV), Th(IV), Np(V) and U(VI) on montmorillonite: Linear free energy relationships and estimates of surface binding constants for some selected heavy metals and actinides. Geochim. Cosmochim. Acta 69, 875-892.

Bradbury M.H. and Baeyens B. (2009) Sorption modelling on illite Part I: Titration measurements and the sorption of Ni, Co, Eu and Sn. Geochim. Cosmochim. Acta 73, 990-1003.

Bradl H. (2005) Heavy Metals in the Environment: Origin, Interaction and Remediation, 1st Edition ed. Elsevier Academic Press, London, UK.

Brayden T.H., Poropatic P.A. and Watanabe J.L. (1988) Iterative target testing for calculation of missing data points. Anal. Chem. 60, 1154-1158.

Brewitz W. (1982) Eignungsprüfung der Schachtanlage Konrad für die Endlagerung radioaktiver Abfälle. Institut für Tiefenlagerung, Neuherberg, Germany.

Brinkmann H., Patzschke M., Kaden P., Raiwa M., Rossberg A., Kloditz R., Heim K., Moll H. and Stumpf T. (2019) Complex formation between $UO_2^{(2+)}$ and alpha-isosaccharinic acid: insights on a molecular level. Dalton Trans. 48, 13440-13457.

Butcher E.J. (2008) Results and interpretation of Advacast 550 complexation studies, Nexia Solutions Report 9080.

Catalano J.G. and Brown G.E. (2005) Uranyl adsorption onto montmorillonite: Evaluation of binding sites and carbonate complexation. Geochim. Cosmochim. Acta 69, 2995-3005.

Chang J. and Fang Y. (2015) Quantitative analysis of accelerated carbonation products of the synthetic calcium silicate hydrate(C-S-H) by QXRD and TG/MS. J. Therm. Anal. Calorim. 119, 57-62.

Chen X., Peng S. and Wang J. (2014) Retention profile and kinetics characteristics of the radionuclide 90-Sr(II) onto kaolinite. J. Radioanal. Nucl. Chem. 303, 509-519.

Cherian C., Kollannur N.J., Bandipally S. and Arnepalli D.N. (2018) Calcium adsorption on clays: Effects of mineralogy, pore fluid chemistry and temperature. Appl. Clay Sci. 160, 282-289.

Chernorukov N.G., Nipruk O.V. and Kostrova E.L. (2016) Synthesis and study of sodium uranate Na2U2O7·6H2O and of products of its dehydration and thermal decomposition. Radiochemistry 58, 124-127.

Chisholm-Brause C., Conradson S.D., Buscher C.T., Eller P.G. and Morris D.E. (1994) Speciation of uranyl sorbed at multiple binding sites on montmorillonite. Geochim. Cosmochim. Acta 58, 3625-3631.

Chisholm-Brause C.J., Berg J.M., Little K.M., Matzner R.A. and Morris D.E. (2004) Uranyl sorption by smectites: spectroscopic assessment of thermodynamic modeling. J. Colloid Interf. Sci. 277, 366-382.

Chisholm-Brause C.J., Berg J.M., Matzner R.A. and Morris D.E. (2001) Uranium(VI) Sorption Complexes on Montmorillonite as a Function of Solution Chemistry. J. Colloid Interf. Sci. 233, 38-49.

Clacher A.P. and Cowper M.M. (2009) Effect of ADVA Cast 551 on the solubility of plutonium(IV) and uranium(VI), Report Serco/TAS/003145/001.

Clacher A.P., Marshall T. and Swanton S. (2013) Solubility Studies: Effect of ADVA Cast 551 at low concentration, Report NPO004236 / RWM005477.

Coleman N.J. (2006) Interactions of Cd(II) with waste-derived 11 Å tobermorites. Sep. Purif. Technol. 48, 62-70.

Comarmond M.J., Steudtner R., Stockmann M., Heim K., Muller K., Brendler V., Payne T.E. and Foerstendorf H. (2016) The Sorption Processes of U(VI) onto SiO2 in the Presence of Phosphate: from Binary Surface Species to Precipitation. Environ. Sci. Technol. 50, 11610-11618.

Cong X.-D. and Kirkpatrick R.J. (1996) Si-29 MAS NMR study of the structure of calcium silicate hydrate. Adv. Cem. Based Mater. 3, 144-156.

Cossi M., Rega N., Scalmani G. and Barone V. (2003) Energies, structures, and electronic properties of molecules in solution with the C-PCM solvation model. J. Comput. Chem. 24, 669-681.

Courdouan A., Christl I., Meylan S., Wersin P. and Kretzschmar R. (2007a) Characterization of dissolved organic matter in anoxic rock extracts and in situ pore water of the Opalinus Clay. Appl. Geochem. 22, 2926-2939.

Courdouan A., Christl I., Meylan S., Wersin P. and Kretzschmar R. (2007b) Isolation and characterization of dissolved organic matter from the Callovo-Oxfordian formation. Appl. Geochem. 22, 1537-1548.

Dai Z., Tran T.T. and Skibsted J. (2014) Aluminum Incorporation in the C-S-H Phase of White Portland Cement-Metakaolin Blends Studied by Al-27 and Si-29 MAS NMR Spectroscopy. J. Am. Ceram. Soc. 97, 2662-2671.

Dario M., Molera M. and Allard B. (2004) Effect of organic ligands on the sorption of europium on TiO_2 and cement at high pH, SKB Technical Report TR-04-04.

Di Pietro P. and Kerridge A. (2016) U-Oyl Stretching Vibrations as a Quantitative Measure of the Equatorial Bond Covalency in Uranyl Complexes: A Quantum-Chemical Investigation. Inorg. Chem. 55, 573-583.

Dransfield J.M. (2004) Leaching of organic admixtures from concrete, Cement Admixtures Association Homepage, www.admixtures.org.uk/downloads/AES 9 leaching of admixture.pdf (Copyright 2004, Download am 01.10.2014).

Drits V.A. and Tchoubar C. (1990) X-ray Diffraction by Disordered Lamellar Structures: Theory and Applications to Microdivided Silicates and Carbons. Springer-Verlag, Berlin.

Drobot B., Bauer A., Steudtner R., Tsushima S., Bok F., Patzschke M., Raff J. and Brendler V. (2016) Speciation Studies of Metals in Trace Concentrations: The Mononuclear Uranyl(VI) Hydroxo Complexes. Anal. Chem. 88, 3548-3555.

Duff M.C., Coughlin J.U. and Hunter D.B. (2002) Uranium co-precipitation with iron oxide minerals. Geochim. Cosmochim. Acta 66, 3533-3547.

Dullies P. (2019) Untersuchungen zum Einfluss von Isosaccharinsäure auf die U(VI)-Rückhaltung an Ca-Bentonit unter alkalischen Bedingungen. Hochschule für Technik und Wirtschaft (HTW) Dresden, Dresden, Germany.

Elzinga E.J., Tait C.D., Reeder R.J., Rector K.D., Donohoe R.J. and Morris D.E. (2004) Spectroscopic investigation of U(VI) sorption at the calcite-water interface. Geochim. Cosmochim. Acta 68, 2437-2448.

Fanghänel T., Kim J.I., Paviet P., Klenze R. and Hauser W. (1994) Thermodynamics of Radioactive Trace-Elements in Concentrated Electrolyte-Solutions - Hydrolysis of Cm^{3+} in NaCl-Solutions. Radiochim. Acta 66-7, 81-87.

Fanghänel T., Könnecke T., Weger H., Paviet-Hartmann P., Neck V. and Kim J.I. (1999) Thermodynamics of Cm(III) in concentrated salt solutions: Carbonate complexation in NaCl solution at 25 degrees C. J. Solution Chem. 28, 447-462.

Fanghänel T. and Neck V. (2002) Aquatic chemistry and solubility phenomena of actinide oxides/hydroxides. Pure Appl. Chem. 74, 1895-1907.

Farooq U., Tweheyo M.T., Sjöblom J. and Øye G. (2011) Surface Characterization of Model, Outcrop, and Reservoir Samples in Low Salinity Aqueous Solutions. J. Disper. Sci. Technol. 32, 519-531.

Faucon P., Delagrave A., Petit J.C., Richet C., Marchand J.M. and Zanni H. (1999) Aluminum incorporation in calcium silicate hydrates (C-S-H) depending on their Ca/Si ratio. J. Phys. Chem. B 103, 7796-7802.

Feldman I., Havill J.R. and Neuman W.F. (1954) Polymerization of Uranyl-Citrate, -Malate, -Tartrate and -Lactate Complexes1. J. Am. Chem. Soc. 76, 4726-4732.

Feldman I. and Neuman W.F. (1951) The Uranyl—Citrate System. I. Spectrophotometric Studies in Acid Solution1. J. Am. Chem. Soc. 73, 2312-2315.

Fellhauer D., Gaona X., Rothe J., Altmaier M. and Fanghänel T. (2017) Neptunium(VI) solubility in alkaline $CaCl_2$ solutions: evidence for the formation of calcium neptunates Ca x NpO_3+x (s,hyd). Monatsh. Chem. - Chemical Monthly 149, 237-252.

Fenter P., Park C., Nagy K.L. and Sturchio N.C. (2007) Resonant anomalous X-ray reflectivity as a probe of ion adsorption at solid–liquid interfaces. Thin Solid Films 515, 5654-5659.

Fernández R., Mäder U., Rodríguez M., Virgil de la Villa R. and Cuevas J. (2009) Alteration of compacted bentonite by diffusion of highly alkaline solutions. Eur. J. Mineral. 21, 725-735.

Fialips C.-I., Petit S., Decarreau A. and Beaufort D. (2000) Influence of synthesis pH on Kaolinite "crystallinity" and surface properties. Clay Clay Miner. 48, 173-184.

Foerstendorf H., Heim K. and Rossberg A. (2012) The complexation of uranium(VI) and atmospherically derived CO2 at the ferrihydrite-water interface probed by time-resolved vibrational spectroscopy. J. Colloid Interf. Sci. 377, 299-306.

Fox P.M., Davis J.A. and Zachara J.M. (2006) The effect of calcium on aqueous uranium(VI) speciation and adsorption to ferrihydrite and quartz. Geochim. Cosmochim. Acta 70, 1379-1387.

Frisch M.J., G. W. Trucks, H. B. Schlegel, G. E. Scuseria, M. A. Robb, J. R. Cheeseman, et al. (2009) Gaussian 09, Gaussian 09, Revision A.02 ed. Gaussian Inc., Wallingford, CT, USA.

Fritsch K. (2018) Investigation of uranium(VI) retention by montmorillonite at high ionic strengths. Technische Universität Dresden, Dresden, Germany.

Gampp H., Maeder M., Meyer C.J. and Zuberbühler A.D. (1985) Calculation of equilibrium constants from multiwavelength spectroscopic data—II132, 95.: Specfit: two user-friendly programs in basic and standard fortran 77. Talanta 32, 257-264.

Gaona X., Dähn R., Tits J., Scheinost A.C. and Wieland E. (2011) Uptake of Np(IV) by C-S-H Phases and Cement Paste: An EXAFS Study. Environ. Sci. Technol. 45, 8765-8771.

Gaona X., Fellhauer D. and Altmaier M. (2013) Thermodynamic description of Np(VI) solubility, hydrolysis, and redox behavior in dilute to concentrated alkaline NaCl solutions. Pure Appl. Chem. 85, 2027-2049.

Garbev K., Bornefeld M., Beuchle G. and Stemmermann P. (2008) Cell dimensions and composition of nanocrystalline calcium silicate hydrate solid solutions. Part 2: X-ray and thermogravimetry study. J. Am. Ceram. Soc. 91, 3015-3023.

Garbev K., Stemmermann P., Black L., Breen C., Yarwood J. and Gasharova B. (2007) Structural features of C-S-H(I) and its carbonation in air - A Raman spectroscopic study. Part I: Fresh phases. J. Am. Ceram. Soc. 90, 900-907.

Gascó G. and Méndez A. (2005) Sorption of Ca^{2+}, Mg^{2+}, Na^{+} and K^{+} by clay minerals. Desalination 182, 333-338.

Geipel G., Reich T., Brendler V., Bernhard G. and Nitsche H. (1997) Laser and X-ray spectroscopic studies of uranium-calcite interface phenomena. J. Nucl. Mater. 248, 408-411.

George G.N. and Pickering I.J. (1995) EXAFSPAK: A Suite of Computer Programs for Analysis of X-ray Absorption Spectra, Stanford Synchrotron Radiation Laboratory, Stanford, CA. USA.

Glaus M.A., Laube A. and Van Loon L.R. (2004) A generic procedure for the assessment of the effect of concrete admixtures on the sorption of radionuclides on cement: Concept and selected results, In: Smith, B., Geschwend, B. (Hrsg.): PSI Report 2003, Vol. IV: Nuclear Energy and Safety, pp. 101-107.

Glaus M.A. and Van Loon L.R. (2004) A generic procedure for the assessment of the effect of concrete admixtures on the retention behaviour of cement for radionuclides: Concept and case studies, Nagra Technical Report 03-09.

Grambow B., Fattahi M., Montavon G., Moisan C. and Giffaut E. (2006) Sorption of Cs, Ni, Pb, Eu(III), Am(III), Cm, Ac(III), Tc(IV), Th, Zr, and U(IV) on MX 80 bentonite: An experimental approach to assess model uncertainty. Radiochim. Acta 94.

Grangeon S., Claret F., Lerouge C., Warmont F., Sato T., Anraku S., Numako C., Linard Y. and Lanson B. (2013a) On the nature of structural disorder in calcium silicate hydrates with a calcium/silicon ratio similar to tobermorite. Cement Concrete Res. 52, 31-37.

Grangeon S., Claret F., Linard Y. and Chiaberge C. (2013b) X-ray diffraction: a powerful tool to probe and understand the structure of nanocrystalline calcium silicate hydrates. Acta crystallogr. Section B, Structural science 69, 465-473.

Greenfield B.F., Ilett D.J., Ito M., McCrohon R., Heath T.G., Tweed C.J., Williams S.J. and Yui M. (1998) The effect of cement additives on radionuclide solubilities. Radiochim. Acta 82, 27-32.

Griffin L.R., Browning K.L., Lee S.Y., Skoda M.W., Rogers S. and Clarke S.M. (2016) Multilayering of Calcium Aerosol-OT at the Mica/Water Interface Studied with Neutron Reflection: Formation of a Condensed Lamellar Phase at the CMC. Langmuir 32, 13054-13064.

Gückel K., Rossberg A., Brendler V. and Foerstendorf H. (2012) Binary and ternary surface complexes of U(VI) on the gibbsite/water interface studied by vibrational and EXAFS spectroscopy. Chem. Geol. 326-327, 27-35.

Guo X.L., Meng F.J. and Shi H.S. (2017) Microstructure and characterization of hydrothermal synthesis of Al-substituted tobermorite. Constr. Build. Mater. 133, 253-260.

Hakanen M., Ervanne, H. (2006) The influence of organic cement additives on radionuclide mobility: A literature survey, Posiva Oy Working Report 2006-06.

Häußler V., Amayri S., Beck A., Platte T., Stern T.A., Vitova T. and Reich T. (2018) Uptake of actinides by calcium silicate hydrate (C-S-H) phases. Appl. Geochem. 98, 426–434.

He Y., Chen Y.-G. and Ye W.-M. (2016) Equilibrium, kinetic, and thermodynamic studies of adsorption of Sr(II) from aqueous solution onto GMZ bentonite. Environ. Earth Sci. 75.

Hellebrandt S. (2017) Grenzflächenreaktionen von Actiniden an Muskovit. Technische Universität Dresden, Dresden, Germany.

Hellebrandt S., Lee S.S., Knope K.E., Lussier A.J., Stubbs J.E., Eng P.J., Soderholm L., Fenter P. and Schmidt M. (2016) A Comparison of Adsorption, Reduction, and Polymerization of the Plutonyl(VI) and Uranyl(VI) Ions from Solution onto the Muscovite Basal Plane. Langmuir 32, 10473−10482.

Hennig C. (2007) Evidence for double-electron excitations in the L-3-edge X-ray absorption spectra of actinides. Phys. Rev. B 75, 1-7.

Hennig C., Reich T., Dähn R. and Scheidegger A.M. (2002) Structure of uranium sorption complexes at montmorillonite edge sites. Radiochim. Acta 90, 653-657.

Henry W. (1803) Experiments on the Quantity of Gases Adsorbed by Water, at Different Temperatures and under Different Pressures. Phil. Trans. R. Soc. Lond. 93.

Herterich U., Volland G., Wustholz T. and Stegmaier M. (2004) Leaching properties of self compacting concrete (SCC). Otto-Graf-J. 15, 153-175.

Hill J., Harris A.W., Manning M., Chambers A. and Swanton S.W. (2006) The effect of sodium chloride on the dissolution of calcium silicate hydrate gels. Waste Manage. 26, 758-768.

Hiltmann W. and Stribrny B. (1998) Tonmineralogie und Bodenphysik. Springer Verlag, Heidelberg, Germany.

Ho C. and Handy R.L. (1963) Electrokinetic properties of lime-treated bentonites. Clay Clay Miner. 12, 267-280.

Holliday K., Handley-Sidhu S., Dardenne K., Renshaw J., Macaskie L., Walther C. and Stumpf T. (2012) A New Incorporation Mechanism for Trivalent Actinides into Bioapatite: A TRLFS and EXAFS Study. Langmuir 28, 3845-3851.

Hubbard A.T. (2002) Encyclopedia of surface and colloid science, Encyclopedia of surface and colloid science. Dekker, New York (USA); Basel (Switzerland).

Huittinen N., Rabung T., Andrieux P., Lehto J. and Geckeis H. (2010) A comparative batch sorption and time-resolved laser fluorescence spectroscopy study on the sorption of Eu(III) and Cm(III) on synthetic and natural kaolinite. Radiochim. Acta 98, 613-620.

Huittinen N., Rabung T., Schnurr A., Hakanen M., Lehto J. and Geckeis H. (2012) New insight into Cm(III) interaction with kaolinite – Influence of mineral dissolution. Geochim. Cosmochim. Acta 99, 100-109.

Huittinen N., Scheinost A.C., Ji Y., Kowalski P.M., Arinicheva Y., Wilden A., Neumeier S. and Stumpf T. (2018) A spectroscopic and computational study of Cm^{3+} incorporation in lanthanide phosphate rhabdophane ($LnPO_4 \times 0.67H_2O$) and monazite ($LnPO_4$). Inorg. Chem. 57, 6252-6265.

Hummel W. (2008) Radioactive contaminants in the subsurface: the influence of complexing ligands on trace metal speciation. Chem. Monthly 139, 459-480.

Hummel W., Anderegg G., Puigdomènech I., Rao L. and Tochiyama O. (2005) Chemical Thermodynamics of Compounds and Complexes of U, Np, Pu, Am, Tc, Se, Ni and Zr with Selected Organic Ligands, Elsevier, Amsterdam.

Ibanez J., Artus L., Cusco R., Lopez A. and Menendez E. (2007) Hydration and carbonation of monoclinic C_2S and C_3S studied by Raman spectroscopy. J. Raman Spectrosc. 38, 61-67.

Ingram K.I., Haller L.J. and Kaltsoyannis N. (2006) Density functional theory investigation of the geometric and electronic structures of $[UO_2(H_2O)m(OH)n](2 - n)$ (n + m = 5). Dalton Trans., 2403-2414.

Irico S., Bovio A.G., Paul G., Boccaleri E., Gastaldi D., Marchese L., Buzzi L. and Canonico F. (2017) A solid-state NMR and X-ray powder diffraction investigation of the binding mechanism for self-healing cementitious materials design: The assessment of the reactivity of sodium silicate based systems. Cement Concrete Comp. 76, 57-63.

Jahn S. and Sönnke J. (2013) Endlagerstandortmodell Nord (AnSichT) - Teil II Zusammenstellung von Gesteinseigenschaften für den Langzeitsicherheitsnachweis - Zwischenbericht. BGR, Hannover, Germany.

Jasmund K. and Lagaly G. (1993) Tonminerale und Tone. Steinkopff Verlag Darmstadt, Darmstadt, Germany.

Jobmann M., Bebiolka A., Jahn S., Lommerzheim A., Maßmann J., Meleshyn A., Mrugalla S., Reinhold K., Rübel A., Stark L. and Ziefle G. (2017) Projekt ANSICHT - Sicherheits- und Nachweismethodik für ein Endlager im Tongestein in Deutschland - Synthesebericht, DBE TECHNOLOGY & GRS, Peine, Germany.

Joseph C., Stockmann M., Schmeide K., Sachs S., Brendler V. and Bernhard G. (2013) Sorption of U(VI) onto Opalinus Clay: Effects of pH and humic acid. Appl. Geochem. 36, 104-117.

Kaiser H.F. (1958) The varimax criterion for analytic rotation in factor analysis. Psychometrika 23, 187–200.

Kakihana M., Nagumo T., Okamoto M. and Kakihana H. (1987) Coordination structures for uranyl carboxylate complexes in aqueous solution studied by IR and carbon-13 NMR spectra. J. Phys. Chem. 91, 6128-6136.

Kapeluszna E., Kotwica L., Rozycka A. and Golek L. (2017) Incorporation of Al in C-A-S-H gels with various Ca/Si and Al/Si ratio: Microstructural and structural characteristics with DTA/TG, XRD, FTIR and TEM analysis. Constr. Build. Mater. 155, 643-653.

Kienzler B., Borkel C., Metz V. and Schlieker M. (2016) Long-Term Interactions of Full-Scale Cemented Waste Simulates with Salt Brines. Karlsruher Institut für Technologie (KIT).

Kienzler B., Metz V., Brendebach B., Finck N., Plaschke M., Rabung T., Rothe J. and Schild D. (2010) Chemical status of U(VI) in cemented waste forms under saline conditions. Radiochim. Acta 98, 675-684.

Kim J.I. and Czerwinski K.R. (1996) Complexation of metal ions with humic acid: Metal ion charge neutralization model. Radiochim. Acta 73, 5-10.

Kitamura A., Yamamura T., Haseb H., Yamamoto T. and Moriyama H. (1998) Measurement of Hydrolysis Species of U(VI) by Time-Resolved Laser Induced Fluorescence Spectroscopy. Radiochim. Acta 82, 147-152.

Klimesch D.S. and Ray A. (1998) Effects of quartz particle size and kaolin on hydrogarnet formation during autoclaving. Cement Concrete Res. 28, 1317-1323.

Komarneni S., Roy D.M., Fyfe C.A. and Kennedy G.J. (1987) Naturally-Occurring 1.4 nm Tobermorite and Synthetic Jennite - Characterization by Al-27 and Si-29 MAS NMR Spectroscopy and Cation-Exchange Properties. Cement Concrete Res. 17, 891-895.

Komarneni S., Roy R., Roy D.M., Fyfe C.A. and Kennedy G.J. (1985a) Al-Substituted Tobermorite - the Coordination of Aluminum as Revealed by Solid-State Al-27 Magic Angle Spinning (MAS) NMR. Cement Concrete Res. 15, 723-728.

Komarneni S., Roy R., Roy D.M., Fyfe C.A., Kennedy G.J., Bothnerby A.A., Dadok J. and Chesnick A.S. (1985b) Al-27 and Si-29 Magic Angle Spinning Nuclear Magnetic-Resonance Spectroscopy of Al-Substituted Tobermorites. J. Mater. Sci. 20, 4209-4214.

Kowal-Fouchard A., Drot R., Simoni E. and Ehrhardt J. (2004) Use of Spectroscopic Techniques for Uranium(VI)/Montmorillonite Interaction Modeling. Environ. Sci. Technol. 38, 1399-1407.

Kresge A. (1964) Solvent isotope effect in H2O–D2O mixtures. Pure Appl. Chem 8, 243-258.

Kretzschmar J., Tsushima S., Drobot B., Steudtner R., Schmeide K. and Stumpf T. (2020) Trimeric uranyl(VI)–citrate forms Na^{+}, Ca^{2+}, and La^{3+} sandwich complexes in aqueous solution. Chem. Comm. 56, 13133-13136.

Kretzschmar J., Tsushima S., Lucks C., Jäckel E., Meyer R., Steudtner R., Müller K., Rossberg A., Schmeide K. and Brendler V. (2021) Dimeric and trimeric uranyl(VI)–citrate complexes in aqueous solution. Inorg. Chem., doi.org/10.1021/acs.inorgchem.1c00522.

Krishnan R., Binkley J.S., Seeger R. and Pople J.A. (1980) Self-consistent molecular orbital methods. XX. A basis set for correlated wave functions. J. Chem. Phys. 72, 650-654.

Küchle W., Dolg M., Stoll H. and Preuss H. (1994) Energy-adjusted pseudopotentials for the actinides. Parameter sets and test calculations for thorium and thorium monoxide. J. Chem. Phys. 100, 7535-7542.

Kwan S., Larosa J. and Grutzeck M.W. (1995) Si-29 and Al-27 MAS NMR Study of Stratlingite. J. Am. Ceram. Soc. 78, 1921-1926.

Lakowicz J.R. (2006) Principles of fluorescence spectroscopy. Springer, New York.

Langmuir I. (1918) The adsorption of gases on plane surfaces of glass, mica and platinum. Journal of the American Chemical Society 40.

Lee C., Yang W. and Parr R.G. (1988) Development of the Colle-Salvetti correlation-energy formula into a functional of the electron density. Phys. Rev. B 37, 785-789.

Lee J.-Y., Vespa M., Gaona X., Dardenne K., Rothe J., Rabung T., Altmaier M. and Yun J.-I. (2017) Formation, stability and structural characterization of ternary $MgUO_2(CO_3)_3^{2-}$ and $Mg_2UO_2(CO_3)_{3(aq)}$ complexes. Radiochim. Acta 105, 171–185.

Lee J.Y. and Yun J.I. (2013) Formation of ternary $CaUO_2(CO_3)_3^{(2-)}$ and $Ca_2UO_2(CO_3)_{3(aq)}$ complexes under neutral to weakly alkaline conditions. Dalton Trans. 42, 9862-9869.

Lee S.S., Fenter P., Nagy K.L. and Sturchio N.C. (2012) Monovalent ion adsorption at the muscovite (001)-solution interface: relationships among ion coverage and speciation, interfacial water structure, and substrate relaxation. Langmuir 28, 8637-8650.

Lefevre G., Kneppers J. and Fedoroff M. (2008) Sorption of uranyl ions on titanium oxide studied by ATR-IR spectroscopy. J. Colloid Interf. Sci. 327, 15-20.

Lefevre G., Noinville S. and Fedoroff M. (2006) Study of uranyl sorption onto hematite by in situ attenuated total reflection-infrared spectroscopy. J. Colloid Interf. Sci. 296, 608-613.

Li G.G., Bridges F. and Booth C.H. (1995) X-ray-absorption fine-structure standards: A comparison of experiment and theory. Phys. Rev. B Condens. Matter 52, 6332-6348.

Lommerzheim A. and Jobmann M. (2014) Endlagerkonzept sowie Verfüll- und Verschlusskonzept für das Standortmodell NORD, TEC-08-2014-Z. DBE Technology, Germany.

Lothenbach B., Scrivener K. and Hooton R.D. (2011) Supplementary cementitious materials. Cement Concrete Res. 41, 1244-1256.

Maher K., Bargar J.R. and Brown G.E., Jr. (2013) Environmental speciation of actinides. Inorg. Chem. 52, 3510-3532.

Malinowski E.R. (2002) Determination of the number of factors and the experimental error in a data matrix. Anal. Chem. 49, 612-617.

Marques Fernandes M., Baeyens B., Dähn R., Scheinost A.C. and Bradbury M.H. (2012) U(VI) sorption on montmorillonite in the absence and presence of carbonate: A macroscopic and microscopic study. Geochim. Cosmochim. Acta 93, 262-277.

Marques Fernandes M., Stumpf T., Rabung T., Bosbach D. and Fanghänel T. (2008) Incorporation of trivalent actinides into calcite: A time resolved laser fluorescence spectroscopy (TRLFS) study. Geochim. Cosmochim. Acta 72, 464-474.

Martínez-Torrents A., Meca S., Baumann N., Martí V., Giménez J., de Pablo J. and Casas I. (2013) Uranium speciation studies at alkaline pH and in the presence of hydrogen peroxide using time-resolved laser-induced fluorescence spectroscopy. Polyhedron 55, 92-101.

Matz W., Schell N., Bernhard G., Prokert F., Reich T., Claussner J., Oehme W., Schlenk R., Dienel S., Funke H., Eichhorn F., Betzl M., Prohl D., Strauch U., Hüttig G., Krug H., Neumann W., Brendler V., Reichel P., Denecke M.A. and Nitsche H. (1999) ROBL - a CRG beamline for radiochemistry and materials research at the ESRF. J. Synchrotron Radiat. 6, 1076-1085.

Mayordomo N. (2017) Experimental and theoretical studies of mixed smectite and Al_2O_3 nanoparticles to improve pollutant retention in geochemical barriers, Departamento de Química Analítica, Química Física e Ingeniería Química. Universidad de Alcalá, Madrid, Spain.

McGlynn S.P., Smith J.K. and Neely W.C. (1961) Electronic Structure, Spectra, and Magnetic Properties of Oxycations. III. Ligation Effects on the Infrared Spectrum of the Uranyl Ion J. Chem. Phys. 35, 105-116.

Meca A. (2009) Doctoral Thesis: Processos Que Afecten La Mobilitat De L'urani En Entorns Hiperalcalins Oxidants I Sediments Contaminats. Universitat Politècnica de Catalunya, MANRESA.

Meleshyn A., Azeroual M., Reeck T., Houben G., Riebe B. and Bunnenberg C. (2009) Influence of (Calcium-)Uranyl-Carbonate Complexation on U(VI) Sorption on Ca- and Na-Bentonites. Environ. Sci. Technol. 43, 4896–4901.

Milodowski A.E., Norris S. and Alexander W.R. (2016) Minimal alteration of montmorillonite following long-term interaction with natural alkaline groundwater: Implications for geological disposal of radioactive waste. Appl. Geochem. 66, 184-197.

Missana T. and García-Gutiérrez M. (2007) Adsorption of bivalent ions (Ca(II), Sr(II) and Co(II)) onto FEBEX bentonite. Phys. Chem. Earth, Parts A/B/C 32, 559-567.

Missana T., Garcia-Gutierrez M. and Alonso U. (2008) Sorption of strontium onto illite/smectite mixed clays. Phys. Chem. Earth, Parts A/B/C 33, S156-S162.

Moll H., Reich T. and Szabo Z. (2000) The hydrolysis of dioxouranium(VI) investigated using EXAFS and O-17-NMR. Radiochim. Acta 88, 411-415.

Moll H., Rossberg A., Steudtner R., Drobot B., Mueller K. and Tsushima S. (2014) Uranium(VI) Chemistry in Strong Alkaline Solution: Speciation and Oxygen Exchange Mechanism. Inorg. Chem. 53, 1585-1593.

Moroni L.P. and Glasser F.P. (1995) Reactions between cement components and U(VI) oxide. Waste Manage. 15, 243-254.

Morris D.E., Conradson S.G., Chisholm-Brause C.J., Barr M.E. and Eller P.G. (1994) Optical spectroscopic studies of the sorption of UO_2^{2+} species on a reference smectite. Geochim. Cosmochim. Acta 58, 3613-3623.

Moulin C., Laszak I., Moulin V. and Tondre C. (1998) Time-Resolved Laser-Induced Fluorescence as a Unique Tool for Low-Level Uranium Speciation. Appl. Spectrosc. 52, 528-535.

Moulin V., Tits J., Moulin C., Decambox P., Mauchien P. and Deruty O. (1992) Complexation Behavior of Humic Substances Towards Actinides and Lanthanides Studied by Time-Resolved Laser-Induced Spectrofluorometry. Radiochim. Acta 58-9, 121-128.

Müller K. (2010) The sorption of uranium(VI) and neptunium(V) onto surfaces of selected metal oxides and alumosilicates studied by in situ vibrational spectroscopy. Technische Universität Dresden, Dresden, Germany.

Müller K., Brendler V. and Foerstendorf H. (2008) Aqueous uranium(VI) hydrolysis species characterized by attenuated total reflection Fourier-transform infrared spectroscopy. Inorg. Chem. 47, 10127-10134.

Müller K., Foerstendorf H., Brendler V., Rossberg A., Stolze K. and Gröschel A. (2013) The surface reactions of U(VI) on γ-Al_2O_3 — In situ spectroscopic evaluation of the transition from sorption complexation to surface precipitation. Chem. Geol. 357, 75-84.

Müller K., Foerstendorf H., Meusel T., Brendler V., Lefèvre G., Comarmond M.J. and Payne T.E. (2012) Sorption of U(VI) at the TiO_2–water interface: An in situ vibrational spectroscopic study. Geochim. Cosmochim. Acta 76, 191-205.

Neck V. and Kim J.I. (2000) An electrostatic approach for the prediction of actinide complexation constants with inorganic ligands-application to carbonate complexes. Radiochim. Acta 88, 815–822.

Neck V. and Kim J.I. (2001) Solubility and hydrolysis of tetravalent actinides. Radiochim. Acta 89, 1-16.

Nguyen-Trung C., Palmer D.A., Begun G.M., Peiffert C. and Mesmer R.E. (2000) Aqueous Uranyl Complexes 1. Raman Spectroscopic Study of the Hydrolysis of Uranyl(VI) in Solutions of Trifluoromethanesulfonic Acid and/or Tetramethylammonium Hydroxide at 25°C and 0.1 MPa. J. Solution Chem. 29, 101-129.

Noubactep C., Sonnefeld J., Merten D., Heinrichs T. and Sauter M. (2006) Effects of the presence of pyrite and carbonate minerals on the kinetics of the uranium release from a natural rock. J. Radioanal. Nucl. Chem. 270, 325-333.

Nowak T. and Maßmann J. (2013) Endlagerstandortmodell Nord (AnSichT) - Teil III: Auswahl von Gesteins- und Fluideigenschaften für numerische Modellberechnungen im Rahmen des Langzeitsicherheitsnachweises. Bundesanstalt für Geowissenschaften und Rohstoffe (BGR), Hannover, Germany.

Nunes M.T. and Gil V.M.S. (1987) New NMR evidence on the uranyl□citrate complexes. Inorganica Chimica Acta 129, 283-287.

Ortaboy S., Li J.Q., Geng G.Q., Myers R.J., Monteiro P.J.M., Maboudian R. and Carraro C. (2017) Effects of CO_2 and temperature on the structure and chemistry of C-(A-)S-H investigated by Raman spectroscopy. RSC Advances 7, 48925-48933.

Parkhurst L. and Appelo C. (2013) Description of input and examples for PHREEQC version 3—A computer program for speciation, batch-reaction, one-dimensional transport, and inverse geochemical calculations, Techniques and Methods, book 6. U.S. Geological Survey, Denver, USA.

Pasilis S.P. and Pemberton J.E. (2003) Speciation and Coordination Chemistry of Uranyl(VI)−Citrate Complexes in Aqueous Solution. Inorg. Chem. 42, 6793-6800.

Pointeau I., Landesman C., Giffaut E. and Reiller P. (2004) Reproducibility of the uptake of U(VI) onto degraded cement pastes and calcium silicate hydrate phases. Radiochim. Acta 92, 645–650.

Pointeau I., Piriou B., Fedoroff M., Barthes M.G., Marmier N. and Fromage F. (2001) Sorption mechanisms of Eu^{3+} on CSH phases of hydrated cements. J. Colloid Interf. Sci. 236, 252-259.

Pointeau I., Reiller P., Mace N., Landesman C. and Coreau N. (2006) Measurement and modeling of the surface potential evolution of hydrated cement pastes as a function of degradation. J. Colloid Interf. Sci. 300, 33-44.

Qu X.L., Zhao Z.G. and Zhao X.G. (2018) Microstructure and characterization of aluminum-incorporated calcium silicate hydrates (C-S-H) under hydrothermal conditions. RSC Advances 8, 28198-28208.

Rajan K.S. and Martell A.E. (1965) Equilibrium Studies of Uranyl Complexes. III. Interaction of Uranyl Ion with Citric Acid. Inorg. Chem. 4, 462-469.

Ressler T. (1998) WinXAS: a program for X-ray absorption spectroscopy data analysis under MS-Windows. J. Synchrotron Radiat. 5, 118-122.

Richter C., Müller K., Drobot B., Steudtner R., Großmann K., Stockmann M. and Brendler V. (2016) Macroscopic and spectroscopic characterization of uranium(VI) sorption onto orthoclase and muscovite and the influence of competing Ca^{2+}. Geochim. Cosmochim. Acta 189, 143-157.

Rossberg A., Reich T. and Bernhard G. (2003) Complexation of uranium(VI) with protocatechuic acid - application of iterative transformation factor analysis to EXAFS spectroscopy. Anal. Bioanal. Chem. 376, 631-638.

Sato M. and Matsuda S. (1969) Structure of vaterite and infrared spectra. Z. Kristallogr. Krist. 129, 405-410.

Schatz T., Kanerva N., Martikainen J. and Sane P. (2013) Buffer Erosion in Dilute Groundwater. Posiva Oy, Eurajoki, Finland.

Schlegel M.L., Nagy K.L., Fenter P., Cheng L., Sturchio N.C. and Jacobsen S.D. (2006) Cation sorption on the muscovite (001) surface in chloride solutions using high-resolution X-ray reflectivity. Geochim. Cosmochim. Acta 70, 3549-3565.

Schmeide K., Fritsch K., Lippold H., Poetsch M., Kulenkampff J., Lippmann-Pipke J., Jordan N., Joseph C., Moll H., Cherkouk A. and Bader M. (2016) Joint project: Retention of radionuclides relevant for final disposal in natural clay rock and saline systems - Subproject 2: Geochemical behavior and transport of radionuclides in saline systems in the presence of repository-relevant organics. HZDR-068, Wissenschaftlich-Technische Berichte, Helmholtz-Zentrum Dresden-Rossendorf, Dresden, Germany.

Schmeide K., Gürtler S., Müller K., Steudtner R., Joseph C., Bok F. and Brendler V. (2014) Interaction of U(VI) with Äspö diorite: A batch and in situ ATR FT-IR sorption study. Appl. Geochem. 49, 116-125.

Schmidt M., Lee S.S., Wilson R.E., Soderholm L. and Fenter P. (2012) Sorption of tetravalent thorium on muscovite. Geochim. Cosmochim. Acta 88, 66-76.

Schmidt M., Stumpf T., Walther C., Geckeis H. and Fanghänel T. (2009) Incorporation versus adsorption: substitution of Ca^{2+} by Eu^{3+} and Cm^{3+} in aragonite and gypsum. Dalton Trans., 6645-6650.

Schmidt M., Stumpf T., Walther C., Geckeis H. and Fanghänel T. (2010) Phase transformation in $CaCO_3$ polymorphs: A spectroscopic, microscopic and diffraction study. J. Colloid Interf. Sci. 351, 50-56.

Schnurr A. (2015) Untersuchungen zur Radionuklidsorption an Tonmineraloberflächen bei hohen Ionenstärken, Fakultät für Chemie und Biowissenschaften. Karlsruher Institut für Technologie (KIT), Karlsruhe, Germany.

Schnurr A., Marsac R., Rabung T., Lützenkirchen J. and Geckeis H. (2015) Sorption of Cm(III) and Eu(III) onto clay minerals under saline conditions: Batch adsorption, laser-fluorescence spectroscopy and modeling. Geochim. Cosmochim. Acta 151, 192-202.

Smith K.F., Bryan N.D., Swinburne A.N., Bots P., Shaw S., Natrajan L.S., Mosselmans J.F.W., Livens F.R. and Morris K. (2015) U(VI) behaviour in hyperalkaline calcite systems. Geochim. Cosmochim. Acta 148, 343-359.

Stade H. and Wieker W. (1982) On the structure of ill-crystallized calcium hydrogen silicates. 3. Incorporation of Al^{3+} ions into C-S-H(di,poly), and formation of an instable 11-Å tobermorite. Z. Anorg. Allg. Chem. 494, 179-188.

Steudtner R., Sachs S., Schmeide K., Brendler V. and Bernhard G. (2011) Ternary uranium(VI) carbonato humate complex studied by cryo-TRLFS. Radiochim. Acta 99, 687-692.

Stumm W. (1992) Chemistry of the Solid-Water Interface Processes at the Mineral-Water and Particle-Water Interface in Natural Systems. John Wiley & Sons, Inc., New York, USA.

Stumpf T., Tits J., Walther C., Wieland E. and Fanghänel T. (2004) Uptake of trivalent actinides (curium(III)) by hardened cement paste: a time-resolved laser fluorescence spectroscopy study. J. Colloid Interf. Sci. 276, 118-124.

Sun G.K., Young J.F. and Kirkpatrick R.J. (2006) The role of Al in C-S-H: NMR, XRD, and compositional results for precipitated samples. Cement Concrete Res. 36, 18-29.

Suzuki Y., Tanaka K., Kozai N. and Ohnuki T. (2010) Effects of Citrate, NTA, and EDTA on the Reduction of U(VI) by Shewanella putrefaciens. Geomicrobiology J. 27, 245-250.

Sylwester E.R., Hudson E.A. and Allen P.G. (2000) The structure of uranium (VI) sorption complexes on silica, alumina, and montmorillonite. Geochim. Cosmochim. Acta 64, 2431-2438.

Takita Y., Eto M., Sugihara H. and Nagaoka K. (2007) Promotion mechanism of co-existing NaCl in the synthesis of $CaCO_3$. Mater. Lett. 61, 3083-3085.

Thoenen T., Hummel W., Berner U. and Curti E. (2014a) The PSI/Nagra Chemical Thermodynamic Database 12/07, PSI report 14-04. Paul Scherrer Institut (PSI), Villigen, Switzerland.

Thoenen T., Hummel W., Berner U. and Curti E. (2014b) The PSI/Nagra Chemical Thermodynamic Database 12/07, PSI report 14-04. Paul Scherrer Institut (PSI), Villigen, Switzerland.

Tits J., Fujita T., Tsukamoto M. and Wieland E. (2008) Uranium(VI) Uptake by Synthetic Calcium Silicate Hydrates. MRS Proceedings 1107, 467-474.

Tits J., Gaona X., Laube A. and Wieland E. (2014) Influence of the redox state on the neptunium sorption under alkaline conditions: Batch sorption studies on titanium dioxide and calcium silicate hydrates. Radiochim. Acta 102.

Tits J., Geipel G., Macé N., Eilzer M. and Wieland E. (2011) Determination of uranium(VI) sorbed species in calcium silicate hydrate phases: A laser-induced luminescence spectroscopy and batch sorption study. J. Colloid Interf. Sci. 359, 248-256.

Tits J., Stumpf T., Rabung T., Wieland E. and Fanghänel T. (2003) Uptake of Cm(III) and Eu(III) by calcium silicate hydrates: A solution chemistry and time-resolved laser fluorescence spectroscopy study. Environ. Sci. Technol. 37, 3568-3573.

Tits J., Walther C., Stumpf T., Mace N. and Wieland E. (2015) A luminescence line-narrowing spectroscopic study of the uranium(VI) interaction with cementitious materials and titanium dioxide. Dalton Trans. 44, 966-976.

Tits J. and Wieland E. (2018) Actinide Sorption by Cementitious Materials. Paul Scherrer Institut (PSI), Nuclear Energy and Safety Research Department (NES), Laboratory for Waste Management (LES), Villigen, Switzerland.

Tits J., Wieland E. and Bradbury M.H. (2005) The effect of isosaccharinic acid and gluconic acid on the retention of Eu(III), Am(III) and Th(IV) by calcite. Appl. Geochem. 20, 2082-2096.

Torrents A.M. (2014) Doctoral Thesis: Effect of Alkaline Conditions on Near-field Processes of a Spent Nuclear Fuel Geological Repository, Department of Chemical Engineering. Universitat Politècnica de Catalunya-Barcelona Tech, Catalunya.

Tournassat C., Tinnacher R.M., Grangeon S. and Davis J.A. (2018) Modeling uranium(VI) adsorption onto montmorillonite under varying carbonate concentrations: A surface complexation model accounting for the spillover effect on surface potential. Geochim. Cosmochim. Acta 220, 291-308.

Tsushima S. (2011) On the "yl" bond weakening in uranyl(VI) coordination complexes. Dalton Trans. 40, 6732-6737.

Tsushima S., Nagasaki S., Tanaka S. and Suzuki A. (1998) A Raman Spectroscopic Study of Uranyl Species Adsorbed onto Colloidal Particles. J. Phys. Chem. B 102, 9029–9032.

Van Loon L.R., Glaus M.A., Stallone S. and Laube A. (1997) Sorption of isosaccharinic acid, a cellulose degradation product on cement. Environ. Sci. Technol. 31, 1243-1245.

Vanura P. and Kuca L. (1980) Citrate complexes of uranyl in solutions with high citrate concentrations. Collection of Czechoslovak Chemical Communications 45, 41-53.

Viallis-Terrisse H., Nonat A. and Petit J.-C. (2001) Zeta-Potential Study of Calcium Silicate Hydrates Interacting with Alkaline Cations. J. Colloid Interf. Sci. 244, 58-65.

Vuorinen U., Lehikoinen J., A. L. and Ervanne H. (2006) Effects of Salinity and High pH on Crushed Rock and Bentonite – Experimental Work and Modelling, POSIVA 2006-01. Posiva Oy, Olkiluoto, Finland.

Wang Z., Zachara J.M., Boily J.-F., Xia Y., Resch T.C., Moore D.A. and Liu C. (2011) Determining individual mineral contributions to U(VI) adsorption in a contaminated aquifer sediment: A fluorescence spectroscopy study. Geochim. Cosmochim. Acta 75, 2965-2979.

Wang Z., Zachara J.M., Gassman P.L., Liu C., Qafoku O., Yantasee W. and Catalano J.G. (2005a) Fluorescence spectroscopy of U(VI)-silicates and U(VI)-contaminated Hanford sediment. Geochim. Cosmochim. Acta 69, 1391-1403.

Wang Z.M., Zachara J.M., McKinley J.P. and Smith S.C. (2005b) Cryogenic laser induced U(VI) fluorescence studies of a U(VI) substituted natural calcite: Implications to U(VI) speciation in contaminated Hanford sediments. Environ. Sci. Technol. 39, 2651-2659.

Wang Z.M., Zachara J.M., Yantasee W., Gassman P.L., Liu C.X. and Joly A.G. (2004) Cryogenic laser induced fluorescence characterization of U(VI) in Hanford vadose zone pore waters. Environ. Sci. Technol. 38, 5591-5597.

Warwick P., Evans N., Hall T. and Vines S. (2004) Stability constants of uranium(IV)-α-isosaccharinic acid and gluconic acid complexes. Radiochim. Acta 92.

Warwick P., Evans N. and Vines S. (2006) Studies on some divalent metal α-isosaccharinic acid complexes. Radiochim. Acta 94.

Wazne M., Korfiatis G.P. and Meng X. (2003) Carbonate Effects on Hexavalent Uranium Adsorption by Iron Oxyhydroxide. Environ. Sci. Technol. 37, 3619-3624.

Wieland E., Lothenbach B., Glaus M.A., Thoenen T. and Schwyn B. (2014) Influence of superplasticizers on the long-term properties of cement pastes and possible impact on radionuclide uptake in a cement-based repository for radioactive waste. Appl. Geochem. 49, 126-142.

Wieland E. and Van Loon L.R. (2003) Cementitious Near-Field Sorption Data Base for Performance Assessment of an ILW Repository in Opalinus Clay, PSI Bericht Nr. 03-06. Paul Scherrer Institut, Villigen, Switzerland.

Wieland E., Wanner H., Albinsson Y., Wersin P. and Karnland O. (1994) A surface chemical model of the bentonite-water interface and its implications for modelling the near field chemistry in a repository for spent fuel. Swedish Nuclear Fuel and Waste Management Company (SKB), Stockholm, Sweden.

Wolfgramm M., Thorwart K., Rauppach K. and Brandes J. (2011) Zusammensetzung, Herkunft und Genese geothermaler Tiefengrundwässer im Norddeutschen Becken (NDB) und deren Relevanz für die geothermische Nutzung. Z. Geol. Wissenschaft 339, 173-193.

Young A.J. (2012) The stability of cement superplasticiser and its effect on radionuclide behaviour, Dissertation, Loughborough University.

Young S.D., Bache B.W., Welch D. and Anderson H.A. (1981) Analysis of the potentiometric titration of natural and synthetic polycarboxylates. J. Soil Sci. 32, 579-592.

Yu P., Kirkpatrick R.J., Poe B., McMillan P.F. and Cong X.D. (1999) Structure of calcium silicate hydrate (C-S-H): Near-, mid-, and far-infrared spectroscopy. J. Am. Ceram. Soc. 82, 742-748.

11. Publications of the Helmholtz-Zentrum Dresden-Rossendorf (HZDR) within the GRaZ project

Publications (peer-reviewed):

Lippold, H., Zedek, L.: Metal dissociation from humic colloids: Kinetics with time-dependent rate constants. Chemosphere 275, 130045 (2021).

Kretzschmar, J., Tsushima, S., Drobot, B., Steudtner, R., Schmeide, K., Stumpf, T.: Trimeric uranyl(VI)–citrate forms Na^{+}, Ca^{2+}, and La^{3+} sandwich complexes in aqueous solution. Chemical Communications 56, 13133-13136 (2020).

Kretzschmar, J., Strobel, A., Haubitz, T., Drobot, B., Steudtner, R., Barkleit, A., Brendler, V., Stumpf, T.: Uranium(VI) complexes of glutathione disulfide forming in aqueous solution. Inorganic Chemistry 59, 4244-4254 (2020).

Wolter, J.-M., Schmeide, K., Huittinen, N., Stumpf, T.: Cm(III) retention by calcium silicate hydrate (C-S-H) gel and secondary alteration phases in carbonate solutions with high ionic strength: A site-selective TRLFS study. Scientific Reports 9, 14255 (2019).

Philipp, T., Shams Aldin Azzam, S., Rossberg, A., Huittinen, N., Schmeide, K., Stumpf, T.: U(VI) sorption on Ca-bentonite at (hyper)alkaline conditions – Spectroscopic investigations of retention mechanisms. Science of the Total Environment 676, 469-481 (2019).

Wolter, J.-M., Schmeide, K., Weiss, S., Bok, F., Brendler, V., Stumpf, T.: Stability of U(VI) doped calcium silicate hydrate gel in repository-relevant brines studied by leaching experiments and spectroscopy. Chemosphere 218, 241-251 (2019).

Ph.D. theses / Master theses:

Wolter, J.-M.: Stability of U(VI) and Cm(III) doped calcium (alumino)silicate hydrate phases at high ionic strengths. Ph.D. thesis, Technische Universität Dresden (2020).

Philipp, T.: U(VI) retention by Ca-bentonite and clay minerals at (hyper)alkaline conditions. Ph.D. thesis, Technische Universität Dresden (2020).

Dullies, P.: Untersuchungen zum Einfluss von Isosaccharinsäure auf die U(VI)-Rückhaltung an Ca-Bentonit unter alkalischen Bedingungen (Studies on the influence of isosaccharic acid on the U(VI) retention of Ca-bentonite under alkaline conditions). Master thesis, Hochschule für Technik und Wirtschaft Dresden (2019).

Oral presentations:

Schmeide, K., Philipp, T., Wolter, J.-M., Kretzschmar, J., Dullis, P., Schymura, S., Lippold, H., Stumpf, T.: Einfluss erhöhter Ionenstärken auf die Wechselwirkung von Actiniden/Lanthaniden mit Ca-Bentonit, Zementphasen und organischen Liganden unter hyperalkalinen Bedingungen. Abschlussworkshop des Verbundprojektes "Geochemische Radionuklidrückhaltung an Zementalterationsphasen (GRaZ)", 21.-22.01.2020, Mainz, Germany.

Kretzschmar, J., Tsushima, S., Jäckel, E., Meyer, R., Steudtner, R., Müller, K., Schmeide, K., Brendler, V., Stumpf, T.: Dimeric Uranium(VI)–Citrate Complexes: Structures and Dynamics. Jahrestagung der Fachgruppe Nuklearchemie der GDCh 2019, 25.-27.09.2019, Dresden, Germany.

Philipp, T., Schmeide, K., Rossberg, A., Huittinen, N., Stumpf, T.: Influence of pH, carbonate and calcium concentration on U(VI) retention by clay minerals at (hyper)alkaline conditions – A batch sorption and spectroscopy study. International Conference on Clay Science and Technology – EUROCLAY 2019, 01.-05.07.2019, Paris, France.

Philipp, T., Schmeide, K., Stumpf, T.: Influence of calcium on uranium and neptunium sorption on clay minerals at (hyper)alkaline conditions. 2nd International Conference on Radioanalytical and Nuclear Chemistry (RANC 2019), 05.-10.05.2019, Budapest, Hungary.

Philipp, T., Schmeide, K., Rossberg, A., Stumpf, T.: U(VI) sorption by Ca-bentonite at pH 8-13: Spectroscopic investigation of retention mechanisms. 28th Goldschmidt Conference 2018, 12.-17.08.2018, Boston, USA.

Steudtner, R., Müller, K., Schmeide, K., Brendler, V.: The uranium citric acid system and its sorption onto hematite. GDCh-Wissenschaftsforum Chemie 2017, 11.-14.09.2017, Berlin, Germany.

Posters:

Lippold, H., Becker, M., Schymura, S.: Einfluss polymerer Zementadditive auf die Mobilität von Radionukliden unter Nahfeldbedingungen eines Endlagers. Jahrestagung der Fachgruppe Nuklearchemie der GDCh 2019, 25.-27.09.2019, Dresden, Germany.

Wolter, J.-M., Schmeide, K., Huittinen, N., Bok, F., Weiss, S., Brendler, V., Stumpf, T.: Comparison of the stability of U(VI) and Cm(III) doped calcium (aluminum) silicate hydrate (C-(A)-S-H) phases at saline conditions. Migration 2019 - 17th International Conference on the Chemistry and Migration Behavior of Actinides and Fission Products in the Geosphere, 15.-20.09.2019, Kyoto, Japan.

Wolter, J.-M., Schmeide, K., Huittinen, N., Bok, F., Weiss, S., Brendler, V., Stumpf, T.: Leaching of U(VI) and Cm(III) doped calcium (aluminum) silicate hydrate gel (C-(A)-S-H) and tobermorite in saline brines. 5th International Workshop on "Mechanisms and Modelling of Waste/Cement Interactions". 25.-27.03.2019, Karlsruhe, Germany.

Philipp, T., Schmeide, K., Rossberg, A., Stumpf, T.: Competition of U(VI) hydroxide and carbonate complexation in alkaline solutions − implications for U(VI) retention by Ca-bentonite. RadChem 2018 - 18th Radiochemical Conference, 13.05.-18.05.2018, Mariánské Lázně, Czech Republic.

Wolter, J.-M., Schmeide, K., Huittinen, N., Stumpf, T.: Stability investigations of actinide doped calcium silicate hydrate phases in highly saline electrolytes. RadChem 2018 - 18th Radiochemical Conference, 13.05.-18.05.2018, Mariánské Lázně, Czech Republic.

Wolter, J.-M., Schmeide, K., Huittinen, N., Stumpf, T.: Stability of U(VI) and Cm(III) doped calcium silicate hydrate phases in highly saline brines. 2nd Workshop on Calcium Silicate Hydrates containing Aluminium: C-A-S-H II, 23.04.-24.04.2018, Dübendorf, Switzerland.

Philipp, T., Schmeide, K., Stumpf, T.: Retention of uranium(VI) by Ca-bentonite at high ionic strength and high pH studied by batch sorption tests and TRLFS. 7th International Conference on Clays in Natural and Engineered Barriers for Radioactive Waste Confinement, 24.-27.09.2017, Davos, Switzerland.

Wolter, J.-M., Schmeide, K., Stumpf, T.: Interactions between U(VI) doped CSH phases and high saline brines. Migration 2017 - 16th International Conference on the Chemistry and Migration Behaviour of Actinides and Fission Products in the Geosphere, 10.-15.09.2017, Barcelona, Spain.

Philipp, T., Schmeide, K., Stumpf, T.: U(VI) sorption by Ca-bentonite under alkaline and saline conditions as a function of pH and carbonate content. Migration 2017 - 16th International Conference on the Chemistry and Migration Behaviour of Actinides and Fission Products in the Geosphere, 10.-15.09.2017, Barcelona, Spain.

Wolter, J.-M., Schmeide, K., Stumpf, T.: Interactions between U(VI) doped CSH phases and high saline brines. ABC Salt V Actinide and Brine Chemistry in a Salt Repository Workshop (V), 26.-28.03.2017, Ruidoso, USA.

Becker, M., Lippold, H.: Complexation and adsorption of [^{152}Eu]Eu(III) to superplasticizers and bentonite at variable salt concentrations. 2nd Petrus-OPERA PhD and Early-Stage Researchers Conference on Radioactive Waste Management and Disposal, 27.06.-01.07.2016, Delft, Netherlands.

Acknowledgements

The authors thank the Federal Ministry for Economic Affairs and Energy (BMWi) and the Project Management Agency Karlsruhe - Water Technology and Waste Management (PTKA-WTE) for financial support (no. 02E11415B).

For support during spectroscopic measurements and help in spectra interpretation we thank Dr. André Rossberg (EXAFS), Dr. Nina Huittinen (site-selective TRLFS), Dr. Gerhard Geipel, Dr. Robin Steudtner and Hannes Brinkmann (TRLFS), Dr. Katharina Müller and Dr. Harald Foerstendorf (ATR FT-IR), Dr. Moritz Schmidt (CTR/RAXR) and Dr. Frank Bok (thermodynamic calculations).

Furthermore, we would like to thank Dr. Silvia Paasch (TU Dresden) and Kaitlin Kammerlander (TU Dresden) for ^{27}Al and ^{29}Si MAS NMR measurements. Dr. Atsushi Ikeda, Andrea Scholz and Dr. Jörg Grenzer is thanked for XRD measurements and helpful discussions in terms of XRD pattern improvement.

Prof. Thorsten Stumpf, Prof. Vinzenz Brendler, Dr. Jan Tits (PSI) and Dr. Barbara Lothenbach (Empa) is thanked for helpful discussions and advice.

For essential support in the daily laboratory work we thank Salim Shams Aldin Azzam and Stephan Weiss. Furthermore, we thank Carola Eckardt, Sabrina Beutner, Birke Pfützner, Stephanie Bachmann, Karsten Heim, Kathrin Nebe, Anette Rumpel, Susanna Jiminez, Christa Müller and Steffen Henke for ICP-MS analyses, ion chromatography, TIC measurements, BET determinations, IR and LSC measurements as well as for support in various other laboratory applications and radiation protection issues.

Measurements outside of Rossendorf were only possible thanks to the help of Peter Eng (at GeoSoilEnviroCARS (Sector 13), Advanced Photon Source (APS) of the Argonne National Laboratory, Lemont, IL 60439 USA), Klaus Meier (Helmholtz-Institut Freiberg für Ressourcentechnologie, 09599 Freiberg) and the cooperation with Prof. Tobias Reich, Dr. Samer Amayri, Verena Häußler and Tobias Stern (all at Johannes Gutenberg-Universität Mainz, Institut für Kernchemie, 55099 Mainz).

Finally, we would like to thank all other colleagues who contributed to the success of the project.

HELMHOLTZ ZENTRUM
DRESDEN ROSSENDORF

Institute of Resource Ecology
Bautzner Landstr. 400
01328 Dresden, Germany
Tel. +49351260-2436
Fax +49351260-12436
k.schmeide@hzdr.de
http://www.hzdr.de